DEVELOPMENT AND EVALUATION OF CONDUCTIVE NANOWIRESUSING DEOXYRIBONUCLEIC ACID AS A TEMPLATE

BY

MOMOH JIMOH ZUBAIRU SIYAKA

DEPARTMENT OF CHEMISTRY
FACULTY OF SCIENCE
AHMADU BELLO UNIVERSITY, ZARIA
NIGERIA

JULY, 2015

DEVELOPMENT AND EVALUATION OF CONDUCTIVE NANOWIRESUSING DEOXYRIBONUCLEIC ACID AS A TEMPLATE

BY

Momoh jimoh Zubairu SIYAKA
(B.Sc. (Hons.) Chemistry (ABU), M.Sc. Inorganic Chem., ABU), AMRSC
(PhD/SCIEN/07502/2009-2010)

A THESIS SUBMITTED TO THE SCHOOL OF POSTGRADUATE STUDIES, AHMADU BELLOUNIVERSITY, ZARIA

INPARTIAL FULFILLMENT OF THE REQUIREMENTS FOR THE AWARD

OF THE

DEGREE OF DOCTOR OF PHILOSOPHY IN INORGANIC CHEMISTRY

DEPARTMENT OF CHEMISTRY
FACULTY OF SCIENCE
AHMADU BELLO UNIVERSITY, ZARIA,
NIGERIA

JULY, 2015

Declaration

I declarethat the work in this Thesis entitled “DEVELOPMENT AND EVALUATION OF CONDUCTIVE NANOWIRES USING DEOXYRIBONULEIC ACID AS A TEMPLATE” has been carriedout by me in the Department of Chemistry, Ahmadu Bello University, Zaria and School of Chemistry, Newcastle University, United Kingdom under the supervision of Dr S. O. Idris, Prof. J. F. Iyun, Prof. C. E. Gimba, Prof. AdamuUzairu and Dr B.R. Horrocks. The information derived from literature has been duly acknowledged within the text and a list of references provided. No part of this work was previously presented for another degree or diploma at this or any other university.

…… ….….....

Momohjimoh Zubairu SIYAKA Date

Certification

This thesis entitled "DEVELOPMENT AND EVALUATION OF CONDUCTIVE NANOWIRES USING DEOXYRIBONULEIC ACID AS A TEMPLATE'' by Momohjimoh Zubairu SIYAKA meets the regulations governing the award of the degree of Doctor of Philosophy (PhD) Inorganic Chemistry of the Ahmadu Bello University, Zaria and is approved for its contribution to knowledge and literary presentation.

……. ……

Dr S. O. Idris Date
(Chairman, Supervisory Committee)

……. …….

Prof. J. F. Iyun Date
(Member, Supervisory Committee)

…… ……

Prof. C. E. Gimba Date
(Member, Supervisory Committee

…… ……

Prof. A. Uzairu Date
(Member, Supervisory Committee)

B. R. Horrocks 25th August,2015

Dr B. R. Horrocks Date
(Member, Supervisory Committee)

…… ……

Prof. V. O. Ajibola Date
(Head of Department)

…… ……

Prof. A. Z. Hassan Date
(Dean, School of Postgraduate Studies)

Dedication

This work is dedicated to the merciful GodandProf. J. F. Iyun (RIP) who, until his death, was the Chairman, Supervisory Committee.

Acknowledgements

Alhamdulillah, glory be to the Almighty Allah, the most high for His guidance and favour throughout the duration of this doctoral journey. I am grateful to Prof. J.F. Iyun for his guidance, encouragement, vision, support and unimaginable troubleshooting advice. Taken the stars from the night and the sun from the day! Gone, and a cloud in OUR hearts. RIP Prof JF Iyun.

Special thanks toother members of the Supervisory Committee, Dr S.O. Idris,Prof. C.E. Gimba andProf A. Uzairu for their guidance and helpful suggestions. Their guidance have served me well and I owe them a lot of gratitude.I am also indebted to Dr B.R. Horrocks, an interim supervisor of the School of Chemistry, Newcastle University, UK, for giving me the opportunity to fast-track my mission in the UK in his state-of-the-art laboratory. He made available his support and insights in a number of ways.

My friends in the UK, Thailand, Malaysia,Libya and other parts of the World were sources of joy and support.Thanks toDr Liadi Kola, Hassan Daw, Niza, Naoko Sano, Corinne Wills, ChrisMcgurk, Jerry Hagon. I also thank Dr Scott Watson of the Chemical Nanoscience Laboratoryand Dr Matthew German of the School of Dental Sciences at Dental Materials Unit for their assistance in the AFM training. Thumbs up to Dr Jonathan Pate for training on bottom-up DNA templating reaction strategies, in addition to Tracey Davey and Budhika Mendis for TEM/EDX training. Not forgetting Prof. Peter Cumpson and Naoko Sano both at EPSRC NEXUS XPS NanoLAB Research centre for the XPS training.I wish to thank my parents, Mr and Mrs SalamatuSiyaka and Mrs Suleiman (Mummy KD). Their love provided my inspiration and was my driving force.I owe them everything. Sincere gratitude to my wife, Ummil Kaltume Zubairu, for her love, encouragement and patience.

Prof. A. J. Kagbuof blessed memory, a thumb up for him even though he is not with us to see the end of the draft designwork he proofread and appreciated. The Petroleum Technology Development Fund, (PTDF) Nigeria, Nexus @ nanoLAB and Chemical Nanoscience Lab. (CNL) are all acknowledged for funding and support.

Lastly, I offer my regards to all my friends and well-wishers (too numerous to mention) who supported me during the course of the research.

List of Acronyms

Δθ	Phase shift
0D	Zero dimensional
1D	One dimensional
2D	Two dimensional
3D	Three dimensional
A	Adenine
AAO	Anodic alumina oxide
AFM	Atomic force microscopy
BE	Binding energy
C	Cytosine
C-AFM	Conductive atomic force microscopy
CMOS	Complementary metal-oxide-semiconductor
CNT	Carbon nanotube
CPs	Conductive polymers
CT-DNA	Calf-thyme DNA
CV	Cyclic Voltammetry
d	Diameter of nanowires
DMF	Dimethyl formamide
DNA	Deoxyribonucleic acid
DSC	Differential Scanning Calorimetry
dsDNA	Double-stranded-deoxyribonucleic acid
DTA	Differential Thermal Analysis
EDTA	Ethylenediaminetetracetic acid
EDX	Energy dispersive X-ray analysis
EFM	Electrostatic force microscopy

Ep	peak potential
eV	Electron volt
$f0$	Resonance frequency
Fe_2O_3 Hematite	
FeOOH	Goethite
FT-IR	Fourier transform-infrared (spectroscopy)
FWHM	Full-width-at-half maximum
G	Guanine
HRP/H_2O_2	Horseradish peroxidase
HT-DNA	Herring testes DNA
IBM	International Business Machines
Im	Imadazole
ITRS	International Technology Roadmap for semiconductors
I-V	Current voltage
k	Cantilever spring constant
L	Length of nanowire
Me_3SiCI	Chlorotrimethylsilane (CTMS)
MFM	Magnetic force microscopy
mM	Millimolar
µm	Micrometre
µL	Microlitre
NP	Nanoparticles
PANI	polyaniline
PC	polycarbonate
PEDOT	Poly(3,4-EthyleneDioxyThiopene)
PImi	Polyimidazole

PIn	Polyindole
Ppy	Polypyrrole
Py	Pyrrole
Q-dot	Quantum dot
SAED	Selected Area Electron Diffraction
SCM	Scanned Capacitance microscopy
SPM	Scanning probe microscopy
SWNTs	Single walled carbon nanotubes
T	Thymine
TEM	Transmission Electron Microscopy
TG	Thermogravimetry
Tm	Melting Temperature
UV	Ultraviolet
XPS	X-ray photoelectron Spectroscopy
XRD	Powder X-ray diffraction
λ-DNA	Lambda Deoxyribonucleic acid

Table of Contents

Title page		ii
Declaration		iii
Certification		iv
Dedication		v
Acknowledgements		vi
List of Acronyms		vii
Table of Contents		x
List of Figures		xv
List of Tables		xxi
List of Plates		xxii
List of Schemes		xxiii
List of Appendices		xxiv
Abstract		xxv
CHAPTER ONE		
1.0	**INTRODUCTION**	1
1.1	**Nanoscience, Nanotechnology and NanoChemistry**	1
1.2	**Size Matters**	3
1.3	**Classification of Nanomaterials**	4
1.4	**Nanowires**	5
1.5	**Preparation of Nanowires and Bottom-up Synthetic Strategies**	5
1.6	**Template-directed Synthesis**	7
1.6.1	Templating nanowires	7

1.6.2 Templating using biopolymer nanostructure 9

1.7 **DNA Structure and Properties** 10

1.8 **Conducting Polymers** 13

1.9 **Conducting Polymers Templated on DNA** 14

1.9.1 Inorganic semiconductors templated on DNA 15

1.9.2 DNA-templated nanowires synthesis and alignment 16

1.10 **Justification of the Research** 18

1.11 **Aim and Objectives** 19

1.11.1 Objectives 19

CHAPTER TWO

2.0 **LITERATURE REVIEW** 20

2.1 **Semiconductor Compound Templated on DNA** 20

2.2 **Conducting Polymer Templated on DNA** 24

2.3 **Metal Templated on DNA** 31

2.4 **Nanowires Characterization Techniques** 38

2.4.1 Cyclic voltammetry 38

2.4.2 Ultraviolet/Visible spectrophotometry 39

2.4.3 Fourier transform infrared (FTIR) spectroscopy 40

2.4.4 Transmission electron microscopy (TEM) and energy dispersive X-ray spectroscopy 41

2.4.5 Thermalanalytical techniques, TGA/DTG/DSC 42

2.4.6 Powder x-ray diffraction, XRD 43

2.4.7 X-rayphotoelectron spectroscopy, XPS 45

2.4.8 Atomicforce microscopy (AFM) 47

2.4.9 Scanned conductance microscopy (SCM) 50

CHAPTER THREE

3.0 **MATERIALS AND METHODS** 53

3.1 Materials 53

3.1.1 Reagents 53

3.1.2 Wafers and apparatus 53

3.2 Cleaning of $1 \times 1cm^2$ pieces Si wafers 54

3.3 Preparation of DNA-templated Nanowires 55

3.3.1 Preparation of DNA/FeOOH nanowires 55

3.3.2 Preparation of DNA/FeOOH nanowires for characterisations 55

3.3.3 Preparation of bulk FeOOH nanoparticles 60

3.3.4 Preparation of bulk FeOOH nanoparticles for characterizations 61

3.4 **Preparation of DNA/Fe_2O_3 Nanowires** 62

3.4.1 Preparation of DNA/Fe_2O_3 nanowires for characterisations 62

3.4.2 Preparation of bulk Fe_2O_3 nanoparticles 63

3.5 **Polymerization ofPyrrole (Py) on DNA Solution** 64

3.5.1 Preparation of Ppyand DNA/Ppy nanowires 64

3.5.2 Preparation of DNA/Ppy nanowires for characterisations 65

3.5.3 Formation of Bulk (Ppy) 66

3.5.3.1 Formation by oxidation with $FeCl_3$ 66

3.5.3.2 Formation of Ppy by electrochemical reduction 66

3.6 **Polymerization of Imidazole on DNA Solution** 68

3.6.1 Preparation of DNA/PImi nanowires and bulk PImi 68

3.6.2 Preparation of DNA/Plmi nanowires for characterisations 68

3.7 **Alignment of DNA-templated Nanowires using N_2 flow Assisted** 69

CHAPTER FOUR

4.0 **RESULTS** 71

4.1 **Cyclic Voltammetry** 71

4.2 **FT-IR** 71

4.3 **UV-vis Spectra** 71

4.4 **Thermal Measurements** 91

4.5 **XRD Patterns** 91

4.6 **TEM Analyses** 91

4.7 **EDX Analyses** 91

4.8 **XPS Analyses** 91

4.9 **AFM Analyses** 121

4.10 **EFM (Electrical Studies)** 168

CHAPTER FIVE

5.0 **DISCUSSION** 181

5.1 **CyclicVoltammetric Studies** 181

5.2 **FTIRSpectroscopy Studies** 182

5.3 **UV–vis Spectra of net DNA and its Templated** 187

5.4 **TG/DTA/DSC Measurements** 188

5.5 **X-ray Diffraction Patterns** 189

5.6 **Transmission Electron Microscopy (TEM) and EDX Studies** 191

5.7 **X-ray Photoelectron Spectroscopy (XPS) Measurements** 193

5.8 **Atomic Force Microscopy (AFM) Studies** 199

5.9 **Electrical Properties of all the DNA-Templated Nanowires** 203

CHAPTER SIX

6.0 **SUMMARY AND CONCLUSIONS** 206

6.1 **Summary** 206

6.2 **Conclusions** 208

6.3 **Recommendations** 210

REFERENCES 212

APPENDICES 226

List of Figures

Fig. 1.1 Moore's law trend line plot 2

Fig. 1.2Scanning Tunnelling Microscopy (STM) images of 35 Xe atoms on a Nickel surface 3

Fig. 1.3 Illustration of Templating approach to produce Nanowires from porous Membrane by Electrochemical Reduction 9

Fig 2.1AFM/SEM Images of CdS Nanoparticles at DNA on Mica 21

Fig. 2.2AFM Image of DNA/PANI Nanowires on Si wafer at pH = 5, (b) Oxidative Polymerization for DNA/PANI Nanowires at pH = 3.2 with incomplete Coverage, (c) Oxidative Polymerisation at pH = 4 25

Fig. 2.3AFM Image of DNA/Ppy Nanowires prepared on Mica after Polymerization scale bar, 200 nm, and height scale 4 nm 27

Fig. 2.4AFM Images of DNA/Ppy Nanowires on Si wafer after (a) 2 days, scale bar 500 nm height scale 8 nm. (b) After 6 days, and (c) 1month, scale bar 500 nm height scale 12 nm 27

Fig. 2.5AFM Images of DNA/Pin Nanowires on Si wafers showing the effectof time on Morphology of the Nanowires 28

Fig. 2.6AFM Images (in tapping mode) of DNA/TPT Nanowires on Si wafer.(b) AFM image showing rope-like assemblies of DNA/TPT Nanowires with branches, scale height 20 nm 29

Fig 2.7DNA/PImi/Pd AFM Image as Nanowire Network 30

Fig 2.8AFM Image of a DNA-Templated Ag^0 Nanowires bridging between Gold Electrode 31

Fig. 2.9TEM Image of Metallized DNA strands at an early stage of Metallization Process 32

Fig. 2.9.1 AFM height image of DNA/Cu nanowires with arrows showing specific Cu deposition 33

Fig. 2.9.2AFM image of a section of DNA/Cu nanowire with bead-on-a-string morphology 34

Fig. 2.9.3 UV-Vis spectra showing the photoinduced sequence forDNA/Ag^{+}, pure DNA and DNA/Ag 36

Fig. 2.9.4 AFM Image of Ag nanoparticles on DNA network 36

Fig. 2.10Illustration for current as a function of Voltage for CV 38

Fig. 2.11X-ray beams feature on Solid Lattice 44

Fig. 2.12Illustration of Photoemission showing XPS basis of Ni $2p_{3/2}$ 46

Fig. 2.13Illustration of AFM Major Components 48

Fig. 2.14 AFM basic mode of Operation(a) Contact mode(b) Tapping mode 49

Fig. 2.15 Schematic of SCM in the interleave line (second) scan with tip at Fixed height above the Sample 51

Fig. 2.16SCM Technique to detect the Conductive Properties of Nanowires using dual pass method. (a) 1^{st} pass to acquire Material Topography. (b) Interleave (2nd) pass for Phase Shift signal 52

Fig. 3.1Modification of Si wafer through Self-Assembly of Monolayer of CTMS 54

Fig. 4.1Cyclic Voltammograms of ppy and λ-DNA /Ppy 73

Fig. 4.2Cyclic Voltammograms of PImi and λ-DNA/PImi 74

Fig. 4.3FTIR Spectra ofNet DNA and DNA/Ppy 75

Fig. 4.4FTIR Spectra of and Net DNA and DNA/PImi 76

Fig. 4.5FTIR Spectra ofnet DNA and DNA/Fe_2O_3 77

Fig. 4.6FTIR Spectra of net DNA and DNA/FeOOH 78

Fig. 4.7FTIR Spectrum of Bare HT-DNA 80

Fig. 4.8FTIR Spectra of Pyrrole/Polypyrrole 82

Fig. 4.9FTIR Spectra of Imidazole/Polyimidazole 83

Fig. 4.10FTIR Spectra of net inorganic oxide Semiconductor FeOOH Nanoparticles 84

Fig. 4.11FTIR Spectra of net inorganic oxide Semiconductor Fe_2O_3Nanoparticles 85

Fig. 4.12 UV-Vis Absorption Spectrum of neat HT-DNA 86

Fig. 4.13 UV-Vis Absorption Spectrum of neat HT-DNA and HT-DNA/FeOOH 87

Fig. 4.14 UV-Vis Absorption Spectrum of neat HT-DNA and HT-DNA/Fe_2O_3 88

Fig. 4.15 UV-Vis Absorption Spectrum of neat HT-DNA and HT-DNA/Ppy 89

Fig. 4.16UV-Vis Absorption Spectrum of neat HT-DNA and HT-DNA/PImi 90

Fig. 4.17 TG-DTA of FeOOH Nanoparticles 92

Fig. 4.18 DSC of FeOOH Nanoparticles 93

Fig. 4.19 TG-DTA of Fe_2O_3 Nanoparticles 94

Fig. 4.20 DSC of (a). Fe_2O_3 Nanoparticles 95

Fig. 4.21XRD Patterns of a) FeOOH Nanoparticles and HT-DNA/FeOOH Nanowires 96

Fig. 4.22XRD Patterns of a) Fe_2O_3 Nanoparticles and b) HT-DNA/Fe_2O_3Nanowires 97

Fig. 4.23 XRD patterns of Ppy nanoparticles 98

Fig.4.24XRD patterns of PImi nanoparticles and HT-DNA/PImi Nanowires 99

Fig. 4.25 TEM of FeOOH Nanoparticles in different Magnifications 100

Fig. 4.26 TEM of DNA/FeOOH Nanowire, its ED patterns and Dark and

Bright field Micrographs 101

Fig. 4.27 TEM Images of Fe_2O_3 Nanoparticles in different Magnifications 102

Fig. 4.28TEM Images of DNA/Fe_2O_3 Nanowires 103

Fig. 4.29TEM Images of Polypyrrole (ppy) Nanoparticles 104

Fig. 4.30TEM Images of DNA/Ppy Nanowires 105

Fig. 4.31TEM Images of PImi Nanoparticles 106

Fig. 4.32TEM Images of DNA/PImi Nanowires 107

Fig. 4.33EDX Spectra of (a) DNA/FeOOH, (b) DNA/Fe_2O_3 Nanowires 108

Fig. 4.34XPS Survey Spectrum of FeOOH Thin Film 109

Fig. 4.35XPS High-Resolution Spectra of FeOOH Thin film Components(a) Fe 2p and (b) O 1s 110

Fig. 4.36XPS Survey Spectrum of HT-DNA/FeOOH Nanowires thin film 112

Fig. 4.37XPS High-Resolution Spectra of HT-DNA/FeOOH Nanowires (a) P 2p(b) N 1s (c) O 1s (d) Fe 2p and (e) C 1s 113

Fig. 4.38XPS Survey Spectrum of Fe_2O_3 Thin Film 118

Fig. 4.39XPS High-Resolution Spectra of Fe_2O_3 Thin film Components (a) Fe 2p, and (b) O 1s 119

Fig. 4.40 XPS Survey Spectrum of HT-DNA/Fe_2O_3 Nanowires 122

Fig. 4.41 XPSHigh-Resolution Spectra of HT-DNA/Fe_2O_3 Components (a) P 2p, (b) N 1s (c) O 1s (d) Fe 2p and (e) C 1s 123

Fig. 4.42 XPS Survey Spectrum of Ppy Thin Film 128

Fig. 4.43 XPS High-Resolution Spectra of Ppy Thin Film Components (a) C 1s (b) N 1s 129

Fig. 4.44 XPS Survey Spectrum of HT-DNA/Ppy Thin Film 131

Fig. 4.45 XPS High-Resolution Spectra of HT-DNA/Ppy Components (a) P 2p (b) N 1s (c) O 1s and (d) C 1s 132

Fig. 4.46 XPS Survey Spectrum of PImi Thin film 136

Fig. 4.47 XPS High-Resolution Spectra of PImi Thin Film Components (a)C 1s, and (b) N 1s 137

Fig. 4.48 XPS Survey Spectrum of HT-DNA/PImi Thin Film 139

Fig. 4.49 XPS High-Resolution Spectra of HT-DNA/PImi Nanowires (a) P 2p(b) N 1s (c) O 1s and (d) C 1s 140

Fig. 4.50 Low resolution XPS Spectra of Fe 2p following Etching of the HT-DNA/FeOOH Nanowires by Ar+ Sputtering for (a) 0 s, (b) 402 s (c) 803 s (d)1204 s and e) 1606s 144

Fig. 4.51 XPS Spectra of O1s following Etching of the HT-DNA/FeOOH NanowiresAr+ Sputtering for (a) 0s, (b) 402s (c) 803s (d)1204s and (e) 1606s 149

Fig. 4.52 Low Resolution XPS Spectra of Fe 2p following Etching of the HT-DNA/Fe_2O_3 Nanowires by Ar+ sputtering for (a) 0s, (b) 402s (c) 803s (d)1204s and (e) 1606s 154

Fig. 4.53 XPS Spectra of O1s following Etching of the HT-DNA/Fe_2O_3 Nanowires by Ar+ Sputtering for (a) 0s, (b) 402s (c) 803s (d)1204s and (e) 1606s 159

Fig 4.54 Tapping mode AFM Image of Bare λ-DNA Nanowires (top). (below) AFM Image Nanostructure with diameter as shown along the Wire-length and Cross-section of Measured Diameter (right) 164

Fig 4.55 Tapping mode AFM Image of bare λ-DNA Nanowires (top) Cross-section of Measured Diameter (below) 165

Fig 4.56 Tapping mode AFM Image of bare λ-DNA Nanowires (top). Cross-section of Measured Diameter (below) 166

Fig 4.57 Tapping mode AFM image of DNA/Ppy Nanowires

and Cross-section of Measured Diameter 167

Fig 4.58 Tapping mode AFM Image of DNA/PImi Nanowires with Cross-section of Measured Diameter. Inset: shows the Zoomed-in-region of the Nanowire 169

Fig 4.59 Tapping mode AFM Image of DNA/FeOOH Nanowires in Tapping mode with Cross-section of Measured Diameter 170

Fig 4.60 Tapping mode AFM Image of DNA/Fe_2O_3 Nanowires in Tapping mode with Cross-section of Measured Diameter 171

Fig 4.62 EFM Phase Images of same DNA/Ppy Nanowires at different locations showing the phase angle of the tip oscillation as a function of tip/sample Biases 173

Fig 4.63 Corresponding Phase Shift as a function of Applied Voltage of DNA/Ppy Nanowires at different Diameter at grey scale of 5.0^0 174

Fig 4.64 EFM Phase Images of same DNA/PImi Nanowires at different locations showing the Phase angle of the tip Oscillation as a functionof tip/sample Biases 175

Fig 4.65 Corresponding Phase Shift as a function of Applied Voltage of DNA/PImi Nanowires at different Diameters at grey scale of 5.0^0 176

Fig 4.66 EFM Phase Images of same DNA/Fe_2O_3 Nanowires at Different locations showing the Phase angle of the tip Oscillation as a function of tip/sample Biases 177

Fig 4.67 Corresponding Phase Shift as a function of Applied Voltage of DNA/Fe_2O_3 Nanowires at different Diameters at grey scale of 5.0^0 178

Fig 4.68 EFM Phase Images of same DNA/FeOOH Nanowires at different locations showing the Phase Angle of the tip oscillation as a function of tip/sample Biases 179

Fig 4.69 Corresponding Phase Shift as a function of Applied Voltage of DNA/FeOOH Nanowires at different Diameters at grey scale of 5.0^0 180

List of Tables

Table 4.1 Measured bands assignment of FTIR spectrum of HT-DNA and HT-DNA/templated at 400-4000 cm^{-1} 79

Table 4.2 FT-IR absorption in peak position of bare DNA 81

List of Plates

Plate 3.1Cyclic voltammetry set up (a) degassing the mixture with N_2 (b) actual Cyclic Voltammograms taken 67

Plate 4.1Optical images of AFM cantilever positioned on protruding dried mass of all the DNA-templated nanowires taken at the edgesof dense network before EFM probe measurements 172

List of Schemes

Scheme 1.1 Illustration of Nanomaterials Classification 4

Scheme 1.2 Structural elements of DNA showing chains of four nucleotides with sequence 5'-ACGT-3' (b) Schematic diagram of the DNA double stranded helix. (c) A-T & G-C base pair and their Watson-Crick hydrogen bond pattern 11

Scheme 1.3 Structures of some Conducting Polymers 13

Scheme 1.4 Scheme showing the DNA-Templating strategy for conducting Polymer 15

Scheme 1.5 Schematic illustration for the growth of semiconductor materials at DNAtemplate 16

Scheme 1.6 Schematic representation of nanowires alignment using molecular combing technique 18

Scheme 3.1 Schematic diagram for HT-DNA/FeOOH nanowires formation 56

Scheme 3.2 Templating by DNA molecules in directing the growth of Ppy 65

Scheme 3.3 The Ppy formation oxidatively with $FeCI_3$ 67

Scheme 3.4Polymerization of imidazole using $FeCI_3$ as oxidant 69

Scheme 3.5 DNA aligning illustration on Si substrate by molecular combing technique 71

List of Appendices

Plate A1	AFM image of DNA/Ppy	226
Plate A2	AFM image of DNA/Fe_2O_3in 3D	227
Plate A3	AFM image of DNA/PImi in 3D	228
Plate A4	AFM image of DNA/FeOOH in 3D	229
Fig. A5	XPS for Net Herring testes DNA	230
Plate A6	TEM image of DNA/Ppy Nanowire	231
Fig. A7	TEM image of DNA/FeOOH Nanowire	232
Fig. A8	TEM image of DNA/Fe_2O_3 Nanowire	233
Fig. A9	TEM image of DNA/PImi	234
Fig. A10	FeOOH transformation at 400 ^oC into Fe_2O_3 Nanoparticles	235
Fig. A11	Raman Spectra of FeOOH & Fe_2O_3 Nanoparticles	236
Fig. A12	FTIR for bare DNA drop-casted as solid	237
Fig. A13	TG/DTG/DSC of FeOOH	238
Fig. A14	TG/DTG/DSC of Fe_2O_3	239

Abstract

FeOOH, Fe_2O_3, polyimidazole (PImi) and polypyrrole (Ppy) were grown on λ-DNA as template strategy using bottom-up approach by the oxidation of the corresponding precursors into leaf-like and wire-like structures,respectively with diameters ranging between 6 and 30 nm. The bottom-up synthetic approach is based on the DNA π-stacking and base-pairing interaction with the precursor or the coordination of the donor site on the DNA nuleobases and phosphate group with the nanoparticles. These promote the growth of the templated materials into 1D nanostructured architecture by co-precipitation of iron oxide from their salt solutions and/or induce polymerisation with $FeCl_3$. All the nanowires were synthesised in aqueous solution and aligned on oxidized silicon wafers by molecular combing method that relies on a combination of fluid flow and surface tension forces. Combination of microscopic and spectroscopic techniques for chemical family/identity, the structural character and electronic pathways showed that the nanowires considered comprised of crystallographic phases of the two iron oxide semiconductor nanoparticles,Ppy and PImi films bound to the template strands over time in a process analogous to Ostwald ripening. The TEM morphologies of the two iron oxides show parallel rough continuous leaf-like topography so elongate along the duplex DNA template axis to yield the dendritic morphology of the final nanowires, unlike the two DNA/templated polymers that displayed continuous beads-on-a-string chain-like arrays on the DNA phases. The AFM topographies translated the interaction into the directing ability of the template into high aspect ratio nanostructured materials with densely packed nanoparticles linearly arranged as nanowires. The diameter typically lies in the 6.5-33 nm for DNA/Ppy, 7.0-28 nm for DNA/Plmi, 5-27 nm for DNA/FeOOH and 3.0-26 nm for DNA/Fe_2O_3nanowires from statistical treatment of the nanowires size distributions. Analysis of the nanostructures reveals symmetrical distribution of the structure heights around the above modal values. Overall TEM

morphology accounts for the phenomena observed in the AFM studies. Electronic probe of the nanowires by non-contact method via scanned conductance microscopy identifies DNA/FeOOH, DNA/Ppy and DNA/PImi to follow negative parabolic dependence,an indication of conductive characteristic. On the other hand, DNA/Fe_2O_3 was observed to follow positive parabolic dependence indicating non-conductive behaviour. These investigations demonstrate that duplex DNA-based nanowires with predictable and controllable shape, size, morphology and composition hold promise for downscaling and extension of Moore's law with application in gas sensorsfabrication and assessing (*in vitro*) cancer cells as target binding bio-diagnostic assays.

CHAPTER ONE

1.0INTRODUCTION

1.1 Nanoscience, Nanotechnology and Nanochemistry

Nano is a prefix denoting a factor of 10^{-9}. It has its origin in the Greek word *nanos,* meaning dwarf but in science, nano means 1 billionth or 1×10^{-9}(Ozin *et al*., 2009).This term is often associated with the time interval of nano second, a billionth of a second, and the length scale of a nanometer, a billionth of a meter. Nanoscience and nanotechnology opens up vision for making, manipulating, imaging, and utilizing small particles. Nanoscience study to manipulate nanoscale particles and systems (Rao*etal*., 2004) and nanotechnology refers to the design, characterization and application of nanostructures device and systems at length scales. Nanoscience and nanotechnology involve research and development at the atomic and molecular scale within the length scale of 1-100 nm range where properties are size dependent. The current drive in nanotechnology is partly due to the shrinking of devices in the semiconductor industry and this is supported by the availability of new method of synthesizing nanomaterials, characterization tools and manipulation at the nanometer scale. Bottom-up conceptual basis for the generation of structural nanomaterials was first envisaged by Richard Feynmanin 1959 during his nanoworld imagination speech, "There's Plenty of Room at the Bottom" (Feynman, 1992). The possibility of "making, visualizing and controlling things on a small scale" based on atom by atom approach for the creation of molecular architecture that would not violate any physical laws was envisaged. Feynman added that it might be possible to arrange atoms the way we want it. The continued shrinking in device dimension has followed the Moore's law envisaged in 1965 as illustrated in Figure 1.1(Moore,1965).

Figure 1.1: Moore's law trend line plot of transistor size decrease over time(Moore, 1965).

Nanochemistry is the use of synthetic Chemistry to produce nanoscale building blocks of different sizes, shapes, and surface structures, charges and functionalities. In other words, nanochemistry is a blueprint for the future development of teaching and research in materials Chemistry that is tailored around materials with the caption "matter has a shape and shape matters"(Ozin *etal*., 2009). Assembly of atoms or molecules can be achievedthrough spontaneous chemically driven approach, templated self-assembly or directed lithography. The approach to materials discovery through nanochemistry shows the world of materials that had previously not existed. The scanning tunnelling microscopy (STM) invented by Binning and Rohrer, the 1986 physics Nobel prize winner in 1981 has allowed Don Eligler and Erhard Schweizer at the IBM Almaden Research centre in San Jose, California to fulfil Feynman's vision by arranging individual atom around a surface as depicted in Figure 1.2. In this case, arranging individual 35 Xe atoms on a Ni surface to spell out letters ''IBM''Eigler and Schweizer(1990) in a way that was not possible ten decades ago when molecular and atomic structure principles were discovered. The illustration shows how atoms can be moved and arranged individually.

Figure. 1.2: Scanning Tunnelling Microscopy images of 35 Xe atoms on a nickel surface(Eigler and Schweizer, 1990).

1.2Size Matters

Size reduction at nanoscale can have direct consequences on the surface-to-volume ratio and thus their properties also can be modified significantly compared to bulk materials. If one of the dimensions of the sample is comparable to the wavelength of the carrier, the variation of the density of the state can produce drastic change in the transport properties compared to the bulk materials. This is known as quantum size regime. In this regime, the energy levels available for electron are different from the traditional continuum bands that can be found in the bulk materials(Dresselhaus*et al.*, 2007).An example of this can be visualized on Au size dependence on colour and melting temperature. Au nanoparticles and Au in the bulk form, where the former at 10 nm appears red with melting point depression, whereas the latter displayed properties not evident in the nanomaterials as shiny yellowish non-magnetic with the melting point elevation (Roduner, 2006). Quantum and surface-volume ratio which depict fraction of atoms residing at the surface effects are critical for nanomaterials to be distinct due to size quantization phenomena. This presents numerous potentials for a variety of applications such as intercellular processes probing, chemical and biological sensing and nanoscale electronics (Patolsky and Leiber,2005; Schiffrin *et al*.,2004).

1.3**Classification of Nanomaterials**

Nanoscale materials are classified based on dimensions which are within the nanosize regime. These new classes of materials are building blocks that may be used for nanomaterials design en route nanotechnology innovations. These materials all have diameters less than 100 nm. The classification is very important due to their interesting electricaland optical properties and quantum confinement effects. Scheme 1.1 shows the classification of the various nanostructure materials according to their dimensions as zero dimensional (0D) materials, (it has no dimension with a length larger than 100 nm) such as nanoparticles, nanoclusters, nanocrystals (quantum dots);one dimensional (1D) materials, (if it has a length larger than 100 nm in one direction only) such as nanowires, nanofibers, nanotubes, nanoribbons, nanorods, nanospindles and nanosprings;two dimensional (2D) such as thin film, plates or networksand three dimensional (3D) materials such as nanofilms and nanolayers, nanocubes, nanobelts, nanorings, as well as hollow and porous nanostructures (Taniguchi *etal*., 2009; Nasibulin*et al*., 2009 ; Jia, 2008).

Scheme 1.1:Illustration of Nanomaterials Classification (Taniguchi *etal*., 2009; Nasibulin*et al*., 2009; Jia, 2008).

All, except 3D, are confined to their corresponding dimensions. Three dimensional materials are also known as nanomaterials in bulk form with no dimension at nanoscale. As a result, they are being studied as building blocks for their intriguing electrical,

chemical and optical properties, as interconnect, molecular nanosensors to nanocomputing and functional units in fabricating nanodevices (Watson *etal*., 2012; Wang *etal*., 2004; Law *etal*., 2005).

1.4Nanowires

Nanowires are good approximation to 1D nanostructures in the range of 1to 100 nm. It representsthe smallest nanostructure with transport properties. They have a high surface-to-volume ratio and low dimensionality due to their small diameter and therefore are potential materials for critical components as interconnects and nanoelectronic devices (Xia *etal*., 2003). Nanowires are useful in biological and chemical sensors for single molecule detection and a highly sensitive 1D nanostructure with large conductivity. These 1D nanostructures have become the focus of research, not only because of their peculiar properties but also for many potential applications such as in drug delivery, photonic, sensors, medical diagnostics, catalysis, electronic and magnetic materials (Liu *etal*., 2005; Ding *etal*., 2004).

1.5Preparation of Nanowires and Bottom-up Synthetic Strategies

One of the critical factors in the synthesis of nanowires is the control of shape, size, surface structure, crystallinity, and composition. On the basis of thought pattern for nanotechnology, synthesis of 1D nanostructures can be carried out by many methods using top-down or bottom-up strategies. The top-down synthesis (an approach that uses natural or man-made blockcan be casted into products whether small or large) such as UV lithography, X-ray, electron beam lithography (McCord and Rooks,1997), and focused-ion beam writing, all these aimed at macroscale manufacturing operations for nanosize materials. This approach engineers powerful building blocks that can deliver microscaled objects reproducibly. As the dimension of the target microscaled objects

approaches nanoscale, the top-down is increasingly challenged. Patterned structure using top-down approach by lithographic ion implantation method is the cornerstone of silicon integrated chip technology. However, these methods along with the conventional photolithography are slow processes, very expensive and continued scaling down may pose a problem in the future such as challenging task of depositing metal within the etched trenches in the silicon substrate as well as high fabrication cost associated with the use of making sub 100 nm structures e.g. extreme ultraviolet lithography and electron beam lithography (Ito and Okazaki, 2000; Xia *et al*., 1999; Cao and Wang, 2011). In addition, such technologies are approaching their limits (Heath *etal*., 2003), due to physical limitation in terms of atomic size and radiation wavelength used in lithography (Khalid *etal*., 2010).

Method for bottom-up approaches is a technique based on organising individual atoms or molecules into defined configurations similar to living organism molecular processes that prepared nanostructure materials through atoms or molecules self-assembly into large structure either by physical or chemical interactions (Parviz *etal*., 2003). Such methods include template-directed synthesis (Penner, 2002), vapour deposition growth (Huang *etal*., 2001), hydrothermal methods (Yan *etal*.,2002), and solution-liquid-solid methods (Holmes *etal*., 2000). Among all of these, only the soft Chemistry method whichis solution-phase preparation(Xia *etal*., 2003) can organise nanoscale units into large quantities of fascinating and ordered functional super structure of high yield, low cost and offering varied materials to be fabricated.

Another straightforward approach for the preparation of novel nanostructure involves the use of templateto manipulate the growth of materials with desired morphology. The template serves as structural framework by localizing crystal growth within confined space, or to localize the metallic reduction within a confined spaceto limit the

dimensions and morphology of the resulting nanostructure. With that, the nanostructure possesses dimensions similar to that of the template in term of size and morphology. The template can be made using a variety of materials such as biological scaffolds for instance, peptide and lipids, polymer, micelles, liquid crystals and anodic alumina oxide membrane (AAO), track-etched polycarbonate (PC)(Zhou *etal*., 2008; Mao *etal*., 2007; Zhou etal., 2006; Zhang *etal*., 2006) andDNA (Padalkar *etal*., 2010).

Preparation of nanowires using membrane-based synthesis produces 1D nanostructure of the target materialsand can be used to prepare metal and polymer nanowires through electrochemical reduction of metal ions inside the pores of the membrane, and oxidative polymerization, chemical vapour deposition (CVD) or sol-gel (Hulteen and Martins, 1997; Sarkar *etal*., 2007). Conductive polymer nanowires such as polythiophene, polypyrrole and polyaniline can be achieve through either monomer oxidative polymerization inside the pores of the membrane or by electro-deposition method. All geared toward polymer growth on the walls of the nanopores with resultant formation oftubules (Parlhasarathy and Martins, 1994; Penner and Martin, 1986).

1.6Template-Directed Synthesis

1.6.1Templating nanowires

The most straight forward and general methods for making nanoscale wires with high-aspect ratio structure is by filling nanoscale cylindrical holes as template with a given materials (Huczko, 2000). This involves the use of porous materials as a template in the fabrication of 1D nanostructures (Martin, 1994). If the holes are completely filled with materials of interest, nanowires or nanorods may be formed, while a partial filling with a continuous coating gives rise to nanotubes. In addition, the use of natural minerals such as microporous zeolitewith arrays of poresis also a good choice that can be filled

with other materials (Schuth, 2003). Synthesised templates such as liquid crystal templated mesoporous aluminosilicate (Coleman *et al*., 2001), electrochemically synthesised templates such as anodically etched aluminium and track-etched polymer membrane can all be used to create a membrane with randomly distributed uniform shaped pores thus nanowires replica can be generated (Martin, 1994).

Using membrane-based synthesis, nanowires of the target materials (metal or polymer) complimentary to the template can be produced. These can be achieve through methods such as polymerization, electrochemical deposition/reduction, sol-gel and chemical vapour deposition (Hulteen and Martin, 1997), with several ways of coating the inside of the porous template such as allowing fluid spontaneously wet the template pores or layer-by-layer growth procedure to coat the inside of the pores of gases species.

Metal nanowires aresimple examples that can be prepared by electrochemical reduction of the corresponding metal ions inside the template pores and coating one face with metal film to serve as cathode for electro-depositionas shown in Figure 1.3(Brumlik *et al*., 1992). With this, various metals can be deposited within nanochannels of membrane pores as detailed inFoss *et al*., (1992), where electrochemical deposition of metallic gold inside the AAO as membrane produces Au nanowire, thus length of the resulting nanowires can be controlled by varying the quantity of metal to be deposited.

Conductive polymer nanowires can also be prepared using membrane-based synthesis either through oxidative polymerization or electrochemical method of the desired monomers right inside the pores of the membrane (Martin, 1994). It can be achieved by immersing the template (membrane) in a solution of the monomer and polymerization induced. The polymer can grow on the walls of the pores with resultant formation of

tubules and subsequent nanowires after longer polymerization time (Parthasarathy and Martin, 1994).

Figure 1.3: Illustration of templating approach to produce nanowires from porous membrane by electrochemical reduction (Brumlik *et al*., 1992)

1.6.2Templating using biopolymer nanostructure

Biologically inspired approaches have provided an eco-friendly and energy-efficient alternative of synthesizing nanostructure materials through the mediation of biological species such as viruses, DNA and peptides (Becerri and Woolley, 2009; Padalkar, 2010). Among the biopolymers, DNA has emerged as a potential template to arrange and bind circuit components to a surface, taking advantage of the high specificity with which DNA base-pair interact. The molecules provide an excellent construction patterned material for soft templates because they are chemically robust and are able to react with nano-object without any obvious structural changes (Ma *etal*., 2004; Xia *etal*., 2010). Its double helix strands offer a variety of binding sites for metals ions (Spiro, 1980) and can be used to assemble stable and complex structures (Winfree *etal*.,1998). Nevertheless, this approach offers an attractive method for bottom-up components localization using the DNA base pair selective affinity, but it has limited use as an active native DNA due to its high resistance, thus,has low conductivity

property (Storm *etal*., 2001; Bockrath *etal*., 2002). Bottom-up is a strategy which can overcome this electrical insulating property by taking advantage of the programmable self-assemble molecular recognition properties of the biopolymer to grow metals, polymer or semiconductors.

1.7 DNA Structure and Properties

DNA is a biomolecule that carries essential genetic information of life. It is a linear copolymer composed of four monomer nucleotides (Watson and Crick,1953). Each strand of DNA is made of three components which are nitrogen-containing bases, deoxyribose (carbohydrate) and phosphate groups with one of the monomersnucleotides linked to each sugar molecules. A unit of the phosphate, a sugar molecule and base is called a nucleotide of about 0.34 nm long (Khalid *etal*., 2010).These nucleotides, the nitrogen-containing bases are adenine (A), cytosine (C), guanine (G) and thymine (T) (Stryer, 1988; Becerril and Woolley, 2009). The sugar deoxyribose with phosphate groups form the long backbone. These nucleotides are linked together by a pair of helical sugar phosphate,(Scheme 1.2). The native double-stranded DNA molecules have a diameter of about 2 nm whereas the length is typically on the micrometre scale, 20 μm(Berg *etal*., 2002; Bensimon *etal*., 1994; Bensimon *etal*., 1995). DNA backbone is composed of phosphate deoxyribose sugars linked by hydrogen bonding base pairs A with T and G with C at the fifth position of the first sugar to the second antiparallel molecule at the third position (Scheme1.2).

Scheme 1.2: (a). Structural elements of DNA showing chains of four nucleotides with sequence 5'-ACGT-3' (b) Schematic diagram of the DNA double stranded helix. (c) A-T and G-C base pair and their Watson-Crick hydrogen bond pattern(Stryer, 1988).

The hydrogen bonding between (Aand T) and GandC,(Figure 1.5 b) along with π-π stacked aromatic bases act as a π-way for the transfer of electrons (Hall *et al*., 1996). Adenine and thymine are paired with two hydrogen bonds while guanine and cytosine are linked together with three hydrogen bonds as showed in Figure 1.5 c. These hydrogen bonds between the DNA bases holdtwo similar single strands together to form a double-stranded DNA (dsDNA) molecule, (Figure 1.5 b)thus the hydrogen bonds with aromatic stack interactions increase the stability of the ds-DNA platform as in Figure. 1.5 c.The inter base-pair separation of DNA is 0.34 nm (Richter, 2003), and therefore its length can be programmed by controllingthe number of base-pairs of interest. This offers the possibility of controlling the length of the nanostructure to be prepared (Houlton *et al*., 2009). Since DNA as a molecular guide has well defined length and large aspect ratio, this makes it suited as a superb platform for the construction of DNA-templated nanostructures.

Moreover, DNA with its versatile stiff structure, does not form a random coil in solution, instead it adopts a linear conformation and the possibility of its length controlwith rich chemical functionality allows it to interact with diverse organic and inorganic materials of interest (Houlton and Watson 2011; Houlton *et al*., 2009). The anionic phosphate backbone and nucleobases provide routes for DNA to interact with other chemical species. These interactions are critical to the fabrication of DNA-templated nanostructure. In addition, DNA can tolerate a wide variety of reagents and is soluble in water.

DNA with the anionic phosphodiester backbone, provides interaction with positively charged species, while the nuleobases are capable of coordinating with metallic cations and thereforecan act as a template that can bind with a wide range of inorganic and organic materials. However, the anionic phosphate in the DNA molecule, metal-

chelating nuleobases and aromatic rings that form a π-stacked core result in electrostatic repulsion of the DNA strands (Watson *et al*., 2008).To neutralize the negative charges on the DNA molecules, the solution media must provide cations that can neutralize the negative charges in order to maintain electrical neutrality. The use of DNA has some limitations, mostly, it is not a high temperature material, therefore, would not be stable at elevated temperature and can be degraded at low pH through depurination, which isloss of purines bases (Mirkin, 2000; Blackburn and Gait 1996). The sensitivity at low acidic condition can also lead to chain cleavage and hence decomposition.

1.8Conducting Polymers

Conducting polymers (CPs) are polyconjugated polymers consisting of alternating single and double bonds (π-electron backbone) with unique electronic properties, low energy transitions, high electron affinity and low ionization energy. This extended π-conjugation network leads to the intrinsically electrically conducting polymers.

Scheme 1.3: Structures of some Conducting Polymers

Most widely known CPs are polypyrrole (PPY), polyaniline (PANI), Polythiophene (PT), polyacetylene (PA), poly (p-phenylene-vinylene) (PPV), poly (3,4-ethylenedioxythiophene)(PEDOT), polyphenylene, polycarbozole and polyindole (Scheme 1.3) and their derivatives. Common features of any CPs is the π-polyconjugation in their backbone and they are promising materials for the synthesis of nanostructured materials (Langea *et al*., 2008; Malinauskas, 2005).

Conducting polymers can be synthesised either by chemical (McCullough, 1998; Chandrasekhar, 1999) or by electrochemical methods (Heinze, 1991; Wallace *etal*., 2002). The template synthesising route can be soft or hard template. Soft template relies on molecular self-assembly into nanostructures, while the hard template uses scaffolds for the growth of conducting polymers to replicate an existing nanostructures against nanochannels by chemical or physical interactions. With biomolecules applications, electrochemical synthesis is normally used at ambient temperature either potentiostatically, amperometrically or with potential scanning. During polymerization, the monomer or its salts supply with synthesis conditions get oxidized to radical cations, then by coupling reaction to oligomers and eventually deposited as polymer on the electrode surfaces. The whole process takes a few seconds.

1.9Conducting Polymers Templated on DNA

DNA molecules are versatile covalent ‘linkers’ for the controlled aggregation of CPs nanoparticles such as Ppy, PIn, or PANI. The double stranded DNA provides rigid spaces called template that allow control integration of nanoparticles into supramolecular structures. In this way, the recognition properties of the DNA trigger the self-assembly process either through non-covalent interactions such as hydrogen bonding or electrostatics forces between DNA and the growing nanoparticles. The advantage of DNA rationalizing nanoparticle assembly can be characterised

spectroscopically,and AFM or TEMare conventionally used to assess DNA reaction with nanoparticles (Houlton and Watson, 2011). Scheme 1.4 shows an approach to using DNA for the controlled assembly of polymer nanoparticles into aggregate structures.

Scheme 1.4: Scheme showing the DNA-Templating strategy for conducting polymer (Houlton *et al*.,2009)

1.9.1Inorganic semiconductors templated on DNA

Confining the growth of semiconductor quantum dots to low dimension provides access to size quantization. This nanosize regime can be exploited for a wide range of applications(Bate, 1975). Therefore, organised assembly in one, two or three dimensions have become a matter of interest in materials science research and development. Conjugate of nanosize semiconductor nanoparticles with biomolecules allow DNA to be used as mediation to fabricate a range of DNA semiconductor nanowires such as 1D nanowires. This is due to the fact that such materials of interest can be formed from precursor that can bind to the anionic backbone of the DNA.

Template reactions arestepwise in which DNA strands are first incubated with an appropriate precursor and subsequent addition of anion (for inorganic materials) as

reducing agents lead to the growth formation of the desired materials along the DNA strands as template. Scheme1.5(Coffer *etal*., 1996),illustrate the DNA ability to stabilise CdS nanoparticles after incubated with a solution of Cd^{2+}, followed by exposure to H_2S.

Scheme 1.5:Schematic illustration for the growth of semiconductor materials at DNA template.

Electron microscopy of the product shows a discontinuous chain of CdS nanoparticles on DNA platform. In more recent years, other semiconductor nanoparticles such as CuS (Dittmer and Simmel, 2004) and iron oxides (Nyamjav and Ivanisevic, 2005)have been grown on DNA templates. None of these reports at all describe electrical conductivity measurements of the materials, though such DNA deposition strategy could be used to create different types of functional nanodevices.

1.9.2 DNA-Templated nanowires synthesis andalignment

The use of DNA biomolecules as a template in nanofabrication requires one to overcome critical challenges such as low conductance over length scales and alignment on surfaces because of aggregation tendencies. For this reason, DNA molecule manipulation is not possible in its natural coiled structure. Strategy was developed for

aligning DNA molecules on solid surfaces using different approaches. The fabrication could be carefully placed or aligned on a substrate or in solution. The most common method is molecular combing,which is a reliable approach for immobilizing and stretching DNA without the need for DNA extremities to be modified (Bensimon, 1995), as opposed to the former approaches which involve stretching DNA using optical or magnetic tweezers (Baumann *etal*., 2000); spin stretching (Yokota *etal*., 1999) or stretching inside nanofluid channels (Gao *etal*.,2004).

This technique involvesa procedure in which under certain conditions of pH and ionic strength, DNA molecules are attacked at one or both ends of the surface and subsequently aligned by the force applied at the air-water interface. In the basic technique, droplets of DNA solution is deposited on a surface, then moving the liquid-air interface in the forward direction drags the hydrated part of DNA and this results in stretching of the molecule with both ends attached to the surface (Scheme 1.6). Different strategies can as well induce moving interface such as gas flow, evaporating a droplet or pulling a solution out of solution containing DNA-templated (Nazari and Gurevich, 2013).Critical factors can impact on the resulting DNA networks, such as the natural tendency to repel each other and the flowing velocity of a solution drop determine the straightness and density of the aligned DNA molecules. Divalent cation can interact with DNA strands to mask this force of repulsion. Adhesion force between DNA molecules and the surface(Stoltenberg, 2004), is also another factor to be controlled when using this method. This is because DNA-templated nanowires adhere strongly to hydrophilic surfaces such as mica or oxidized SiO_2 and would not adhere to highly modified hydrophobic surface, but partial modification (salinisation) of a surface would allow DNA molecules to adhere loosely for surface forces responsible for combing to produce ordered aligned parallel molecules. Different hydrophobic surfaces

have been investigated for combing such as gel, mica, glass or silicon surfaces (Watson *etal*., 2012). To facilitate alignment, surface hydrophobicity need to be modified which is done by exposing the surface tochlorotrimethylsilane(CTMS) (Me_3SiCl vapour for about 10 minutes.

Scheme 1.6:Schematic representation of nanowires alignment using molecular combing technique

1.10Justification of the Research

Growth of semiconductor materials to the low nanometer regime provides access to size quantisation phenomena that can be exploited for a range of applications such as nanoscale electronic, optoelectronic and photonic circuitry.

Continuing scaling down and device shrinkage by order of magnitude in the semiconductor industry according to Moore's law will sooner or later meet with limitations of the materials fundamentals which assume that matter is uniform and continuous. As CMOS transistors dimension drops below 100 nm, the boundary for entry into the nano world, the above assumption will no longer hold true and atoms graininess begins to take over and thus this building block will have a finite size. Then CMOS transistors will hit a brick wall and nanotechnology would rise to the rescue with

new nano-device architectures. This has encouraged research in bottom-up approach in the field of self-assembly inspired by biological moieties.

While control over length scales is well developed for many years now, their forms,dimensionality and subsequent organisation into functional system remain challenging.

One approach being considered in this researchis to explore new materials to develop high tunable fabrication techniques and align them as nanowires for future functional interconnect between components. Thus the use of biopolymer, a DNA as interconnects to achieve a precise size and shape.

To further expand the utility of DNA for other applications, this work is currently aimed at improving on DNA's intrinsically electric conductance.

1.11Aim and Objectives

The aim of this research is to develop nanowires in which DNA acts as a template to assemble two nanoobjects, inorganic semiconductors (FeOOH and Fe_2O_3) and polymer materials (Ppy and Plmi) and observe their evolution from nanoparticles to continuous nanowires with useful applications.

1.11.1Objectives

The above aim can be achieved through the following objectives.

(a) Exploring synthetic routes for the growth of the mentioned nanoobjects on a template;

(b) Elucidating the structural and chemical composition of the nanoparticles by various techniques such as microscopies and spectroscopies;

(c) Carrying out electrical characterisation and structural properties of the nanowires generated which have not been previously prepared as nanowires and or given little attention, i.e. polyimidazole and polypyrrole; FeOOH and Fe_2O_3.

CHAPTER TWO

2.0 LITERATURE REVIEW

2.1 Semiconductor compound Templated on DNA

The use of double helical DNA as a template has enabled the preparation of conducting 1D nanostructure using semiconductors, metals, polymers and other molecular based materials(Houlton *et al*., 2009). This method is similar to the two-step reduction process for organising metals on DNA template and subsequently leading to wires. To date, DNA/CdS, DNA/PbS, DNA/CuS, DNA/Fe_3O_4, DNA/$BaWO_4$, DNA/ZnS and DNA/CdSe have all been prepared in different forms at DNA template strands. Figure 1.8 shows how binding ability of DNA allows the strands to be seeded with binary component of the metal salt.

The first reported binary compound to be seeded on DNA was CdS in which the binding capabilities of calf thymus DNA molecules to direct the growth of CdS nanocrystals into DNA/CdS nanostructure was demonstrated by Coffer*etal*., (1992). This was done by mixing cadmium salt in order to allow the calf thymus (CT) DNA to be seeded with the Cd^{2+} ions component of the binary materials. Subsequent treatment with appropriate anion allows the material of interest to grow along the DNA strand. The resulting product displayed zinc blend lattice structure of nanocrystals with diameter 5.6 nm. This dimension shows quantum-confinement and the expected blue shift luminescence is confirmed. In addition, the role played by individual nucleotides was elucidatedand found that adenosine has much influence on the calf thymus DNA binding capacity (Bigham and Coffer,1995). The ability of individual calf thymus DNA molecules to

direct the growth of CdS quantum-confinement was also further elucidated (Coffer *etal*., 1996). This was done by seeding the DNA with Cd^{2+} ions, then CT/DNA/Cd^{2+} was immobilised on polylysine-coated glass and subsequent exposure to H_2S for quantum-confined CdS templating. The morphological details from the images was not clear enough, though presence of CdS on the DNA was confirmed.

Evidence for DNA/CdS morphology emerged later from the studies on the interaction of charged particles on DNA, with TEM images showing chain-like assemblies of CdS nanoparticles on DNA (Torimoto *et al*., 1999).

Figure 2.1: AFM images of CdS nanoparticles on DNA on mica(Dong *etal*., 2007).

More recently, Dong *et al*., (2007) have shown that by optimising reaction conditions, it was possible for CdS nanoparticles to bind with DNA in different forms using two different immobilizers. For this, templating reactions were performed using initial treatment of cadmium nitrate with immobilised DNA on mica and subsequentlytreated with Na_2S solutions. AFM measurements shows nanoparticles along individual DNA strands with appearance of beads-on-a-string (Figure 2.1 a). The nanoparticles are mono-disperse shown along the DNA strands. Also, photoluminescence spectrum depicted quantum-confinement effect as a result of blue-shift seen.

Comparing analogous templating reaction in solution provided evidence of continuous coverage of the materials isolated as shown in Figure 2.1 c. The coverage was also shown to be gradual and with time upon standing to give a smooth continuous wire-like morphology. The nanowires appeared as individual strands densely packed with nanoobject and little bare DNA with consistence diameter(Dong *et al*., 2007). The resulting nanowire (11 -15 nm in width by AFM) was confirmed to be conducting over a two-terminal device for electrical transport at micron lengths (Fig 2.1 d). An actual electrical device as luminescence image is shown in Figure 2.1 e with emission from single DNA/CdS nanowire bridging two electrodes gap.

Other binary materials have been grown on DNA templates with beads-on-a-string appearance. The growth of PbS nanoparticles on DNA by sequentially treating DNA with $Pb(NO_3)_2$ and Na_2S at a temperature of 100^oC with PbS on DNA emitting infrared at ~1100 nm was alsoobserved. Control experiments in the absence of DNA showed no measurable luminescence but rather aggregated materials (Levina *et al*., 2005).

Other types of chalcogenides as functional materials analogous to CdS as CdSe has also been exploited. It has been exploited as Q-CdSe nanoparticles into 1D nanostructures using a template. In this approach, DNA was used to organise pre-formed cationic CdSe nanorodsusing colloidal solution of CdSe/ZnS on immobilized DNA (Artemyev *et al*., 2004). However, longer incubation shows deposition with linear bundles of filaments about 100 nm thick depicting DNA influence on the self-assembly process using polarised PL measurements which indicated a clear DNA influence on the assembly process.

CuS is one of the few metal sulphides, a p-type semiconductor with band gap of 1.55 eV (Nair *etal*., 2004)which hasalso been prepared on DNA (Dittmer and Simmel, 2004). Two different templating reactions (solution-based and immobilisation on a surface) involving incubation of DNA and $CuCl_2$ followed by treatment with Na_2S gave nanowires for the solution basedreaction with densely covered CuS of diameter 10 nm as measured by AFM. An absorption spectrum taken of the solution exhibit characteristic absorption onset of CuS as well as significant absorption peak of DNA (260 nm). DNA immobilised on mica/silicon approach by drop of the solution on mica substrate showed preference for DNA growth with TEM images as covellite crystal lattice while AFM images displayed DNA densely covered with CuS nanoparticles and other nanoparticles in the background with an average height of 1.2 nm. To date, no electrical measurements have been reported.

Ternary compound has also been subjected to study using DNA as templating strategy(Li *etal*., 2010). This involved incubation of Ba $(NO_3)_2$ solution at low temperature with DNA followed by an anion addition in the form of Na_2WO_4 for 24 hours and subsequent heating to 80-95 ^oC. The isolated materials contained parallel

nanowires as a result of melting of DNA duplex. At least melting properties of DNA duplex were demonstrated.

Hassanien *et al*., (2012) has also used DNA strand for growing Cu_2O nanowires using chemical reduction of Benedict's reagent as Cu source, with ascorbic acid as reducing agent in a one-step reaction. Analysis of probe microscopy (AFM images) indicated crystallite of Cu_2O bound to the DNA molecules in beads-on-a-string manner over time to smooth morphology in a process analogous to Ostwald ripening of colloid. The DNA/Cu_2O showed evidence of conductance within 2.2-3.3Scm^{-1} and strong quantum confinement in the electronic spectra. More detailed studies using optical spectroscopy where dispersion of these nanowires in DMF media indicated an optical gap of over 2.8 eV, gave an indication of quantum confinement.

More recently, Mohammed,*etal*.(2012)carried out an investigationon the synthesis of DNA/Fe_3O_4 magnetic nanowires using electrochemical DNA templating method to direct the formation of metal oxide using solution-based reactions. The resulting nanowire from AFM images revealed densely packed regular continuous coating of metal oxide linearly arranged along the template with wires 30 and 27 nm, respectively, as diameter. Additional microscopic studyhas verified the nanowire structure to be conductive with magnetic behaviour. It has also been shown from additional studies that these DNA/Fe_3O_4 nanowires are conductive and display superparamagnetic behaviour at room temperature.

2.2Conducting Polymer Templated on DNA

Conducting polymers (CP) such as polyacetylene (PA), polyindole (PIn), Polyaniline (PANI), Polypyrrole (Ppy), and Polythiophene (Ptp) formation on DNA template as nanowires have been reported by several groups (Nagarajan*et al*., 2001; Houlton and Watson, 2011; Dong e*t al.*, 2007; Nickel *et al.*, 2004). These are another set of

promising and interesting materials for the syntheses of nanostructured materials and for new types of miniature electronicsthat can provide applications due to their π-conjugated length, flexibility, stability and by molecular design,their conductivity can be tuned along with enabled functionalization. CP nanostructures synthetic approach with template, unlike binary materials, relies on growing polymers interaction non-covalently with DNA and subsequently, the resulting materials comprise of cationic synthesis oligomers strands and anionic DNA and have a supramolecular structure (Watson *etal*., 2012) as shown in Figure 1.6.

Early reports on this was conceived for bulk synthesis of polyaniline with calf thymus DNA which shows two types of polymers in solution as emeraldine salt form of polyaniline and the preferred DNA/PANI handedness with thermal stability. Electrical conductivity measurement on DNA/PANI pellets was also noted though very low as a result of DNA/PANI discontinuity along the template(Nagarajan *et al*., 2001).

The use of DNA strands as template immobilized on oxidised silicon wafer first reported the growth of polyaniline(Ma *et al.,* 2004). Pre-treatment of the surface with (amino propyl) triethoxysilane provided the cationic surfaces for DNA to be stretched by molecular combing. The modified surfaces were incubated with acidic solution of aniline for cationic aniline oligomers to be generated enzymatically with horseradish peroxidase (HRP/H_2O_2) mixture. AFM measurements confirmed increase in the size of the DNA/PANI strands from 0.2-0.3 nm for bare DNA height to 0.8-1.0 nm after oxidation. The reaction was dependent on pH with maximum growth at pH = 4 and PANI nanoparticles along the DNA.



Figure 2.2: (a). AFM image of DNA/PANI nanowires on Si wafer at pH = 5, (b) Oxidative polymerization for DNA/PANI nanowires at pH = 3.2 with incomplete coverage, (c) Oxidative polymerization at pH = 4,(Ma*et al*., 2004).

At pH = 5, beads-on-a-string morphology was observed as shown in Figure 2.2 a, while at low pH, oxidative polymerization was incomplete with the nanowire breakage as shown in Figure 2.2 b. The best coverage at pH = 4 is shown in Figure 2.2 c.Nikeles *etal*., (2004) considered different methods for oxidative polymerisation of PANI on DNA for generating DNA/PANI nanowires using a ruthenium complex as photo-oxidant.The method gave longer polyaniline chains, while ammonium persulphate use gave only isolated polymer particles along the DNA template. UV Visible absorption studies could not be used to probe the reaction mechanism for reaction involving ammonium persulphate due to the low concentration of aniline used in the study. In none of the methods did DNA/PANI exhibit continuous coverage and conductance measurements of DNA/PANI prepared using the second oxidant showed that the materials did not conduct as compared with ruthenium complex or (HRP/H_2O_2) with sizeable rectifying behaviour. Overall, condition for this templating at low pH can cause the DNA to degrade with the resulting decomposition and chain cleavage. This may be critical for the irregular DNA/PANI based materials as shown in Figure 2.2.

An addition to the DNA as guide for nanowire formation using Ppy as conducting polymer was demonstrated Dong *etal*.,(2007) at neutral pH, negating concerns for

envisaged DNA-hybrid decomposition. $FeCl_3$ as oxidizing agent was used to drive the polymerization toward DNA-templating of Ppy. The synthesis was demonstrated in solution and at surface (mica) immobilized. However, as observed for CdS and polyaniline earlier, the resulting hybrid materials on mica showed a bead-on-a-string morphology as shown in Figure 2.3a, while reactions performed in solution produced continuous wires with element of bare DNA,(Figure 2.3b), with improvement in height to 5 nm and height variation along the individual nanowires (Figure 2.3 b) compared to < 2 nm for bare DNA.

Figure 2.3:(a). AFM image of DNA/Ppy nanowires prepared on mica after polymerization isolated from solution (black arrow) and bare DNA strands (white arrow) scale bar, 200 nm, and height scale 4 nm.(b) AFM image showing material isolated from the reaction solution contains thicker DNA/Ppy nanowire (black arrow) and bare DNA molecules (white arrow). (bi)Surface plot of the height variation along a single DNA nanowire. (Dong *et al*., 2007)

Spectroscopic characterization confirmed the presence of bands shift associated with phosphodiester linkages as a result of intimate interactions. Quite an interesting property of temperature dependence of DNA/Ppy nanowire whose morphology was demonstrated in Figure 2.4 to form rope-like structure (Pruneanu et al., 2008).

Figure 2.4: AFM images of DNA/Ppy nanowires on Si wafer after (a) 2 days, scale bar 500 nm height scale 8 nm. (b) after 6 days, and (c) 1month, scale bar 500 nm height scale 12 nm,(Pruneanu *et al*., 2008).

The aqueous pyrrole monomer solution used was of higher concentration over a long incubation time than previouslyused (Dong *etal*., 2007), and a transformation into thicker bundles being formed were observed. AFM reveals twisting of individual wires visible at one end due to partial unravelling as depicted in Fig. 2.4 a. Conductivity was evidenced on the nanoropes as established by two-terminal measurements and c-AFM.

Polyindole as conducting polymer is the recent addition to the range of DNA-based route as DNA/Pin (Hassanien *etal*., 2010) showing the effect of time on morphology of the nanowires with reported changes in the DNA/Pin nanowires in polymerization solution as shown in Figure 2.5. AFM images shows individual nanowires actually combined to form nanoropes as visible in Figure 4d. The resulting nanowires were smooth and had diameter within 5- 30 nm with conductivity (2.5-40 Scm^{-1}) at room temperature much greater than bulk polyindole (10^{-2}-10^{-1} Scm^{-1}). The materials were shown to be photoluminescent and single nanowire could be imaged which allowed transmission line method (TLM) to negate measurements contributed from contact

resistance for device configuration. This was done by drop-casting the nanowire from the solution onto a hydrophilic surface whereby the large mass of the nanowires acts as macroscopic reference point for electrical contact to be made.

Figure 2.5: AFM images of DNA/PIn nanowires on Si wafers showing the effect of time on morphology of the nanowires(Hassanien *et al*., 2010).

Figure 2.5 shows an interesting discrimination compared to Figure 2.4 such that DNA/Pin morphologies are smoother with uniform thickness after a reaction time of 24 hrs along the length of the nanowires.

More efforts to further explore conducting polymers was recently demonstrated by the use 2,5-(Bis-2-thienyl)-pyrrole, a material that is water soluble but possess different hydrogen bonding capability compared to previously used conducting polymer (Watson *et al*., 2012). The formation of supramolecular nanowires were demonstrated as illustrated in Figure 2.6. The polymerisation was done in a solvent mixture (H_2O/MeCN) with $FeCl_3$ as oxidant. The resulting DNA/polyTPT nanowires exhibited clean, uniform, continuous coverage and smooth morphologies with rope-like branches along the main nanowire body. Conductivity assessment surprisingly revealed very low conductivity. The conductivity was size dependent.This was evidencedfrom c-AFM measurements depicting a significant drop in conductivity as the diameter of the nanowires reduces.

Figure 2.6:(a). AFM images (in tapping mode) of DNA/TPT nanowires on Si wafer. b) AFM image showing rope-like assemblies of DNA/TPT nanowires with branches, scale height 20 nm. (Watson *et al*., 2012)

Two-probe I-V study quantitatively between DNA/polyTPT nanowire and bulk polyTPT were used to support the low conductivity. Interestingly, the conductivity of the nanowire (10^{-7} Scm^{-1}) was several order of magnitude lower than the bulk materials ($10^{-2}Scm^{-1}$).

Using similar chemical oxidative polymerisation approach to improve the conductivity of DNA/Pd nanowires, polyimidazoleas scaffold was used to synthesize DNA/polymer/metal (DNA/Plmi/Pd) nanowiresusing a template assisted method(Mariam, 2015). In this case, DNA/PImi served as template to organise Pd particles into DNA/Plmi/Pd more conductive Pd nanowires, probably to enhance the morphology of the DNA/metal nanostructures. AFM images of DNA/Plmi/Pd were rather a network of nanowires between Au electrodes as shown in Figure2.7.

Figure 2.7: DNA/PImi/Pd AFM image as nanowire network (Mariam, 2013)

Electrical characterization using a different method showed that conductivity did not really improve by Pd on DNA/PImi, though EFM phase images confirmed DNA/Pd and DNA/PImi/Pd to be conductive and c-AFM with a conductance much lower, probably on the grounds of nanogaps between Pd nanoparticles along the DNA template which mighthave presented a discontinuous coverage. There was no evidence that Pd ions interacted with DNA molecules or PImi through its pyridine-type N atoms.

2.3Metal Templated on DNA

Reduction of metal salts on DNA is one of the most studied areas of DNA-based nanowires. The two-step approach exploit the metal-ion binding properties of DNA and it involves the initial seeding of DNA with the metal ions of interest followed by their reduction to the metal state. The seeding of DNA with metal ions can be performed either by mixing DNA with the appropriate metal cations in solution or immobilization of DNA on a substrate before incubation with metal ionsin solution (Houlton and Watson, 2011). Metal ions binding to DNA involve coordination with the donor sites on the DNA nucleobases and the polyanionic phosphate group with additional associations through outer-sphere interactions between metal complexes and the DNA phosphate

groups. Other interactions may also take place through metal cations coordination to electron donor sites within the DNA bases i.e. ring nitrogen atoms (Eichhorn and Shin, 1968). Formation of metal nanostructures along the DNA takes place during the metal reduction of DNA–bound metal ions which over time leads to the formation of metal clusters and nanoparticles along the DNA template. Templating of metal on DNA was earlier investigated by Braun *et al*., (1998) using two-step approaches for the fabrication of silver nanowires.

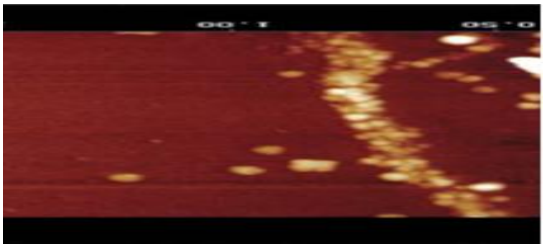


Figure 2.8: AFM image of a DNA-templated Ag nanowire bridging between gold electrodes (Braun *et al*., 1998).

In the approach, DNA immobilized on substrate was first treated with a basic solution of $AgNO_3$ for the formation of Ag^+ on DNA and subsequent reduction with hydroquinone to generate Ag nanoparticles along the template as shown in Figure 2.8consisting of densely packed nanoparticles with diameter ranging from 30-50 nm. Electrical characterisation initially showed non-ohmic behaviour at low voltage bias but has ohmic behaviour at higher bias values.

Since this report, reduction approach has been of choice for a number of studies byRichter *et al*., (2000)subsequently using the procedure for the formation of nanoscale palladium clusters on the DNA template. Here, λ-DNA was activated with Pd^{2+}ions by mixing with a palladium acetate solution followed by reduction using a bath containing sodium citrate, lactic acid and dimethyl amine borane (DMAB). TEM image (Figure 2.9) and SEM images showed chains of Pd^0 clusters with diameter 3-5 nm along the

DNA template, with formation of quasi-continuous palladium coating typically 20-40 nm thicker on the DNA after an extended reaction time. These findings supported Braun et al., (1998) proposal that DNA metallisation takes place via nucleation and growth mechanism where the initial metal cluster on the DNA acts as seed particles for further reduction of Pd^{2+} ions bound to the DNA structure.

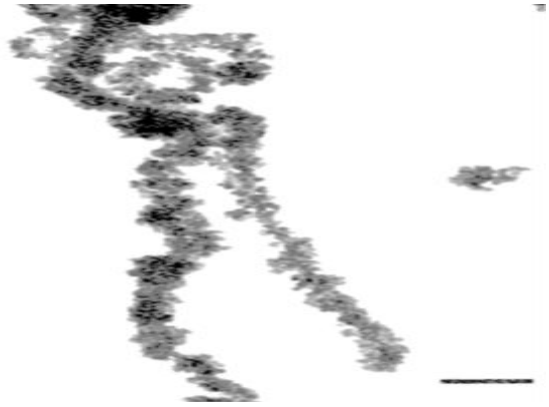


Figure. 2.9: TEM image of metallized DNA strands at an early stage of metallization process (Richter *et al*., 2000)

Though continuous coverage of Pd of the DNA templated was observed as shown in Figure 2.9, Pd coating showedhighly irregular morphology which was granular in nature. This may be due to the rapid reaction rate of the reducing agent (DMAB) with the Pd^{2+} ions.

DNA-templating strategies have also been extended to Cu metal since Cu is a metal of choice for interconnects in IC technologies. The first of such report was by Woolley *et al*., (2003) where cupper deposition on immobilized DNA was monitored by AFM. This was achieved by employing aqueous Cu $(NO_3)_2$ as Cu^{2+} source and ascorbic acid as reducing agent. A granular morphology observed in the nanostructure is an indication of Cu^0 deposition on the template which takes place through chemical reduction of Cu^{2+} ions. More complete coverage was obtained by repeating the Cu^{2+} with ascorbic acid treatment. The image in Figure 2.9.1 shows thicker coverage after two treatments in order to improve Cu deposition as evident in Figure 2.9.1b which indicates structural

heights increase. A refinement of this procedure was carried out by using solvent of low dielectric constantsuch as DMSO in place of water. This probably was to enhance electrostatic interaction between the DNA template and the metal ions. The modified approach resulted in more granular morphologies after a single reduction treatment.

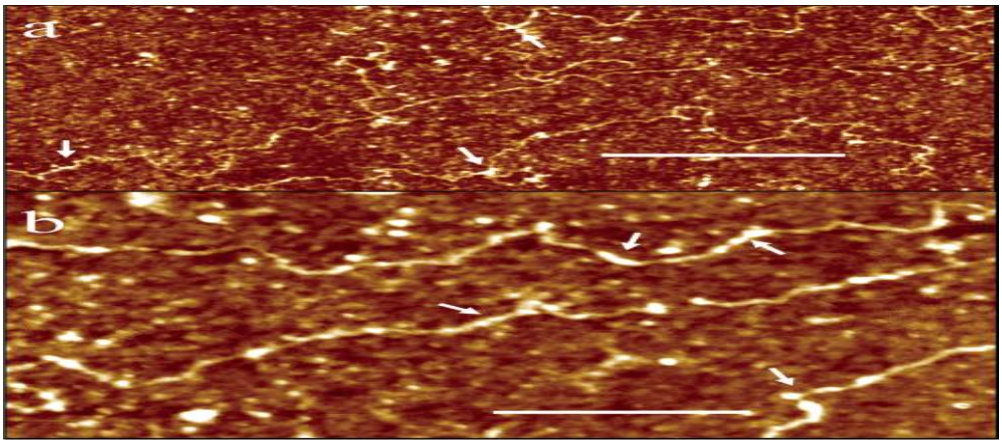


Figure 2.9.1: AFM height image of DNA/Cu nanowires with arrows showing specific deposition (Woolley *et al*., 2003)

Structural characterisation was extensively carried out on the DNA/Cu nanowires, but there was however no electrical study performed on the product to evaluate its conductivity. Other studies by Watson *et al*., (2009) sought to evaluate structural, chemical and electrical properties of materials prepared by a method similar to that by Woolley *and* Stoltenberg, (2004). This was to assess the preferential possibility of Cu_2O and elemental Cu^0 as reduction products on the DNA template. XRD and XPS confirmed the reduction product as Cu^0 along the DNA strands. AFM studies revealed that Cu nanostructures as shown in Fig. 2.9.2 indicated a granular continuous bead-on-a-string appearance. However, electrical conductivity investigations using SCM depicted negligible levels of conductivity along the templates which was ascribed to the consequence of the bead-on-string topography resulting in electron scattering at interparticle interfaces along the DNA strand.

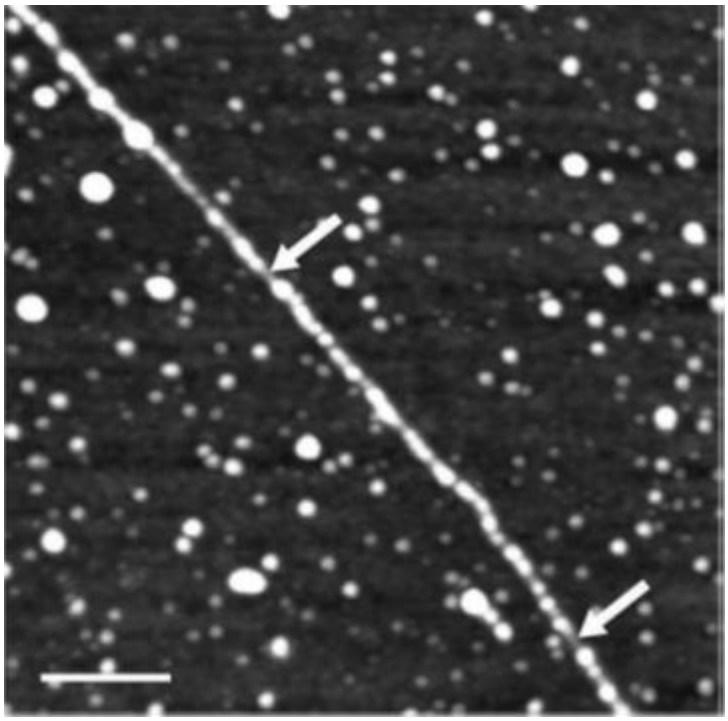


Figure 2.9.2: AFM image of a section of DNA/Cu nanowires with beads-on-a-string morphology (Watson *et al*., 2009)

Growthsof other metals like Pd (Deng and Mao, 2003; Richter *et al*., 2001; Richter *et al*., 2000) nanostructure by DNA-templating strategies have also been extensively studied. Pt nanostructure formation on DNA was also reported by Mertig *et al*., (2002) and provided astudy on reduction and aggregation mechanism of DNA metallisation based on molecular dynamics simulations. The findings suggested that Pt deposition on DNA took place through a growth mechanism involving the formation of Pt^{2+}-DNA adducts as dimers which are more energetically favourable, making the site more preferred for further reduction process to take place than on Pt^{2+} complexes in solution.

The catalytic and magnetic properties of Ni motivated Becerril *et al*., (2006) to study the deposition and growth of nickel on λ-DNA template for the selective and reversible binding of histidine-tagged protein. Thus a high density protein assembly was demonstrated for proteomic analysis.

Photoreduction, in addition to the use of chemical reduction agents, has also been used to induce metallisation on DNA strands (Berti *et al*., 2005). The reduction was achieved

by initial treatment of DNA with $AgNO_3$ solution followed by exposure to UV irradiation (254 nm). The process was monitored by UV-vis spectroscopy which showed the appearance of surface plasmon resonance peak at 420 nm possibly due to the formation of Ag nanoparticles. AFM studies also confirmed the nanoparticles to be within 1.5-3.0 nm in diameter along the DNA. Other photoinduced formationsof DNA-templated Ag nanowireshave alsobeen reported. Lu *et al*., (2009) used sunlight as UV-vis source on DNA/$AgNO_3$ solutions for the reduction of Ag ions-laden on DNA template, whereas nanowire formation through DNA/$PdCl_2$ solution was achieved through exposure to UV irradiation at the 260 nm DNA λ_{max} for 4 hours.Kundu *et al*., (2009) and Lu *et al.*,(2009) hypothesis was tested on DNA/Ag^+ reduction by irradiating at different wavelengths such as 366 nm. However, formation of Ag nanoparticles was not detected under those conditions because of the absence of characteristic plasmon resonance peak. Whereas, exposing the DNA-Ag^+ complex at the DNA λ_{max} (254 nm) resulted in the appearance of a peak at 410 nm, attributed to the resonance peak of Ag nanoparticles. As shown in Figure 2.9.3, the DNA absorption peak appeared at 260 nm concurrently.

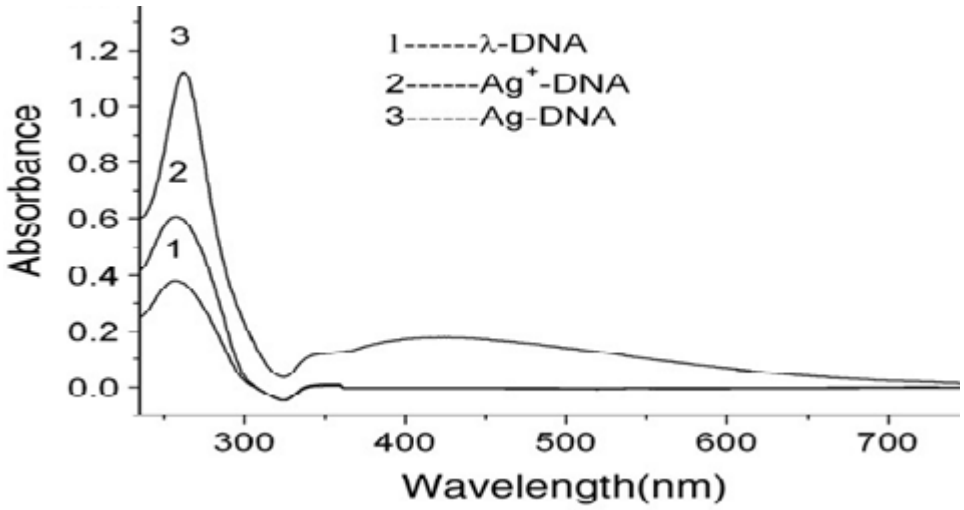


Figure 2.9.3: UV-Vis spectra showing the photoinduced sequence for DNA/Ag^+.
Curve 1 (pure DNA), curve 2 (DNA/Ag+) and curve 3 (DNA/Ag) (Lu *et al*., 2009)

In addition, direct evidence for the formation of network assemblies of Ag nanoparticles induced by DNA was acquired by AFM with uniform and monodisperse Ag nanoparticles with diameter in the range 11.4-13.4 nm (Figure 2.9.4).

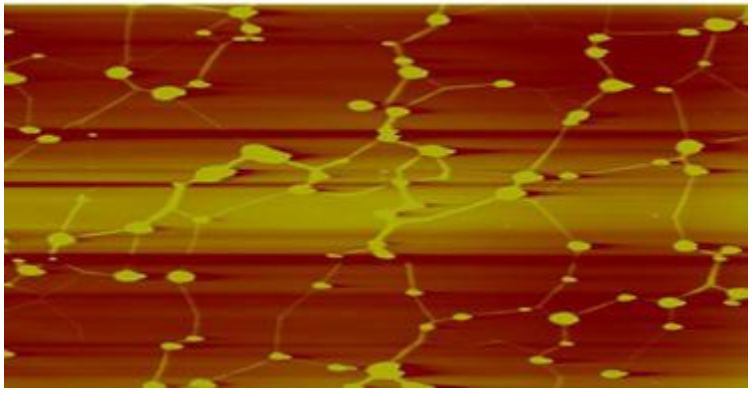


Figure. 2.9.4: AFM image of Ag nanoparticles on DNA network (Lu *et al*., 2009)

Overall, DNA was implicated to play a major role in this process. To buttress this, control experiments were set up in the absence of DNA and irradiating the DNA/$PdCl_2$ solution at 350 nm, far away from the DNA absorption at 260 nm. This demonstrated that Pd nanoparticles growth did not take place upon UV irradiation of $PdCI_2$ solutions without DNA non irradiation with wavelength away form 260 nm absorption of DNA. The electrical characterisation using c-AFM on the nanowires actually confirmed conduction.

2.4Nanowires Characterization Techniques

2.4.1Cyclic voltammetry

Cyclic Voltammetry is the most effective, versatile and widely used electroanalytical technique available for the study of a redox system. It offers a rapid location of redox potential of the electroactive species. Typically, it enables the applied electrode potential to be rapidly scanned in both forward and reverse directions at the same rate in search of redox couples, thus current at the working electrode is measured. That means, the potential is swept back and forth between two defined values at a fixed rate. Once a

redox couple is located, a couple can then be characterized from the potentials of the peak on the voltammogram. In the forward scan, electroactive species is electrochemically generated by electron loss often indicated by anodic current. In the reverse scan, the same species generated is reduced back to its former state (reactant) by electron gain, also indicated by cathodic current(Nicholson, 1965). Important parameters of CV are the magnitude of the peak current as I_{pa} and I_{pc} and the electrode potentials at which peaks occur, E_{pa} and $E_{pc.}$A redox couple in which both anodic and cathodic species rapidly exchange electron with the working electrode is referred to as reversible couple, which means, the value of anodic and cathodic currents are similar, otherwise, it is irreversible couple with considerable behaviour from it reversible counterparts as shown in Figure 2.10.

The CV apparatus is computer controlled andconsist of a potentiostat with scan capability and displays current against voltage. The task of applying a defined potential and measuring current falls on the potentiostat.

Figure 2.10: Illustration of current as a function of voltage in Cyclic Voltammogram

In this work, CV (a computer-interfaced (CH Instrument electrochemical microscopy system) was used with a three electrode system (reference electrode [Ag/AgCl], working electrode [Au electrode)] and counter/auxiliary electrode [tungsten wire]). The electrode system provide the interface across which charges can be transferred(Heinze, 1984). The redox reactions take place at the surface of the working electrode when appropriate potentials are applied with the resultant mass transfer of new materials to the working surface and current generated. Ppy, PImi, DNA/Ppy and DNA/PImi are prepared by the electrochemical redoxof monomer-polymer synthetic route in supporting electrolyte to suppress the charged reactants and products. In general term, this study provide no information on the specie identity

2.4.2Ultraviolet/Visible spectrophotometry

This a widely used technique for measuring the absorption of electromagnetic radiation within the visible and UV region of the electromagnetic spectrum. A spectrophotometer is designed to allow precise measurement at a particular wavelength.

UV-Visible spectroscopy accesses electronic transitions that result from the absorption of energy of incident photos within wavelength of 200-800 nm. In other word transitions are as a result of excitation of electrons which can be used to detect low concentration of materials. When a molecule absorbs UV-Vis. radiation of certain frequency, the absorbed energy excites an electron into an empty higher energy orbital. UV-v spectroscopy. usually utilises light source such as hydrogen or deuterium lamp for the UV light and tungsten lamp for only visible measurements all aligned to a grating monochromator as wavelength separator. The source can emit continuous range of wavelength in both the visible and UV region (Dean *et al*., 2002).

Absorption of light passing through a solution is governed by two fundamental principles. The absorption of light is exponentially related to the number of molecules of the absorbing molecules that are encountered and the absorption of light is exponentially related to the light path length through the absorbing solution. These two principles combined define Beer-Lambert relationship.

Different molecules absorb radiation of certain frequencies or different wavelengths and the absorption spectrum displays absorption bands corresponding to different transitions within the sample of interest. Absorption is a function of wavelength normally recorded with corresponding peaks depicting the absorption of energy at particular wavelengths by molecules in solution. The degree of absorption, depending on the molecular structure is usually a characteristic of that molecule. Typically,a strong absorption band of 260 nm is a characteristic of nucleic acids (DNA).

All UV-Vis measurements in this work were recorded on Cary 100 Bio UV-Visible spectrophotometer (Varian) at room temperature equipped with temperature control within 200-800 nm, which monitors an absorption band change or occurring phenomena as the DNA templating with the nanoobject progresses.

2.4.3 Fourier transform infrared (FTIR) spectroscopy

IR spectroscopy is concerned with the energy changes involved in the stretching and bending of covalent bonds in molecules. This observation is better enhanced by Fourier transformation with rapid speed, enhanced sensitivity with improve resolution of the spectrum. When a sample is exposed to infrared radiation, the covalent bonds vibrate at characteristic frequencies that match their vibration modes. Measuring the absorbed radiation by the molecules as a function of frequency produces a spectrum that can be tailored to identifying functional groups and thus the compound. The IR spectrum is a composite of individual absorptions from various components of the molecule and thus

related to functional groups/type of bond model which give rise to absorption at particular frequencies(Steele, 2002). In thiswork, FTIR was used to confirm the interaction of templating platform (DNA) with nanoparticles or CPs by observing absorption bands changes in the DNA templating reactions.

FTIR spectra in the range 400-4000 cm^{-1}were recorded using drop casting method on Si wafer as support for the nanowire prepared in transmission mode with an 800 FTIR spectrometer system (Varian Inc., Palo Alto CA) and the spectra collected at 4 cm^{-1} resolution. For bulk solid samples, such as CPs and some inorganic materials, KBr or nujol was not used as matrices to avoid contamination from the sample carrier. Rather, direct net drop of the sample was carefully placed onto the diamond crystal plate surface of the FTIR spectrometer.

2.4.4Transmission electron microscopy (TEM) and energy dispersive X-ray spectroscopy (EDX)

TEM or in particular high resolution transmission electron microscopy (HRTEM) is a powerful technique for imaging the internal structure of nanowires at atomic scale and provide greater detailed geometric features than seen in SEM images such as crystal structure, grain size, crystal quality and crystal orientation of the nanowires. When TEM is operated in diffraction mode, patterns from selected area electron diffraction (SAED) can be determined to evaluate the crystal structure of the nanowires thus showing growth direction of the nanowires. The high resolution of the TEM can allow for the determination of surface structure or microstructure of the nanowires in terms of amorphous sheath and crystalline core(Wu *et al*., 2002). In this case surface layer can be modified or studied by an *in situ* reaction and HRTEM imaging can be made while modifications are made.

Powerful imaging capability of TEM can be coupled with other characterisation tools such as energy dispersive X-ray spectroscopy (EDX) or electron energy loss spectrometer (EELS) within the TEM instrumentation to probe extra properties of the nanowires.

EDX measures the energy intensity distribution of x-rays generated by the impact of the electron beam on the sample surface. The elemental map within the probed area can be determined. The technique is very useful in nanowire research especially for determination of compositional characterization of superlattice nanowire (Wu*et al*., 2002).

In this work, TEM/EDX images at Durham University and (TEM) images at the Medical School's Electron Microscopy Research Services, Newcastle University, UK, were collected using JEOL-2100F FEG TEM with 200 kV alignment. The TEM/EDX used have high resolution pole piece with 1.0 mm C giving 2.3 Å point resolution andPiezo-driven stage for precision sample movement at high magnifications. In addition, Gatan Orius camera for acquiring high quality images over a wide field of view as well as diffraction patterns and Video capturing software using Digital Micrograph platform were also integrated.

Oxford INCAx-sight Si (Li) detector for EDX 50 mm^2 area detector at 25^o take off angle providing 130 eV energy resolution with Gatan Digi scan 2 for STEM EELS spectrum imaging with low background double tilt holder were all integrated for EDX analyses.

2.4.5 Thermalanalytical techniques, TGA/DTG/DSC

Thermalanalytical techniques are several materials science techniques in which changes in physical or chemical state viz-a-viz detailed information regarding the thermal stability, decomposition pathway of the materials under investigation are measured as a

function of temperature. Thermogravimetryis a sub-method whereby a change in the weight of a materials is monitored with respect to temperature or time. The result is normally expressed as TG curve, a plot of changing weight as a function of temperature or time. The derivative of TG curve i.e. DTG in which the first derivative of the TG curve is normally plotted as a function temperature gives additional information, such as detailed thermal decomposition and materials purity. Differential scanning calorimetry (DSC) is also a technique in which the energy necessary to establish a zero temperature difference between the materials under probe relative to the reference materials is monitored as a function of temperature. Thermodynamic events can be determined using DSC(Hatakeyama and Quinin 1984).

The principle underlying the DSC technique is that when the sample undergoes a physical transformation such as phase transition, more or less heat would need to flow to it than the reference to maintain both at the same temperature. Whether less or more heat flows to the sample depends on whether the process is endothermic or exothermic. For instance, as a solid sample melts to a liquid due to the absorption of heat as it undergoes the endothermic phase transition from solid to liquid. Likewise, as the sample undergoes exothermic processes such as crystallization, less heat is required to raise the sample temperature. By observing the difference in heat flow between the sample and reference, thecalorimeter can measure the amount of heat absorbed or released during such transitions. DSC may also be used to observe more subtle physical changes, such as glass transition. DSC is widely used in industrial settings as a quality control instrument due to its applicability in evaluating sample purity and for studying polymer curing (Punger, 1995). The result of a DSC determination is a curve of heat flux as a function of temperature or time.

The TGA/DTG/DSC of the samples in this work were carried out on NETZSCH STA 449C and Balzers MID thermal analyzer at a heating rate of 10 K/min from room temperature to 500^0C in N_2 stream, and their corresponding thermograms obtained to identify decomposition region in termsof enthalpy change peak events either exothermic or endothermic. AI_2O_3 was used as reference.

2.4.6Powder X-ray diffraction, XRD

XRD is a technique that provides structural information about the chemical identity and crystallite phases of the nanomaterials. In addition, XRD can also be used to determinethe crystallite size of the probe materials in conjunction with Scherrer's formula:

$$D = K \lambda / \beta \cos \theta \qquad 2.1$$

Where K is the Scherrer constant (0.89), θ is the Bragg's angle, β is the line broadening at half maximum intensity in radians, λ is the wavelength of the X-ray and D is the size or mean diameter of the nanoparticles related to the width of the diffracted peaks(Nuffield, 1966).

In XRD, the beam of X-rays or electrons is incident on crystalline materials (comprising of a regularly spaced three dimensional array of atoms), the incoming rays are scattered or diffracted, as shown in Figure 2.11 at specific angle by the lattice as predicted by Brag's law thus enable the calculation of *d* (lattice spacing of the crystal planes)from the diffractograms with respect to 2θ. Recording the diffraction patterns is such that the sample is rotated through all angles in order to produce all possible reflections (*h, k, l*) such that the beam 2 travels further according to Bragg's law(Duckett and Gilbert, 2000). For a particular pair of *d* and λ, diffraction would occur at a specific angle known as Bragg's equation (nλ = 2d (sin θ)] than the initial beam, where *d* is the lattice

spacings of the crystal planes; λ, the wavelength of the incoming beam; and θ is the angle of the incident (and diffracted: $\theta_{in} = \theta_{out}$) beam. If the difference that exists is an integer number of λ, constructive interference over a range of angles occurs and diffraction lines result from the existence of crystal planes at the appropriate correct angles with the incident rays.



Figure 2.11: X-ray beams feature on solid lattice(Duckett and Gilbert, 2000)

2.4.7X-ray photoelectron spectroscopy, XPS

XPS is a surface–sensitive technique that has found use in various areas of Chemistry such asmaterials science, catalysis, corrosion science, thin film Chemistry and polymer modification as well as electronics. It is a quantitative surface chemical analysis technique used to obtain elemental information and chemical state of the element within a given sample.It is non-destructive surface analysis suitable for information on chemical state, surface composition and electronic structure of nanomaterials quantitatively to a depth of 5 to 10 nm of a solid surface with a detection limit of within 0.1-0.5 atomic present level. It can identify all elements with an atomic number of 3 and above. Quantitatively this implies that, the number of electrons collected for a given transition is proportional to the number of atoms at the materials surface. XPS enables

the accurate determination of photoelectron kinetic energies and the core level binding energies (Smith, 1994; Vickerman, 1997).

This method is based on photoemission effects that depend on emission of electron from materials under investigation when they are irradiated by X-rays photons. In principle, when x-ray of known energy, in this case 1486.7 eV interacts with an atom, photons electrons (core electrons) are emitted via the photoelectric effect, Figure 2.12. This emitted electron's kinetic energy (E_k) can be measured and the atomic core level binding energy (E_b) with respect to the energy difference between the highest and lowest occupied single-particle state (Fermi level) of the materials can be determined using the formula: $E_b = hv - E_k - \Phi$ where Φ is the work function of the spectrometer and hv is the energy of X-ray. The associated emitted energy of the electron contains all the relevant chemical information of the sample for the identification of all elements present.

Figure 2.12: Illustration of photoemission showing XPS basis of Ni $2p_{3/2}$ electron (Smith, 1994)

The XPS spectra observed for a particular material is a plot of intensity/count of emitted electrons against the binding energies in eV of those electrons. The various core level binding energies observed in a spectrum can be used to identify all the elements of the

periodic table except hydrogen and helium. Binding energy depends on the atom and the chemical environments, so chemical state information. Generally, binding energy increases as chemical state number increases. Tabulation of binding energies of known elements can be found in a variety of databases(Wagner *et al*., 2003; Moulder *et al*., 1992).

Depth profiling using XPS is a powerful attribute of XPS. A depth profile of the sample in terms of XPS quantities is done by combining a sequence of ion gun etch cycles interleaved with XPS measurement from the surface. Ion gun was used to etch the surface for a period of time before it was turned off while XPS spectra were acquired. Each ion gun etching exposes a new surface for XPS measurement for surface composition.

XPS analyses were carried out with a Thermo Scientific XPS equipped with a monochromatic AI Kα X-ray source (15kV, 10mA) using a take-off angle of 90 deg., fully integrated monochromator with a selectable spot system (30-400 µm).

CasaXPS processing licensed software (version 2.3.16 PR 1.6) from (NEXUS @ nanoLAB, UK) was used for data acquisition of survey high resolution region scans. Backgrounds were Shirley method subtracted fitted with Gaussian-Lorentzian functions.

2.4.8Atomic force microscopy (AFM)

The atomic force microscopywas invented by Binnig et al., (1986)that provides a method for mapping surface topographical features at atomic resolution. Atomic force microscopy principle involves the use of cantilever tip (10-20 nm in radius)at the end which is used to track the sample surface across by scanning in a raster pattern across it. It is typically a prominent tool for 3D nanoscale measurement capabilities.

The illustrationshown in Figure 2.13 shows the cantilever which can oscillate at its resonance frequency position above the test sample with other major components. The piezoelectric tube 3D scanner controls the position of the probe in three dimensions (x, y, z) with applied voltage across them in relation to the surface and a feedback loop mechanism controls the z sample position and maintain the tip constant amplitude above the sample and constant tip-sample distance. In addition, it excites the tip vertically causing the cantilever to oscillate. An oscillating cantilever with tip as fine probe deflects as the probe tip scans the material surface. It also includes a laser containing set of mirrors and a four-segment photodiode. As the cantilever tip oscillates, the photodetector arrays receive and measure the deflection of the cantilever causing the electronic signal that reveals topographic information about the materials under probe. A system controller and computer control the system for display and data acquisition.



Figure 2.13:Illustration of AFM major components, Adopted from (Bruker Nano Surface Division)(Berquand 2013).

Atomic force microscopy can be operated in two modes, contact and tapping mode. In contact mode, AFM cantilever tip is brought in contact with the sample, indenting into it as the scanning proceeds, (Figure 2.14 a).

As the cantilever tip is brought in contact with the material, the force exerted by the tip on the material is dominated by the electrostatic repulsive force which causes the deflection of the tip, and a feedback signal is relayed. In contact mode operation, a soft material can easily get damaged due to the high force exerted by the tip on the sample, even though a cantilever with low spring constant for gentle positioning on soft materials can reduce such damage.

Whereas in tapping mode, (Figure. 2.14 b), usually for imaging soft materials, the cantilever tip does not remain in contact with the sample materials, rather, it oscillates at or near its resonance frequency close to the surface with tapping slightly the surface whose interaction between the tip and the sample is mainly due to the van der Waal's attraction. As usual, the oscillating tip and it's interaction with the materials surface are monitored by a laser beam deflected off the cantilever into the photodetector. As materials surface features change as cantilever tip amplitude changes, and the topographic image is obtained by monitoring those changes.

Figure 2.14: AFM basic modes of operation. (a) Contact mode. (b) Tapping mode (Yan and Wang, 1990).

AFM images were acquired using Multimode Nanoscope IIIa and Dimension Nanoscope V AFM system (Veeco Instruments Inc., Metrology Group), both operated in tapping mode unless otherwise indicated using TESP7 (n-doped Si cantilevers, with resonance frequency 230-280 kHz, force constant range 20-80 Nm^{-1}) Veeco Instruments Inc., Metrology Group) and Tap300AI-G, Monolithic silicon cantilevers) with resonance frequency of 200-400 kHz and a spring constant of 20-75 Nm^{-1}(Budget Sensors) model AFM probes.

Data acquisition were carried out by using Nanoscope IIIa and Nanoscope 7.20 (Build R1Sr1 37066) software (Veeco Instruments Inc.) and JPK Nano wizard AFM. Vibrational noise was reduced by an isolation table/acoustic enclosure (Veeco Inc., Metrology Group).

2.4.9Scanned conductance microscopy (SCM)

This technique which is a variant of electric force microscopy (EFM) is a scanning probe used to monitor the conductance of nanoscale materials without the need for electrical contact. The technique is used for initial verification and rapid assessment of nanowires electrical performance. It serves to provide a no or yes answer to materials conductivity. It has been previously employed to image potentials of single walled carbon nanotubes (SWCNTs) and to demonstrate the insulating properties of Lambda-DNA (Bockrath *et al*., 2002; De Pablo *et al*., 2000); Bachtold *et al*., 2000), and even to discriminate between insulating and conducting polyaniline/poly(ethylene oxide) nanofibers, on microscopic scale (Zhou *et al*., 2003).

SCM basically is a dual–pass line technique that can display an SCM image, record the oscillation phase of a driven voltage-biased AFM cantilever tip at its resonance frequency as a function of tip position (Figure2.15).Experimentally, the phase shift is measured by changes in the cantilever spring constants with electrical and mechanical components contributing to the total energy stored in the tip. The electrical energy created upon the application of a bias potential can perturb the resonances tip and therefore cause a phase shift. So when the capacitance of the system changes due to the presence of conductive nanowires, the electrical energy stored in the tip changes and this cause the tip to deflect by Δx and the phase of the cantilever shifts appropriately. On the other hand, if the mechanical energy stored in the tip changes too with respect to $\Delta Ø$, then the phase shift can be monitored by altering the spring constant of the cantilever.Lastly, because the capacitance is sensitive to the presence of a conductive nanowire, $\Delta Ø$ can be used to determine if the wire is conductive or not.

Figure 2.15: Schematic of SCM in the interleave line (second) scan with tip at fixed height above the sample (Houlton and Watson, 2011)

AFM data collection is achieved by the use of dual-pass techniques as depicted in Figure 2.15. In the first pass, the AFM cantilever tip is driven at its resonance frequency as dc voltage is applied in tapping mode to acquire the sample topography. In the interleave pass as illustrated inFigure 2.15, the tip with applied voltage-biased is retracted at fixed height above the measured topographic features. The cantilever tip is mechanically driven at its resonance frequency. The phase of the cantilever oscillation is recorded as a function of tip position to generate electrostatic force data equivalent to a gray scale plot of the phase lag ø between the cantilever drive and oscillation with respect to tip position.

Mathematical treatment of SCM quantitative model based on the change in the total capacitance of the tip-material-substrate system was well documented elsewhere (Staii *et al*., 2004; Bockrath *et al*., 2002;Pruneanu *et al*., 2008), where the nanowire is modelled as a dielectric strip lying under a tip of defined radius. This treatment determined the phase shift signal associated with nanowires, deduced an indication of the electronic structural properties with respect to dark-negative shift contrast (electrically conducting), Figure 2.16b), thus trapped charges or bright-positive shift contrast (insulating nanostructure),Figure 2.16a).For a conductor, a plot of this phase shift(ΔØ) against a bias potentials could result to parabolic curve due to second

orderrelationship of electric fields to potentials ($E=1/2CV^2$) with the data presented as a correlation between the phase shifts and the potentials applied to the surface.

Figure 2.16: SCM technique to detect the conductive properties of nanowires using dual pass method. (a) 1st pass to acquire material topography. (b) Interleave (2nd) pass for phase shift signal (Pruneanu *et al*., 2008).

CHAPTER THREE

3.0MATERIALS AND METHODS

3.1 Materials

3.1.1 Reagents

All reagents were purchased from Sigma-Aldrich, St Louis, MO & BDH Chemical Ltd and were all AnalaR grade.(Lambda) λ-phase DNA (48,502 bp) 500 µg/ml) and Herring Testes DNA (HT-DNA) from sigma-Aldrich and its Na salt from New England BioLabs, Ipswich, MA with cat. No. N3011S supplied in 10 mM Tris-HCI (pH 8.0) 1 mM EDTA. $FeCI_3.6H_2O$, >97% Sigma analytical graded, imidazole ≥ 99%, pyrrole, NaOH 98-100% pellets, $NaCl,H_2O_2$, concentrated. H_2SO_4, Me_3SiCI (TMS), $Fe(NO_3)_2.9H_20$ 98^+ %, $MgCI_2.H_2O$ 99.9%, ethanol, acetone ≥ 99.8 %, perchloric acid redistilled 99.99%, hydroflouric acid (HF) tungsten wires, pipette dispenser, micropipettes and Eppendorf tubes.

3.1.2 Wafers and apparatus

SiO_2 wafers(Si n <111>) with 200 nm oxide layer and (Si n <100>) (Virginia Semiconductor Inc., Fredericksburg, VA, USA). Ag/AgCl as reference electrodewasobtained from CH Instruments, Inc, Houston, USA.n-Si <111 > wafers, phosphorous doped, 525 ±25 µm thickness, 1-12 ohm cm, coated with a thermally grown SiO_2 layer and single side polished was used as support for AFM imaging, FTIR and XPS. Si <100> 200 nm thick SiO_2 layer, arsenic doped, < 0.005 Ω cm. double polished in which thermally grown oxide layer was removed from one side using aqueous HF before piranha treated were used for SCM. Deionised water (18 MΩ cm resistivity) for solution preparation was purified with NANOpure Diamond UV

ultrapure water system equipped with a diamond RO reverse osmosis system (Barnstead international).

3.2 **Cleaning of $1 \times 1cm^2$ pieces Si wafers**

All Si wafers were treated with chlorotrimethylsilane (CTMS).n-Si(111) wafers were cut into ~$1 \times 1cm^2$ pieces using tip pen and cleaned with acetone using cotton bud followed by propanol and finally the substrate surface was oxidised with piranha solution (H_2SO_4:H_2O_2in the ratio 4:1) for 45 minutes. *The Piranha solution was prepared by adding H_2O_2 to H_2SO_4in a glass container because the mixture being a very strong oxidant that can react violently with organic materials.* After removal from piranha solution, the wafers were rinsed with large excess of Nanopure water and dried in stream of N_2 and further dried in clean oven for 8 minutes. Actual surface modification of the cleaned Si wafer was done by vapourous deposition ofCTMS vapour to produce self-assembled monolayer of CTMS. Accordingly, this was done by placing the piranha-treated Si wafer on top of a small specimen bottle with polished SiO_2 side facing down inside a large specimen bottle containing about 0.1mL of CTMS and left for about 10 minutes in cupboard hoodat room temperature as shown in Figure 3.1. The Si wafer was then removed and kept on top of a small whatman filter paper for N_2 aided molecular combing.The CTMS modification led to an increase inthe hydrophobic character of the wafer surfaces.

Figure 3.1: Modification of Si wafer through self-assembly of monolayer of CTMS

Wafers for EMF were Silicon p<100> (~1 $\times$ 1cm^2)200 nm thick with SiO_2 layer. Before cleaning and DNA alignment, HF solution was used to removethe oxide layer from one side of the wafer by using drops of HF solution (10 % aq) to provide am electrical contact. The wafer was then rinsed with Nanopure water. Complete removal of the SiO_2 layer was verified by using a digital multimeter (Agilent Digit Multimeter, Agilent Technology UK Ltd). The resulting wafers was treated with piranha solution for 45 minutes,then washed with NANOpure thoroughly, before the wafer was blown dry in a N_2 stream. Finally,CTMS modification was carried out as previously described.

3.3 Preparation of DNA-Templated Nanowires

3.3.1 Preparation of DNA/FeOOH nanowires

FeOOH nanowires templating on DNA was done using $NaOH_{(aq)}$ as precipitant. Typically, DNA/FeOOH nanowires were prepared by mixing 6µL of 200 μgmL^{-1} with 12µL of Fe $(NO_3)_3.9H_2O$ (3mM) in Eppendorf curvette. Under continuous stirring on magnetic stirrer (Scheme 3.1) at room temperature for 30 minutes, NaOH (6µL, 1.7 mM) was added slowly under vigorous stirring until the solution's pH was 12, then incubated for 6 hours at room temperature followed by ageing for 48 hrs at 20^oC for

final DNA templated FeOOH nanowires. Upon completion of the ageing process, tiny faint yellow strands were observed.

3.3.2Preparation of DNA/FeOOH nanowires for characterisations

Herring testes DNA (HT-DNA) was employed for the preparation of DNA-templated FeOOH nanowire for XRD and UV-visible spectroscopy studies because this technique required large samples. Sodium salt of HT-DNA solution (2.0 ml, 162.5µg/ml) was freshly prepared and left to stand for complete dissolution. Stock solution of $Fe(NO_3)_3.9H_2O$ (0.5 ml, 3mM) was mixed with the HT-DNA at a ratio of 2:1 and incubated at 30^oC for an hour to reduce hydrolysis. Then NaOH (55 mM 0.5 ml) was added dropwise.

This was followed by excess addition until the pH was ~12 to precipitate FeOOH on DNA under N_2 flow at room temperature. UV-Visible was recorded on Cary 100 Bio UV-Visible spectrophotometer (Varian) equipped with temperature control within 200-600 nm.

Scheme 3.1: Schematic diagram for HT-DNA/FeOOH nanowires formation, (Zubairu *et al*., 2013).

The Sample for XRD analysis was prepared in the same manner as above except that addition of methanol causedthe precipitation of HTDNA/FeOOH.Afterward, the precipitate was separated by centrifugation, washed with nanopure water repeatedly until pH 7 was observed. Then the component was rinsed with acetone and vacuum dried at 50^{o}C. XRD patterns were recorded on Bruker 2D phaser bench top diffractometer with Cu Kα radiation source (λ= 1.54178 Å) at a scan rate of 1^{o}/s within $10\text{-}70^{o}$ (2θ). Particle size was calculated based on measured Scherrer broadening of the XRD peaks.

All FTIR measurements in the work were carried out using Varian 800 FTIR spectrometer system using a pike technologies diamond crystal plate ATR. Spectra were recorded with 124 scans and 4 cm^{-1} spectral resolution within 400-4000 cm^{-1} in transmission mode. Samples were prepared as thin film on TMS-modified Si wafers as substrates. It was prepared by adding (20µL, 1mg/mL) of HT-DNA to Fe $(NO_3)_3.9H_2O$ (7.0 mM 40µL) stir at 30^{o}C before NaOH 70 mM was added to pH 12, then left for 20 minutes. Drop-cast of 70 µL of the resulting solution was deposited onto the modified Si wafer and solvent allowed to dry in a vacuum hood for an hour, for FTIR spectra to be taken. The same applied to bare HT-DNA preparedas thin film only as control.

DNA-templating material for XPS was prepared in a similar manner as described for FTIR as solid thin film on the TMS modified Si substrate. XPS was recorded on Thermo Scientific equipped with an AI Kα X-ray source (1486.6 eV) and operating power of 100 W (15 kV, 7mA) using a take-off angle 90^{0} with fully integrated monochromator and a selectable spot system (30-400 µm). Samples were prepared for XPS by depositing 5 µL of solution on a clean Si wafer and left to dry at room

temperature in a laminar flow hood to minimize contamination. The above were mounted on Cu sample stubs with carbon tape with neutralizer gun as charge compensation to stabilize the sample surface and ensure the best peak shape, whilst ensuring that peak separation between transitions is independent of the energy at which the electrons are measured. Binding energies were referenced to C1s peak core level of 285 eV. CasaXPS processing licensed software from (NEXUS @ nanoLAB, UK) was used for data acquisition of survey resolution region scans. Backgrounds were Shirley method subtracted fitted with Gaussian-Lorentzian functions (Neal, 2009).

Depth profiling using XPSwas done by combining a sequence of ion gun etch of 200 eV interleaved with XPS measurement from the surface. An ion gun was used to etch the materials surface for a period of time (0, 402, 803, 1204, 1606 seconds) before it was turned off while XPS spectra are acquired. Each ion gun etching exposes a new surface for XPS measurement for surface composition.

The formation of DNA/FeOOH nanowires for AFM and TEM/EDX was done by adding about 3 µL of the templated solution onto the edge of a freshly prepared 1cm^2/square TMS modified Si wafer at room temperature and stretching or dragged across the surface via molecular combing and then allowed to dry in the hood for 7-10 min, in this case, N_2 aided. AFM images were acquired using Multimode Nanoscope III a and Dimension Nanoscope V AFM system (Veeco Instruments Inc., Metrology Group, Germany), both operated in tapping mode unless indicated using TESP7 (n-doped Si cantilevers, with (f0) resonance frequency of 230-280 kHz, force constant range of 20-80 Nm-^{1}), Veeco Instruments Inc., Metrology Group) and Tap300AI-G, Monolithic silicon cantilevers) with resonance frequency of 200-400 kHz and a spring constant of 20-75 Nm^{-1} ((Budget Sensors) model AFM probes. Data acquisitions were carried out using Nanoscope IIIa and Nanoscope 7.2 software (Veeco Instruments Inc.)

and JPK Nano wizard AFM. Vibrational noise was reduced by an isolation table/acoustic enclosure (Veeco Inc., Metrology Group). All the wafers were degreased by immersion in acetone and propanol for 8 minutes, then rinsed with Nanopure water and dried in a stream of N_2 before silanization process.

TEM/EDX (energy dispersive X-ray spectroscopy) images were collected at Durham University and Electron Microscopy Research Services, Medical School, NCL, UK using JEOL-2100F FEG TEM with 200 kV alignment and high resolution pole piece with 1.0 mm C_s 2.3 Å point resolution together with Piezo-driven stage for precision sample movement at high magnifications. For TEM measurements, 2 µL of the templated materials were placed on carbon-coated copper grids 400 mesh after an ultrasonic treatment for 4 min. and allowed to dry before TEM and EDX measurements were taken. The grids were examined using a Philips CM 100 Compustage (FEI). Transmission electron microscope and digital images were collected using an AMT CCD camera (Deben).

Scanning conductance microscopy (SCM) measurements, a variant of electrostatic force microscopy (EFM) were carried out in air with the same Dimension Nanoscope V system using MESP probes (n-doped Si cantilevers) with metallic Co/ Cr coating, Veeco Instrument Inc., and resonance frequency of 60-100 kHz and a spring constant of 1-5 Nm^{-1}. Acquisition and processing of SCM data were done using Nanoscope 7.2 software (Veeco Instrument Inc.) as vibrational noise reduced by acoustic enclosure.

SCM measurements were conducted using a dual-pass mode where topography is fist recorded in the tapping mode, then the vibrating tips tracked the first line scan. At second line scan, the tip travelled at certain lift-height above the sample and a bias potential (dc) applied between the sample and the tip at a driven free oscillation resonant frequency thus an electrostatic field generated betweenthe nanowire surface

and the tip (Staii *et al*., 2004). During the SCM experiments, controlled bias potential was set between -7 and +7 V to the sample while tip was grounded and a constant lift height of 50 nm applied. Preparations for this probe microscopy was carried as 20µL of the diluted λ-DNA 200 ngμL^{-1} was added to Fe $(NO_3)_3.9H_2O$ (5 µL 3.5 mM) with mild shaking before addition of 55 mM, 2.5 µL of NaOH dropwise until in excess to pH 12 under reducedtemperature. Then incubated for hours at room temperature before any probe microscopy process.Samples for SCM studies were prepared on n Si <100> /200 nm SiO_2 thermally grown oxide layer after piranha cleaned and as determined by spectrometric film analyzer.

3.3.3Preparation of bulk FeOOH nanoparticles

The synthesis was performed via one-pot reaction method (Li *etal*., 2004) without growth regulating or morphology controlling agents with modification. This was done via slow hydrolysis (Cornell and Schwertmann,2003), by refluxing (200µL, 3.5 mM) of Fe $(NO_3)_3.9H_2O$ solution in NaOH (100 µL, 1.5 mM) at room temperature under a stream of N_2 with mild magnetic stirring. At the beginning, a precipitate with dark brown colour was observed with the colour changing on standing to reddish brown which is a characteristic of Fe_2O_3. The pH of the solution was adjusted to pHof 12.90. The precipitate was filtered and washed severally with nanopure water till the ring reaction in the wash water was negative. The product was then converted into FeOOH by ageing it in the form of a suspension in 1.5 mM NaOH solution. Bright solid yellow precipitate was observed after 1 day ageing. The resulting mixture was transferred into 40 ml teflon containing an ice slurry with N_2 inlet and maintained at 18^oC for 24 hours. Upon adding more nanopure water, the teflon was sealed and maintained at 80^0C for 10 hours. The solution's colour turned faint yellowish with yellow particles which indicated the formation of nanoparticles. After the reaction was completed, the Teflon

was cooled to room temperature and the resulting precipitate centrifuged, filtered off, washed several times (CI^- free) then with absolute ethanol in sequence followed by water Nanopure severally until pH of 7 was reached. It was vacuum dried at 100^0C for 10 hours. The prepared nanoparticles were purified with 2.0 ml of particle suspension in 10 mM of HCIvial solution with stirring. This was again tested for efficiency by varying its pH within 0-6, and separated by centrifugation (750 rpm) before being calcined in air at 150^0C. This procedure is similar to those used for purifying carbon nanotubes(Kim *etal*., 2007; Chen *etal*., 2007) and gold nanorods(Bushee *etal*., 2003). While purifying, it was observed that some particles dissolved and the solution turned yellow with yellow particles at the bottom. The methodology was verified by XPS, XRD, TEM, FTIR and TG/DTA/DSC.

3.3.4 Preparation of bulk FeOOH nanoparticles for characterizations

Sample for TEMstudies was prepared by placing a drop of fresh DNA/FeOOH solution onto special micromesh grid of conductive metal (holey carbon-coated Cu grid) or dispersing the solid sample in nanopure and sonicating them for 20 minutes. A drop of the sonicated solution was placed on the holey carbon-coated Cu grid and followed by slow evaporation at room temperature prior to TEM micrographs measurements on JEOL 2100F TEM operated at an accelerating voltage of 200 kV interfaced with EDX and on Philips CM 100 Compustage (FEI) TEM.

XRD patterns for crystallographic phase identification was performed on Si wafer with 200 nm SiO_2 layer and recorded on Bruker 2D phaser bench top diffractometer with Cu Kα radiation source (λ= 1.54178 Å / 0.154178 nm) at a scan rate of 1^o/s within a 2θ range of 10-70^o. The Si wafer was thoroughly cleaned with propanol and piranha treated. The nanowires were then stretched across the wafer using the

moving meniscus of a drop of solution. The Particle size calculated as described previously.

Other preparations at lower concentration especially for XPS & TEMwere done by isolating FeOOH nanoparticles from solution by methanol addition using magnetic separation at the stage of ageing in Teflon sealed for 10 hours. In the second step, the as-prepared nanoparticle was converted to Fe_2O_3 via sintering / dehydration at 400^0C for 3 hours in addition to bulk synthesis of Fe_2O_3as alternative.

Thermal analyses (TGA/DTG/DSC) of the samples were carried out on NETZSCH STA 449C and Balzers MID thermal analyzer at a heating rate of 10 K/min from room temperature to 500^oC in N_2 stream, and their corresponding thermograms obtained as shown in Figure 4.5.

3.4Preparation of DNA/Fe_2O_3 Nanowires

Preparation of DNA/Fe_2O_3 nanostructures for AFM andTEM/EDX was carried out as follows. 20 µL, 200 ng/µL of λ-DNA was added to 5 µL, 7.0 mM of aqueous $FeCl_3.6H_2O$ in Eppendorf tube and stirred mildly for 30 min. before NaOH solution(3.0 µL, 55 mM) was finally added dropwise at pH 13.75 with stirring. Subsequently the resulting solution was incubated at 60^oC for an hour to hasten hydrolysis for full Fe_2O_3 formation on the DNA before alignment on wafers.

HT-DNA was used, in this case,as Na salt for the synthesis of DNA-templated Fe_2O_3 for UV-Visible analysis. Sodium salt of HT-DNA solution (2.0 ml, 6.29 mg/ml) was freshly prepared and left for four hours for complete dissolution. Stock solution of $FeCl_3.6H_2O$ (0.5 ml, 3mM) was mixed with the HT-DNA at a ratio of 2:1 and incubated for an hour. Then NaOH (4.4 mM 4.4 ml) was added dropwise. This was followed by excess addition until the pH was ~12 to precipitate Fe_2O_3 on DNA under N_2 flow at

60^{o}C. The UV-visiblespectrum was recorded on Cary 100 Bio UV-Visible spectrophotometer (Varian).

3.4.1 Preparation of DNA/Fe_2O_3nanowires for characterisation

Samples for XRD analysis were prepared in the same manner as DNA/FeOOH templated samples except that Fe $(NO_3)_3.9H_2O$ was replaced with $FeCI_3.6H_20$. For FTIR. The samples were prepared as thin films to localize sufficient product on modified Si wafers. This was done by adding (80 µL. 1mM) of $FeCl_3.6H_20$ solution to 50 µL, 1mg/ml^{-1} of HT-DNA and left at 60^{o}C for an hour before incubation for three hour on mild-magnetic stirrer. Then 60 µL of the resulting nanowires was dropcast on TMS modified Si wafer after cleaning with piranha solution and the solvent evaporated ina vacuum hood for an hour for FTIR. Spectra were recorded with 124 scans and 4 cm^{-1} spectral resolution within 400-4000 cm^{-1} in transmission mode without the use of any matrices.

DNA-templating materials for XPS were prepared in a similar manner as described for FTIR as solid thin film on the TMS modified Si substrate. XPS spectral survey was taken on Thermo Scientific equipped with an AI Kα X-ray source (1.486.6 eV) and operating power of 100 W (15 kV, 7mA) using a take-off angle 90 degree with a fully integrated monochromator with a selectable spot system (30-400 µm). Samples were prepared and mounted for XPS analysis as previously described in section 3.3.1 and depth profiling follows for sputter etching of samples for defined period of time (0, 402, 803, 1204, and 1606 seconds).

For SCM, λ-DNA of defined length (48.502 base pair in length) was used as templating agent for the nanowires. The Sample for this was prepared by adding $FeCl_3.6H_2O$ (5 µL 2.0 mM) solution to λ-DNA, 20µL, 200 ng$µL^{-1}$with mild shaking before addition of

NaOH (1.7 mM, 3.0 µL) dropwise until in excess to pH 12 under increasedtemperature, then incubated for hours at room temperature before 6 µL was deposited on Si <100> wafer, 200 nm thick SiO_2 layer, modified with TMS as described previously (Figure 3.2).

3.4.2Preparation bulk Fe_2O_3 nanoparticles

Fe_2O_3 nanoparticles were prepared through a two-step reaction process by a solvothermal process for FeOOH and calcination of the precursor for Fe_2O_3 formation. The typical precipitation of Fe_2O_3 nanoparticles followed the same one-pot reaction strategy as previously described,(Figure 3.3.2). In this case, $FeCl_3.6H_2O$ was used as precursor. In the synthesis under N_2 flow, $FeCl_3.6H_2O$ (0.503M, 4ml) aqueous solution was mixed with NaOH (3.6 M, 30 ml)solution with the help of magnetic stirrer on teflon container. The suspension pH was adjusted to 12 byaddition of NaOH solution in the reaction process. Further 10ml of nanopure water was added and kept overnight, hydrothermally at 140^oC. Then the red ultra-fine precipitate was filtered off, washed severally with nanopure water til the filtrate was free of acid and methanol and dried at 100^0C for one day. The resultant product was calcined in air from room temperature to 500^0C at a heating rate of 2^oC/min. and maintained at 400^0C for 2 hours. After, the furnace was cooled to room temperature,and the red Fe_2O_3 was obtained. All other previous characterization protocols were used to study the nanoparticles.

3.5Polymerization of Pyrrole (Py) on DNA Solution

3.5.1 Preparation of Ppyand DNA/Ppy nanowires

One-spot synthesis in Eppendorf tube was used to perform DNA/Ppy nanowires involving oxidative polymerisation of pyrrole monomers in aqueous solution (Skotheim,1998) with little modification. It involved addition of pyrrole monomers

solution to λ-DNA and subsequent addition of an oxidant to initiate polymerization process. DNA/Ppy nanowires synthesis was done by adding freshly prepared $MgCl_2.6H_2O$ solution (0.5 mM, 5 µL) to λ-DNA solution (500 ng/µL, 20 µL). The solutions were thoroughly mixed. This would interact with the λ-DNA strands so as to mask the force of repulsion. Then freshly prepared pyrrole monomers (3 mM, 5 µL) with thorough shaking again before the final addition of $FeCl_3$ (1 mM, 5 µL) as oxidant and subsequently incubated at room temperature for three hours for the formation DNA-templated Ppy nanowires structure as mimicked in the Scheme 3.2, highlighting the templating induced by oxidative polymerisation of pyrrole in $FeCI_3$.

Scheme 3.2: Templating by DNA molecules in directing the growth of Ppy(Watson*et al*., 2012)

3.5.2 Preparation of DNA/Ppy nanowires for characterisations

HT-DNA–templated nanowires were prepared as thin film for use in FTIR studies. A solution of HT-DNA (1.65 mg/mL, 20 ml) was freshly prepared and left for 5 hours for complete dissolution before use. Then $MgCl_2.6H_2O$ solution (0.5 mM, 1 ml) was added to the HT-DNA solution. Freshly prepared solution of $FeCl_3$ (2.01 mM, 1 ml) was then added to the solution followed by pyrrole monomer (6.23 Mm, 1ml) addition. This was followed by incubation for a period of 6 hours at room temperature for the final DNA-templated Ppy nanowires. Drop-casting was done onto oxidized Si wafer after piranha treated and solvent evaporated in vacuum hood for an hours for FTIR. FTIR spectra in

the range 400-4000 cm^{-1} were recorded in transmission mode with Varian 800 FTIR spectrometer system and the spectra collected in 124 scans with 4 cm^{-1} resolution.

XPSwas carried out on samples of λ-DNA nanowires dropcast on cleaned Si wafer as substrate. The measurements were carried out as previously described. Depth profile XPS studies were also carried out.

AFM studies were done following incubation of λ-DNA (20 µL, 200 ng/µL), $MgCl_2$ (0.5 mM, 2.5µL), $FeCI_3$ (5 µL 1.0 mM), Ppy (3mM, 5µL) for three hours for the formation of DNA/Ppy nanowires. About 4 µL of resulting solution was applied to the modified wafer surface and left for up to 45s before combing for AFM studies.

As previously described, samples for SCM studies were prepared as above for AFM but the studies were on n Si <100> /200 nm coated SiO_2 layer removed by hydroflouric acid (HF) application, cut into 1 cm^2 square after piranha cleaned. Prior to use, the Si wafer was blown with N_2 stream and further dried in oven and finally CTMS modified as previously stated. Molecular combing was used to align the DNA/Ppy nanowires as to be described later.

3.5.3Formation of Bulk Polypyrrole

3.5.3.1Formation by oxidation with $FeCl_3$

Freshly prepared $FeCl_3$ solution (30 ml, 0.12 M) was added to pyrrole monomer (10 ml, 2.0 M) and left to stand and magnetically stirred for 8 hours under ice cooling conditions. At this stage, a green solution was observed that slowly turned black, after which the solution was centrifuged for 20 minutes to remove the supernatant. The black precipitate was rinsed with nanopure water, centrifuged again,and thenwashed with methanol to remove unreacted pyrrole and any remaining oxidant. This was done after each wash and finally the sample was dried in a vacuum oven at 70^oC for 10 hours. At

this stage, the samples were set for XRD, FTIRand other studies. The induced oxidative polymerisation of pyrrole with $FeCl_3$ forming Ppy is shown in Scheme 3.3 as equations.

3.5.3.2 Formation of Ppy by electrochemical reduction

In the same vain, electrochemical reduction method was used again to synthesize the Ppy via cyclic voltammetry (CV) studies along with the corresponding DNA analogue to obtain redox peaks that can be ascribed to cation/anion movement according to Scheme 3.3.

Scheme 3.3: The Ppy formation oxidatively with $FeCI_3$

In this method, cyclic voltammetry approach was used as the setupshown in Figure 3.5.

Plate3.1: Cyclic voltammetry set up (a) degassing the mixture with N_2(b) actual cyclic voltammograms taken. (This work)

In this as represented in Plate 3.1, 100 mM solution of NaCl was used as electrolyte in pyrrole monomer solution (30 mM) in volume ratio 1:1 and Ag/AgCl as reference electrode, Au electrode as working electrode(W_e) and tungsten wire as counter electrode (C_e) during the electrochemical reduction. As shown in, Figure 3.5 (b), CV was performed using a computer-interfaced (CH Instrument electrochemical microscopy system, Austin, Texas, USA). The CV was run by sweeping the potential between 1.200V and -1.200V, with a scan rate 0-1 v/s, equilibrium time was 10s and sometimes 4 or more number of scans, and 100 μA as current range.After the CV was taken, all the electrodes were removed and a thin film of the product deposited on the Au electrode for FTIR/XRD studies.

3.6Polymerization of Imidazole on DNA Solution

3.6.1 Preparation of DNA/PImi nanowires and bulk PImi

DNA/PImi syntheses were done oxidatively using a similar method to that for DNA/Ppy as well as initial electrochemical reduction that monitors the reduction process as described above. Typically, freshly prepared imidazole solution (2.5 µL 3 mM) was added to DNA (10 µL 500 µg/µL) in Eppendorf tube in the presence of $MgCl_2$. H_2O (2.5 µL 0.5 mM), then (2.5 µL 1Mm) of $FeCl_3$solution was added and thoroughly magnetically shaken, incubated for 2 hours for the formation of DNA-templated PImi nanowires as previously shown, and then alignedfor TEM/EDX, AFM and SCM studies.

3.6.2 Preparation of DNA/PImi and bulk PImi for characterisations

The UV-Vis, FTIR, XRD and XPS measurements, certain milligrams of the sodium salt of HT-DNA (2.75mg/ml, 8 ml) were used. In this case, yellowish viscous solution was seen with spiral suspension after slowly magnetically stirred at 45 ^{o}C for 30 min. and left at room temperature for 4 hours before being treated as dried product prior to the studies.

Scheme3.4: Polymerization of imidazole using $FeCI_3$ as oxidant (this study).

As shown as Scheme 3.4, freshly prepared oxidant, $FeCl_3$. $6H_2O$ (0.503 M) solution was added to imidazole solution (3.40 g, 0.50 M) in the ratio 2:1 as monomers and magnetically stirred. A five hour oxidation time at elevated temperature was adopted to

avoid degradation at longer time in acidic medium before washing in acetone and dried under vacuum without heating for 12 hours. A Viscous dark brown precipitate was observed. This was filtrated, washed in acetone and finally vacuum dried.

As previously mentioned, electrochemical synthesis,(Figure 3.5) was also performed via CV method to get a little bit of cleaner polymer products, aside monitoring the redox pathways.

3.7Alignment of DNA-Templated Nanowires using N_2 flow Assisted

For probe microscopic characterisation, controlling and manipulating DNA are critical in the field of nanotechnology. This is due to the tendency of DNA to aggregate. Strategies are described to immobilize and strengthen DNA strands on a solid substrate using different approaches. In this case, the proposed method by gas flow was used (Jianwei *et al*., 1998). Most of the techniques for aligning DNA require further modification of DNA extremities through biochemical processes. This is a disadvantage for prior modification. Substrate surface modifications using the above methods to facilitate DNA molecular stretching such as silanization based on Langmuir-Blodgett deposition technique (Michalet *etal*., 1997) have also been put forward.

DNA adheres strongly to hydrophilic surfaces such as mica or oxidized SiO_2 to comb well and would not adhere to highly hydrophobic surfaces. For this reaction, minimal modification is important such that few DNA strands adhere loosely to produce aligned DNA molecules. In this work, preliminary report shows that partial silanization using chlorotrimethylsilane (Me_3SiCl vapour),for less than 10 minutes, produces well aligned separated parallel nanowires on SiO_2 wafer. For this, Si/SiO_2 as substrate was a good choice. Aside that, it is widely used in semiconductor industries as silicon chips, because it is inert and smooth. Overall, the most interesting method for stretching/aligning DNA on solid surfaces is the molecular combing without the need

for DNA ends prior modification(Bensimon *etal*., 1995; Bensimon *etal*., 1994; Nasari and Gurevich, 2013)**.**This technique relies on the hydrophobic interactions of DNA ends with the surface. Different protocols have been used in this work to induce the moving interface thus facilitating easy combing.

In its simplest protocol, thermally modified Si wafer was modified with CTMS, a vaporous –phase that provides good adhesion between the wafer surface and the DNA strands. A drop (~ 3 µ L) of an incubated DNA solution or its analogue was deposited on the hydrophobic surface. The sample was allowed to stand at room temperature for less than 2 minutes. The compressed N_2 flow was applied to the sample in such a way that the direction of N_2 stream was at an angle of 45^o to the normal of the substrateas shown in Scheme 3.5. The N_2 flow was pointed on the part of the DNA solution-air-substrate interface. This drove the interface along the substrate through the hydrated part of the DNA molecules with the resulting stretching of the molecules thus stretching the strands. Then the remaining solution was removed by wicking with filter paper, keeping the N_2 stream constant for several seconds to dry the sample completely

Scheme 3.5: DNA aligning illustration on Si substrate by molecular combing technique (this work)

CHAPTER FOUR

4.0RESULTS

4.1 Cyclic Voltammetry Studies

Cyclic voltammetry (CV) was used to study the redox process in the electrochemical synthesis of polypyrrole film and its corresponding DNA analogue from an aqueous solution using a potential sweep rate of 0-1 v/s between +1.200V/Ag/Ag+ and -1.200V/Ag/Ag+.

Typical CV spectra of pyrrole-polypyrrole nanoparticles and DNA/polypyrrole after 2 days, and polyimidazole nanoparticles and DNA/polyimidazole respectively at 2 mm diameter Au disc electrode areshown in Figures 4.1 and 4.2.

4.2 FTIR Studies

The FTIR spectra of both net DNA and DNA-templated are shown from Figures4.3 to4.11with prominent change in band positions. Figures 4.3 and 4.4 show spectra of DNA/Ppy and DNA/Plmi nanowires respectively with band assignments

presented in Table 4.1. While those of DNA/Fe_2O_3 and DNA/FeOOH spectra are illustrated in Figures 4.5 and 4.6.Control FT-IR spectrum of net HT-DNA deposited on Si wafer as thin film from solution is also presented in Figure 4.7and Table 4.2displaying the corresponding features of control DNA.The FT-IR spectra of neat pyrrole film (Py),polypyrrole film (Ppy), neat imidazole thin film (Im), polyimidazole thin film (PImi) are all shown in Figures 4.8 and 4.9.

The FT-IR spectra of neat FeOOH and Fe_2O_3 nanoparticles only are shown in Figures 4.10and 4.11 with the corresponding absorption peaks.

4.3UV-Vis Spectra

UV-visible absorption spectrum of neat DNA and the corresponding DNA-templated nanowires are shown in Figures 4.12 to 4.16.

Figure 4.1:(a)and (b) cyclic voltammograms of Ppy and λ-DNA/Ppy as a function of scan rate with different cycle. NaCI (0.1 M) as supporting electrolyte.
Sweep direction as shown above (black arrow)



Figure 4.2 (c and d): Cyclic voltammograms of PImi and λ-DNA/PImi as a function of scan rate with different cycle. NaCI (0.1 M) was used as supporting electrolyte

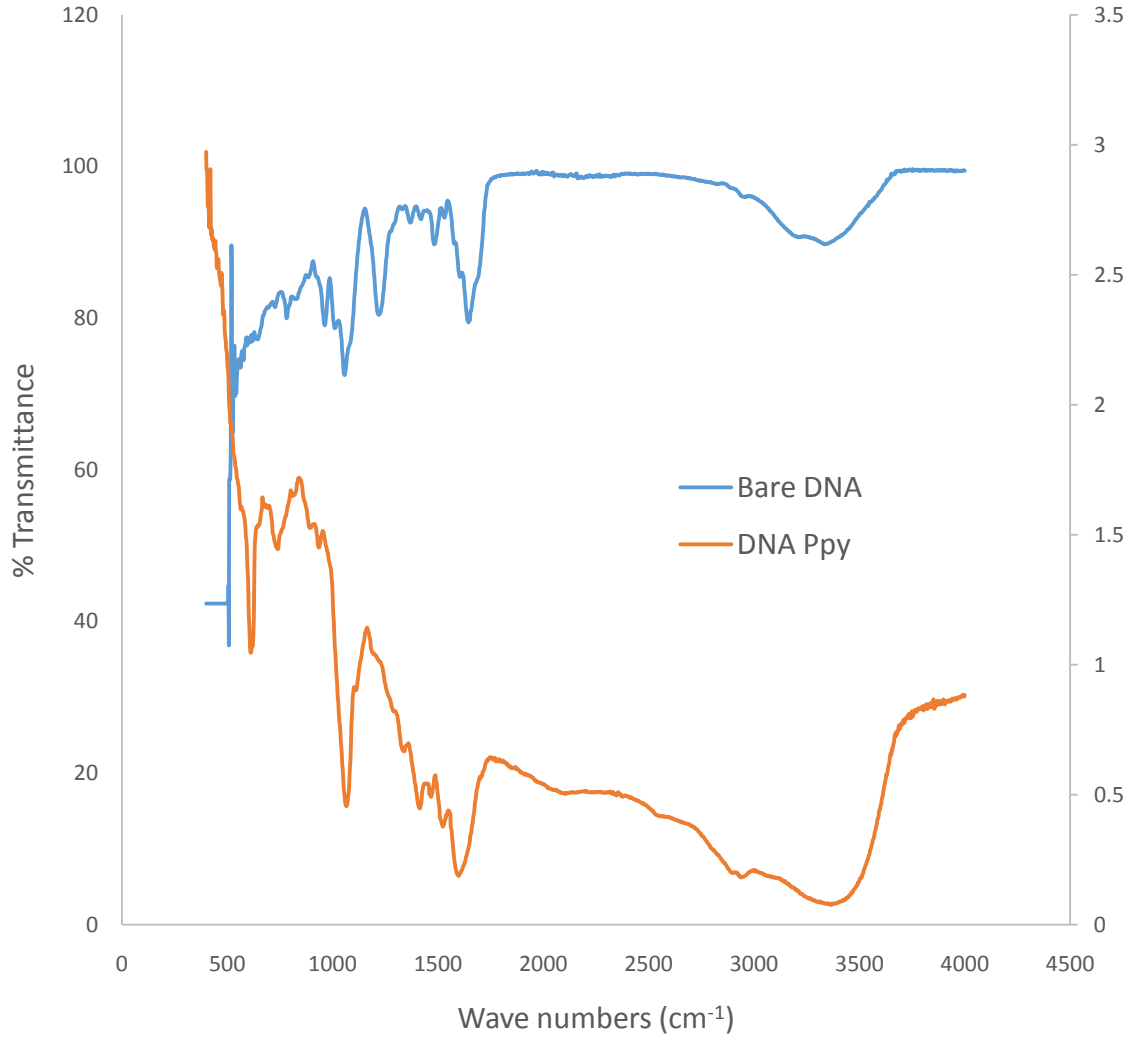


Figure 4.3: FTIR spectra of DNA-templated materials, bare DNA and DNA/Ppy

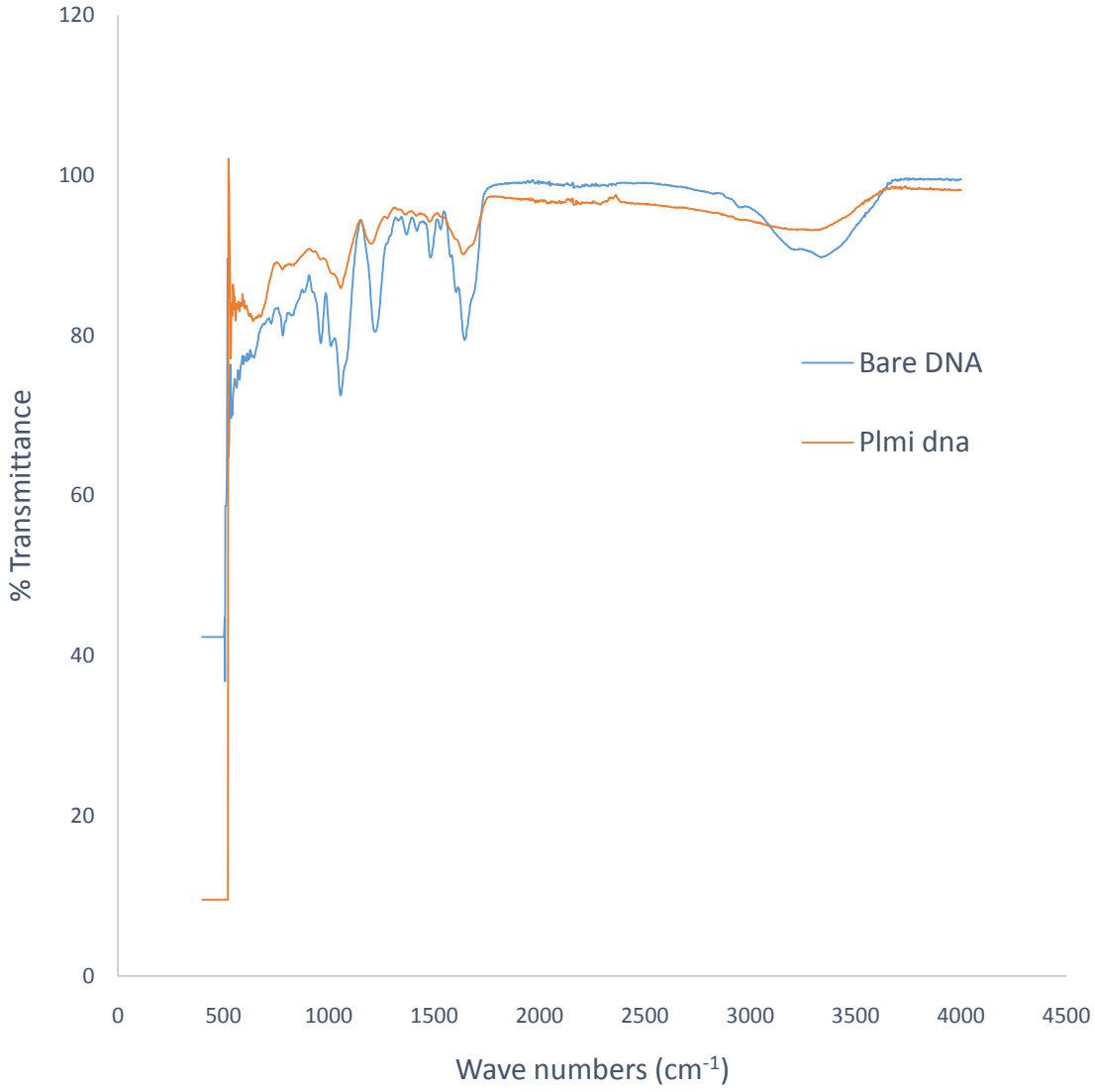


Figure 4.4: FTIR spectra of DNA-templated materials, bare DNA and DNA/PImi

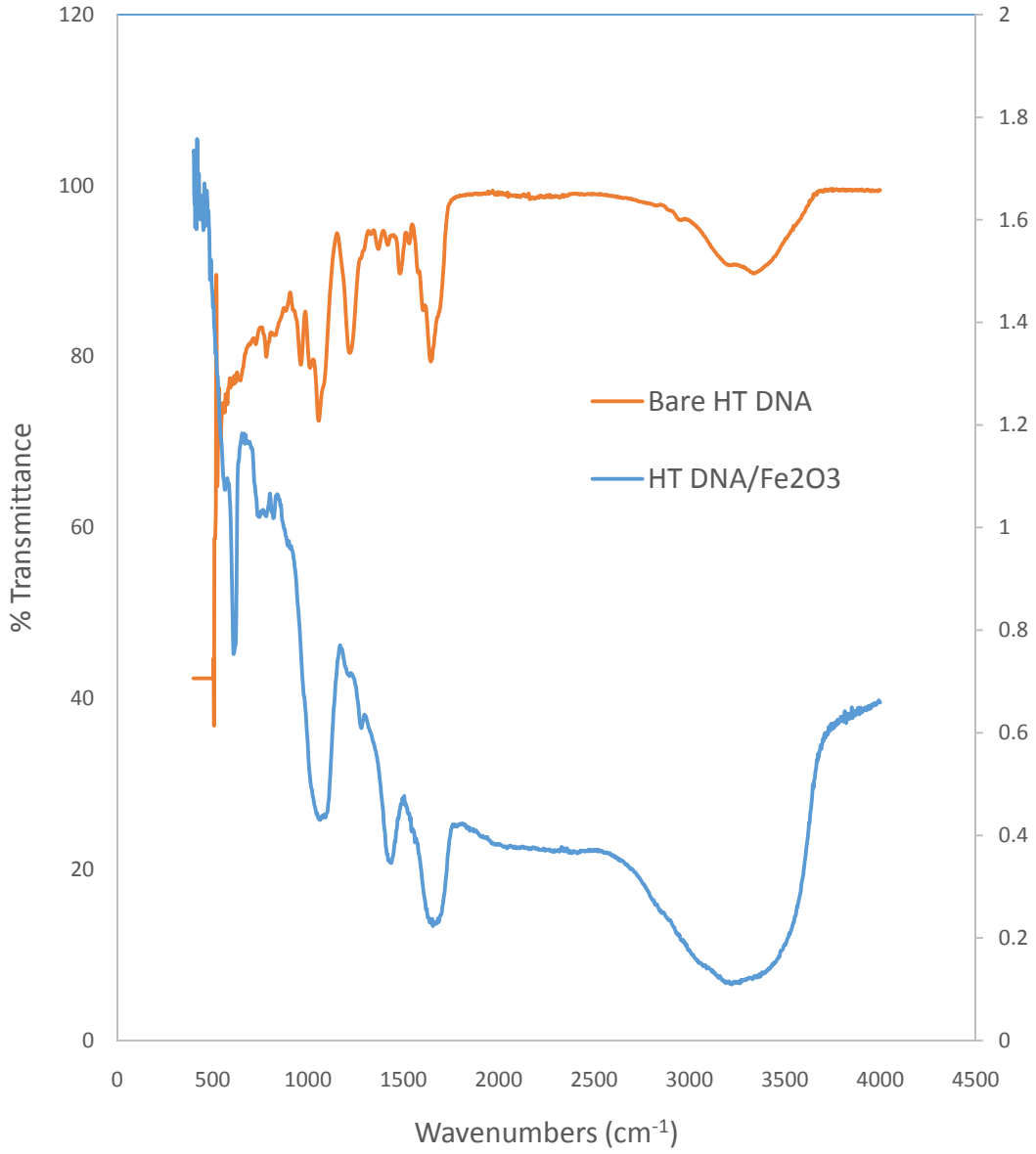


Figure 4.5: FTIR spectra of DNA-templated materials, DNA/Fe_2O_3

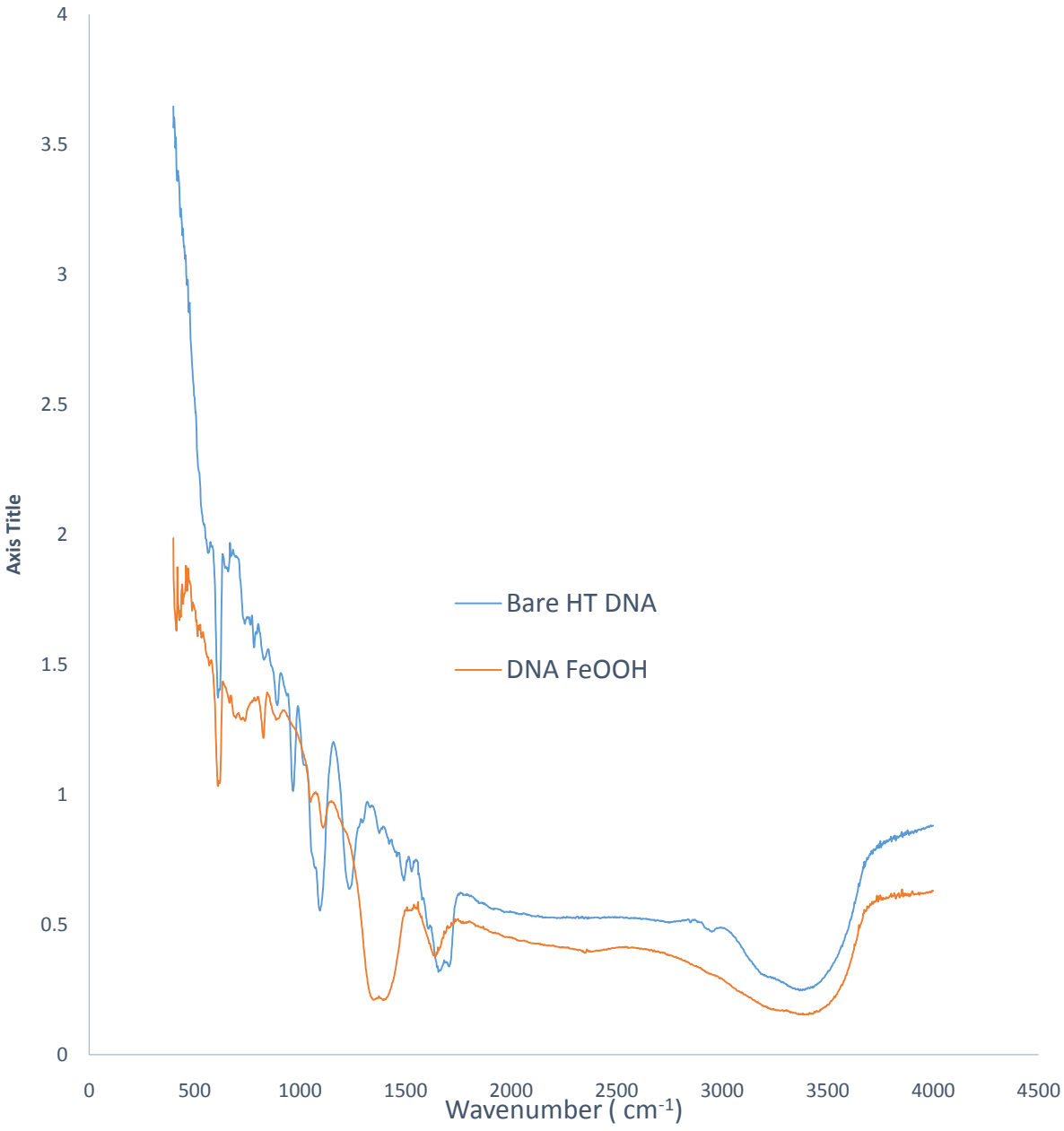


Figure 4.6: FTIR spectra of DNA-templated materials, DNA/FeOOH

Table 4.1: Measured bands assignment of FTIR spectrum of DNA and DNA/templated at 400-4000 cm^{-1}.[sh] peaks appeared as shoulder.[b] this work

DNA[b] cm^{-1}	DNA/Ppy[b] cm^{-1}	DNA/PImi[b] cm^{-1}	DNA/Fe_2O_3[b] cm^{-1}	DNA/FeOOH[b] cm^{-1}	Assignment[a] cm^{-1}
-	-	-	580, 615, 794	611, 738, 825	Fe-O st
-	893	812	821	825	C-H $_{out\ of\ plane}$
962	935	995	906	896	C-C st deoxyribose
1055	1070	1010	1056	1097	P-O/C-O backbone st
1087[sh]	1110	1068	1064	1114	PO_2^- symmetric stretch
1230	1213	1211	1278	-	PO_2^- asymmetric stretch
1296 [sh]	-	1253[sh]	1280[sh]	-	C-N st G/T/C/A
1380	1373	1352	-	-	C-N st G/C
1423	1405	1330	-	-	C-N st T/G/C
1481	1523	1450	1436	1408-1380	C8-N coupled with ring vibration of G
1529	-	-	-	1531	V in-plane of G/C
1587[sh]	1531	-	1535 [sh]	-	C=N st of G/A
1620	-	1639sh	1556[sh]	-	C-N st of G and N-H st A
1645	1606	1620	1676	1641	C-O st of A/C and In-plane vibration of T
1681	1689	1658	-	-	C2=O st of G, N-H st of A and T vibrations
3000-3500	3414	3348	3236	3431	N-H st/O-H st

Figure 4.7: FTIR spectrum of net HT-DNA

Table 4.2: Table of FTIR absorption in peak positions of bare DNA before templating as reference. DNA FTIR spectral features were assigned according to reference (Watson *et al*., 2012;Dorbeshko *et al*., 2000); (Ouameur and Tajmir-Riahi,2000); (Sarka and Mandel,2009); (Guo *et al*., 2009; Sun *et al*., 2007 and Alex and Dupuis 1989).

Peak Number	Assignment	DNA (cm^{-1})
1	N-H stretches	3345
2	O-H stretches	3206
3	C2=O stretch of guanine and N-H of adenine and thymine vibrations	1681
4	C-O st of thymine and cytosine), In-plane vibration of thymine	1645
5	C=N st of guanine and N-H st adenine	1620
6	C=N st of guanine and adenine stretch	1587
7	C8-N coupled with ring vibration of guanine)	1481
8	C-N stretch of Thymine, guanine and cytosine	1423
9	C-N stretch of cytosine and guanine	1381
10	C-N of adenine, guanine, Thymine and cytosine	1296
11	PO_2- asymmetric stretch	1230
12	PO_2- symmetric stretch	1287
13	P-O/C-O deoxyribose stretch	1055
14	C-O deoxyribose stretch	1012
15	C-C deoxyribose stretch	962

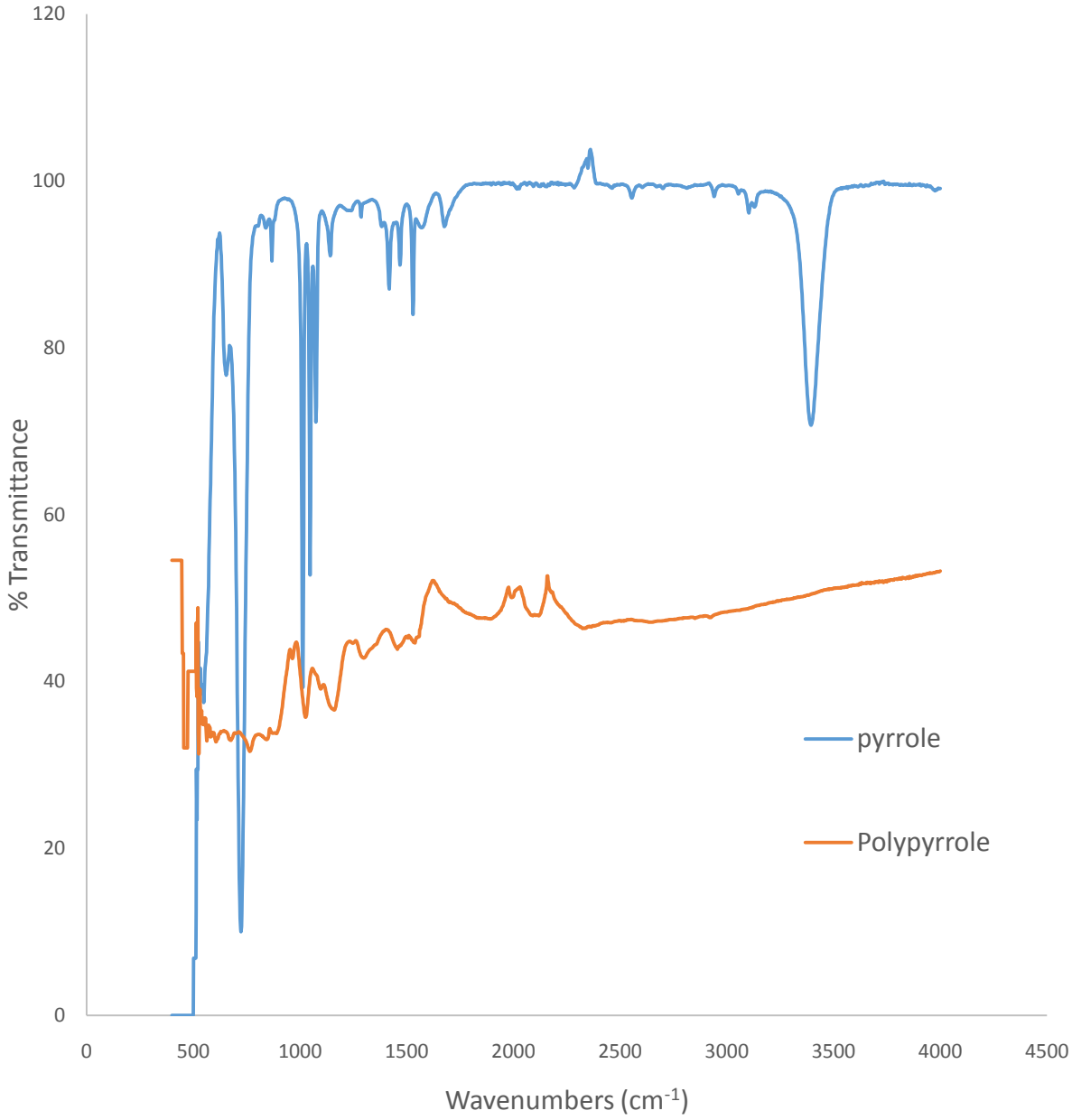


Figure 4.8: FTIR spectra of pyrrole (blue spectrum) and polypyrrole (red spectrum)

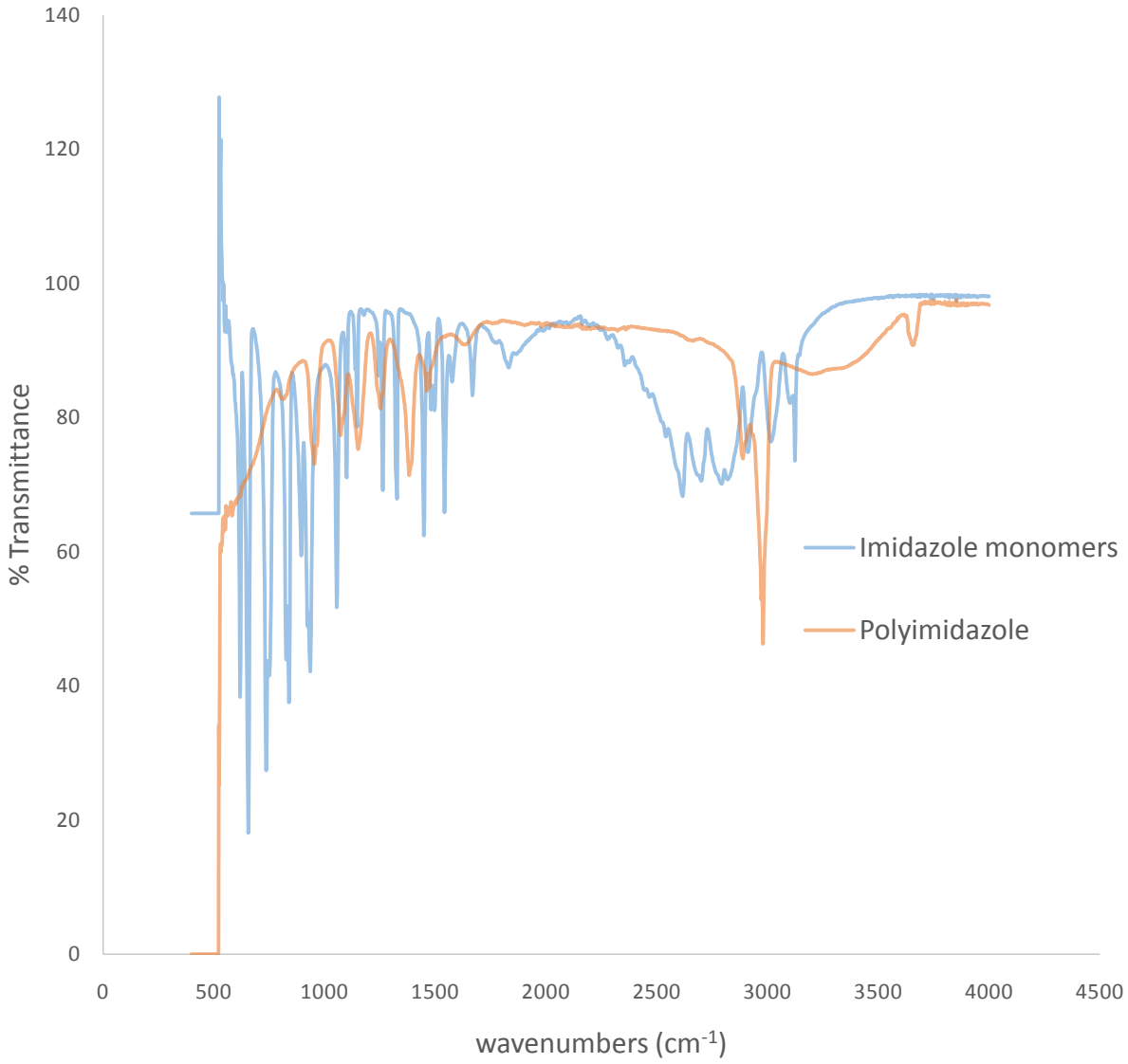


Figure 4.9: FTIR spectra of imidazole (blue spectrum) and polyimidazole (red spectrum)

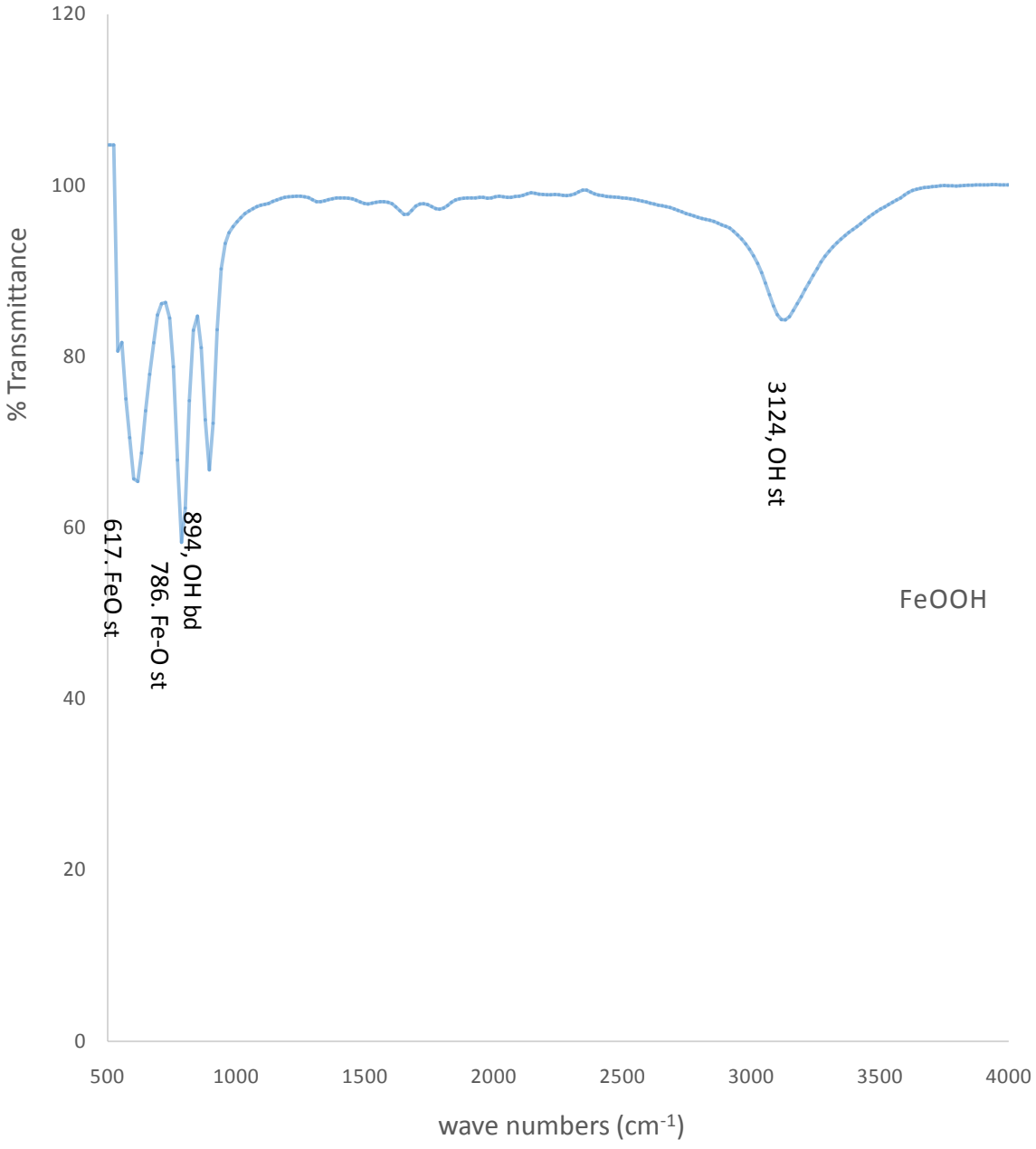


Figure 4.10: FTIR spectra of net inorganic oxide semiconductor (FeOOH nanoparticles)

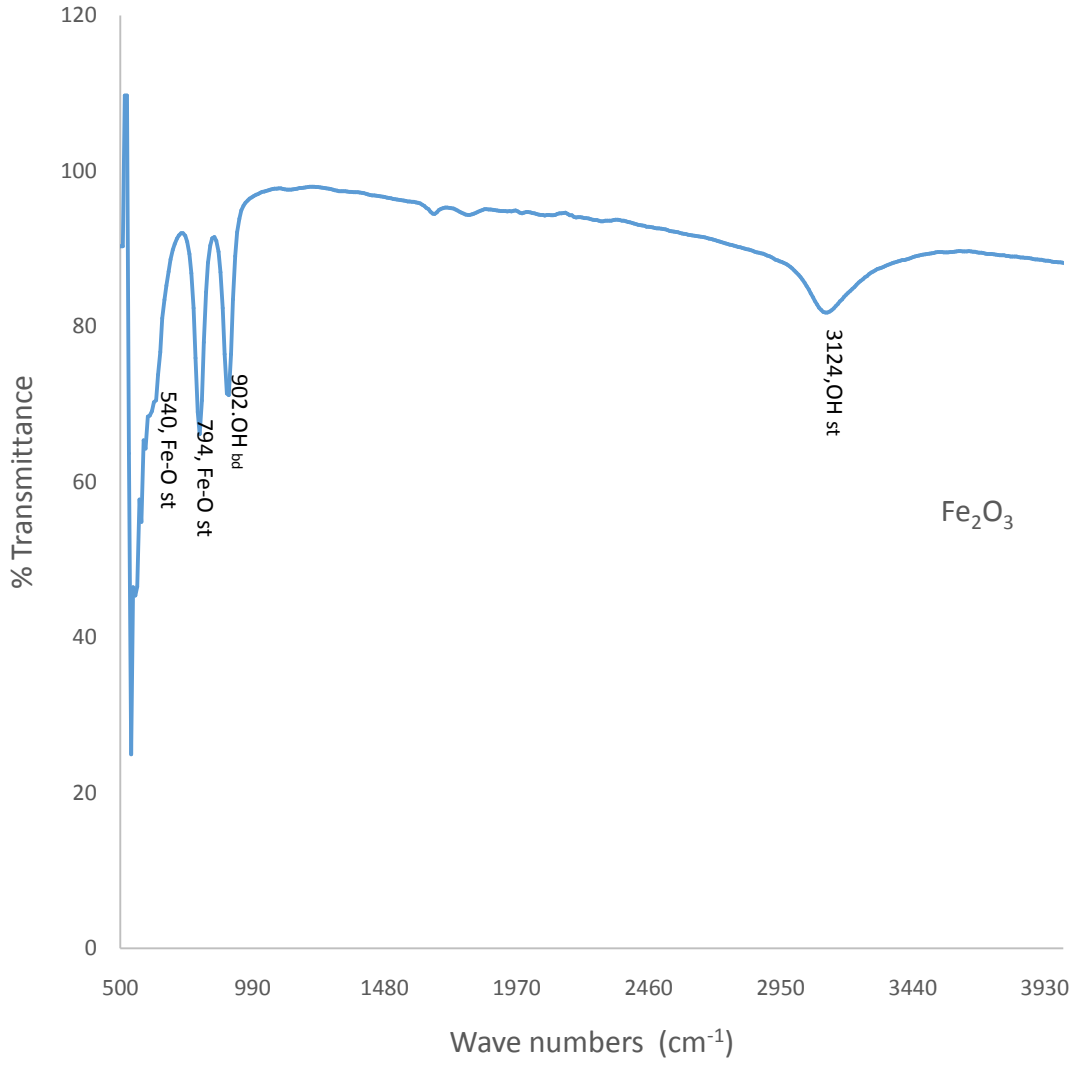


Figure 4.11: FTIR spectra of net inorganic oxide semiconductor Fe_2O_3 nanoparticles

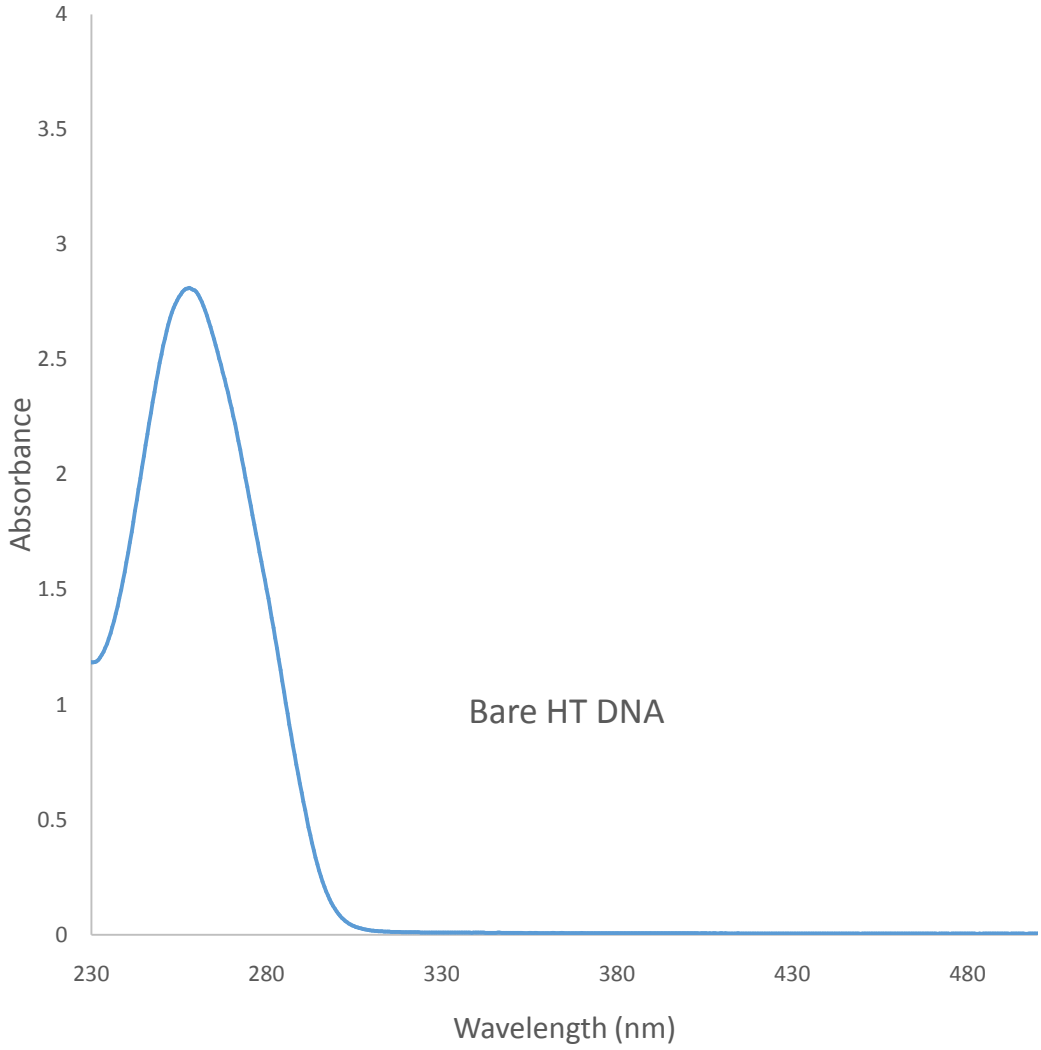


Figure 4.12: UV-vis. absorption spectrum of net HT-DNA

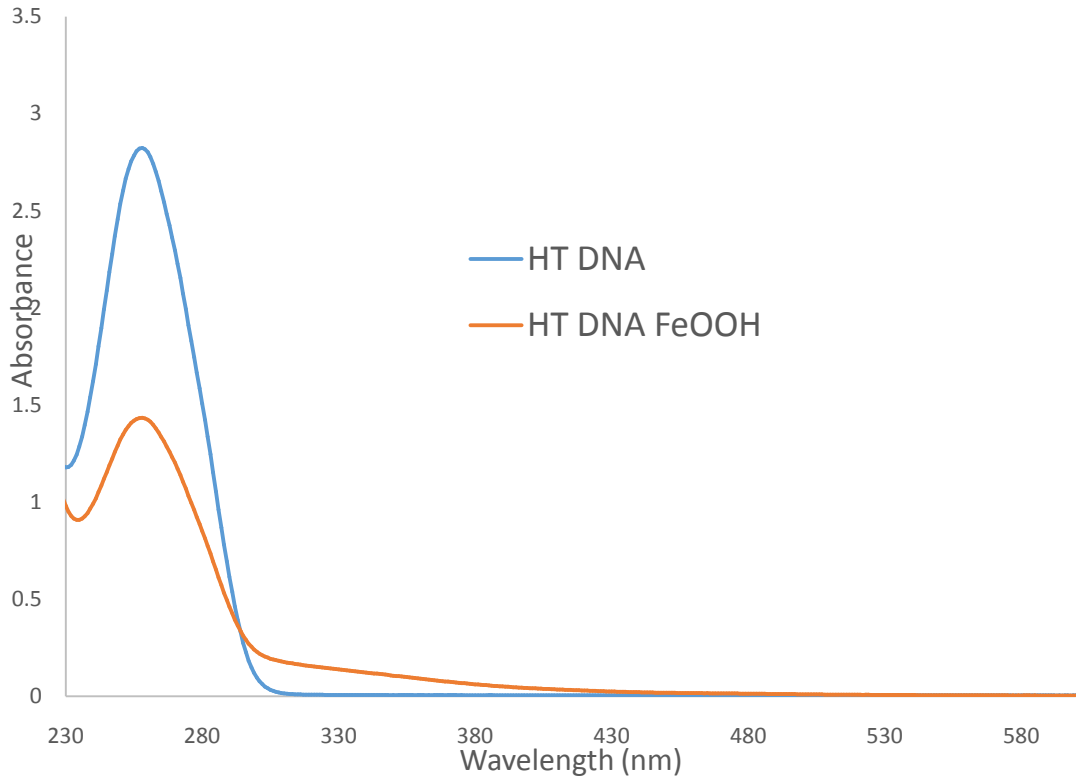


Figure 4.13: UV-vis. absorption spectra of net HT-DNA and HT-DNA/FeOOH

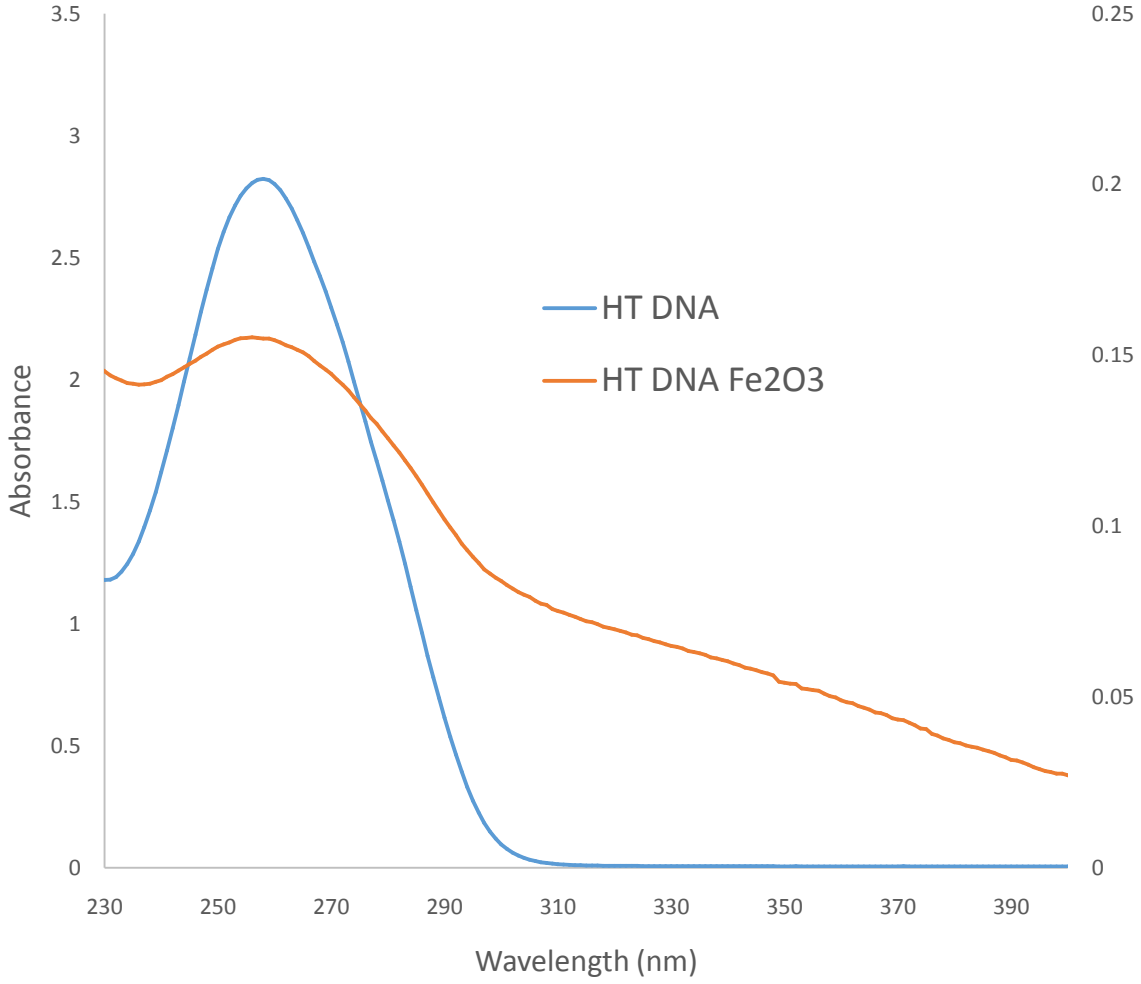


Figure 4.14: UV-vis absorption spectra of net HT-DNA and HT-DNA/Fe_2O_3

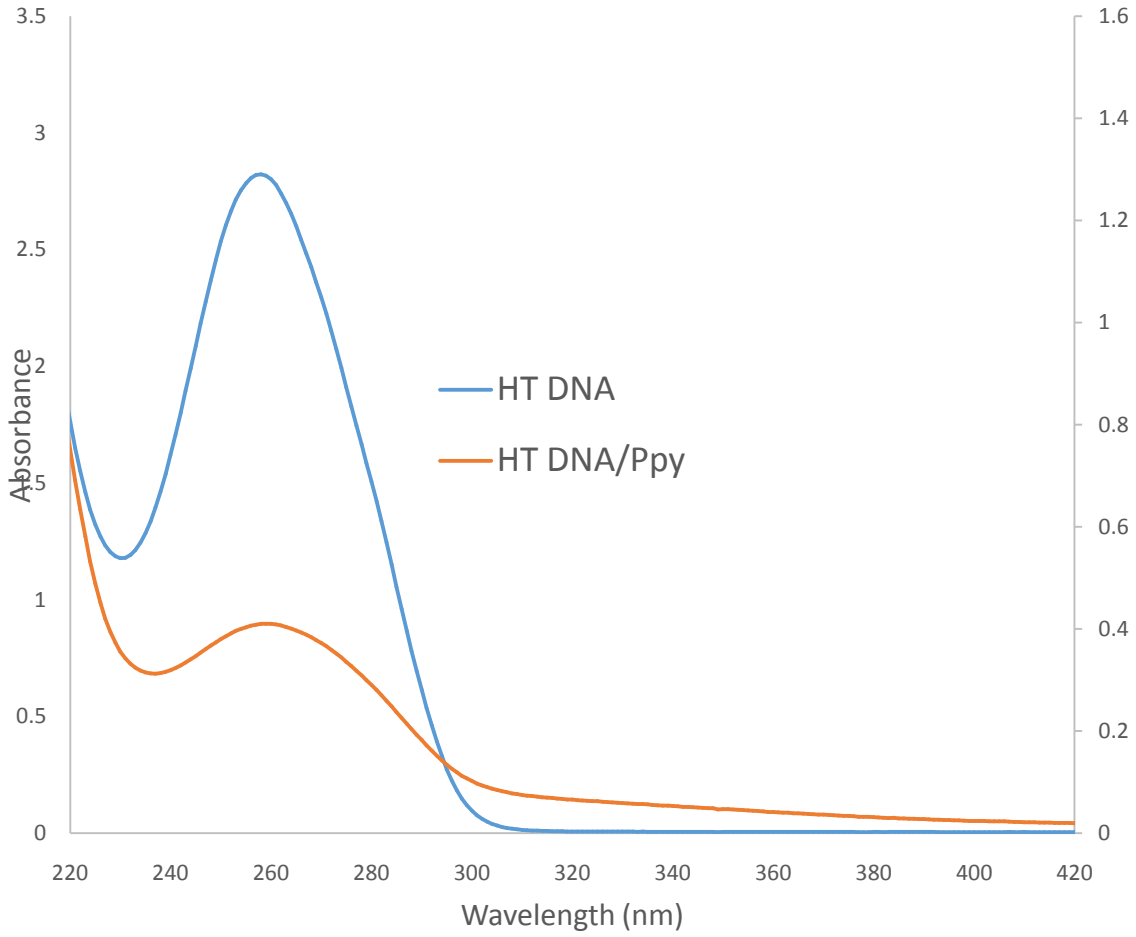


Figure 4.15: UV-vis absorption spectra of net HT-DNA and HT-DNA/Ppy

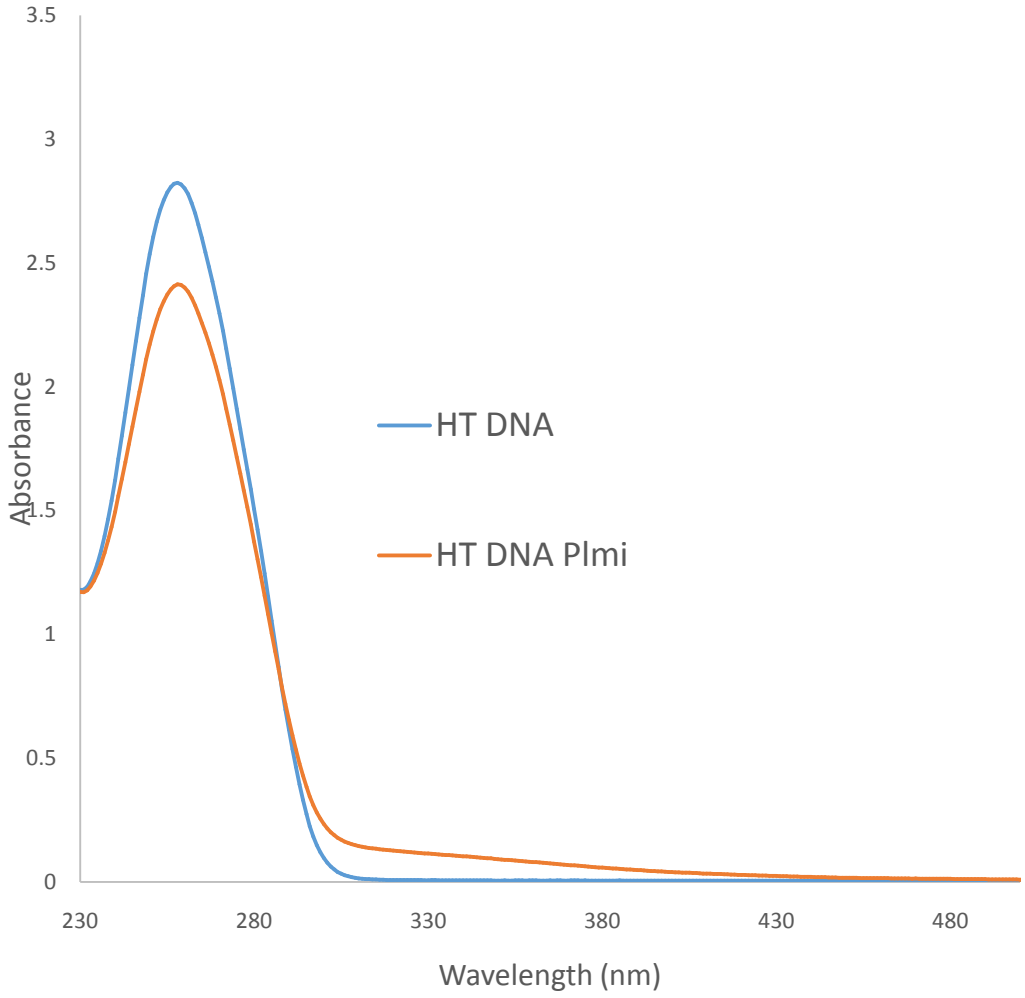


Figure 4.16: UV-Vis absorption spectra of net HT-DNA and HT-DNA/PImi.

4.4 Thermal Measurements

TG, DTA and DSC for the two nanoparticles are shown in Figures 4.17 to 4.20.

4.5 XRD Patterns

XRD patterns of FeOOH nanoparticles and its DNA analogue are displayed in Figure 4.21, The XRD patterns for Fe_2O_3 nanoparticles and its DNA analogue as well arealso presented in Figure 4.22, while the patterns for Ppy, Plmi nanoparticles and the HTDNA/Plm nanowire are shown in Figures 4.23 and 4.24.

4.6 TEM Analyses

TEM images of FeOOH nanoparticles and its DNA/FeOOH nanowires counterpart are shown in Figures 4.25 and 4.26 in different magnifications and electron diffraction patterns together with dark and bright field micrographs as insets.

TEM images of Fe_2O_3 nanoparticles and its DNA/Fe_2O_3 nanowires are shown in Figures 4.27and 4.28in different magnifications with insets at the edges of Figure 4.28.

TEM images of Ppy nanoparticles and it DNA/Ppy nanowires are shown in Figures 4.29 and 4.30 in different magnifications, while those of Plmi nanoparticles and itsDNA/Plmi nanowires are also shown in Figures 4.31 and 4.32 in different magnifications.

4.7 EDX Analyses

EDX spectra of DNA/FeOOH and DNA/Fe_2O_3 nanowires are shown in Figure 4.33.

4.8XPS Analyses

XPS survey spectrum of FeOOH thin film is shown in Figure 4.34 with it's characteristic atom concentrations, while the XPS high resolution spectrum of FeOOH components are shown in 4.35.

XPS survey spectra of HT-DNA/FeOOH nanowires as thin film with characteristic atom concentrations is shown in Figure 4.36 and the XPS high resolution spectra of HT-DNA/FeOOH nanowires components are shown in Figure 4.37.

XPS survey spectrum of Fe_2O_3 nanowires is shown in Figure 4.38 and the XPS high resolution spectra of Fe_2O_3 components are shown in Figure 4.39.

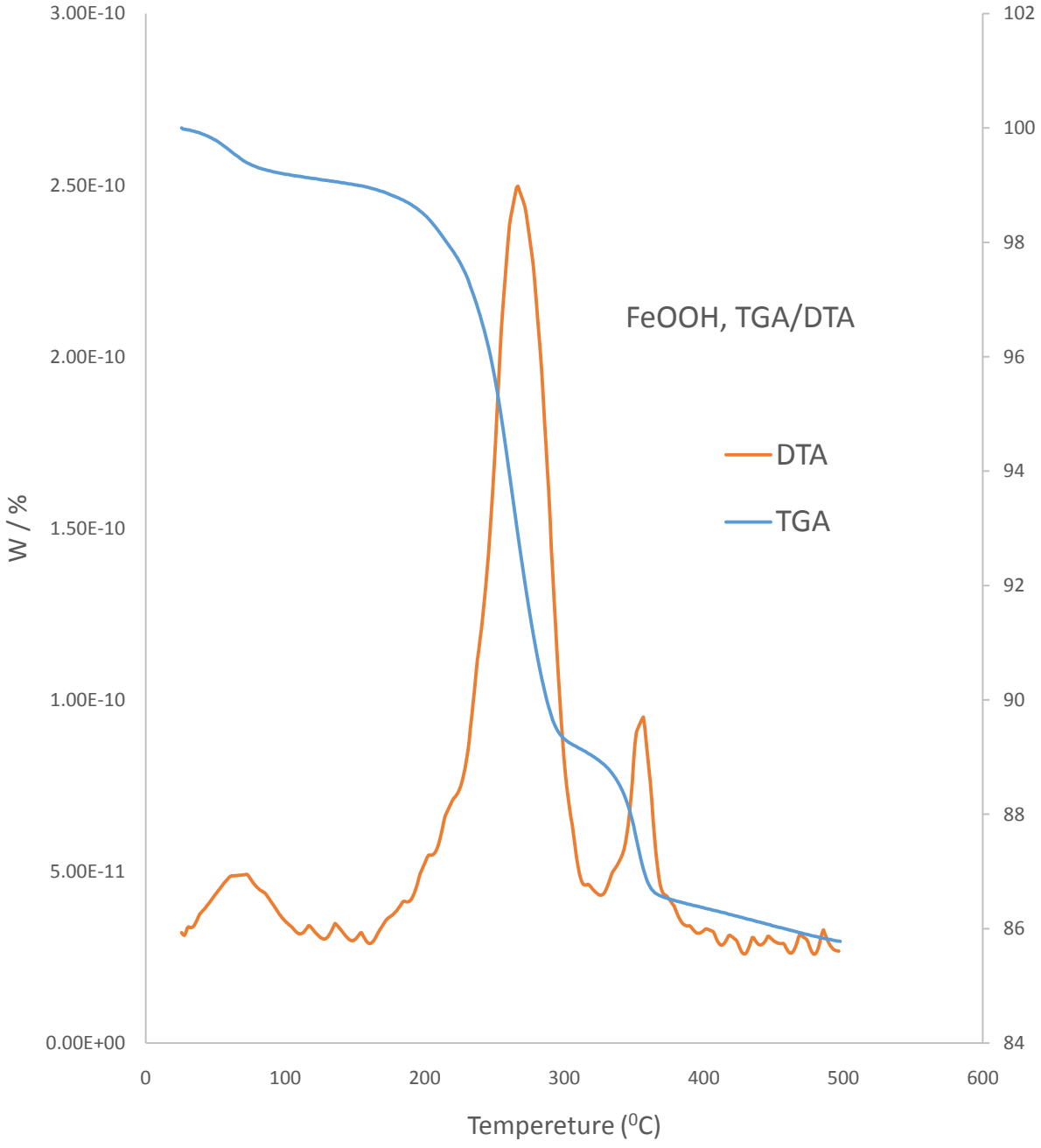


Figure 4.17: TG-DTA of FeOOH nanoparticles

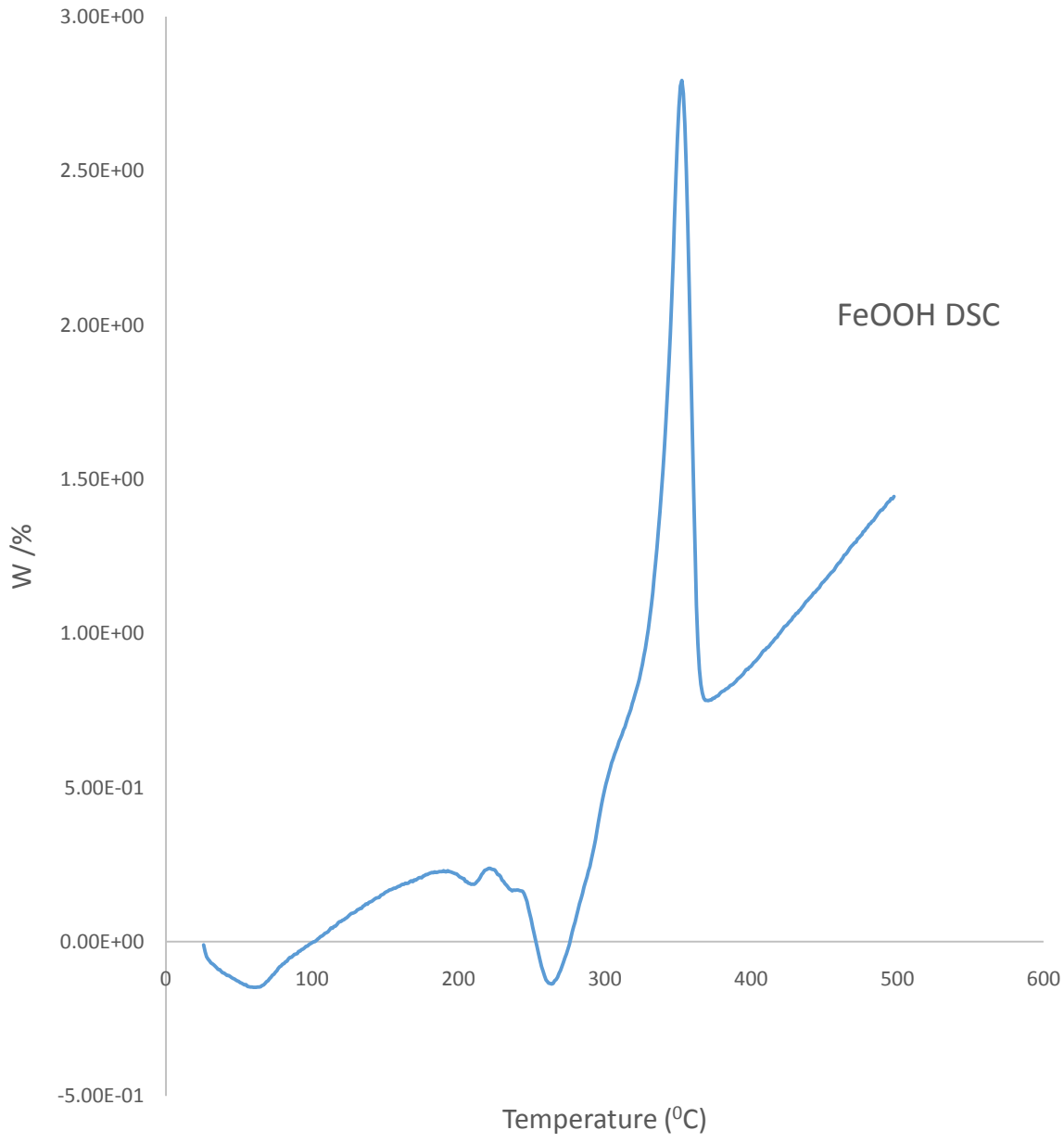


Figure 4.18: DSC of FeOOH nanoparticles

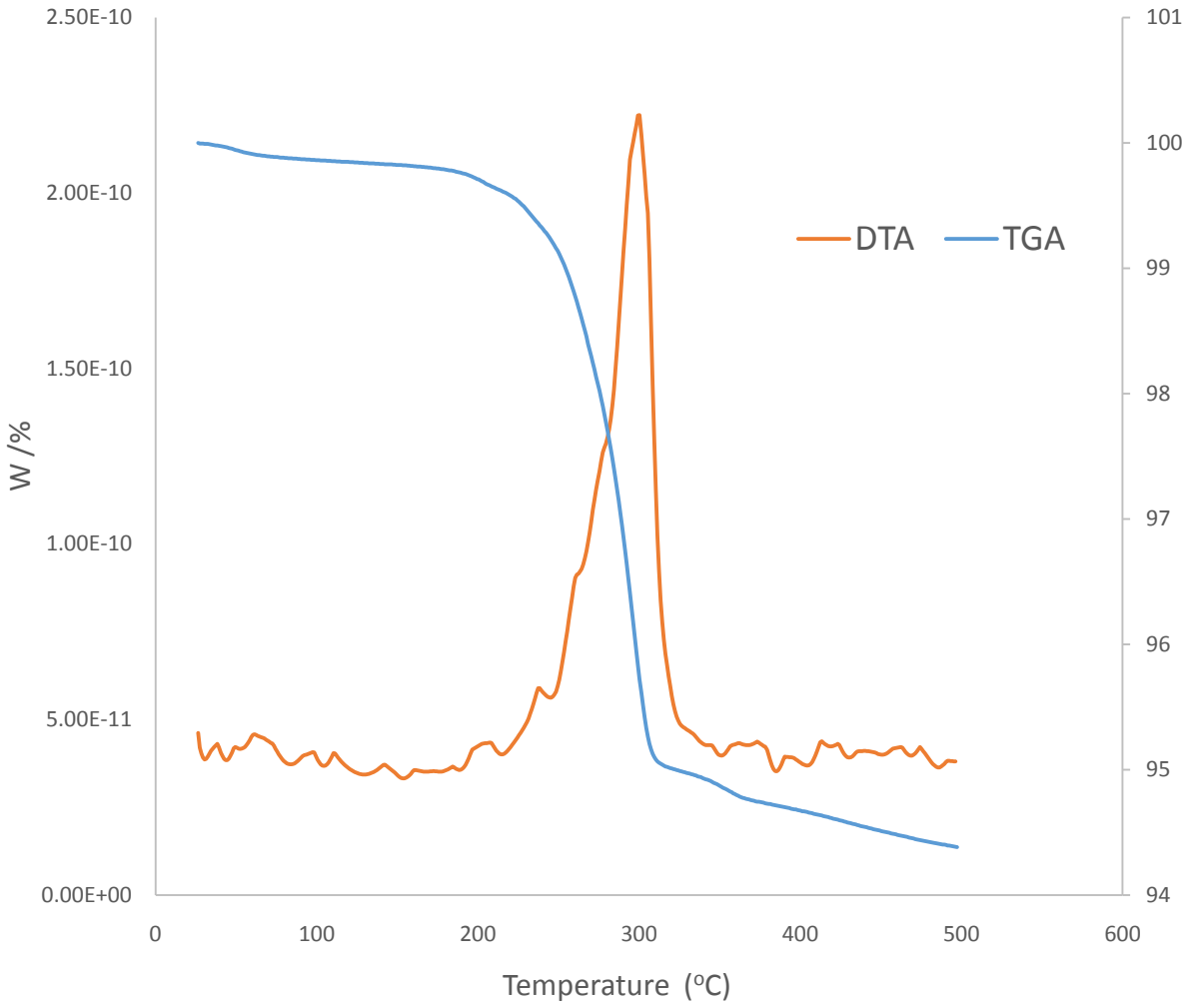


Figure 4.19: TG-DTA of Fe_2O_3nanoparticles

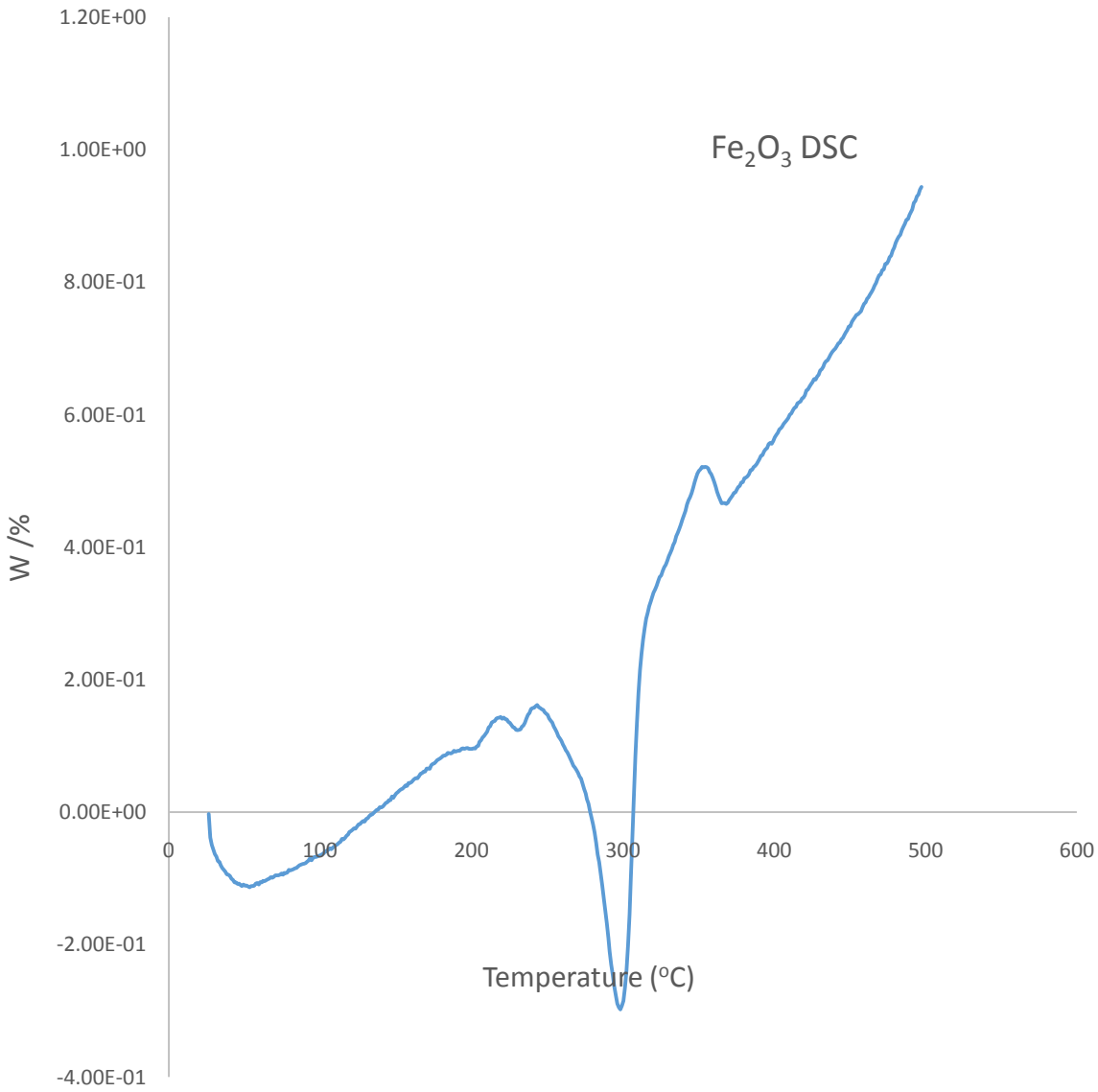


Figure 4.20: DSC of Fe_2O_3nanoparticles

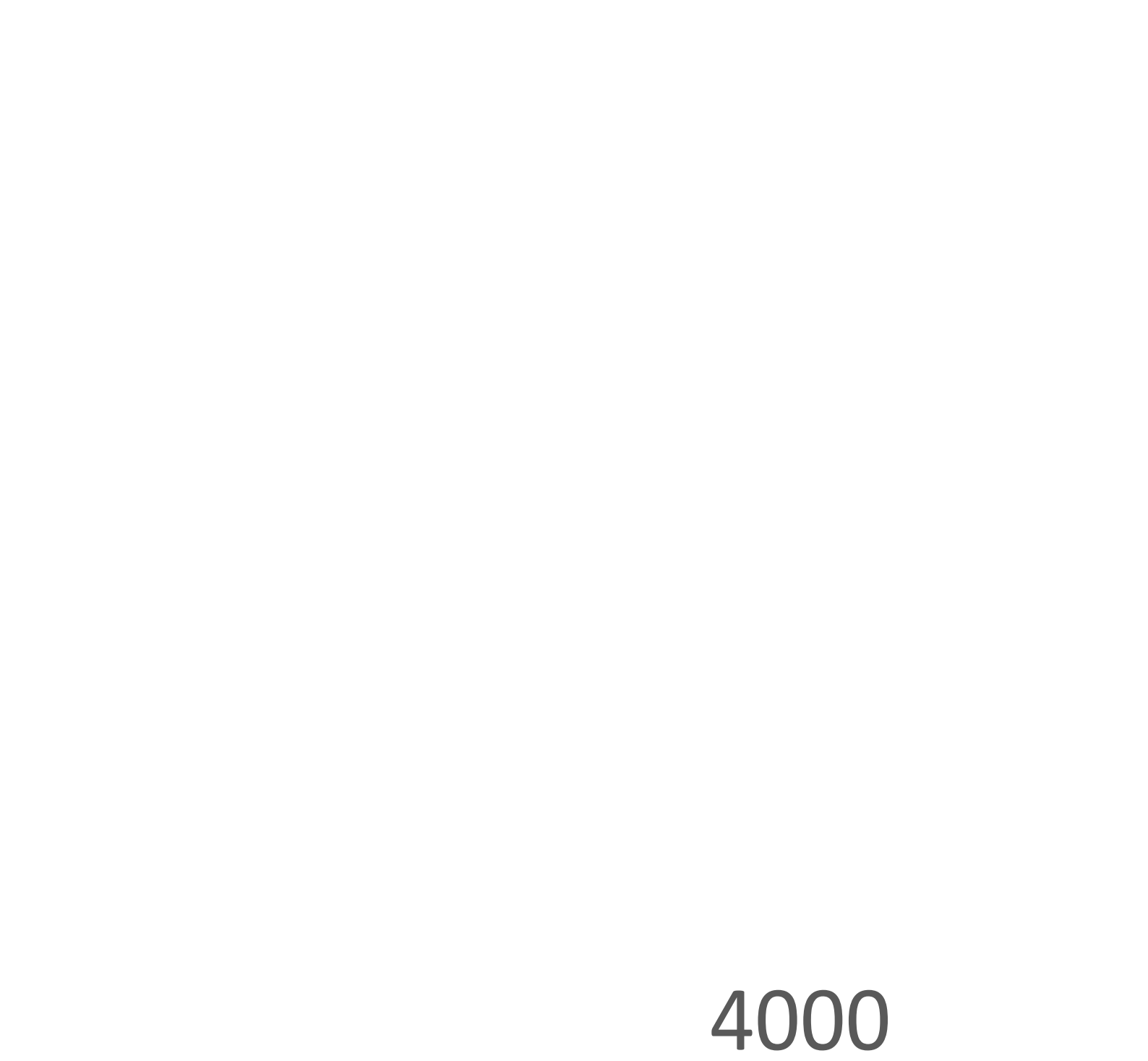


Figure 4.21: XRD patterns of (a) FeOOH nanoparticles and (b) HT-DNA/FeOOH nanowires



Figure 4.22: XRD patterns of (a) Fe_2O_3 nanoparticles and (b) HT-DNA/Fe_2O_3 nanowires

.

Figure 4.23: XRD patterns of Ppy nanoparticles

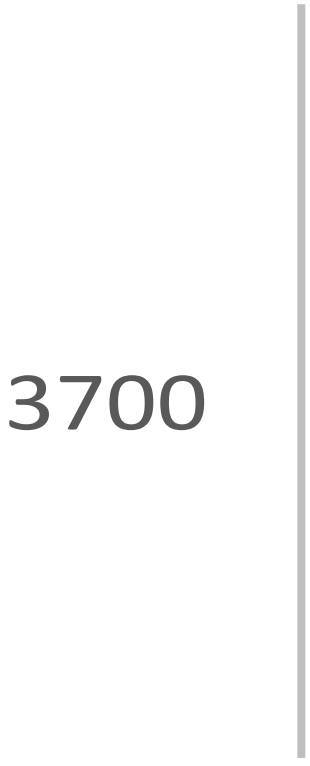


Figure 4.24 XRD patterns of (b) PImi nanoparticles and (c) DNA/PImi nanowires

.



Figure 4.25: TEM images of FeOOH nanoparticles (a) and(b) in different magnifications with particles and aggregates showing rod-like morphology



Figure 4.26: TEM images of DNA/FeOOH.(c) and(d)at different points on Cu grid. Inset between at the edges of (d) in the form of dark field and bright field micrographs and in (c) as electron diffraction patterns

Figure 4.27: TEM of Fe_2O_3nanoparticles (a) and(b) in different magnifications showing rod-like and hollow tube morphology



Figure 4.28: TEM of DNA/Fe_2O_3nanowires (c) and (d) in different magnifications showing rod-like and hollow tube morphology at different points on Cu grid. Inset at the edges of (d) are dark field and bright field micrographs



Figure 4.29: TEM images of Ppy nanoparticles (a) and (b) in differentmagnifications

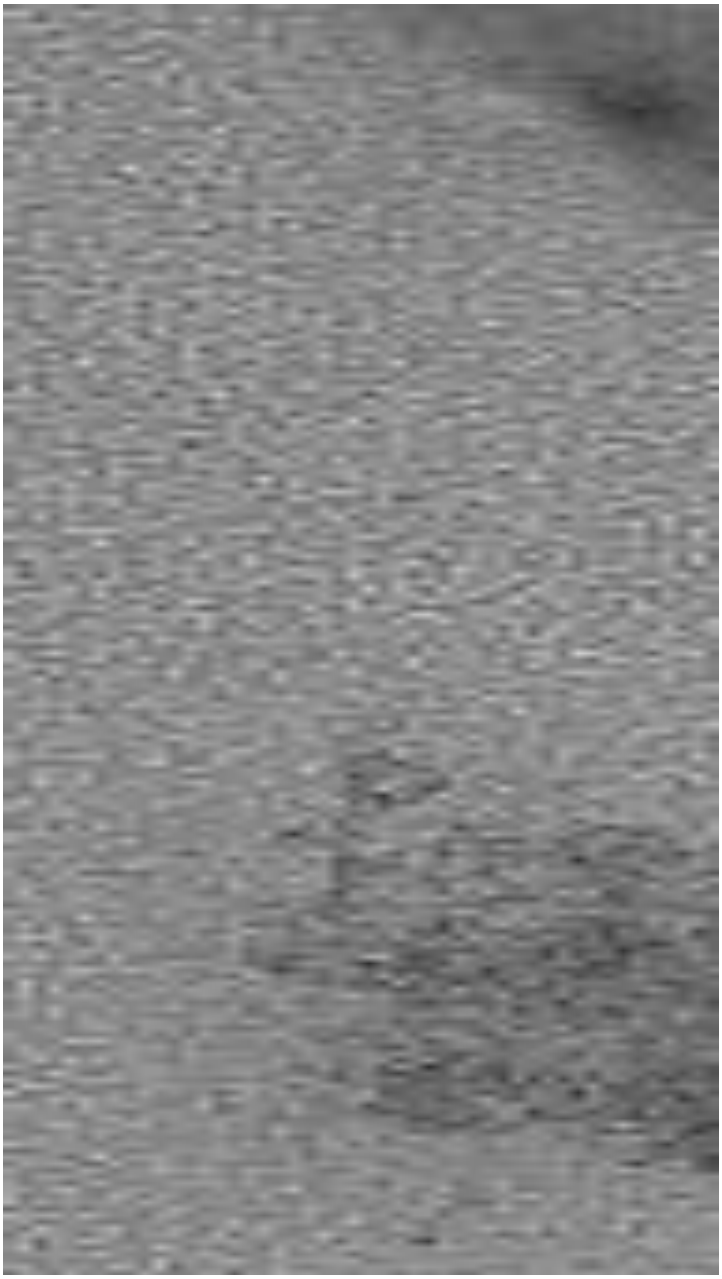


Figure 4.30: TEM images of DNA/Ppy nanowires (c) and (d) in different magnifications



Figure 4.31: TEM images of Plmi nanoparticles (a) and (b) PImi in different magnifications



Figure 4.32: TEM images of DNA/PImi nanowires at different points on the Cu grid

Figure 4.33: EDX spectra of (a) DNA/FeOOH, (b) DNA/Fe_2O_3 nanowires

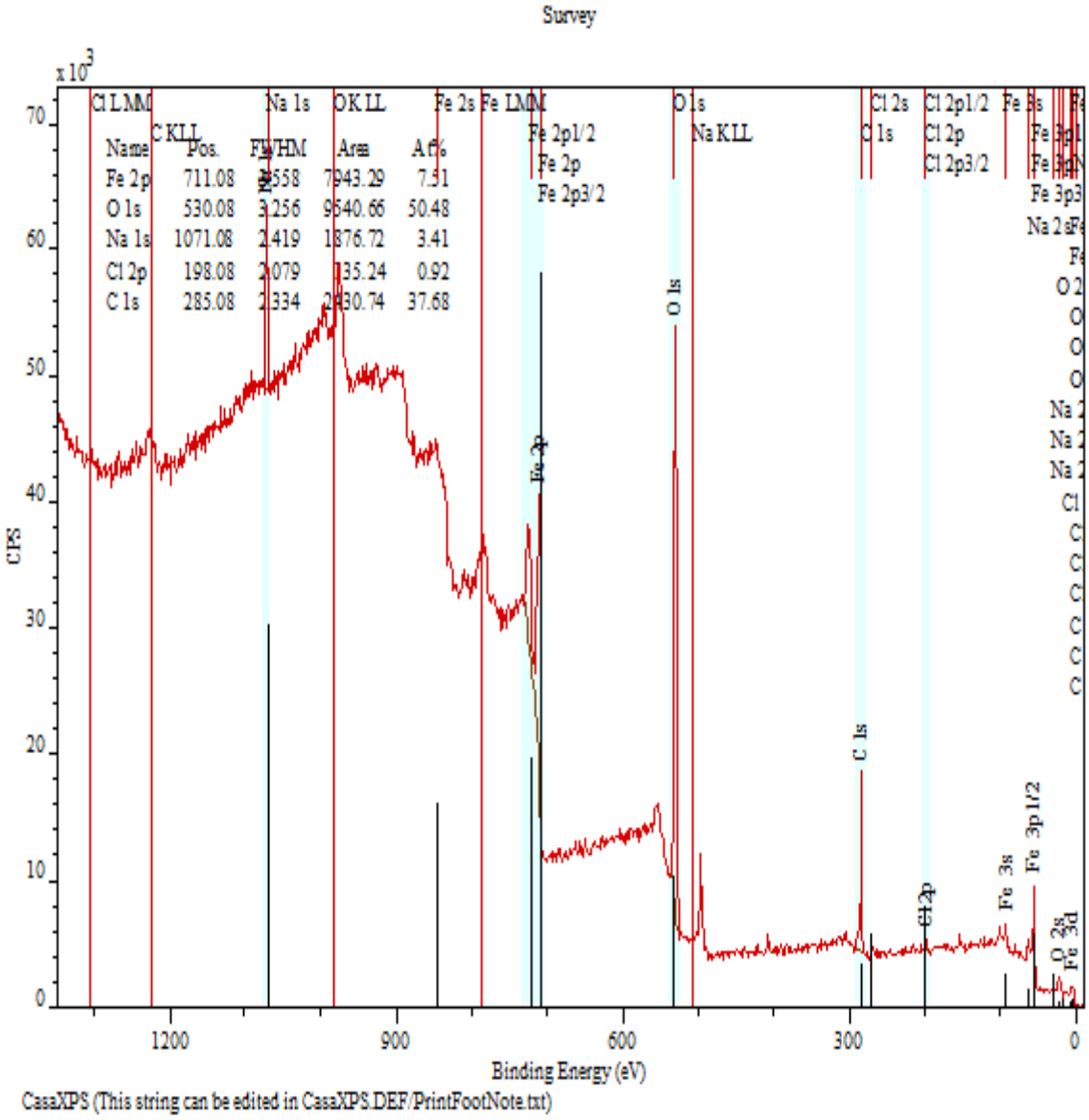


Figure 4.34: XPS survey spectrum of FeOOH thin film

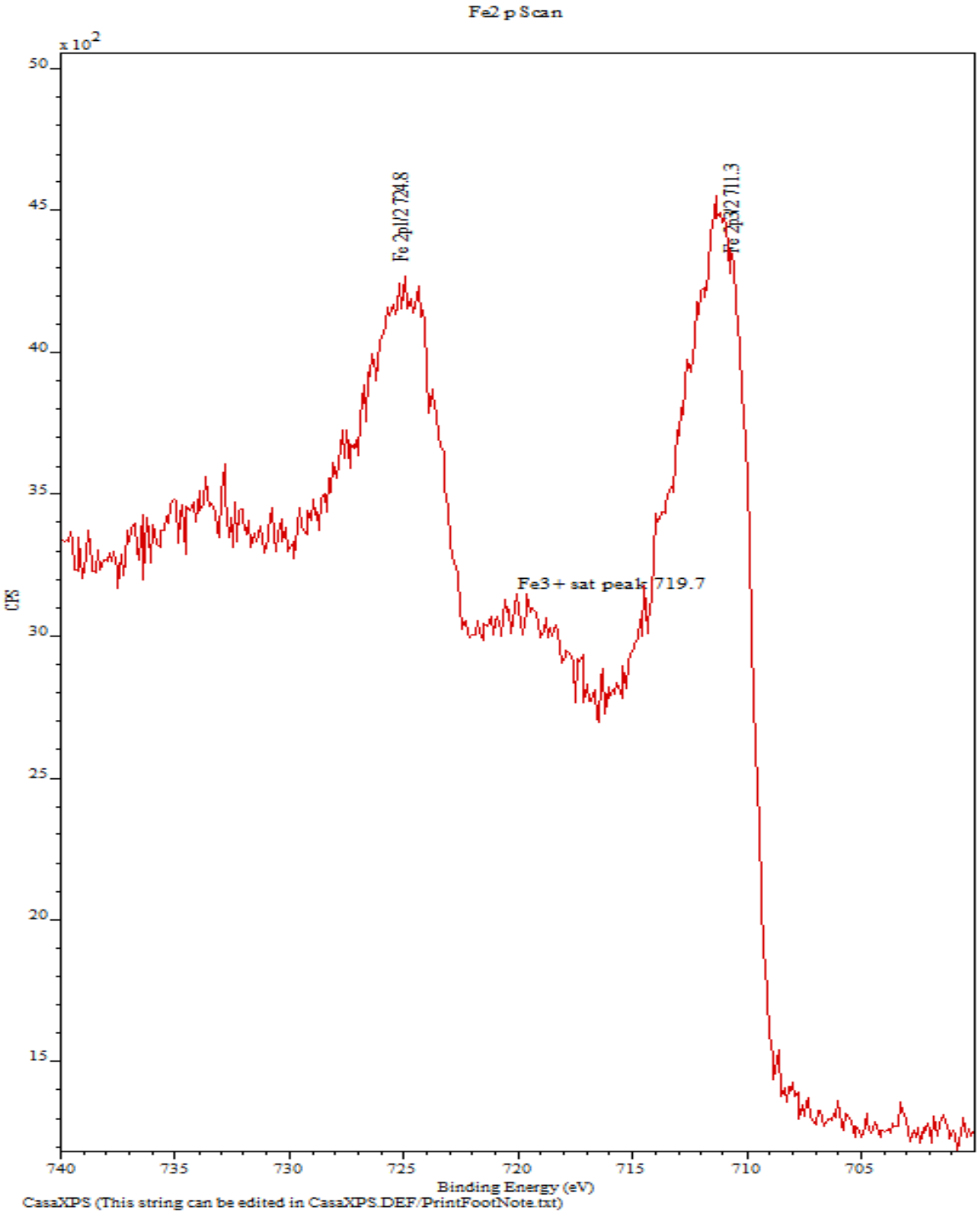


Figure 4.35: XPS high-resolution spectrum of (a) Fe 2p regionacquired from FeOOH thin film

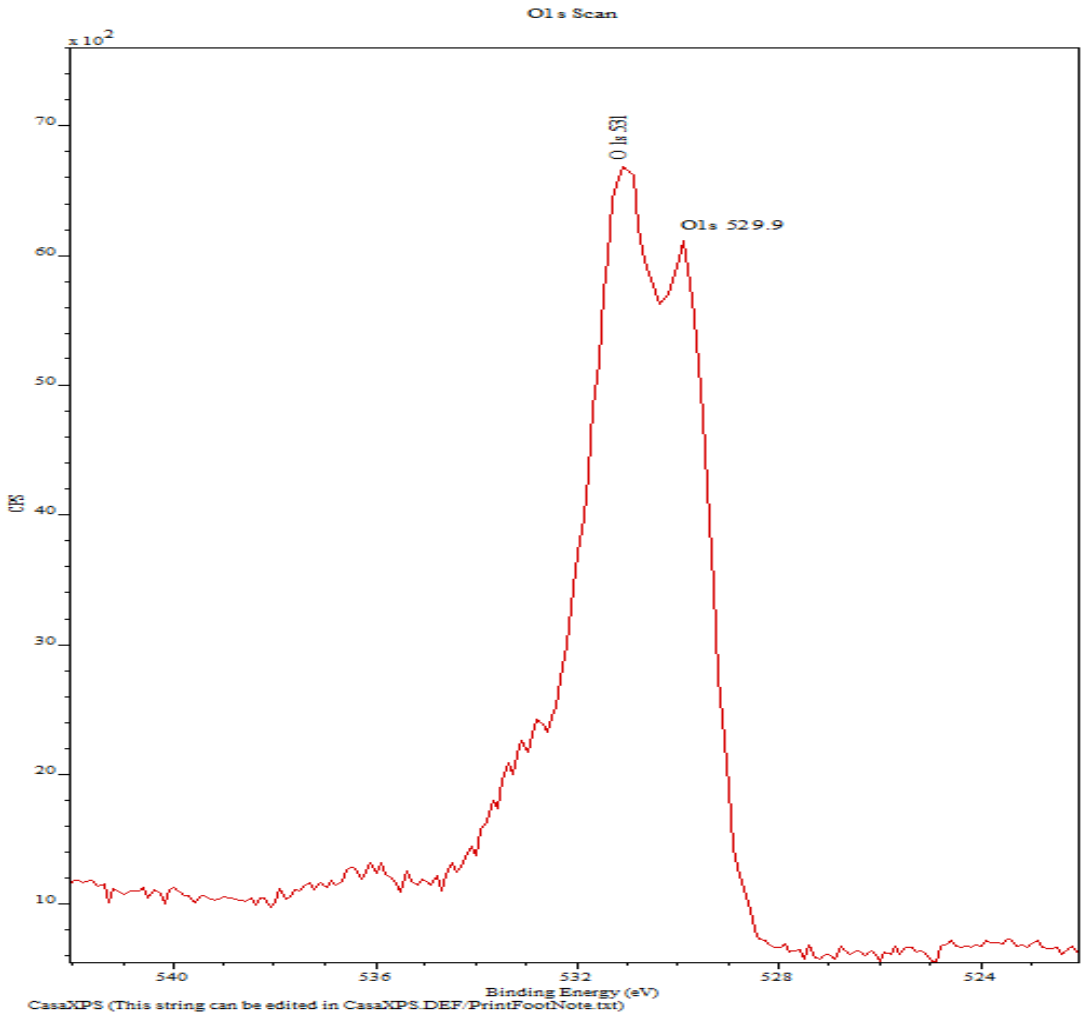


Figure 4.35: XPS high-resolution spectrum of (b) O1s region acquired from FeOOH thin film

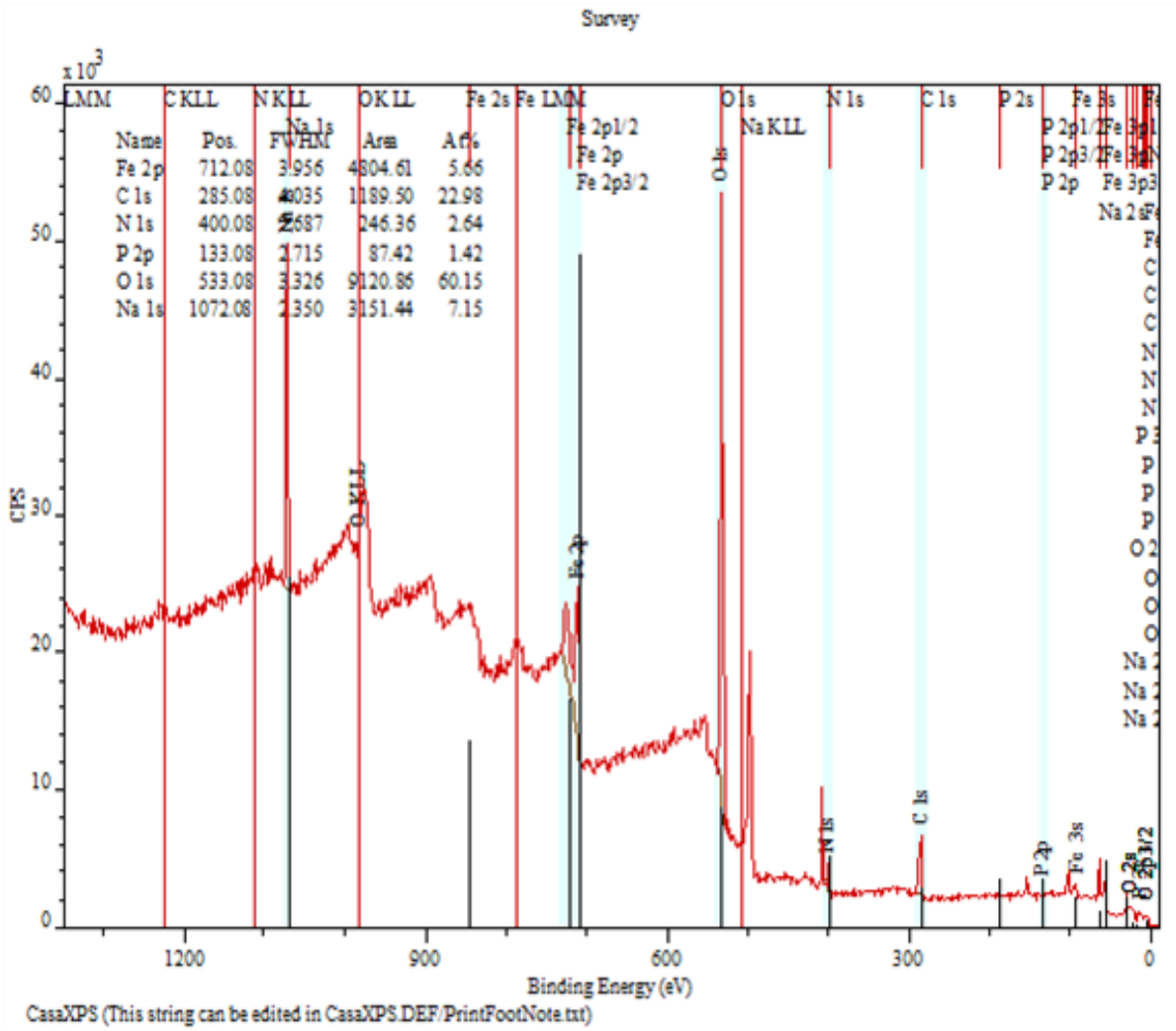


Figure 4.36: XPS survey spectrum of HT-DNA/FeOOH nanowires

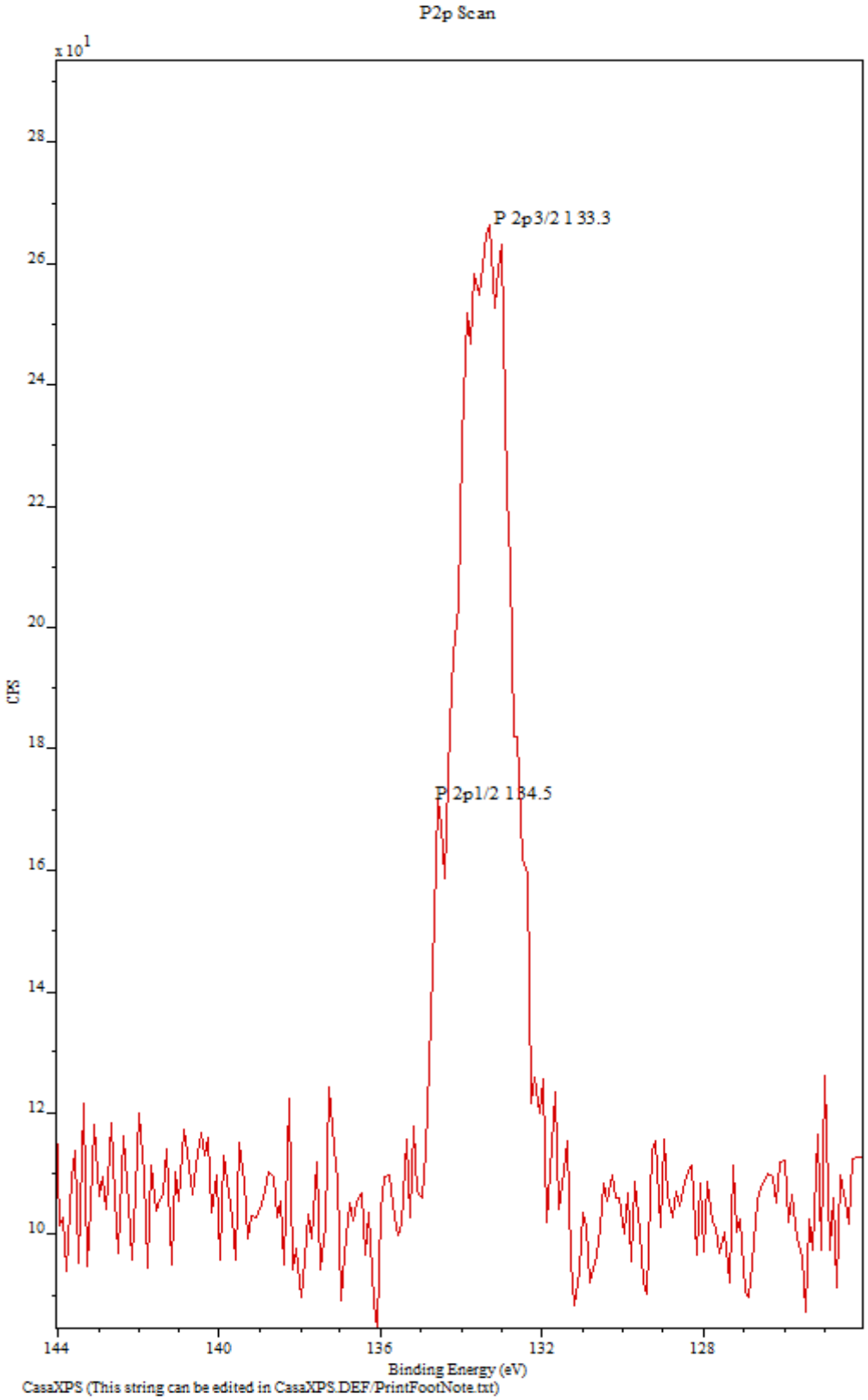


Figure 4.37a: XPS high-resolution spectrum of (a) P2p acquired from HT-DNA/FeOOH nanowires

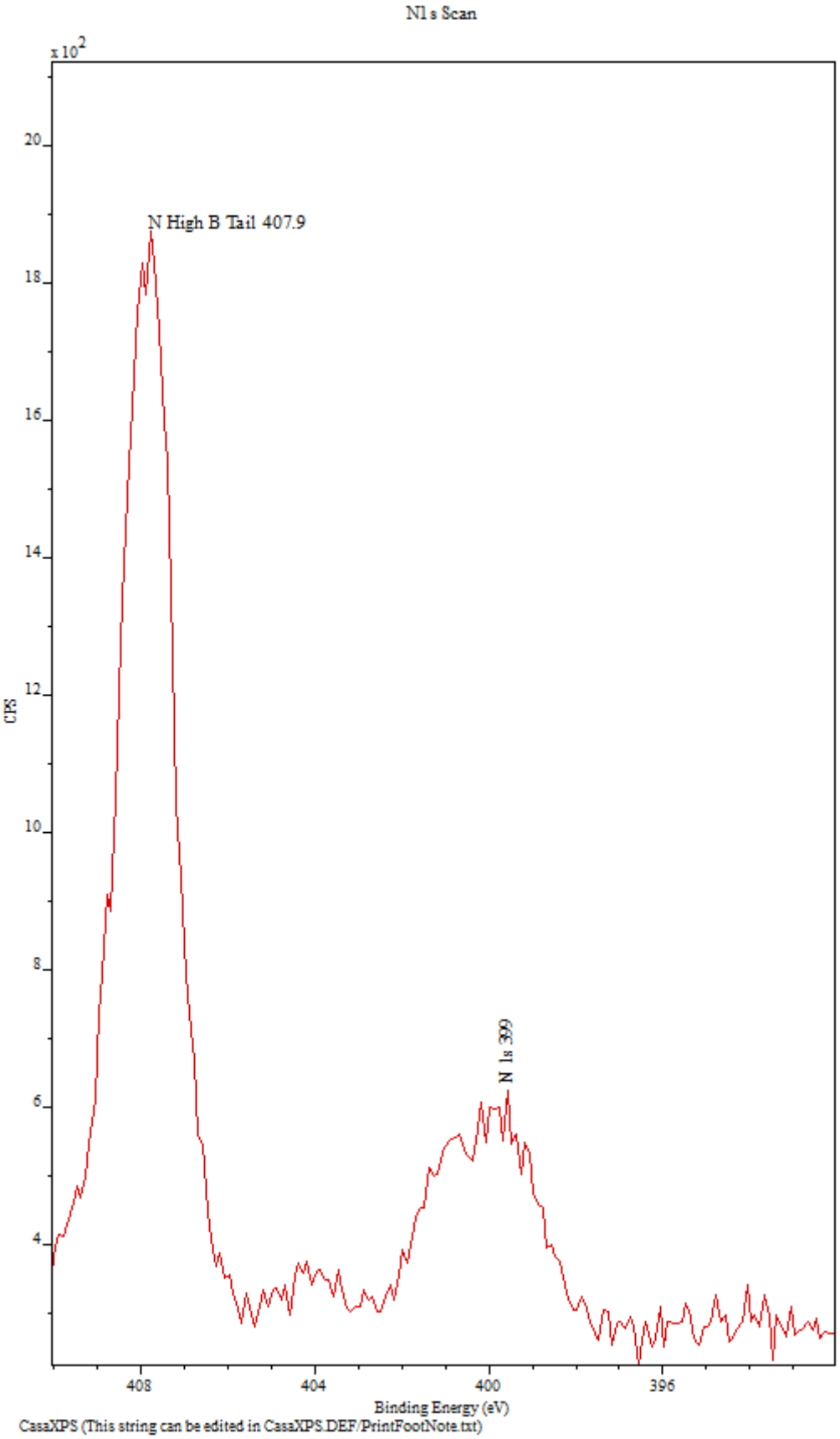


Figure 4.37b: XPS high-resolution spectrum of (b) N 1s acquired from HT-DNA/FeOOH nanowires

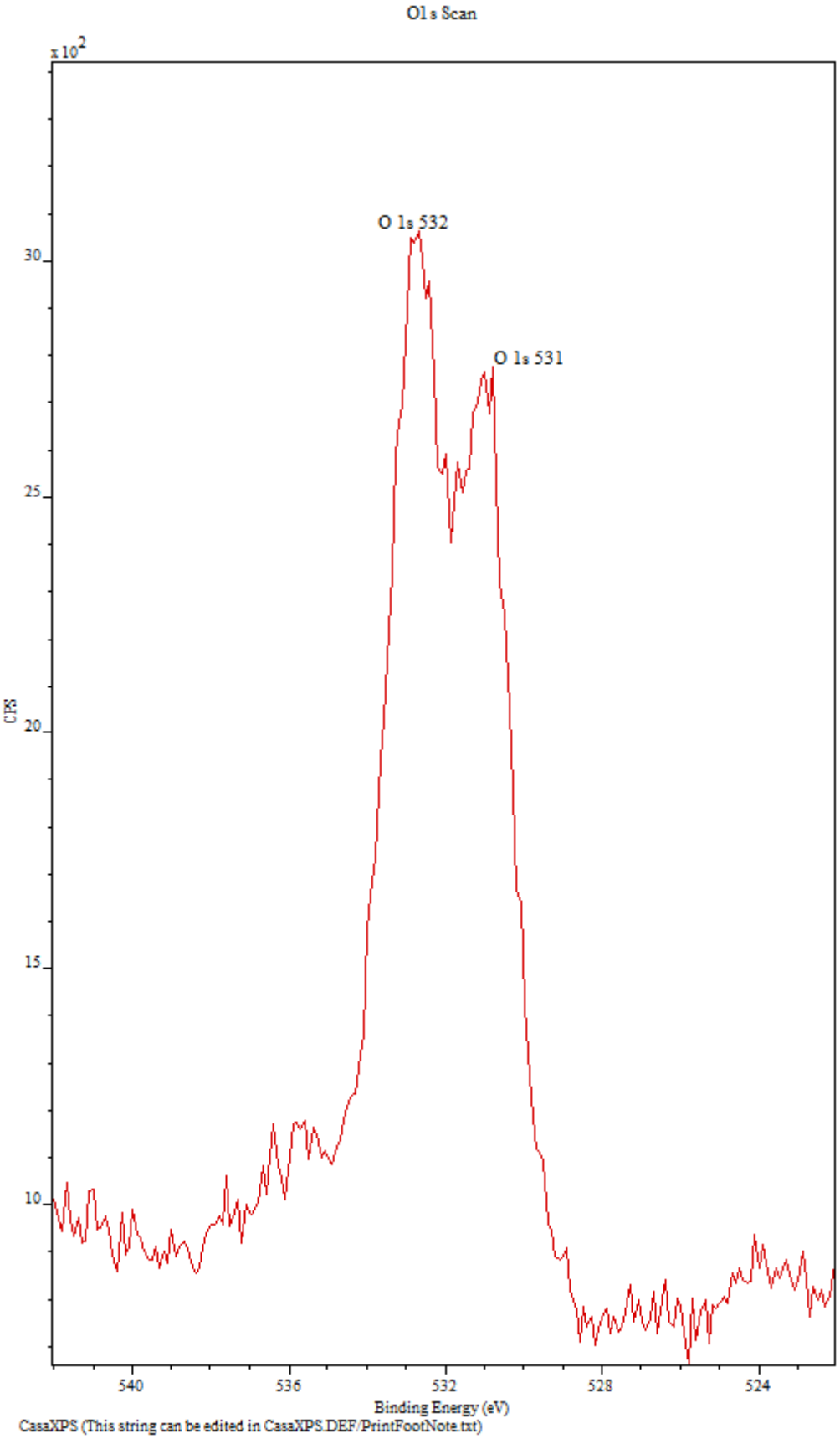


Figure 4.37c: XPS high-resolution spectrum of (c) O 1s acquired from HT-DNA/FeOOH nanowires

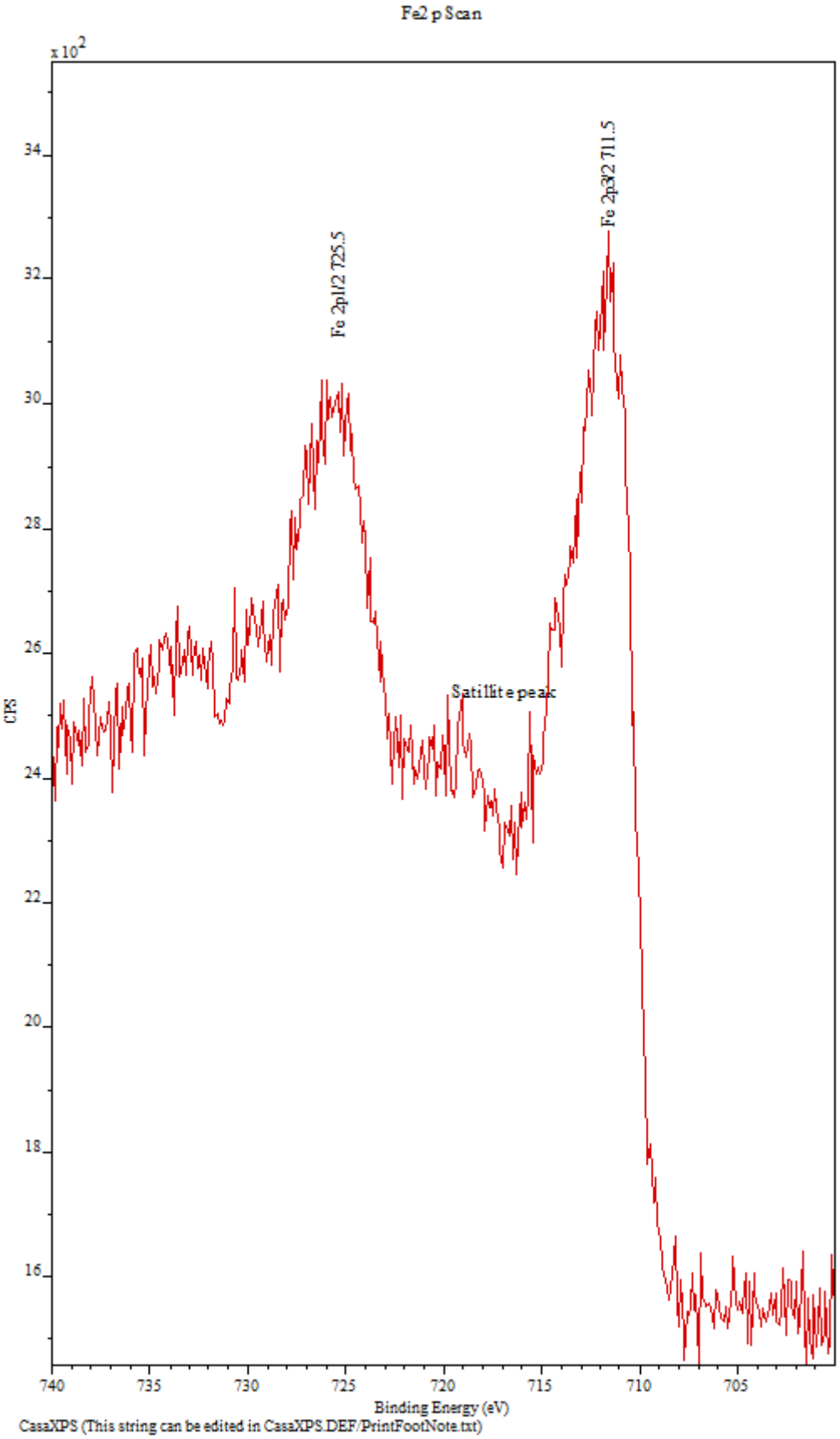


Figure 4.37d: XPS high-resolution spectrum of (d) Fe 2p region acquired from HT-DNA/FeOOH nanowires

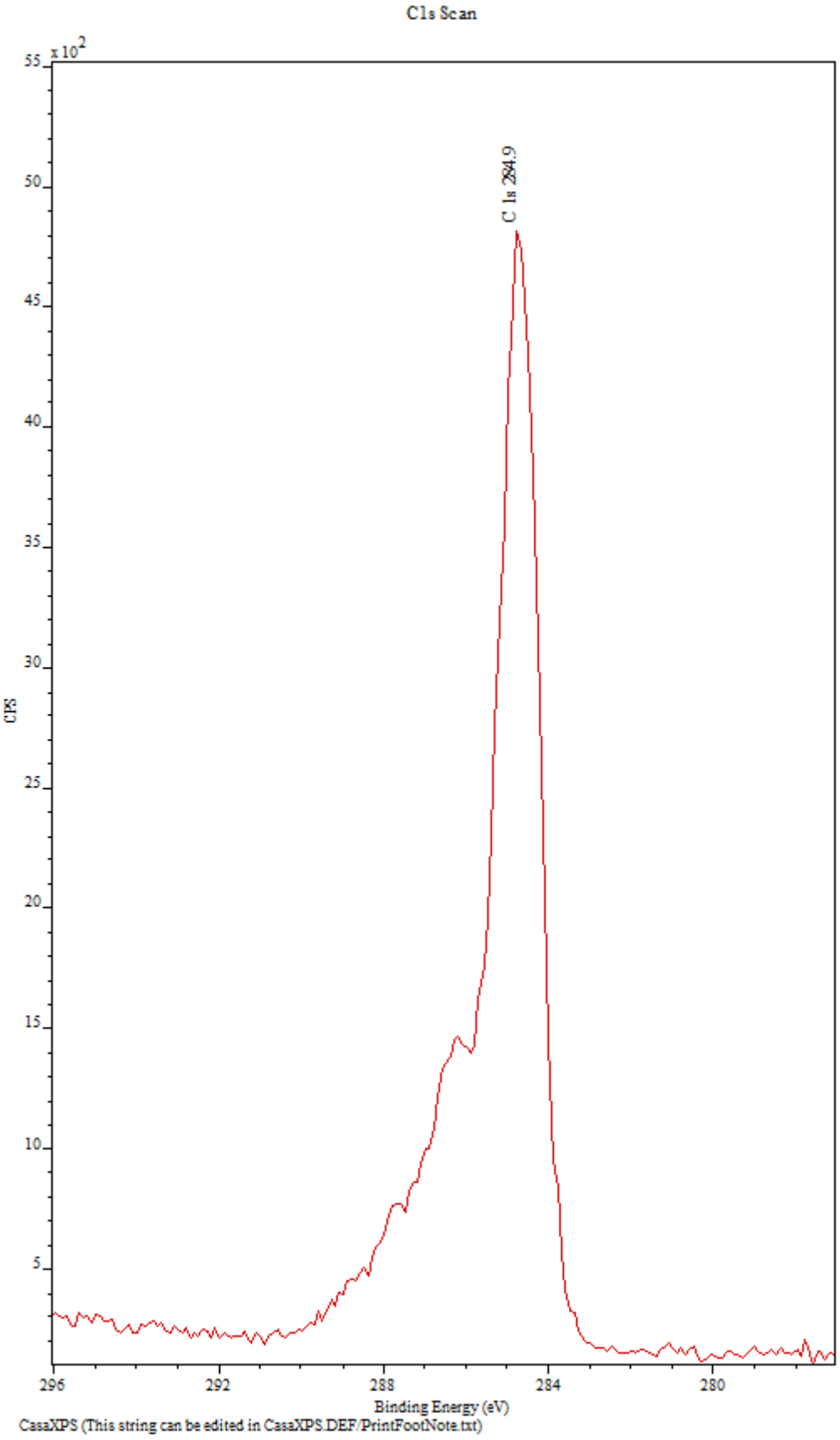


Figure 4.37e: XPS high-resolution spectrum of (e) C 1s region acquired from HT-DNA/FeOOH nanowires

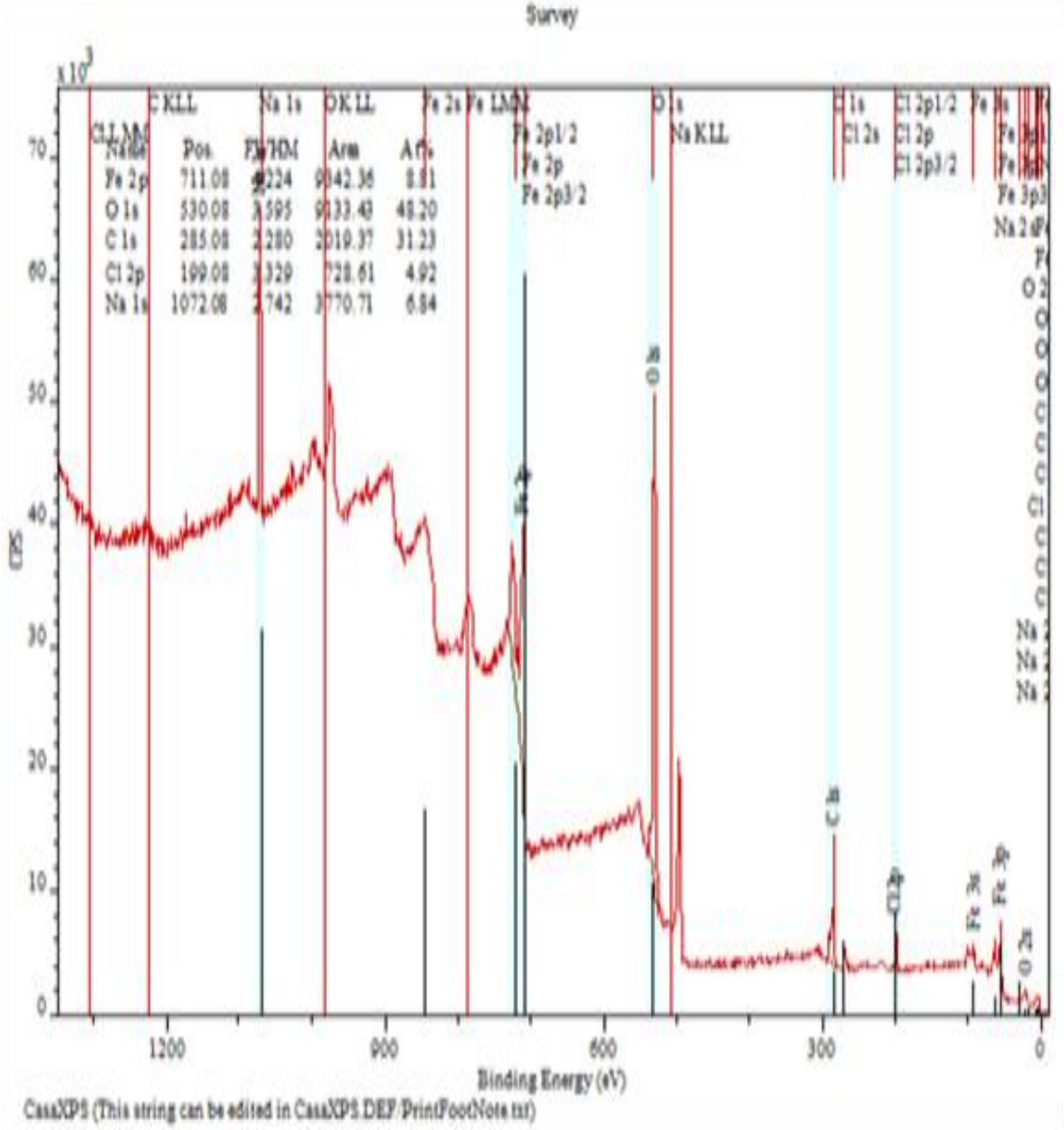


Figure 4.38: XPS survey spectrum of Fe_2O_3 nanowires

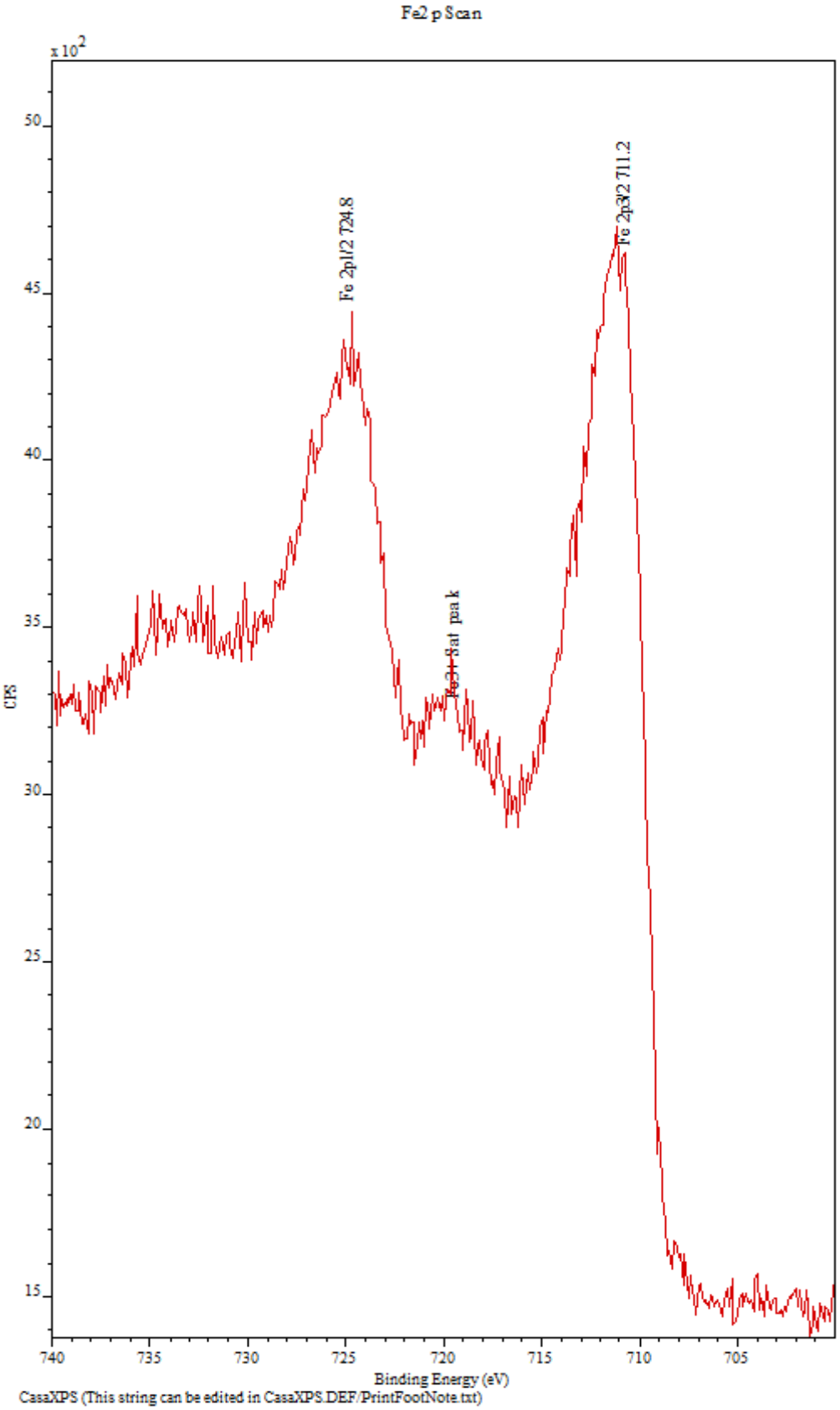


Figure 4.39a: XPS high-resolution spectrum of (a) Fe 2pregion acquired from Fe_2O_3 nanowires

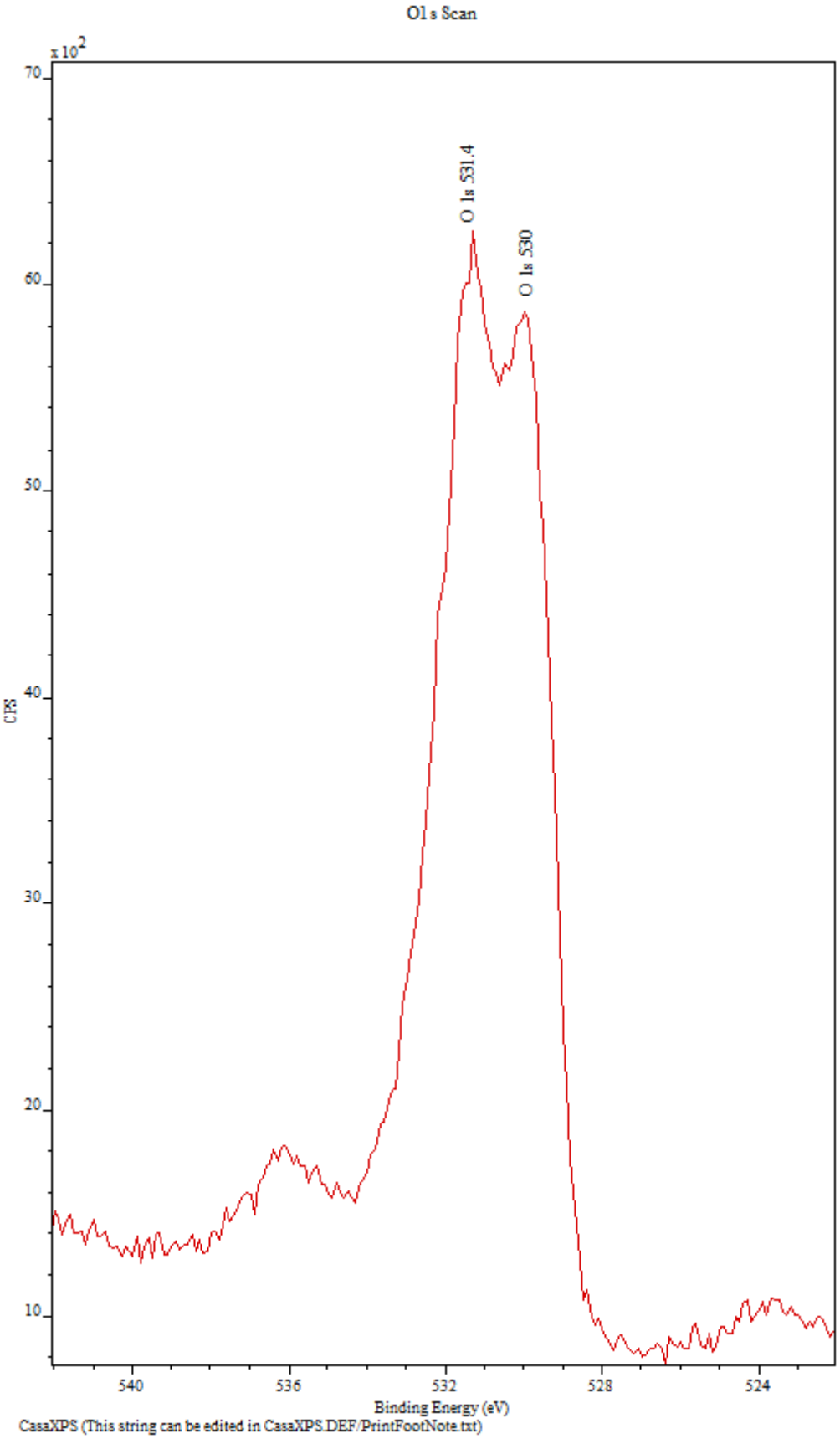


Figure 4.39b: XPS high-resolution spectrum of (b) O 1sregion acquired from Fe_2O_3 nanowires

XPS survey spectrum of HT-DNA/Fe_2O_3 nanowires with its atom concentrations are shown in Figure 4.40, while the XPS high resolution spectra of HT-DNA/Fe_2O_3 components are shown in Figure 4.41.

XPS survey spectrum of Ppy thin film with its atom concentrations is shown in Figure 4.42 while the XPS high resolution spectrum of Ppy components are shown in Figure 4.43.

XPS survey spectrum of HT-DNA/Ppy thin film was illustrated in Figure 4.44 and XPS high resolution spectra of HT-DNA/Ppy nanowires components in Figure 4.45.

XPS survey spectrum of Plmi thin film and its atom concentrations are shown in Figure 4.46 and XPS high resolution spectra of Plmi thin film components are shown in Figure 4.47.

XPS survey spectrum of HT-DNA/Plmi nanowires with its atom concentrations is shown in Figure 4.48 and the XPS high resolution spectra of HT-DNA/Plmi nanowires components are shown in Figure 4.49.

XPS low resolution spectra of Fe 2p after etching of DNA/FeOOH nanowires for a fixed period of time are shown in Figure 4.50.

XPS low resolution spectrum of O 1s after etching of DNA/FeOOH nanowires for a fixed period of time are shown in Figure 4.51, while the XPS low resolution spectra of Fe 2p after etching of HT-DNA/Fe_2O_3 nanowires for a fixed period of time are shown in Figure 4.52.

XPS low resolution spectrum of O 1s after etching of DNA/Fe_2O_3 nanowires for a fixed period of time are shown in Figure 4.53.

4.9 AFM Analyses

AFM tapping mode images of bare DNA nanowires and cross-section area of the measured diameters are shown from Figure 4.54 to 4.56

AFM images of DNA/Ppy with inset and size distributions of the nanowires are shown in Figure 4.57.

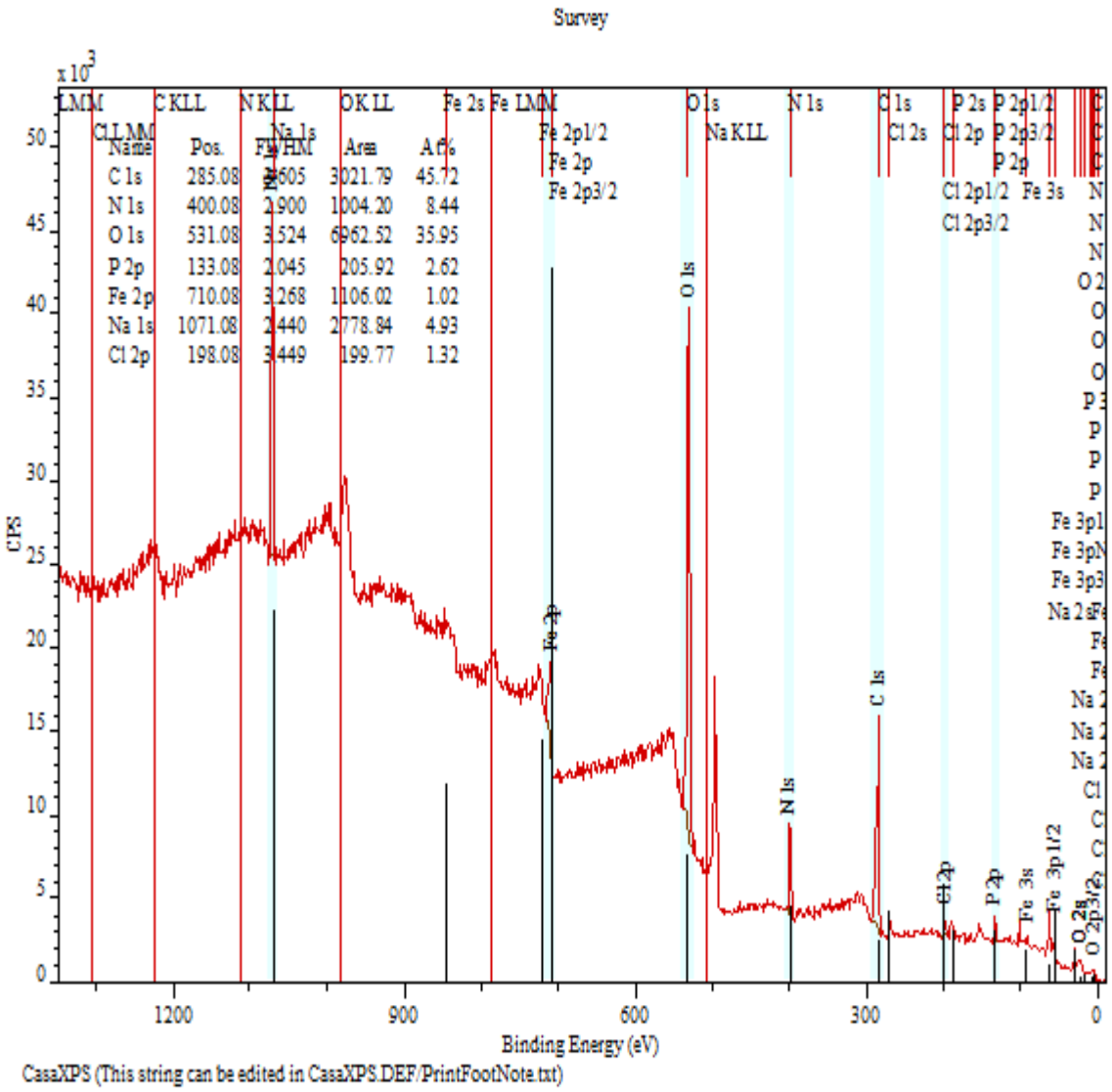


Figure 4.40: XPS survey spectrum of HT-DNA/Fe_2O_3 nanowires

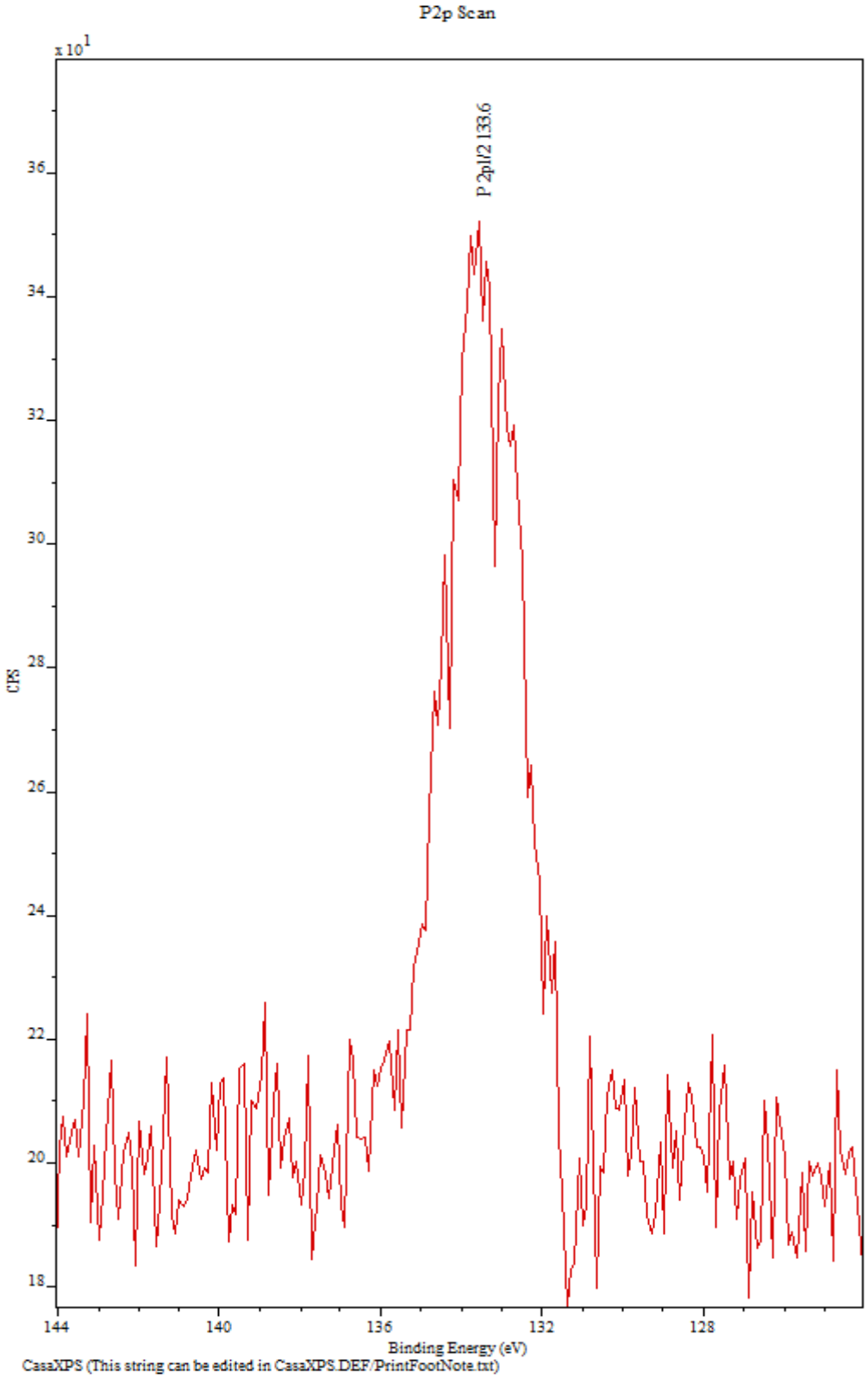


Figure 4.41a: XPS high-resolution spectrum of (a) P 2pregion acquired from HT-DNA/Fe_2O_3 nanowires

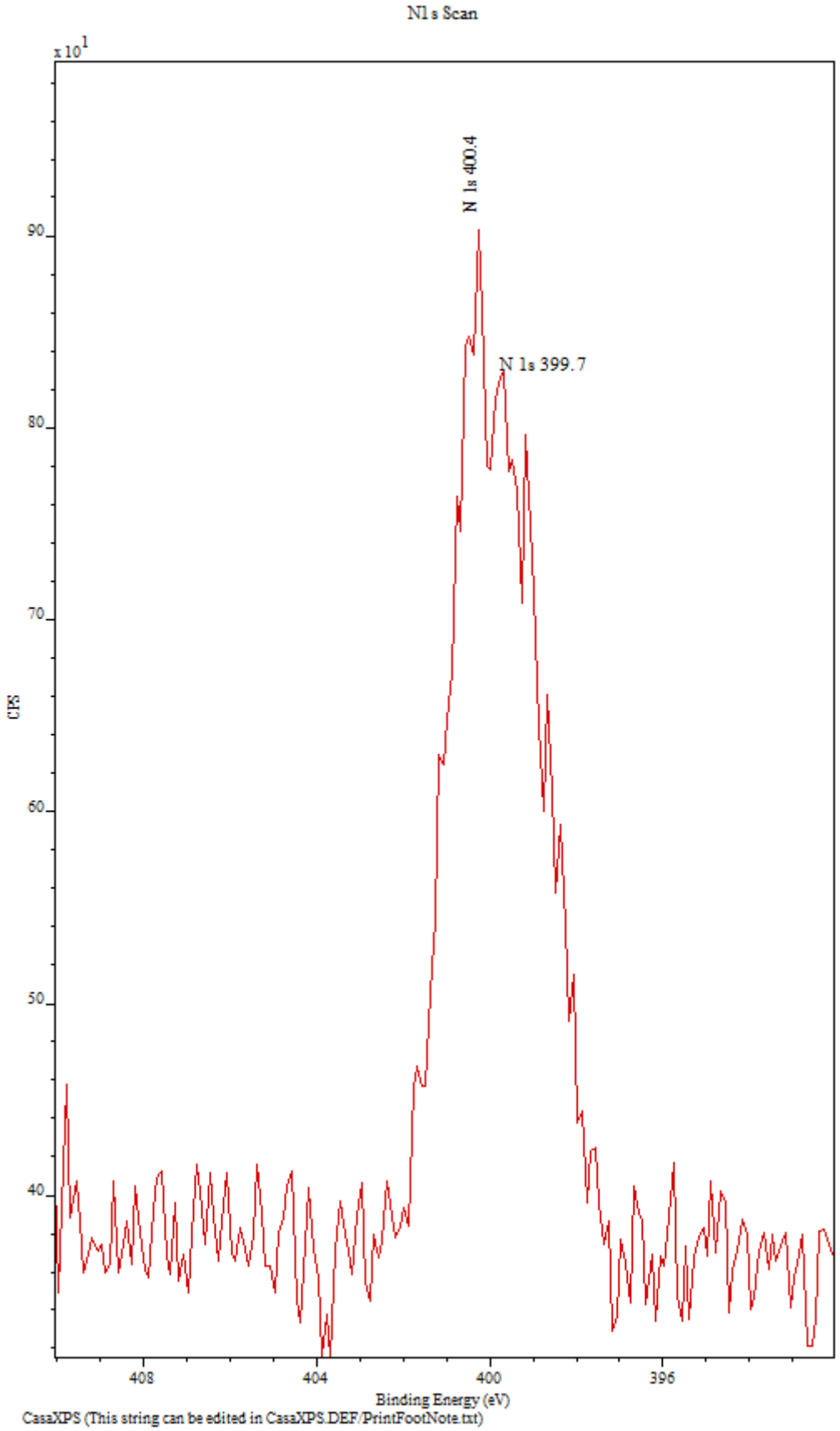


Figure 4.41b: XPS high-resolution spectrum of (b) N 1sregion acquired from HT-DNA/Fe_2O_3 nanowires

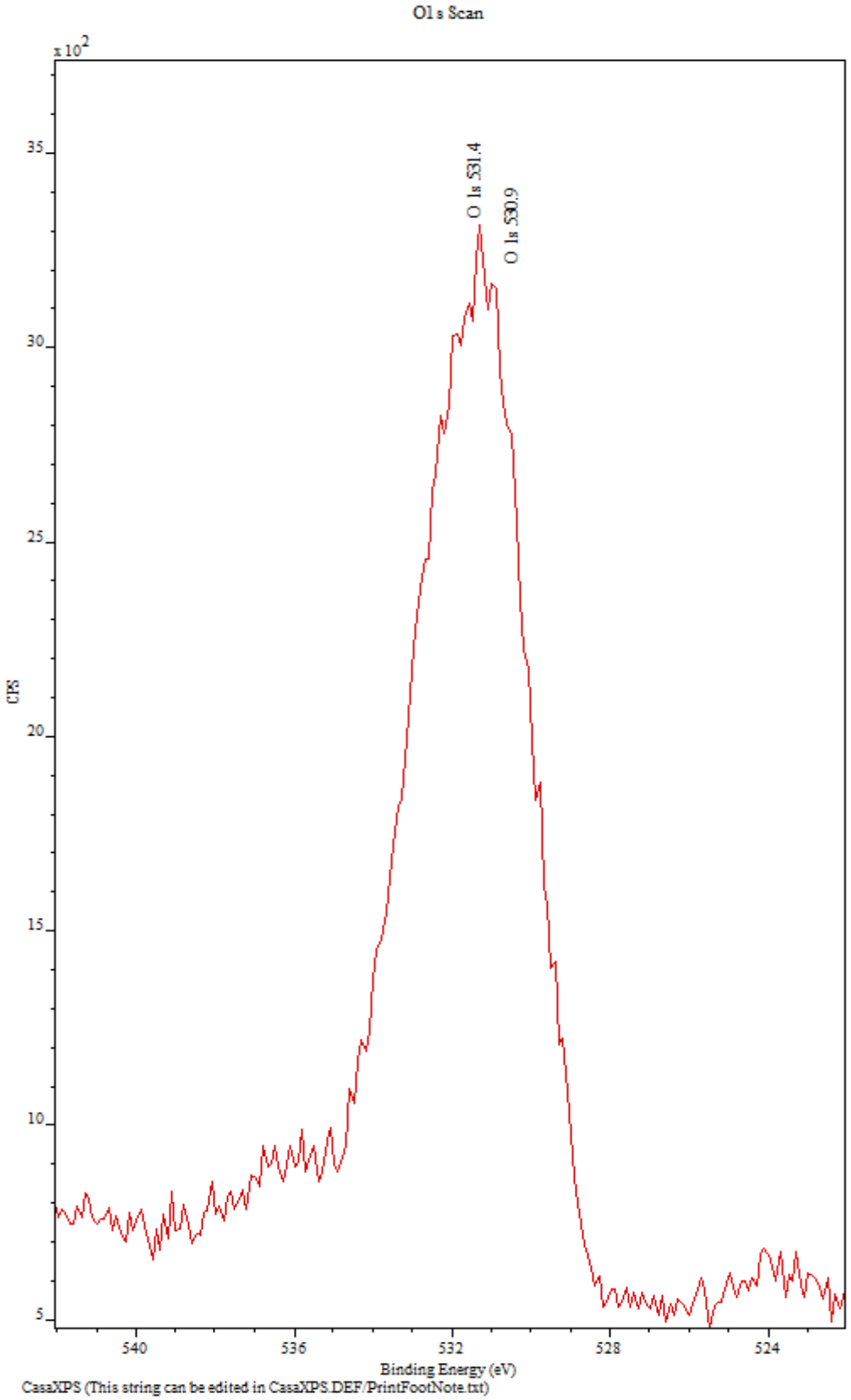


Figure 4.41c: XPS high-resolution spectrum of (c) O 1sregion acquired from HT-DNA/Fe_2O_3 nanowires

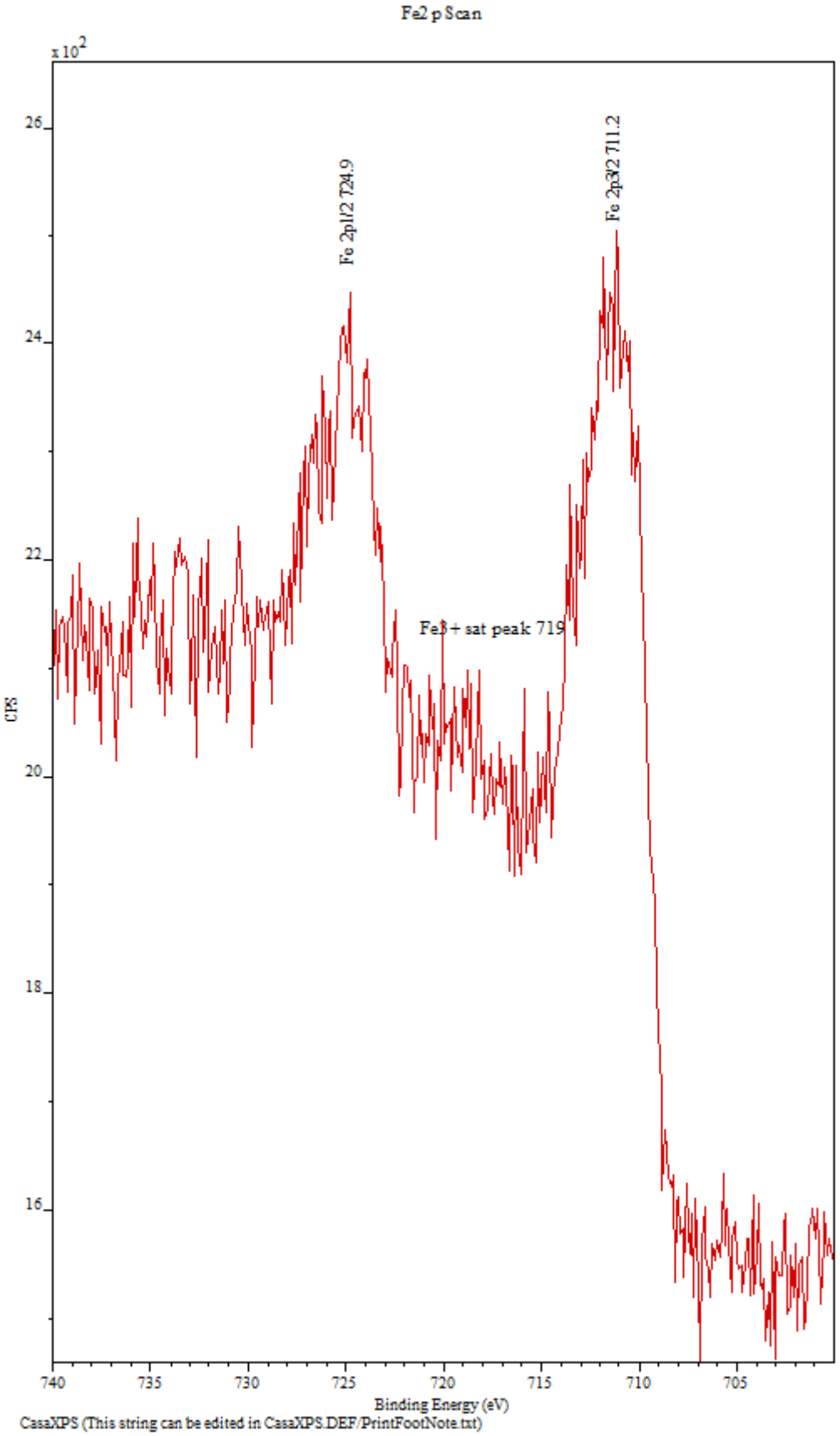


Figure 4.41d: XPS high-resolution spectrum of (d) Fe 2p region acquired from HT-DNA/Fe_2O_3 nanowires

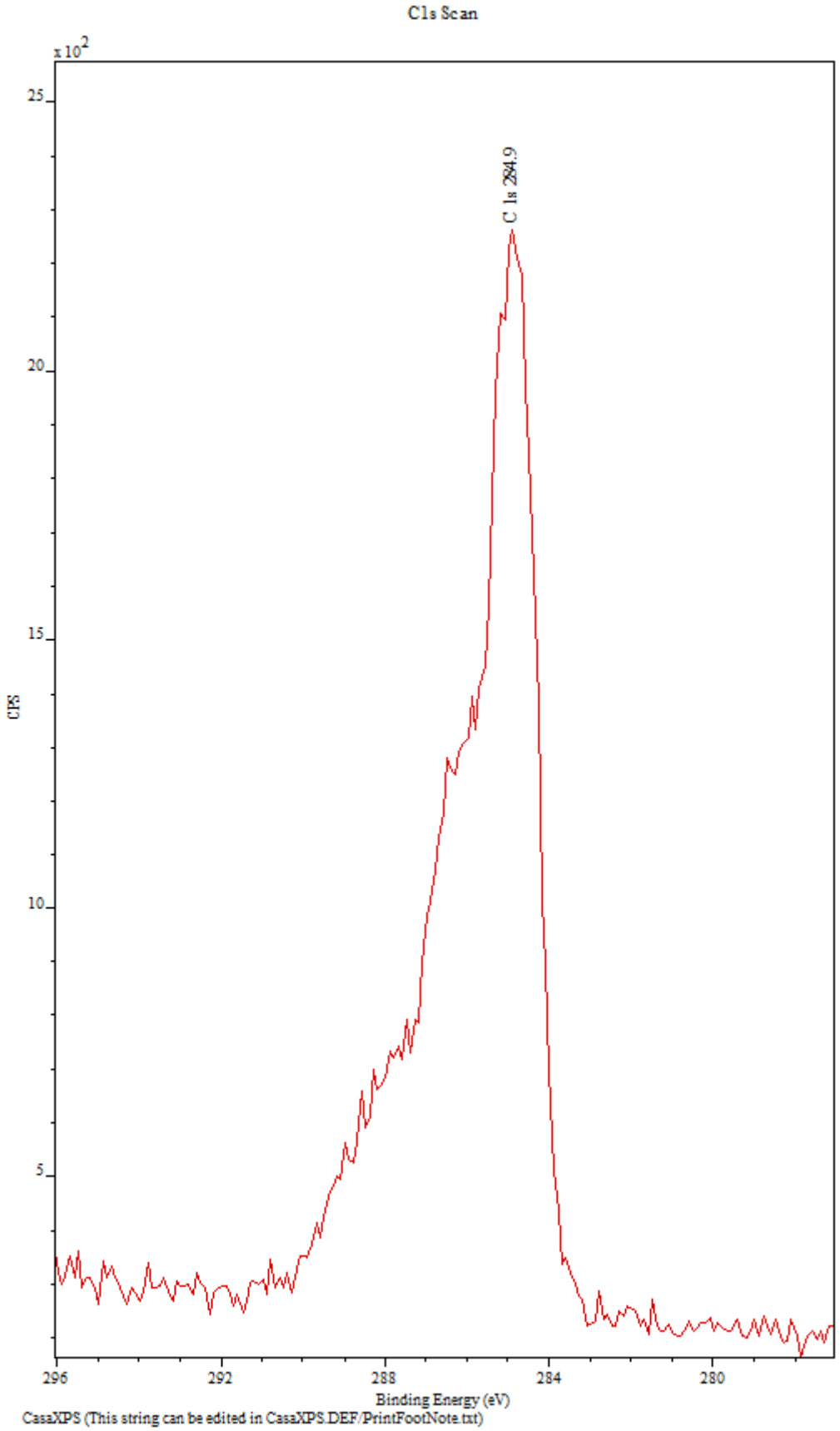


Figure 4.41e: XPS high-resolution spectrum of (e) C 1s region acquired from HT-DNA/Fe_2O_3 nanowires

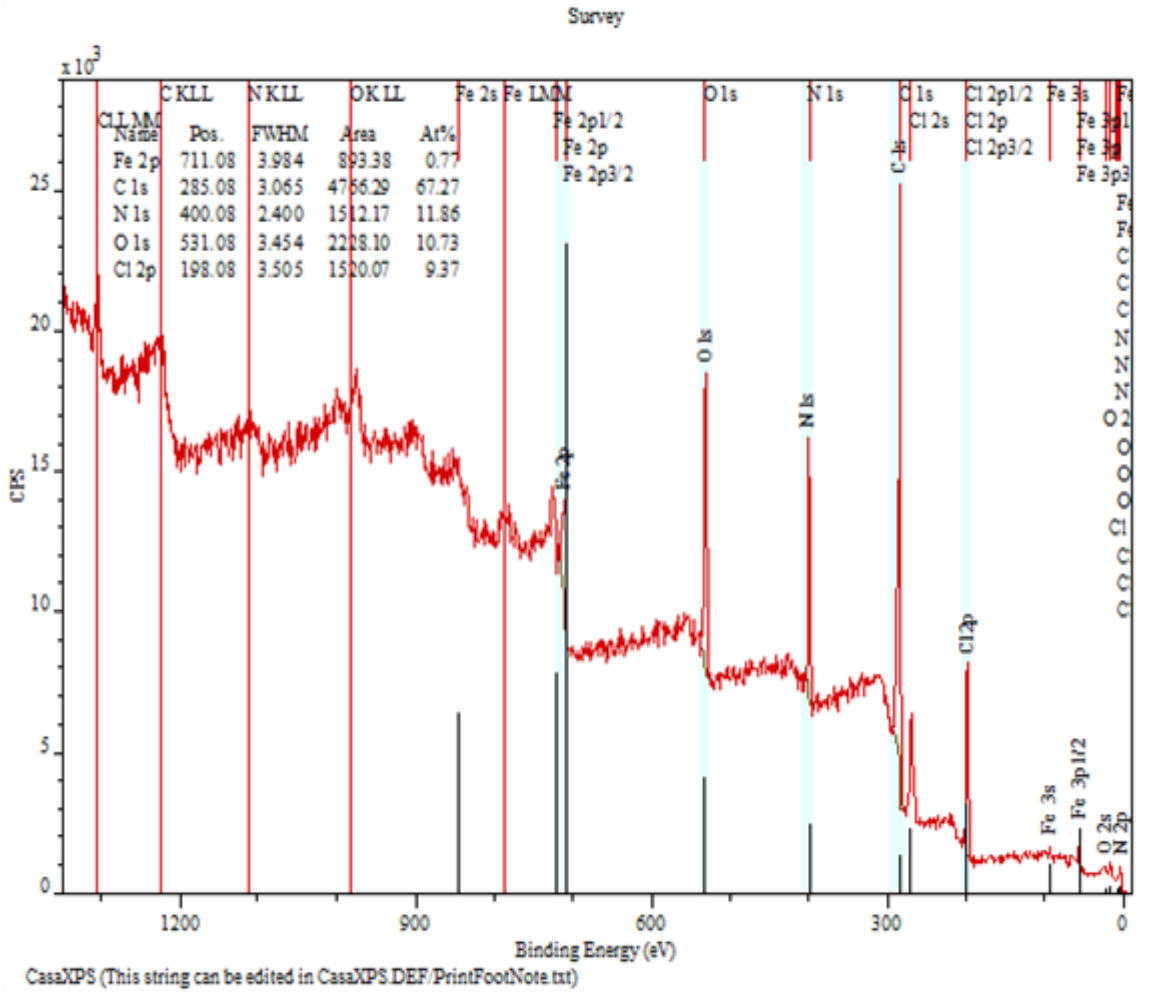


Figure 4.42: XPS survey spectrum of Ppy thin film

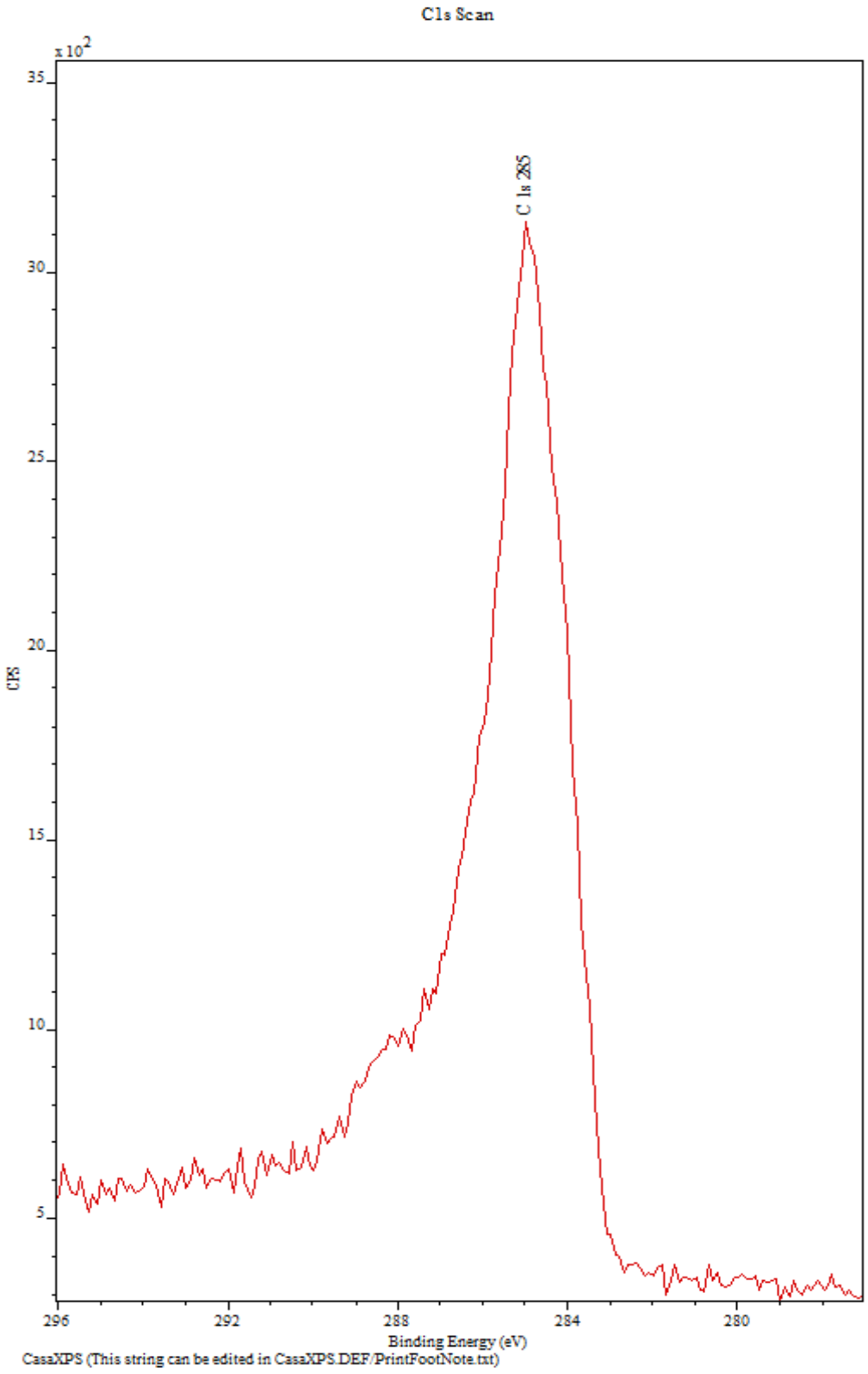


Figure 4.43a: XPS high-resolution spectrum of (a) C 1s region acquired from Ppy component

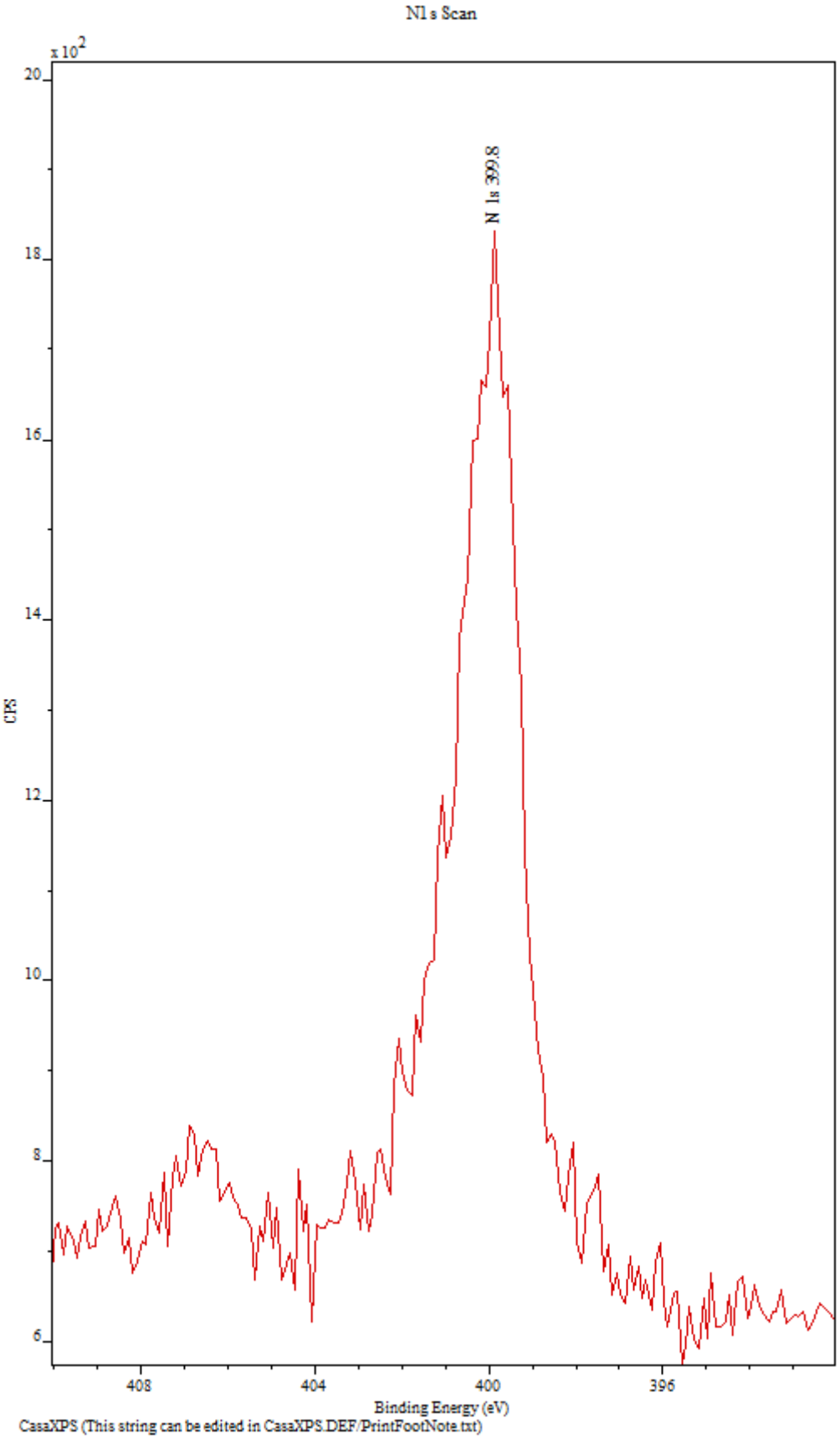


Figure 4.43b: XPS high-resolution spectrum of (b) N 1s region acquired from Ppy component

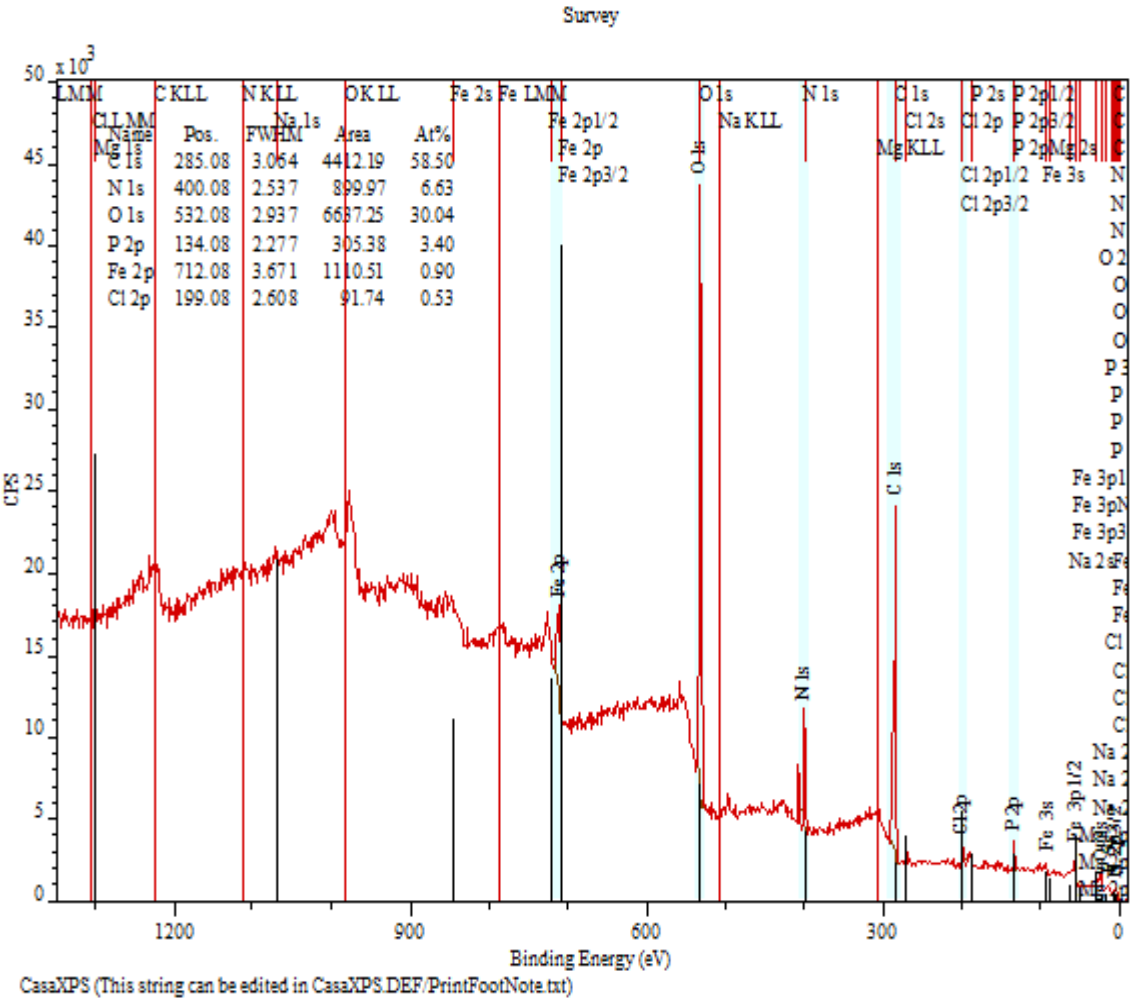


Figure 4.44: XPS survey spectrum of HT-DNA/Ppy thin film

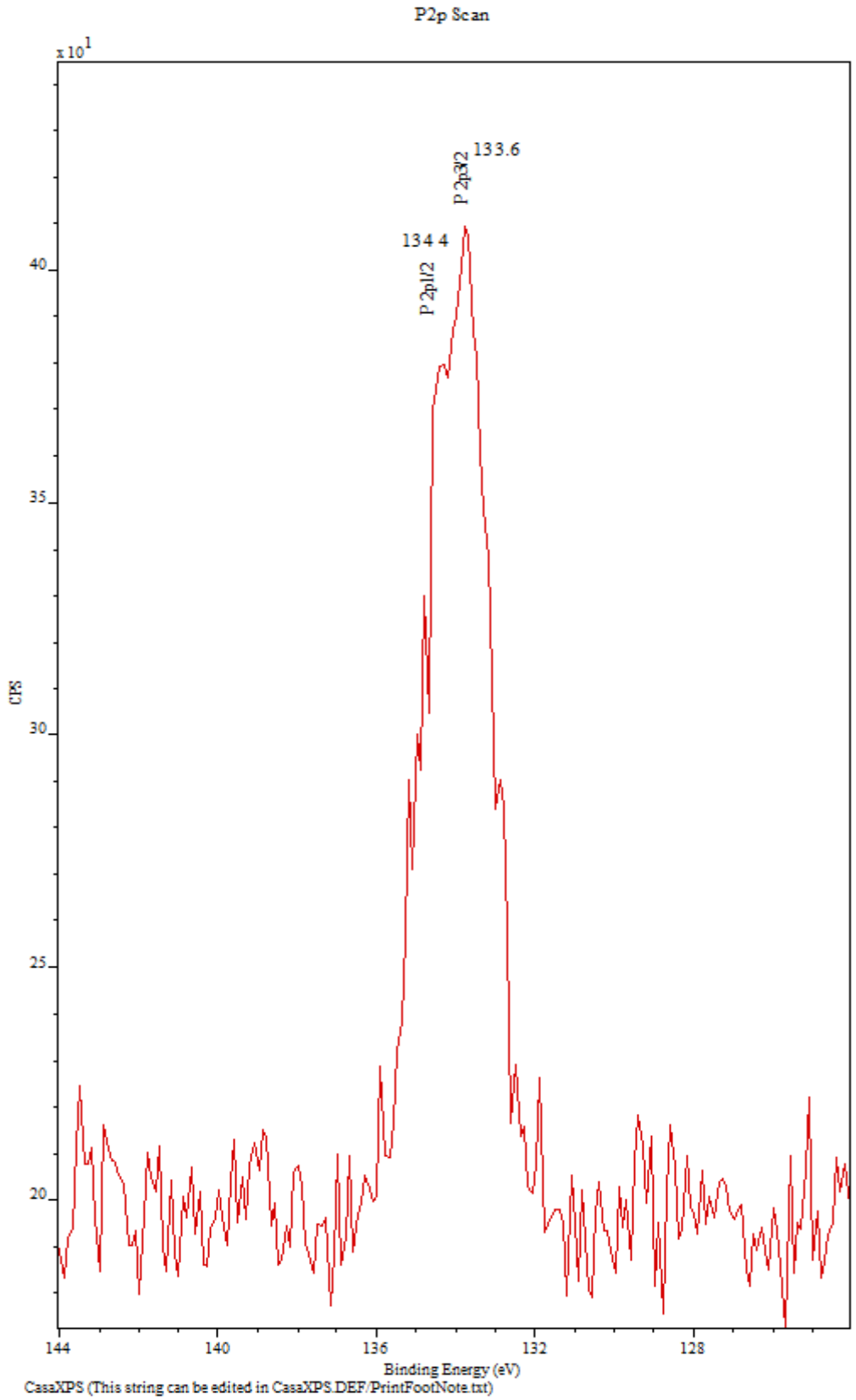


Figure 4.45a: XPS high-resolution spectrum of (a) P 2p region acquired from HT-DNA/Ppy nanowires

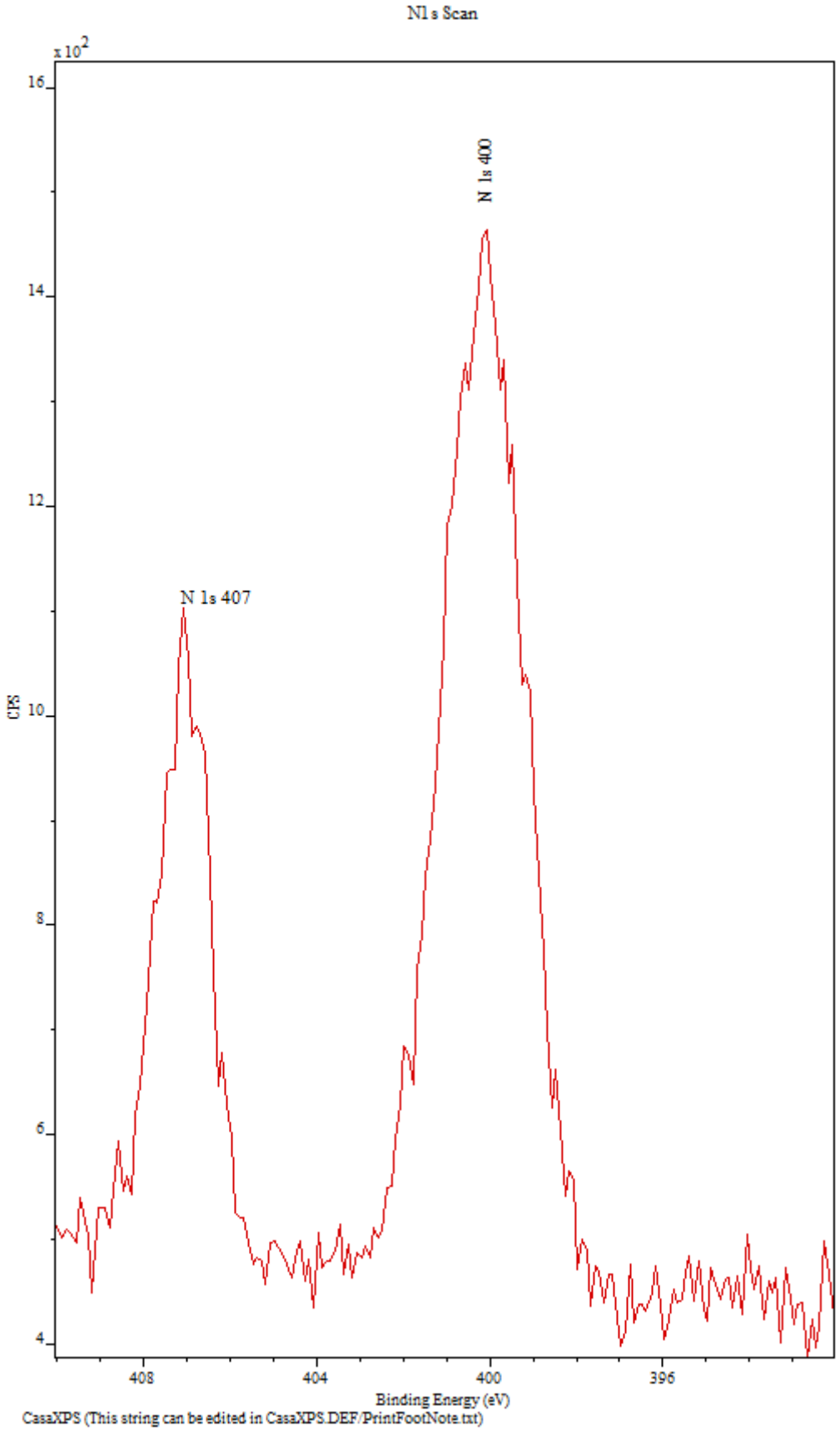


Figure 4.45b: XPS high-resolution spectrum of (b) N1sregion acquired HT-DNA/Ppy nanowires

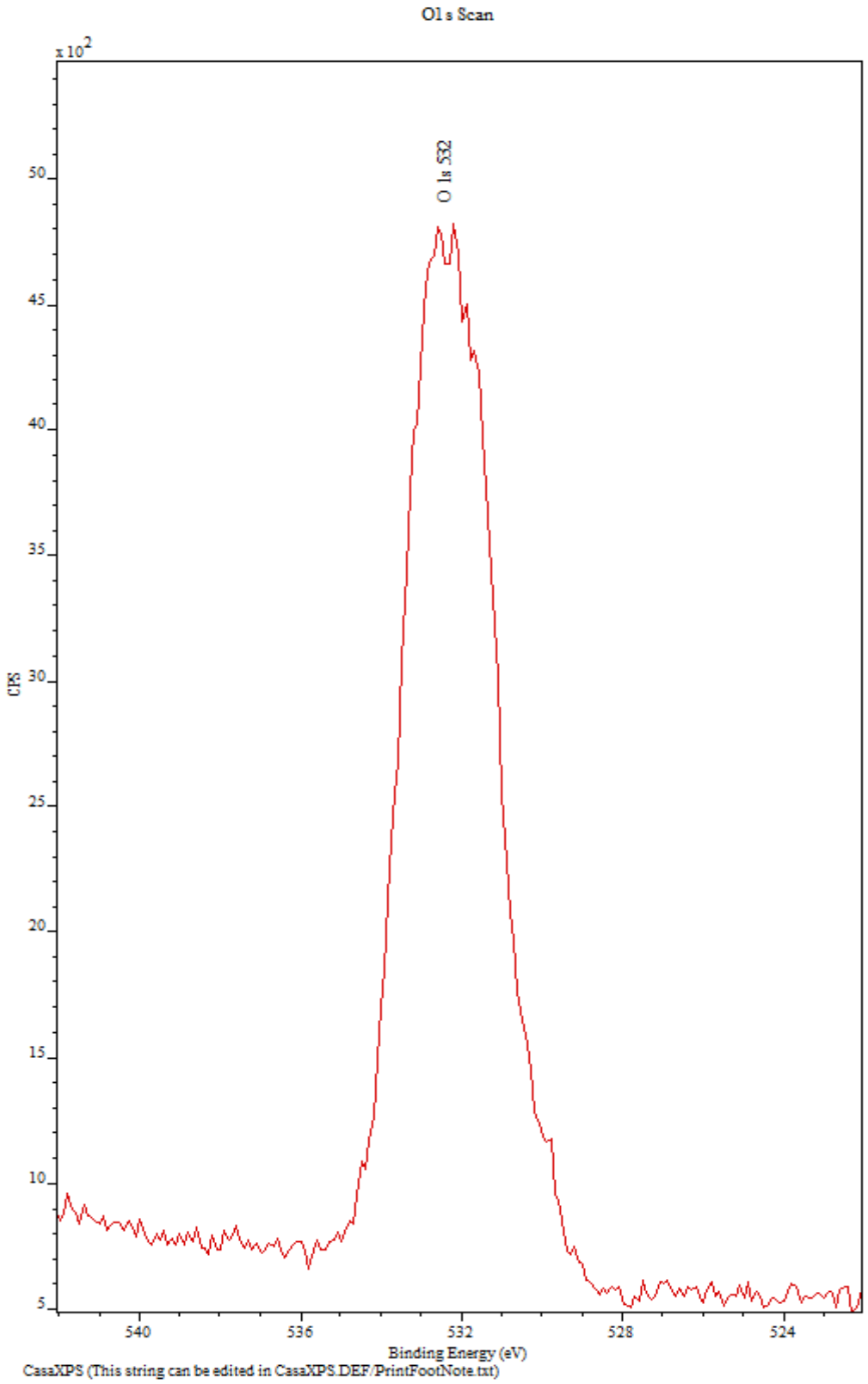


Figure 4.45c: XPS high-resolution spectrum of(c) O 1s region acquired from HT-DNA/Ppy nanowires

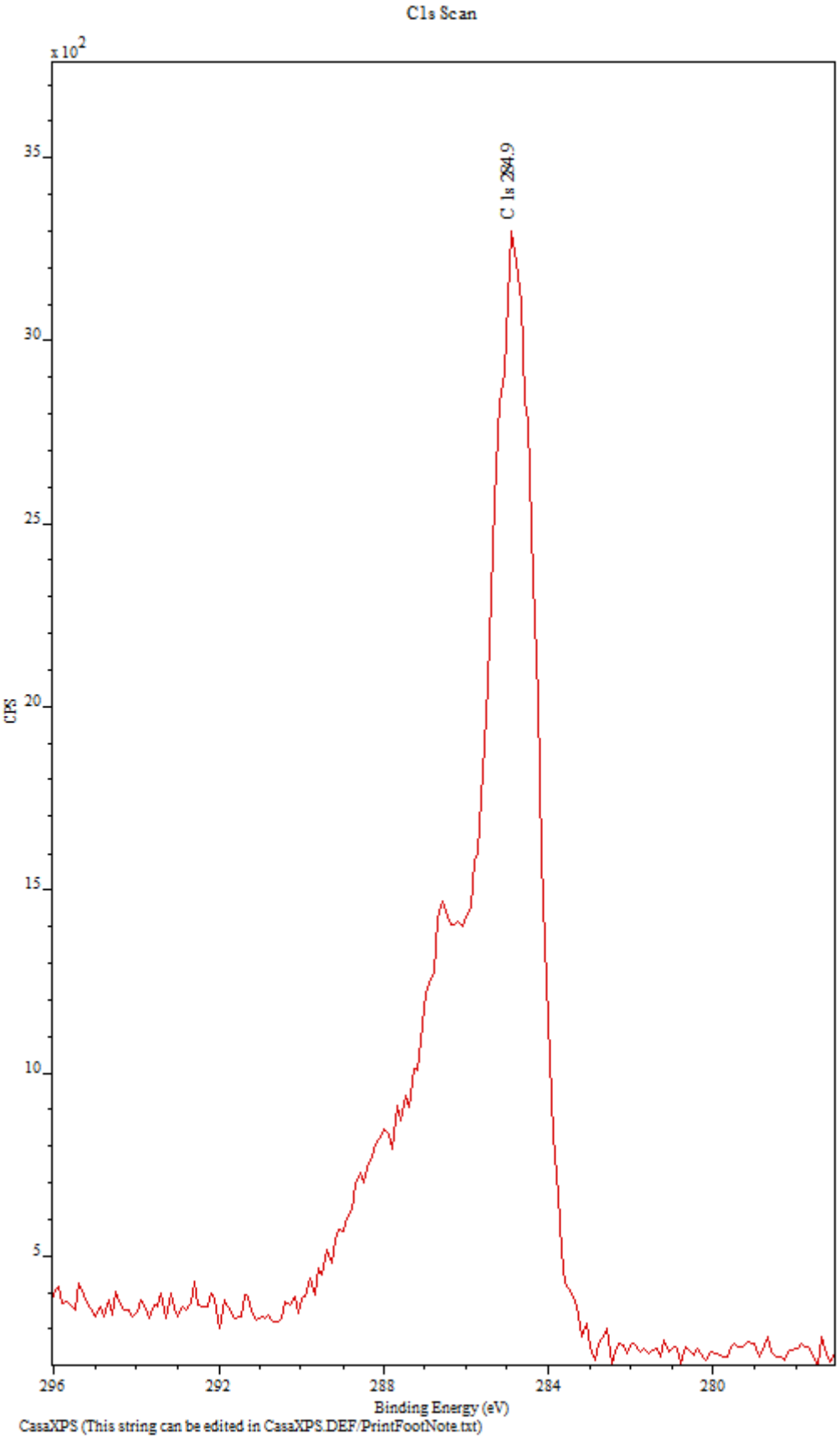


Figure 4.45d: XPS high-resolution spectrum of (d) C 1s region acquired from HT-DNA/Ppy nanowires

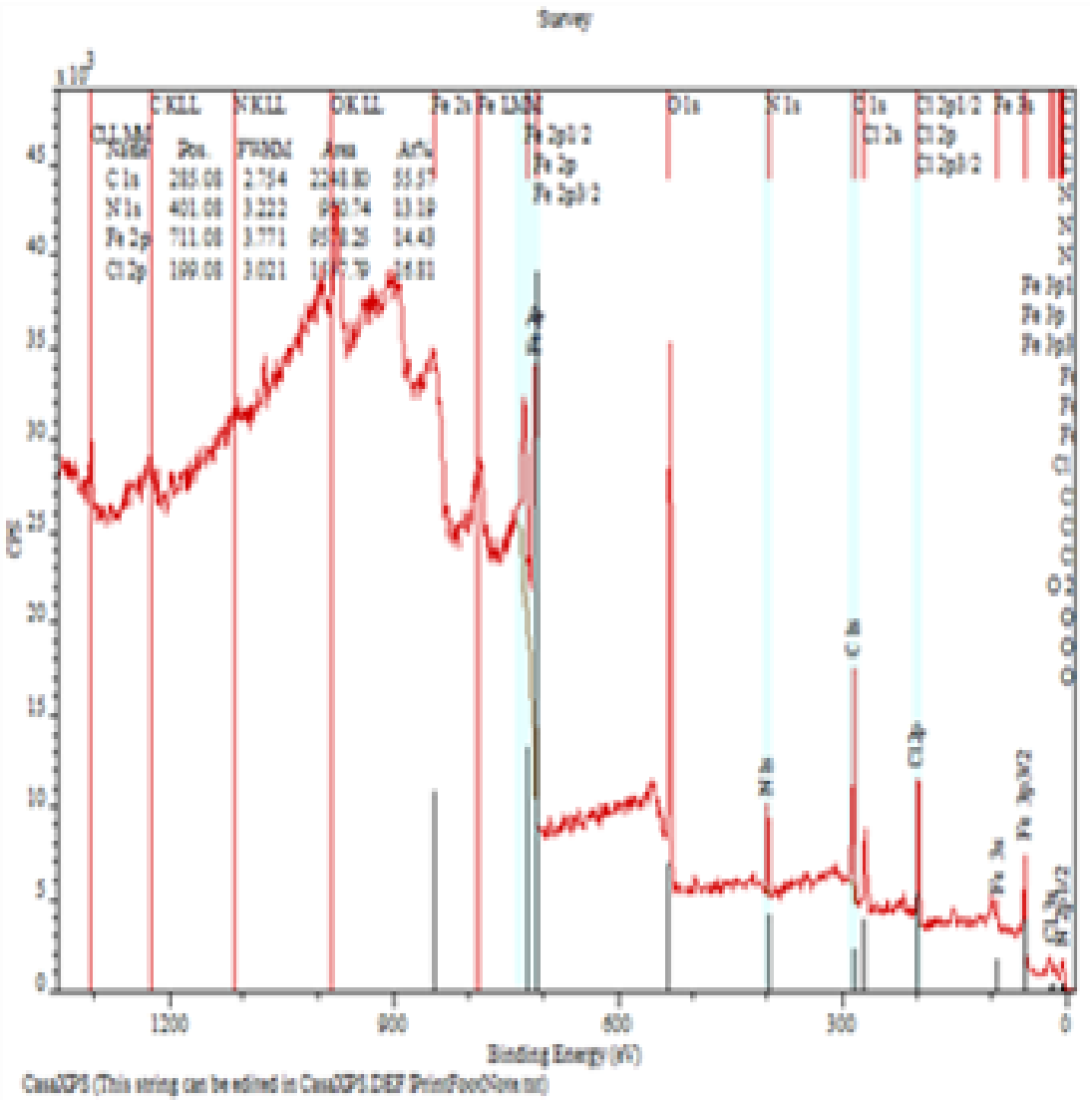


Figure 4.46. XPS survey spectrum of PImi thin film

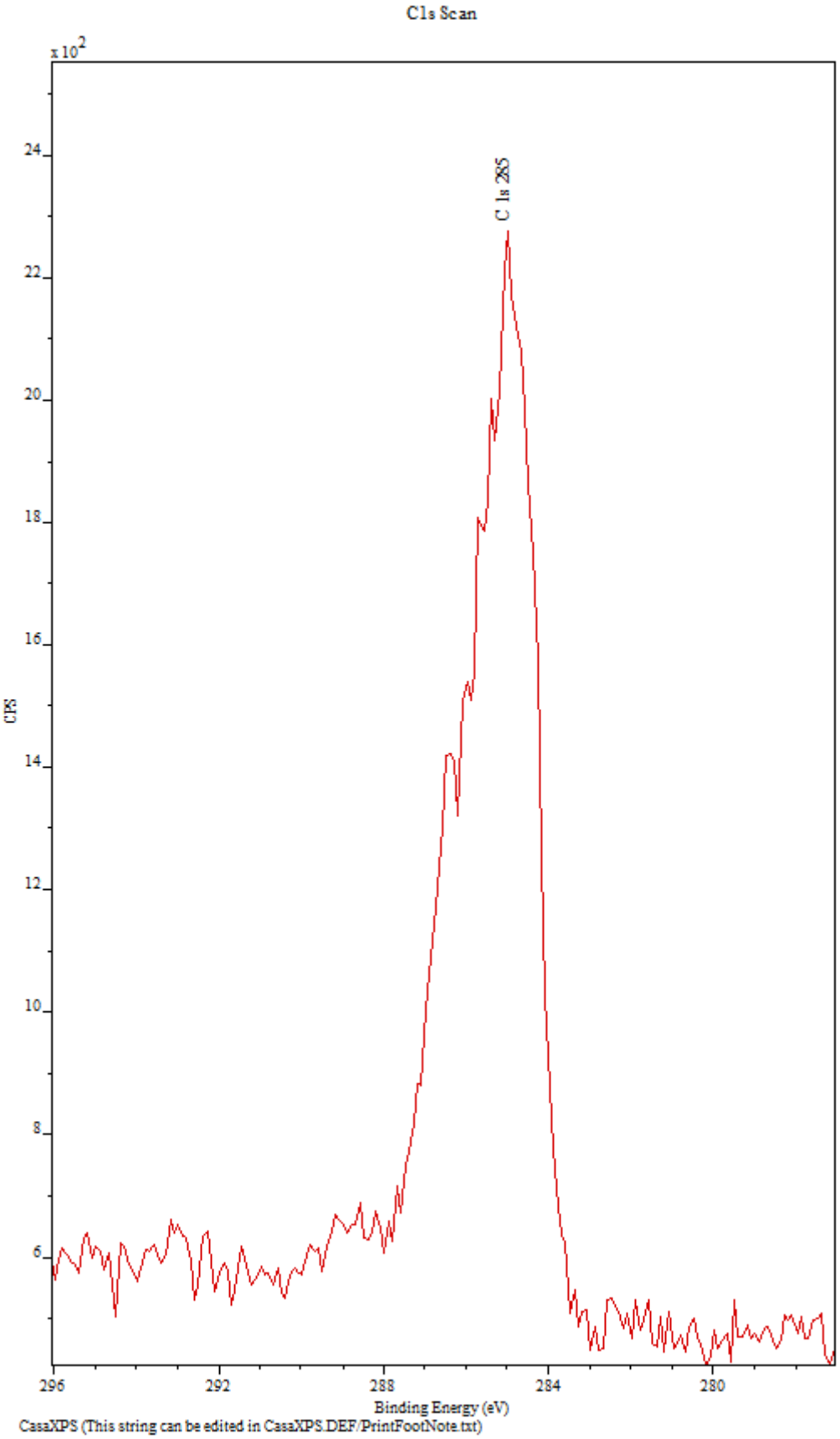


Figure 4.47a: XPShigh-resolution spectra of (a) C 1sregion acquired fromPImi thin film components

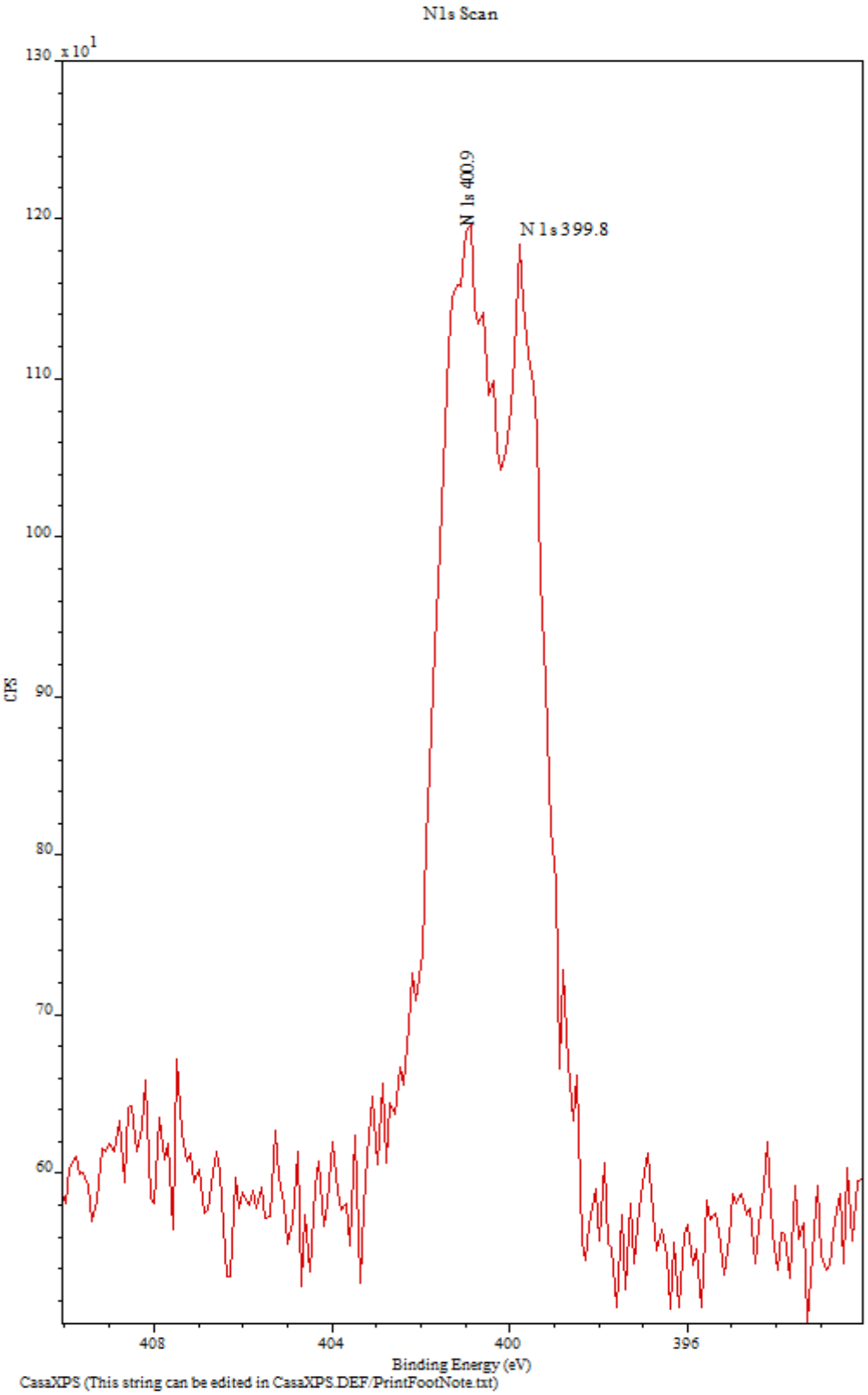


Figure 4.47b: XPShigh-resolution spectra of (b) N 1s region acquired from PImi thin film components

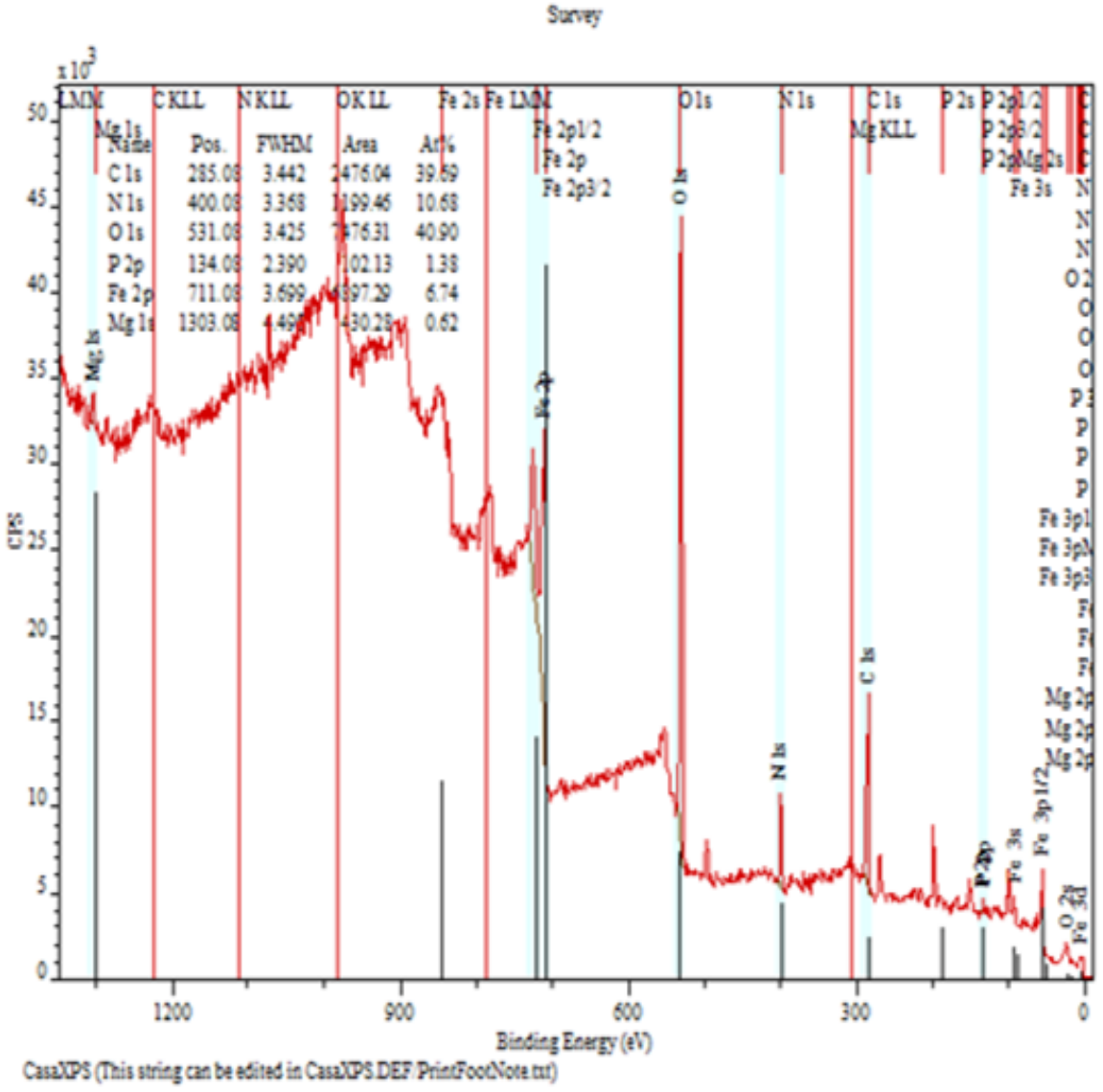


Figure 4.48: XPS survey spectrum of HT-DNA/PImi nanowires

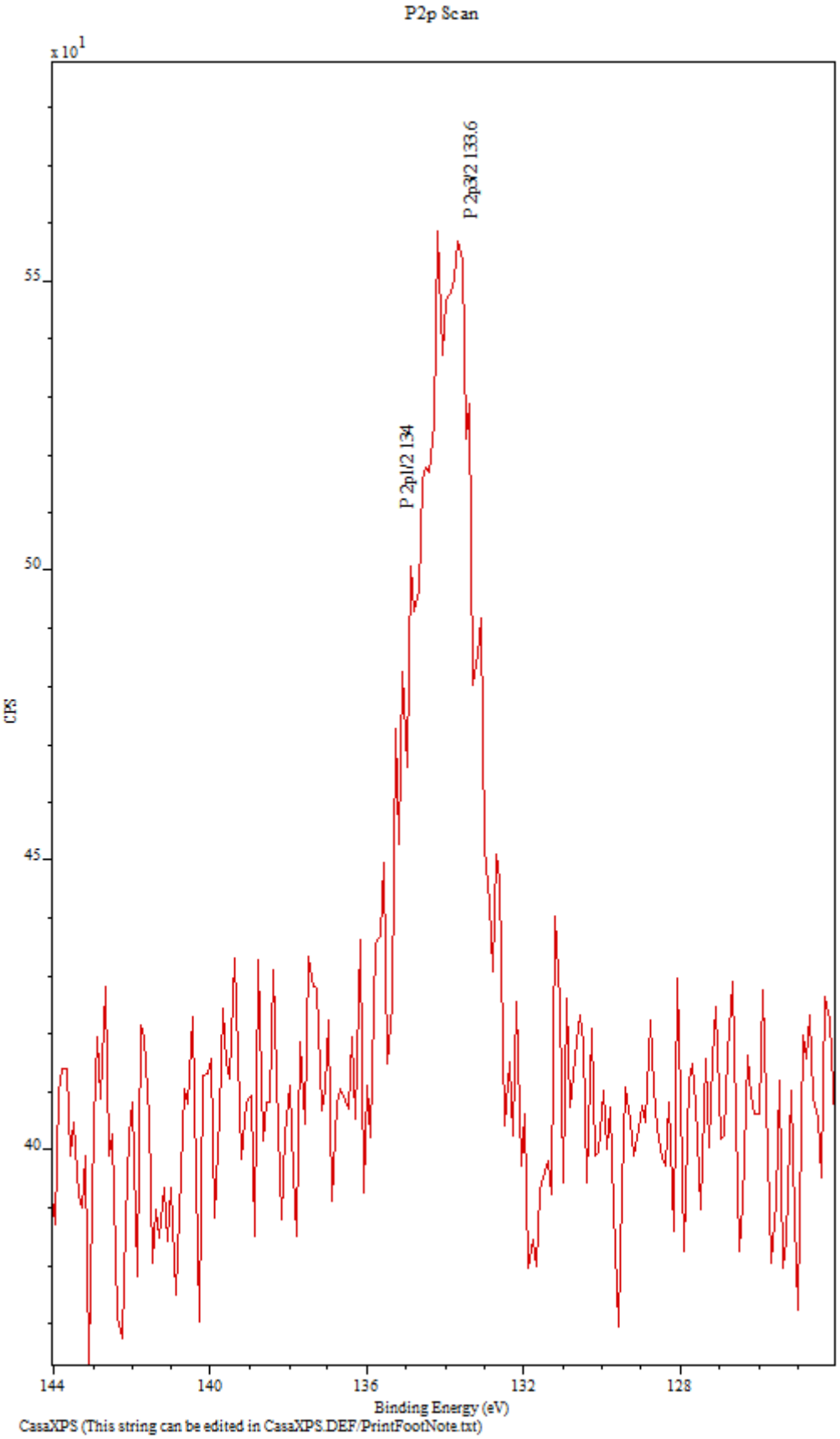


Figure 4.49a: XPS high-resolution spectrum of (a) P 2p region acquired from HT-DNA/PImi nanowires

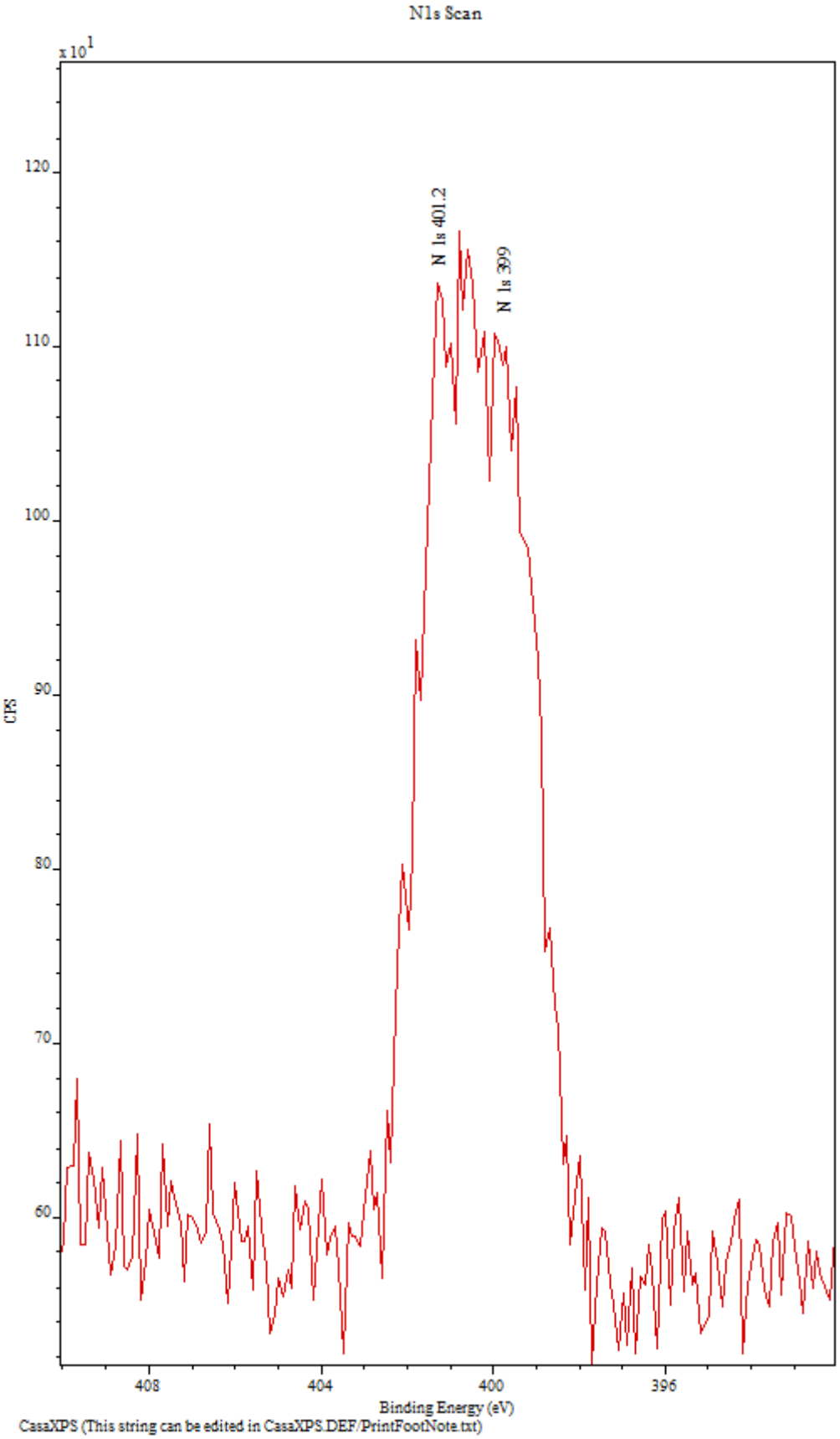


Figure 4.49b: XPS high-resolution spectrum of (b) N 1s region acquired from HT-DNA/PImi nanowires

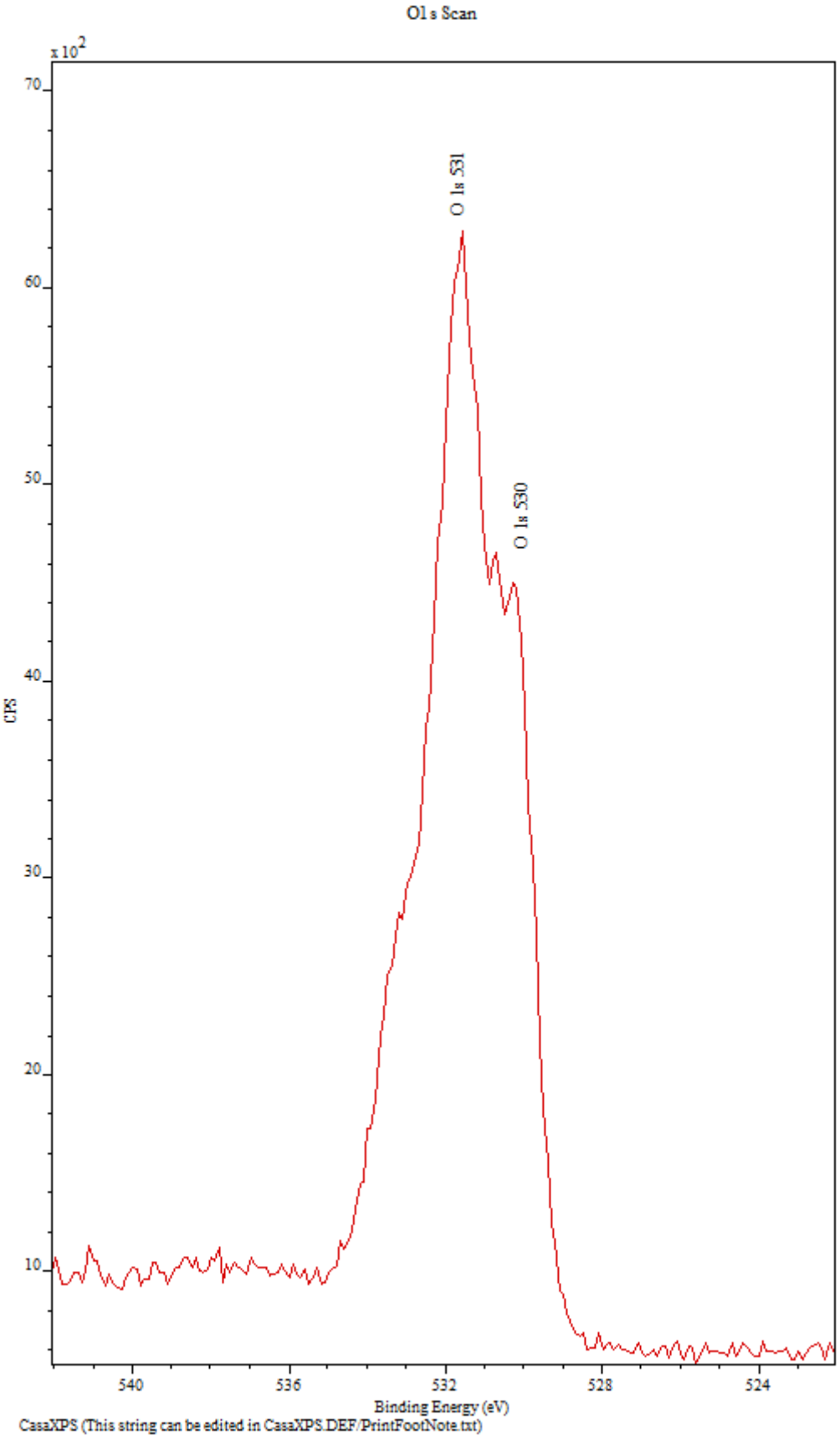


Figure 4.49c: XPS high-resolution spectrum of (c), O1s region acquired from HT-DNA/PImi nanowires

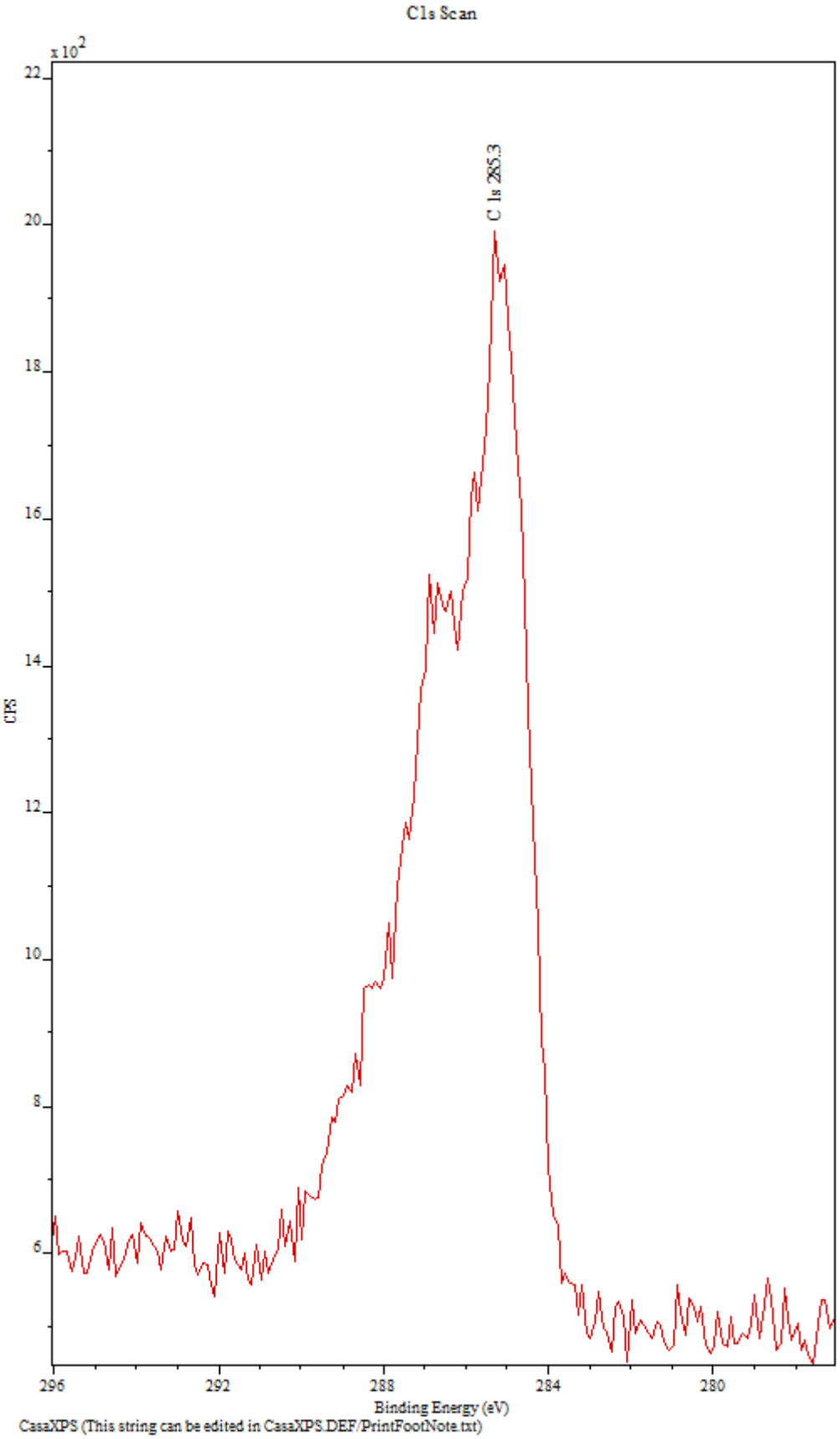


Figure 4.49d: XPS high-resolution spectrum of (d)C 1s region acquired from HT-DNA/PImi nanowires

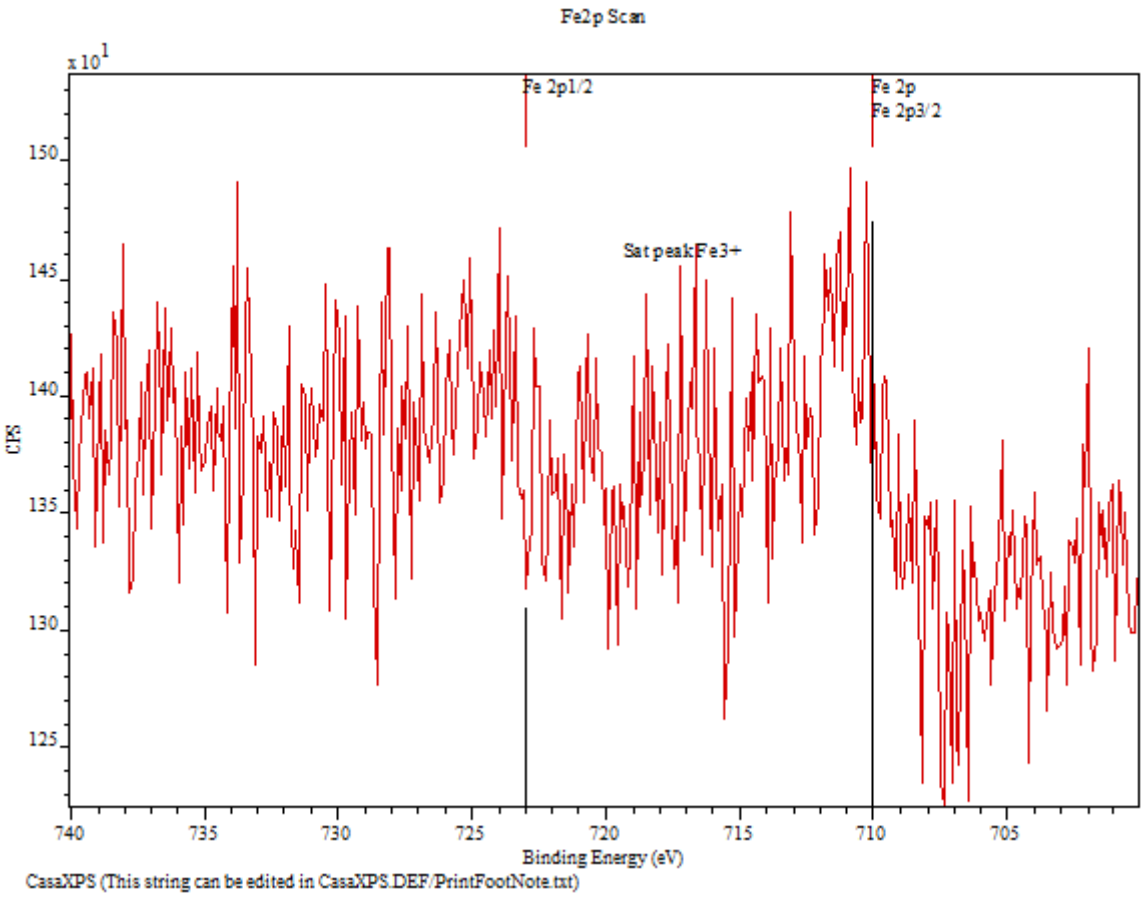


Figure 4.50a: Low resolution XPS spectrum of Fe 2p following etching of the HT-DNA/FeOOH nanowires by Ar+ sputtering for (a), zero second

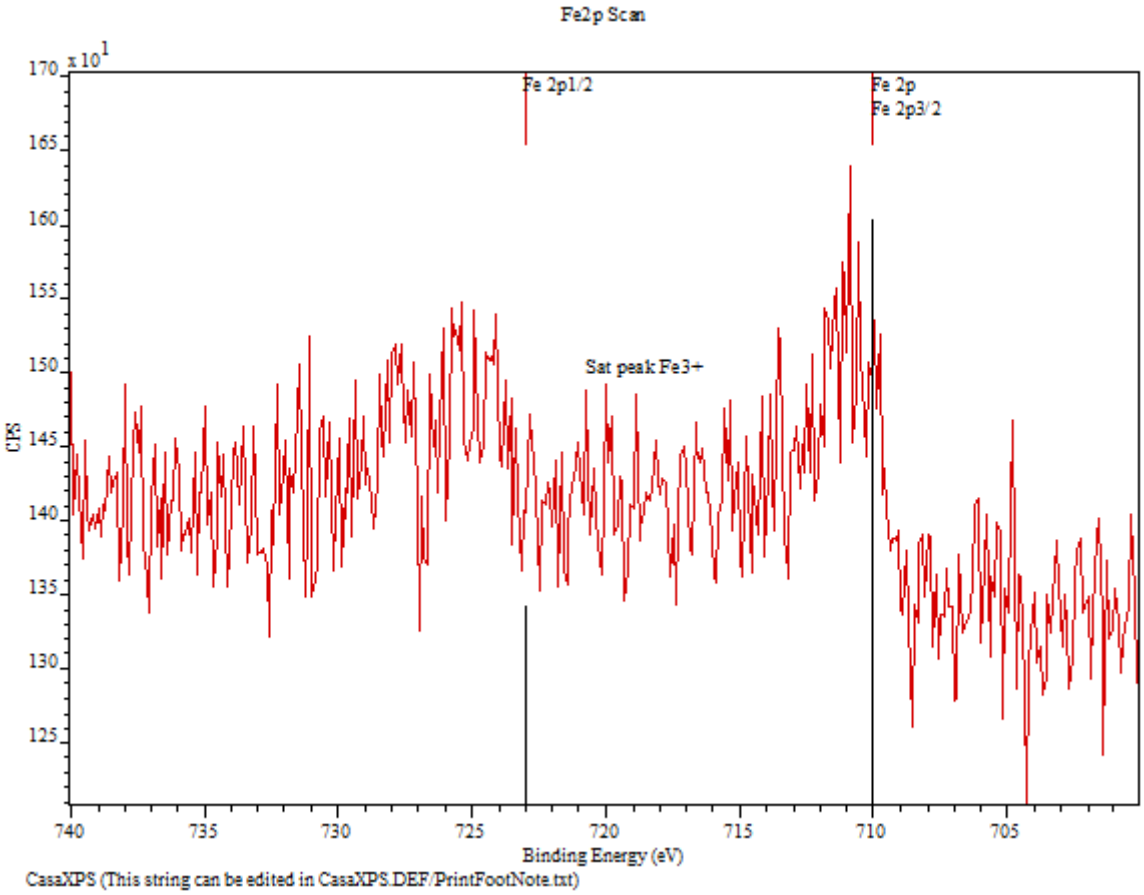


Figure 4.50b: Low resolution XPS spectrum of Fe 2p following etching of the HT-DNA/FeOOH nanowires by Ar+ sputtering for (b), 402seconds

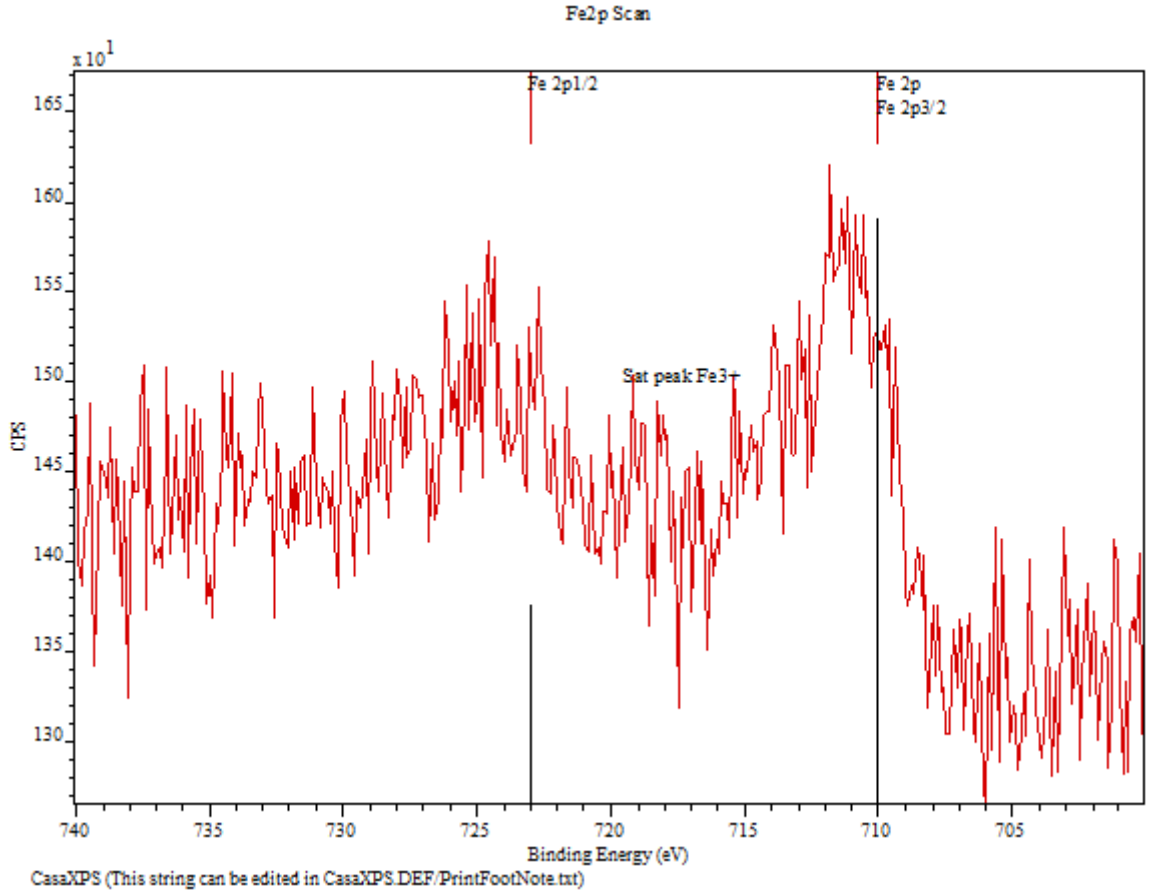


Figure 4.50c: Low resolution XPS spectra of Fe 2p following etching of the HT-DNA/FeOOH nanowires by Ar+ sputtering for(c), 803seconds

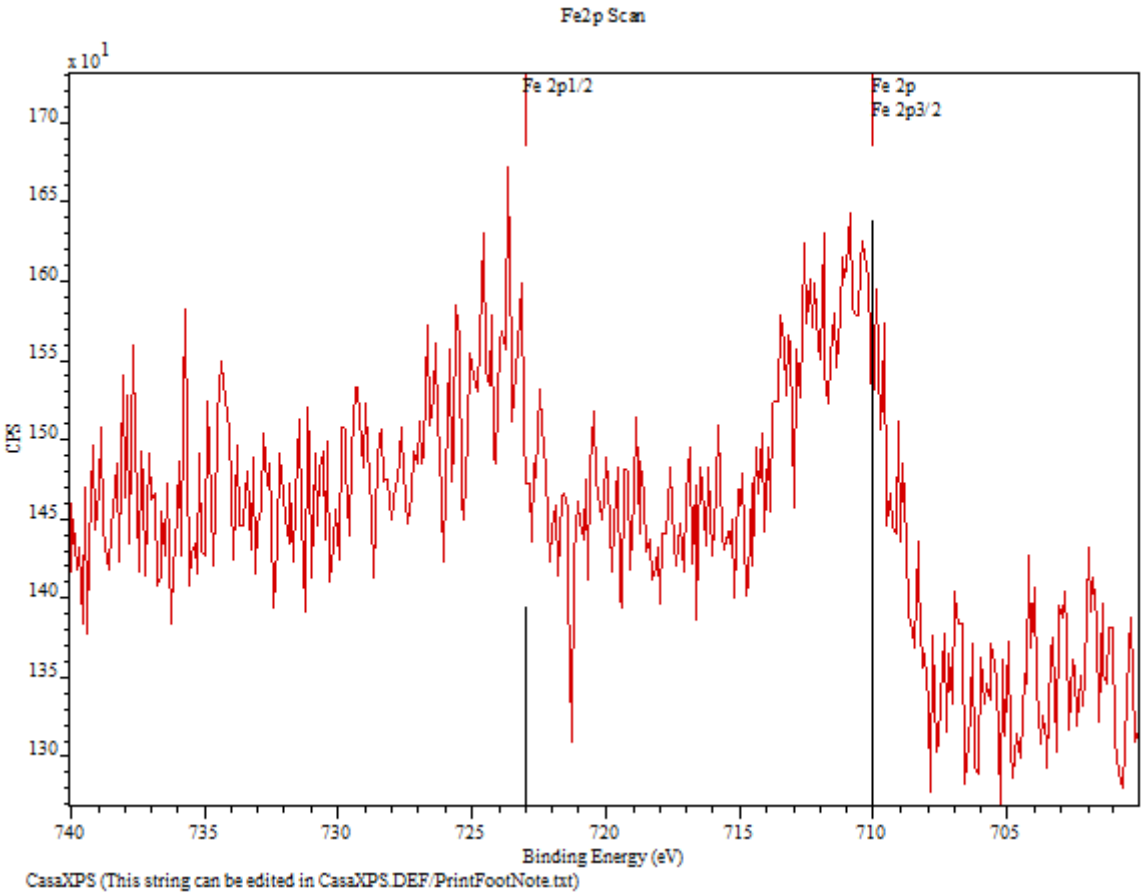


Figure 4.50d: Low resolution XPS spectrum of Fe 2p following etching of the HT-DNA/FeOOH nanowires by Ar+ sputtering for (d),1204seconds

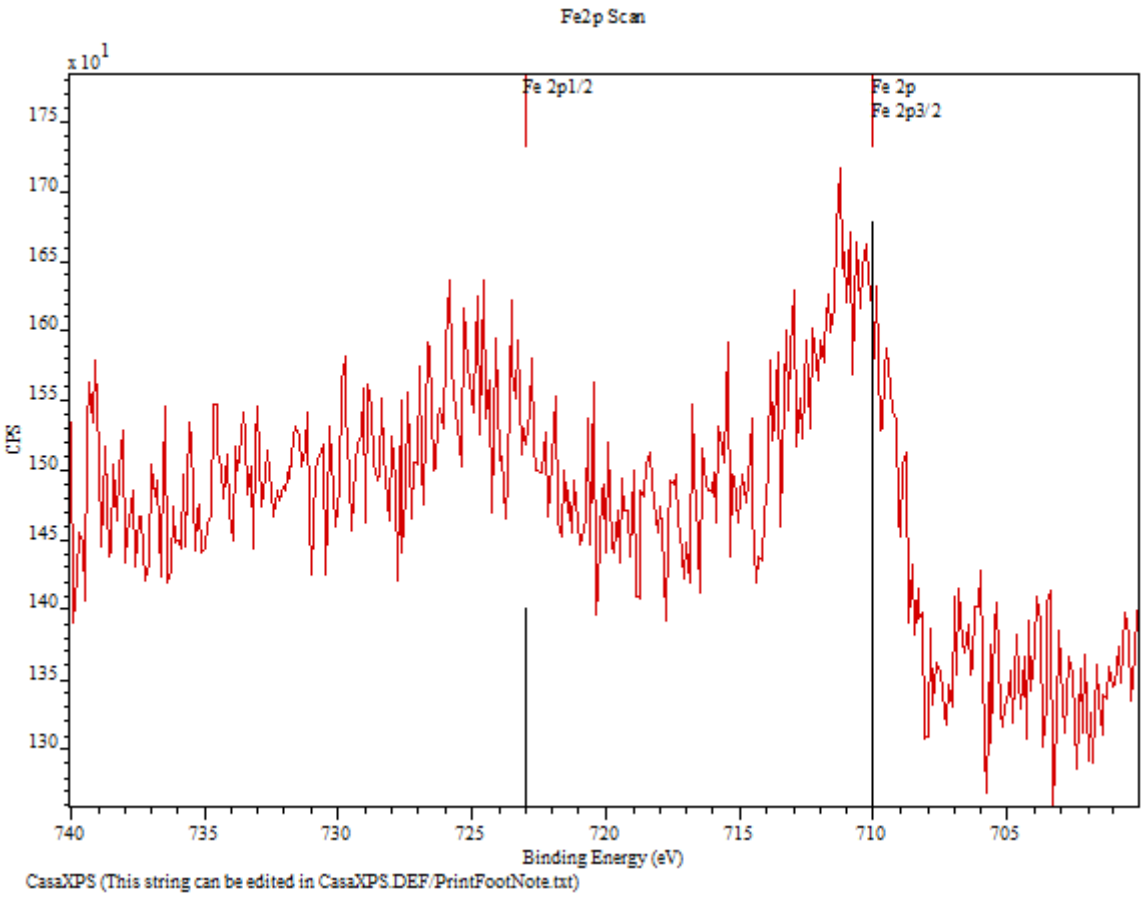


Figure 4.50e: Low resolution XPS spectrum of Fe 2p following etching of the HT-DNA/FeOOH nanowires by Ar+ sputtering for (e), 1606seconds

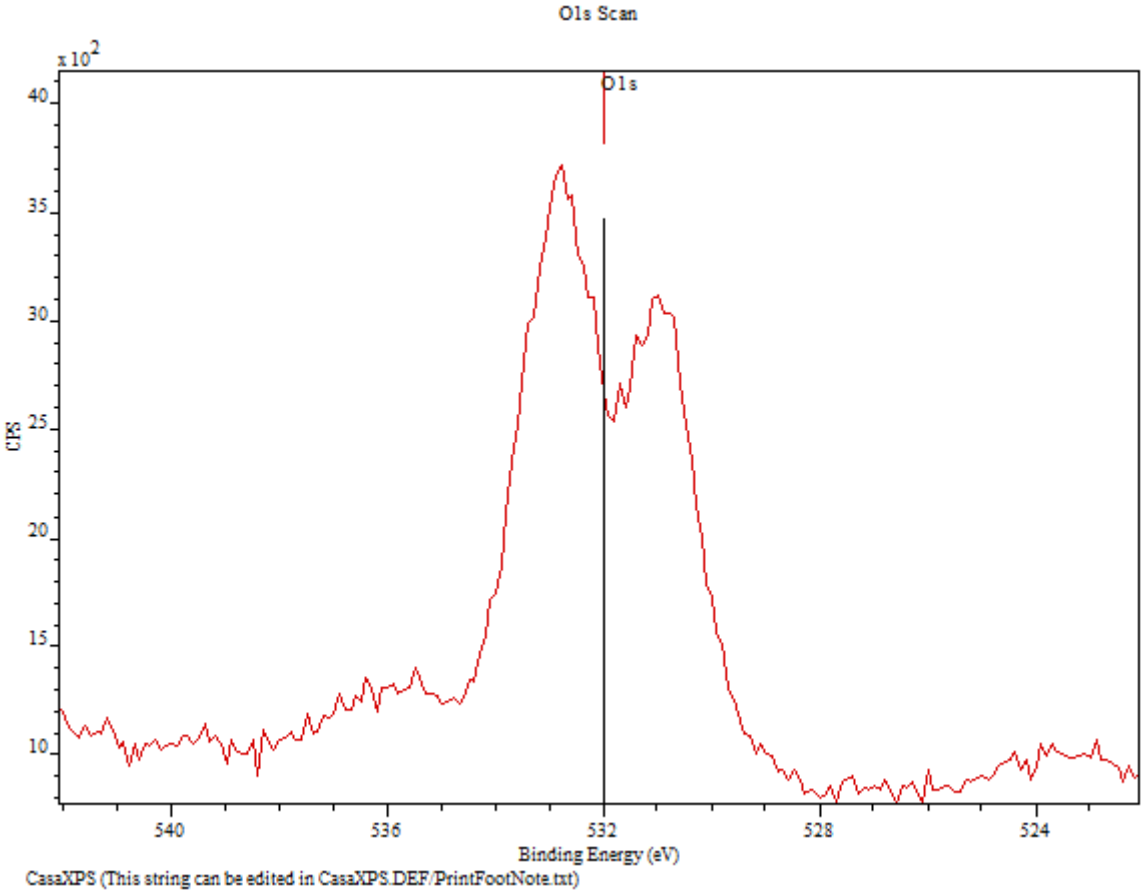


Figure 4.51a: XPS spectrum of O1s following etching of the HT-DNA/FeOOH nanowires by Ar+ sputtering for (a), zero second

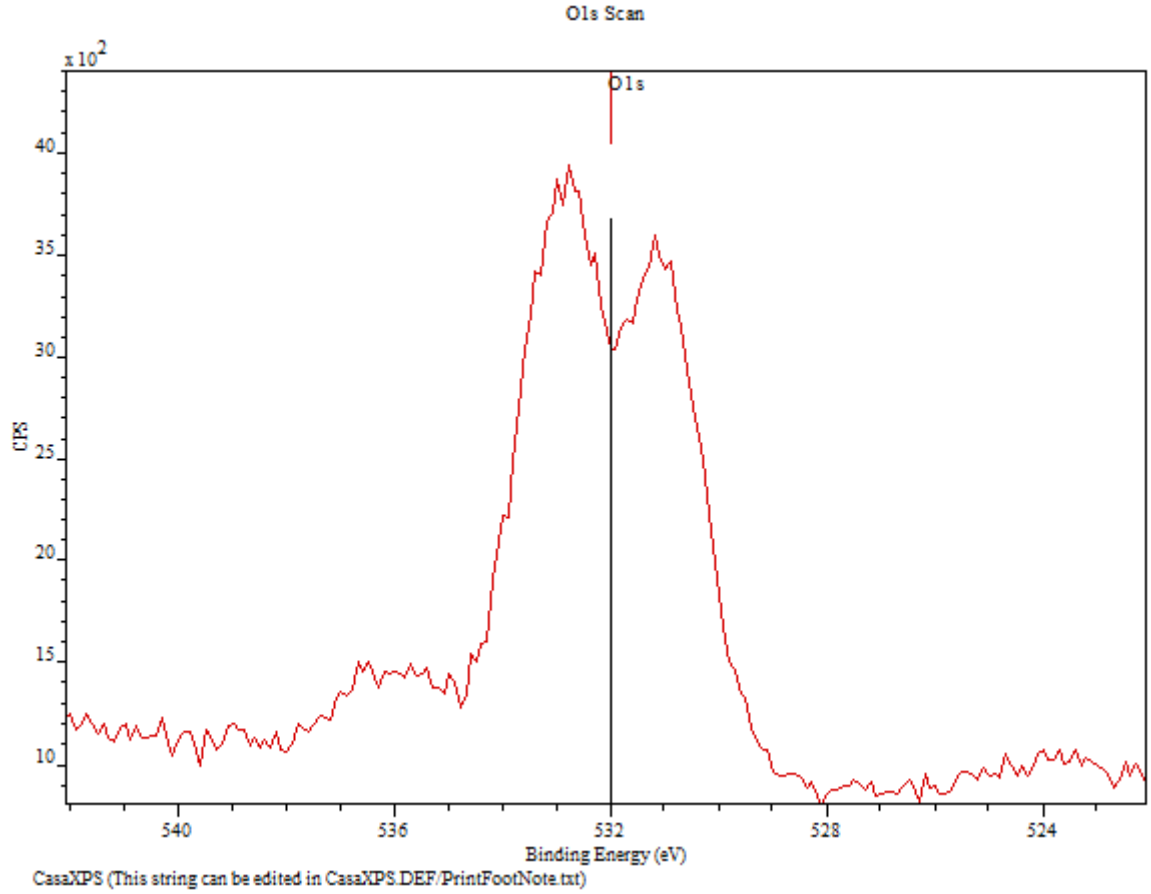


Figure 4.51b: XPS spectrum of O1s following etching of the HT-DNA/FeOOH nanowires by Ar+ sputtering for(b), 402seconds

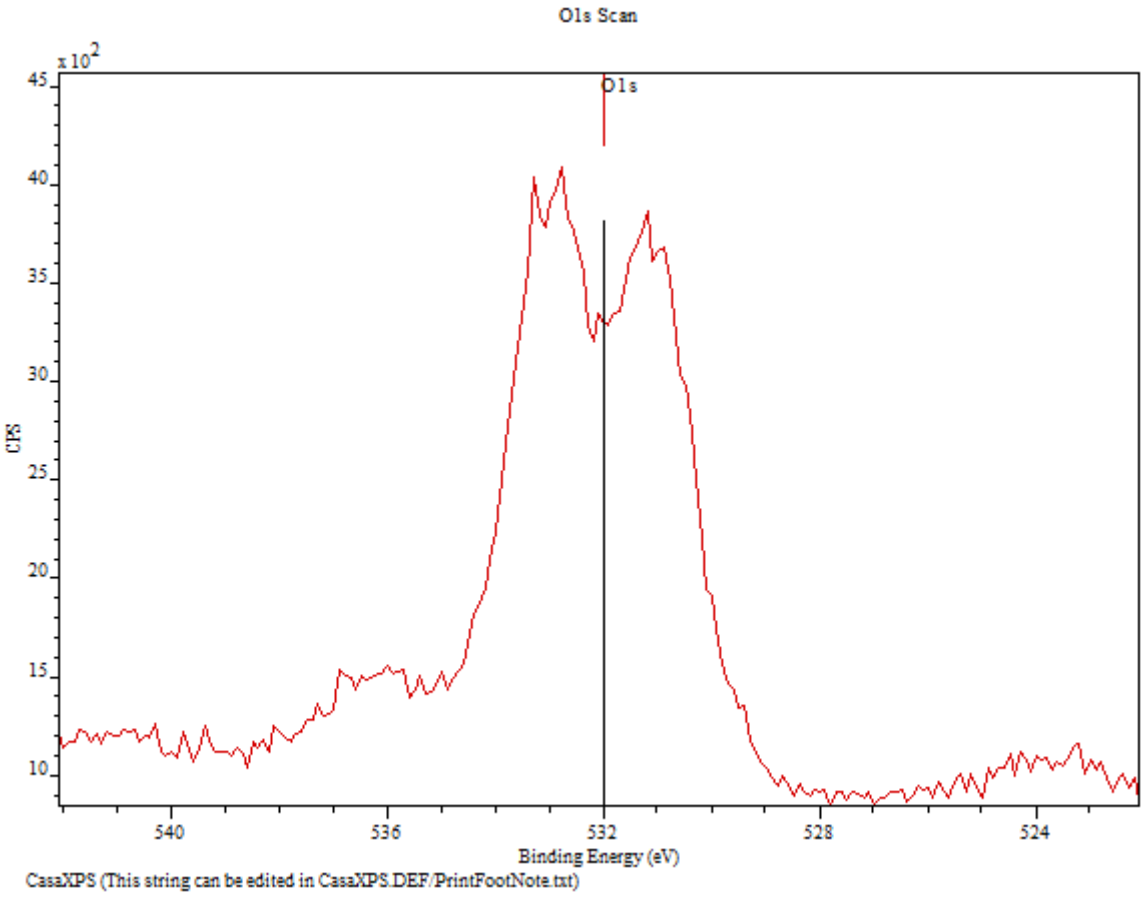


Figure 4.51c: XPS spectrum of O1s following etching of the HT-DNA/FeOOH nanowires by Ar+ sputtering for (c), 803seconds

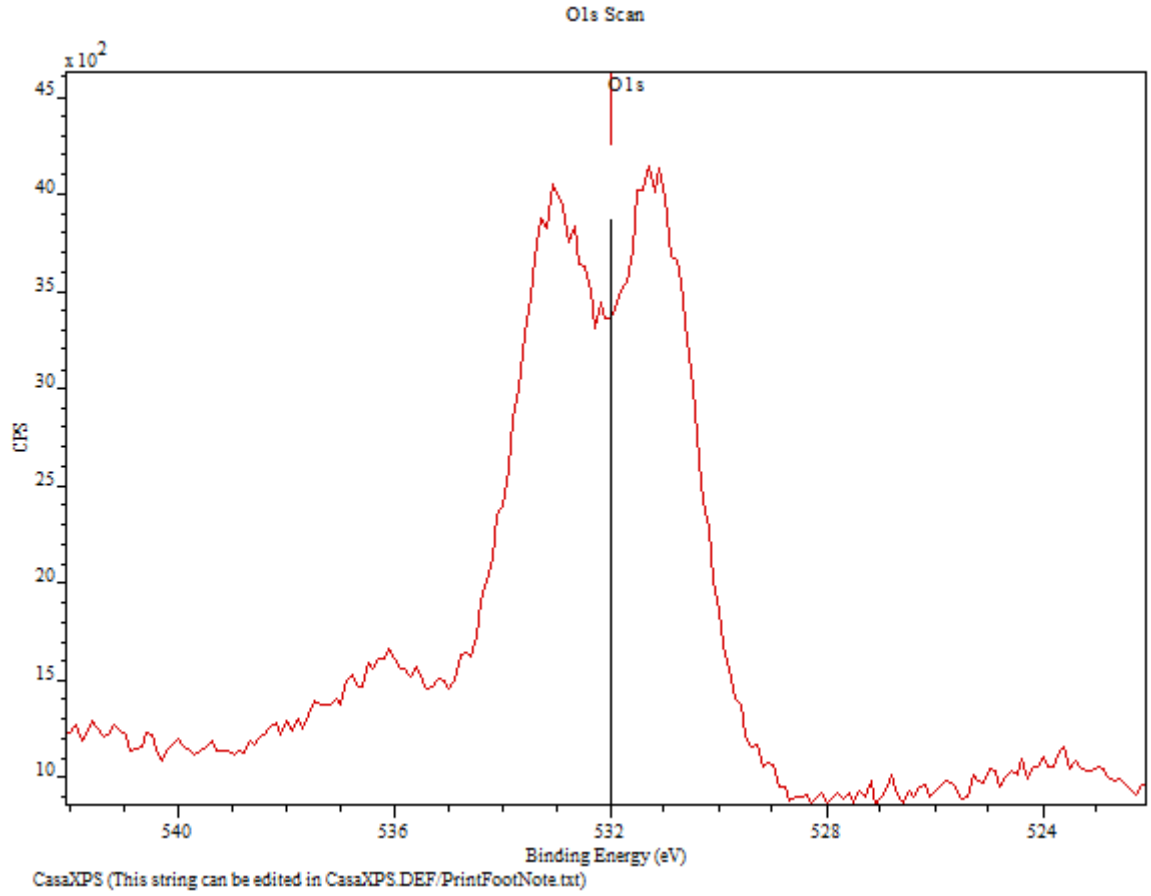


Figure 4.51d: XPS spectrum of O1s following etching of the HT-DNA/FeOOH nanowires by Ar+ sputtering for (d), 1204seconds

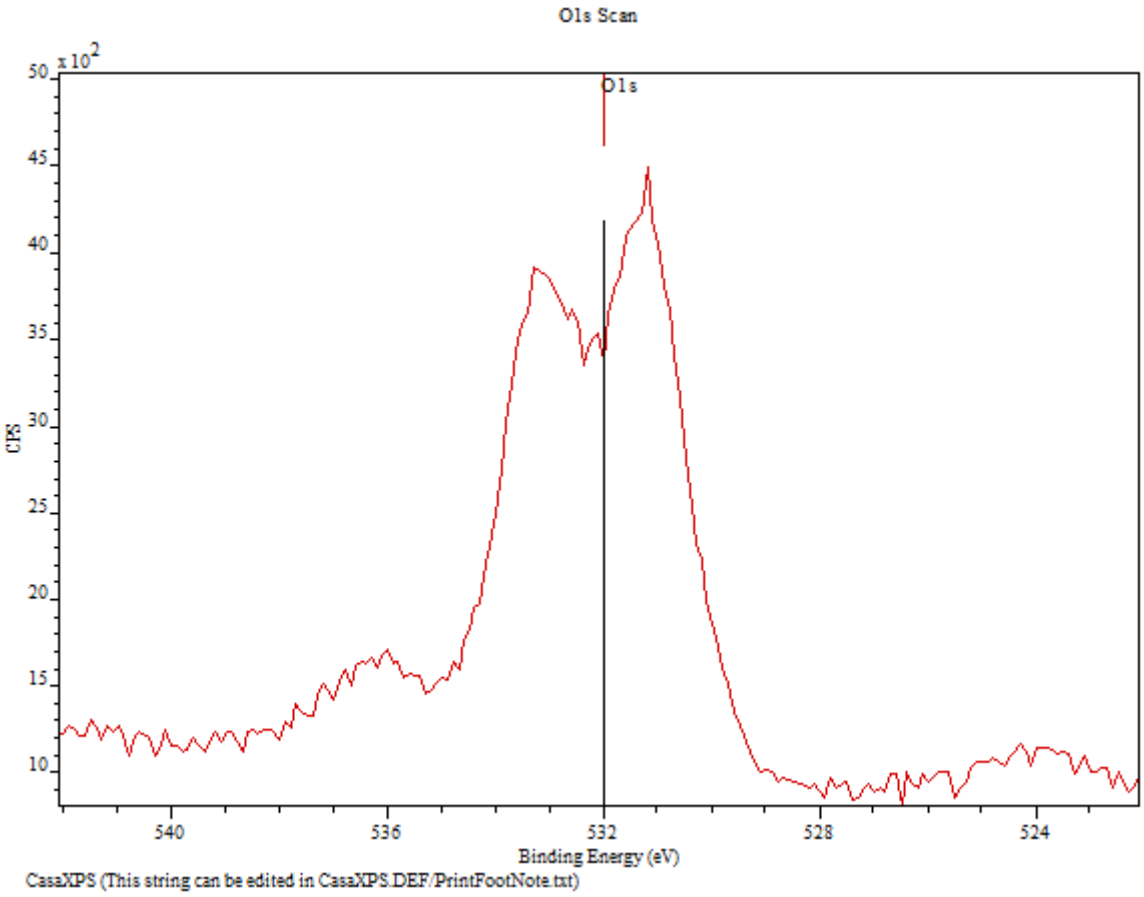


Figure 4.51e:XPS spectrum of O1s following etching of the HT-DNA/FeOOH nanowires by Ar+ sputtering for (e), 1606seconds

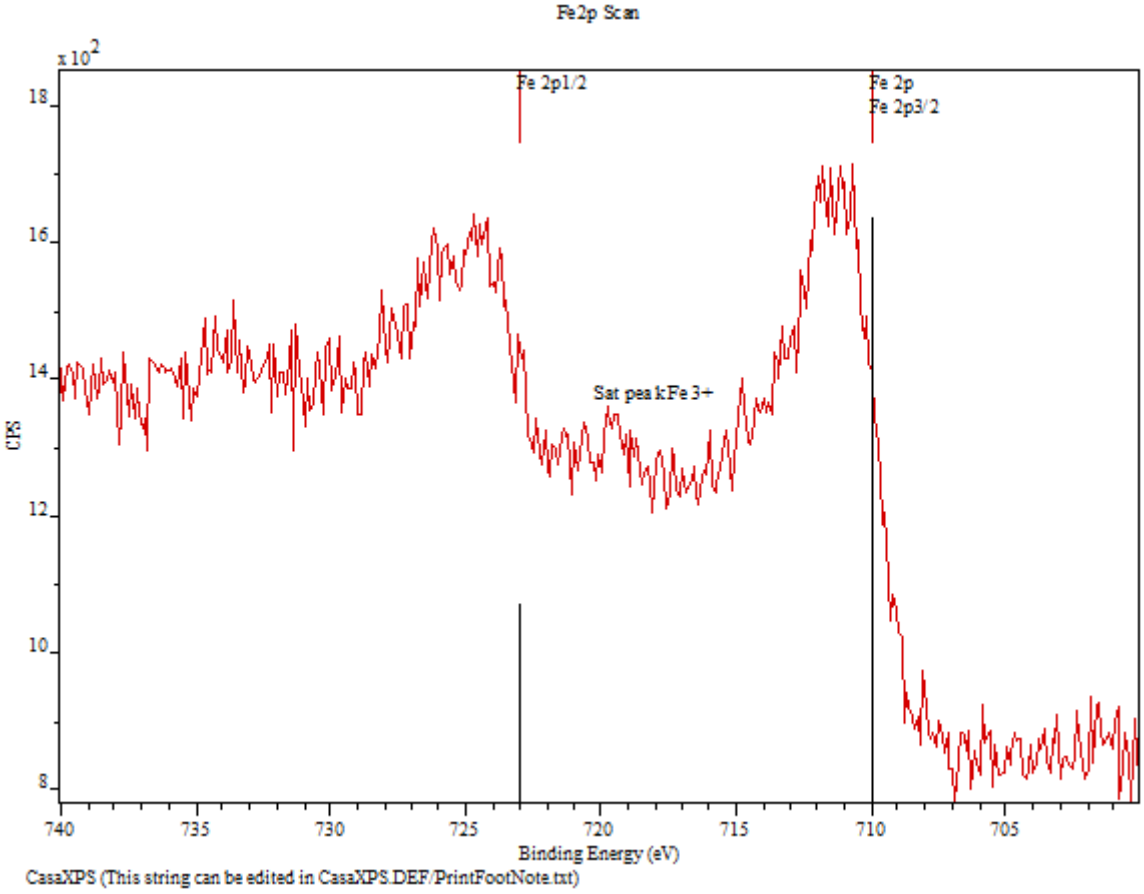


Figure 4.52a: Low resolution XPS spectrum of Fe 2p following etching of the HT-DNA/Fe_2O_3 nanowires by Ar+ sputtering for (a), zero second

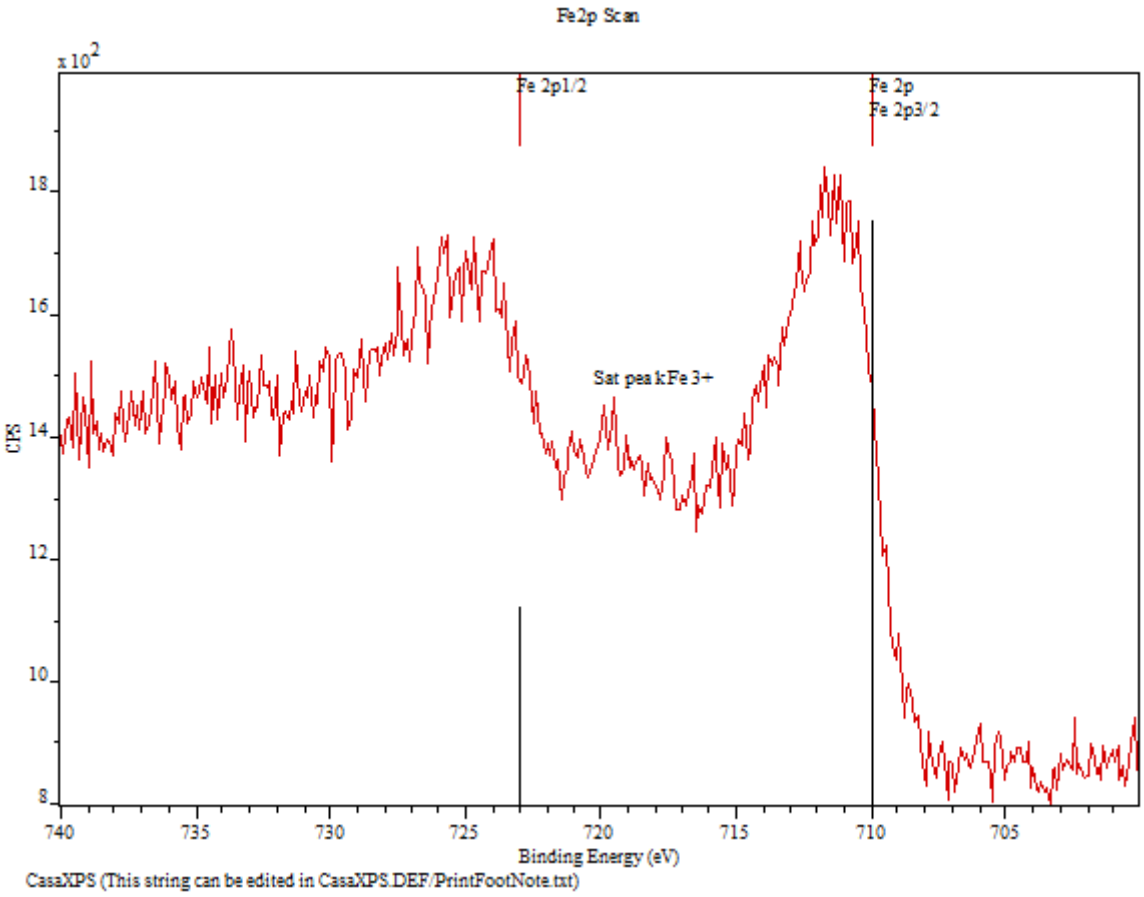


Figure 4.52b: Low resolution XPS spectrum of Fe 2p following etching of the HT-DNA/Fe_2O_3nanowires by Ar+ sputtering for(b), 402seconds

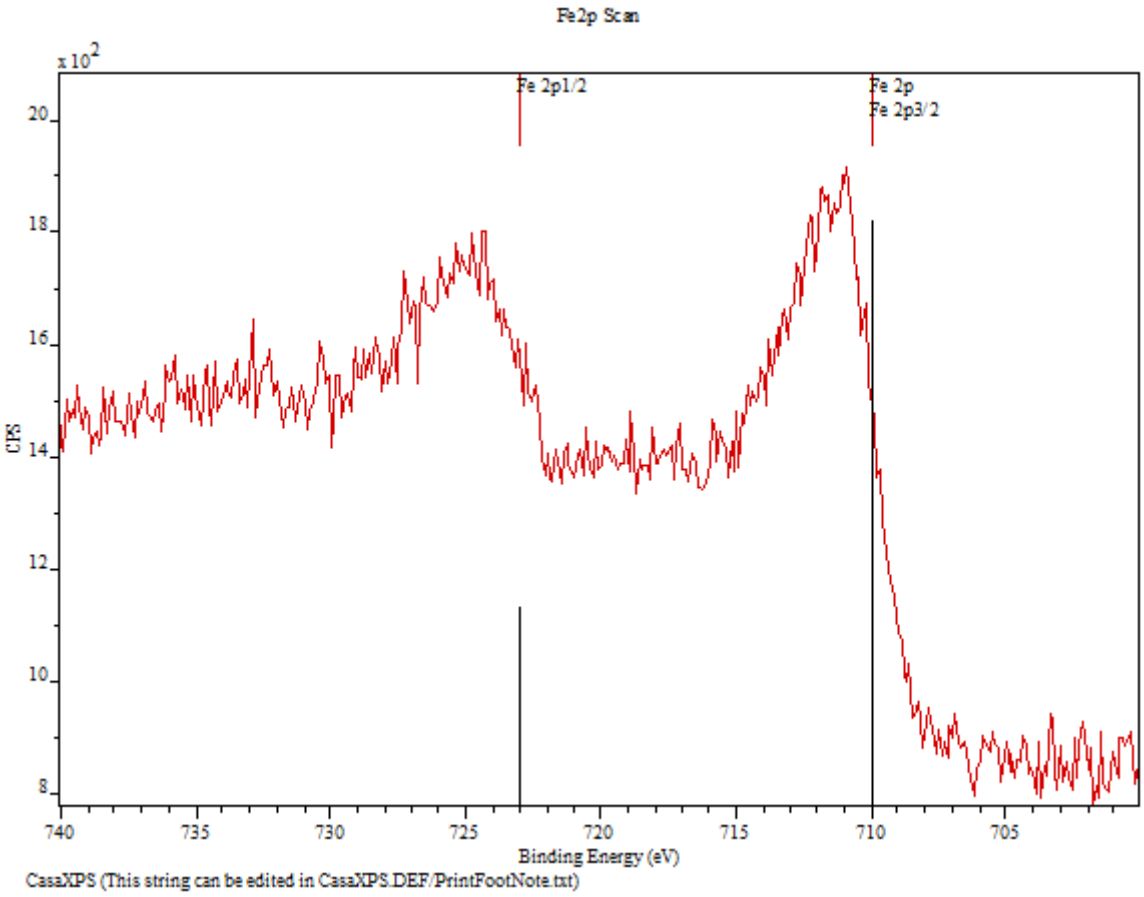


Figure 4.52c: Low resolution XPS spectrum of Fe 2p following etching of the HT-DNA/Fe_2O_3 nanowires by Ar+ sputtering for ((c), 803seconds

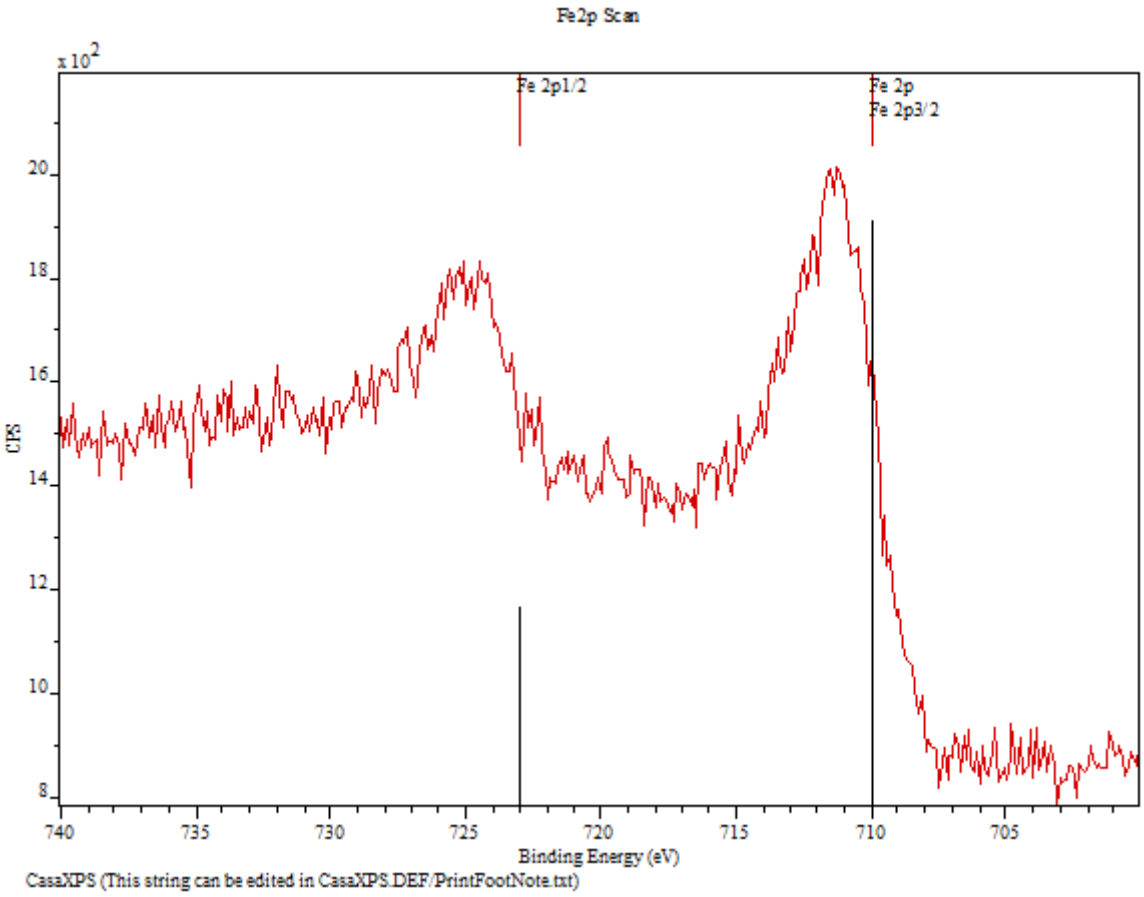


Figure 4.52d: Low resolution XPS spectrum of Fe 2p following etching of the HT-DNA/Fe_2O_3 nanowires by Ar+ sputtering for (d), 1204seconds

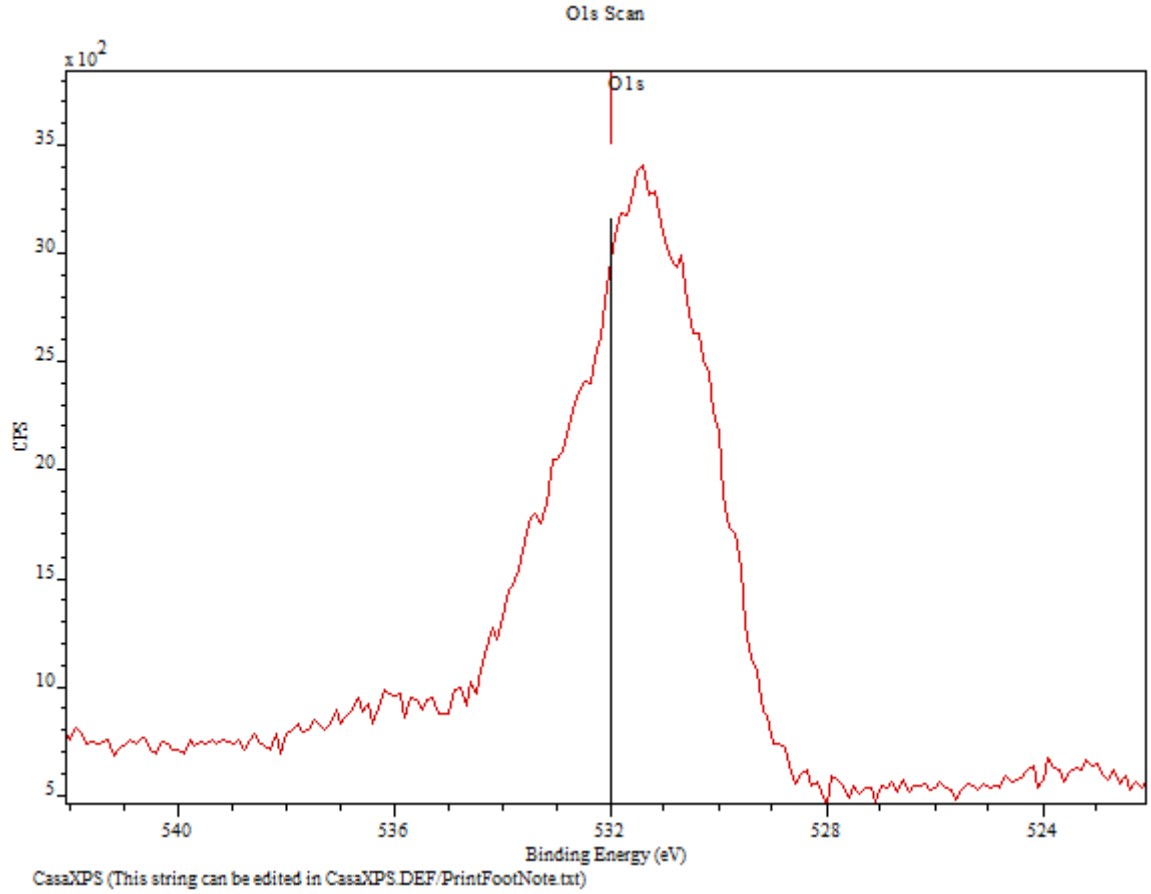


Figure 4.52e: Low resolution XPS spectrum of Fe 2p following etching of the HT-DNA/Fe_2O_3nanowires by Ar+ sputtering for (e), 1606seconds

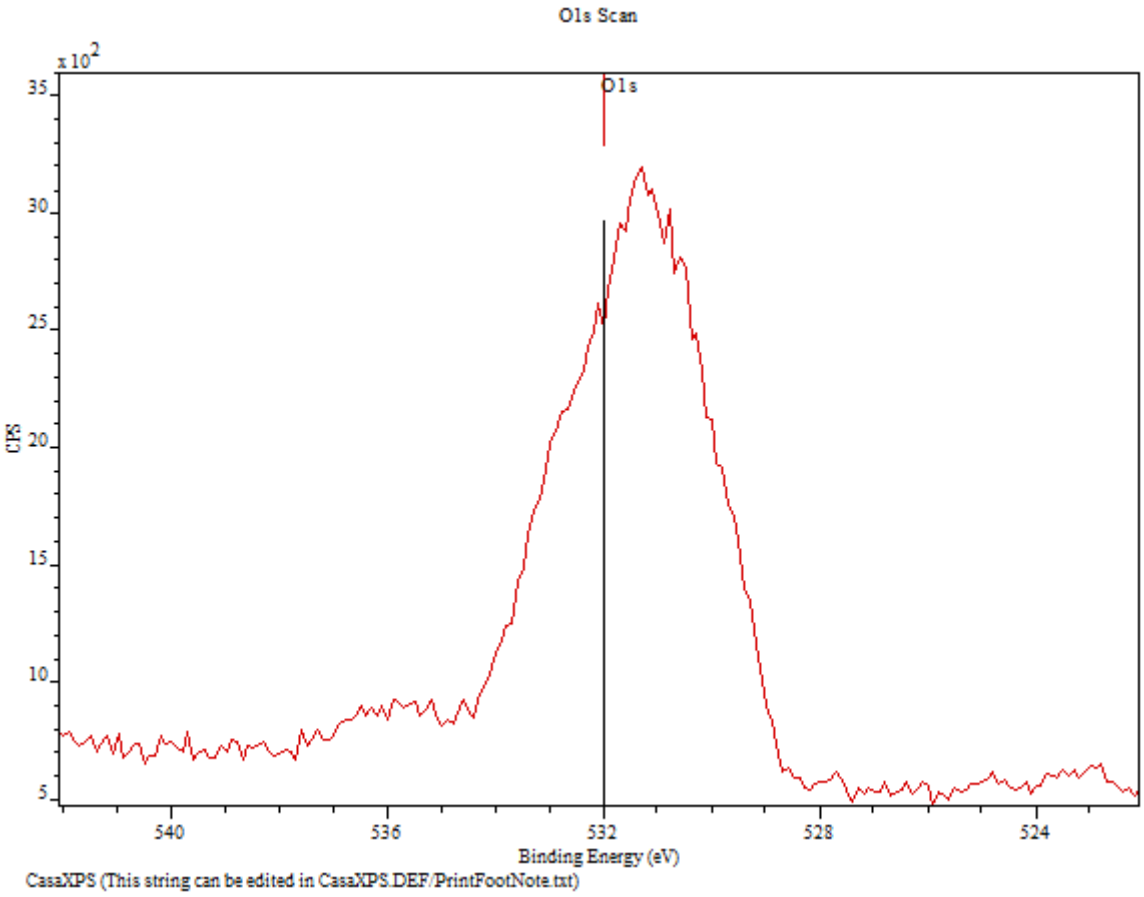


Figure 4.53a: XPS spectrum of O1s following etching of the HT-DNA/Fe_2O_3 nanowires by Ar+ sputtering for (a), zero second

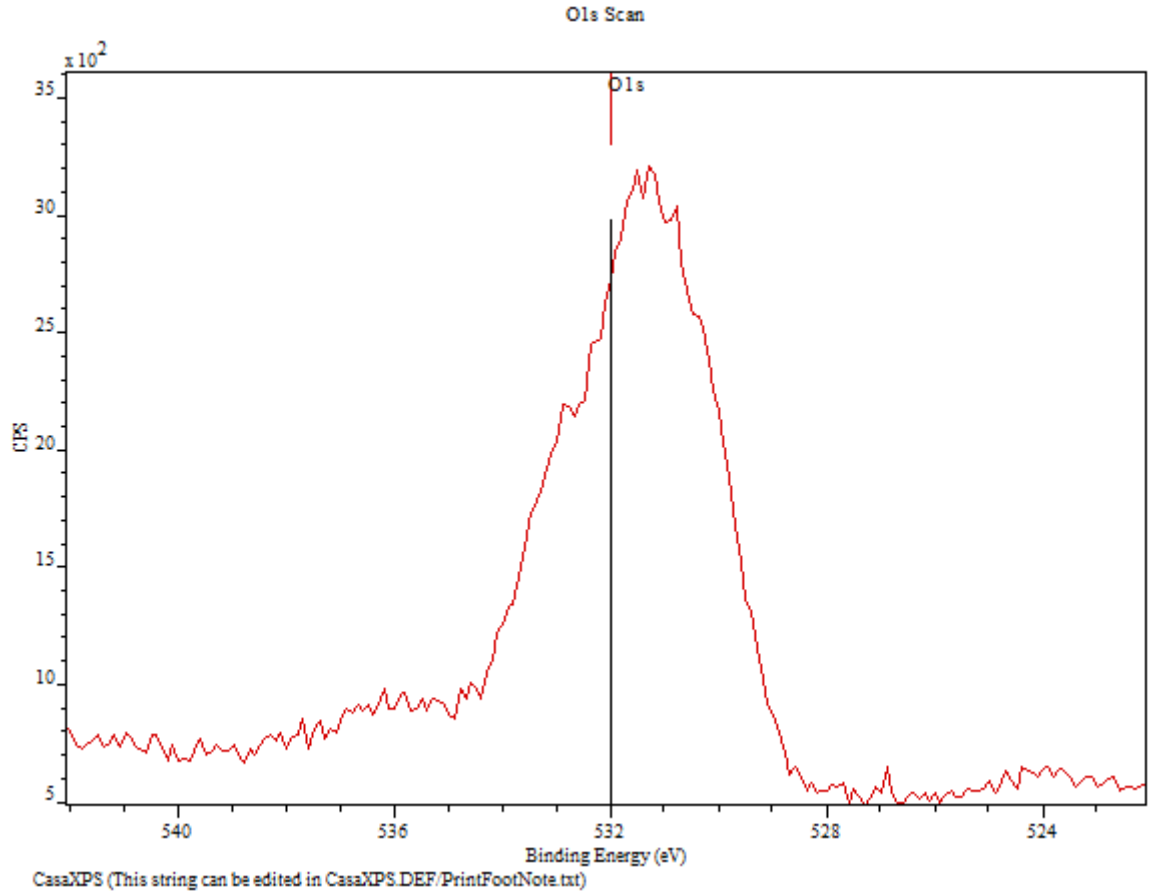


Figure 4.53b: XPS spectrum of O1s following etching of the HT-DNA/Fe_2O_3 nanowires by Ar+ sputtering for(b) 402seconds

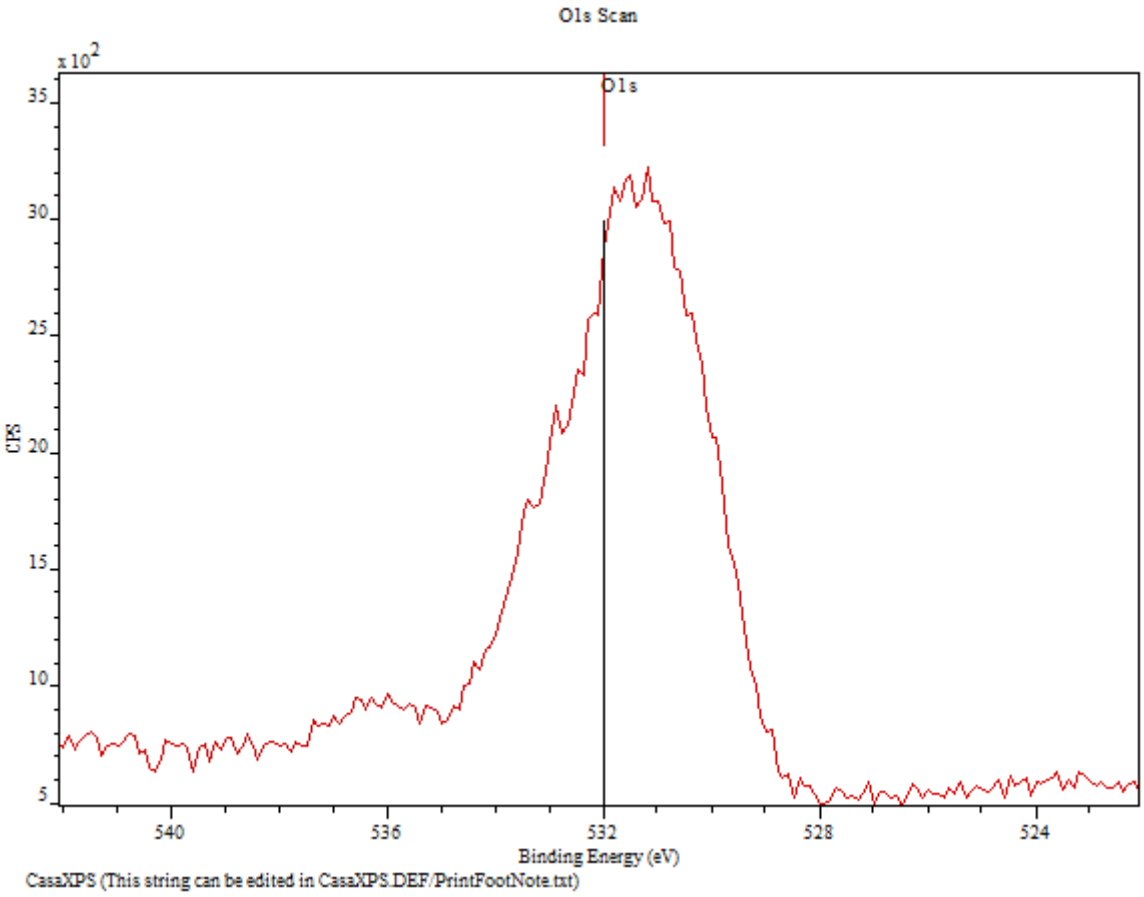


Figure 4.53c: XPS spectrum of O1s following etching of the HT-DNA/Fe_2O_3 nanowires by Ar+ sputtering for (c), 803seconds

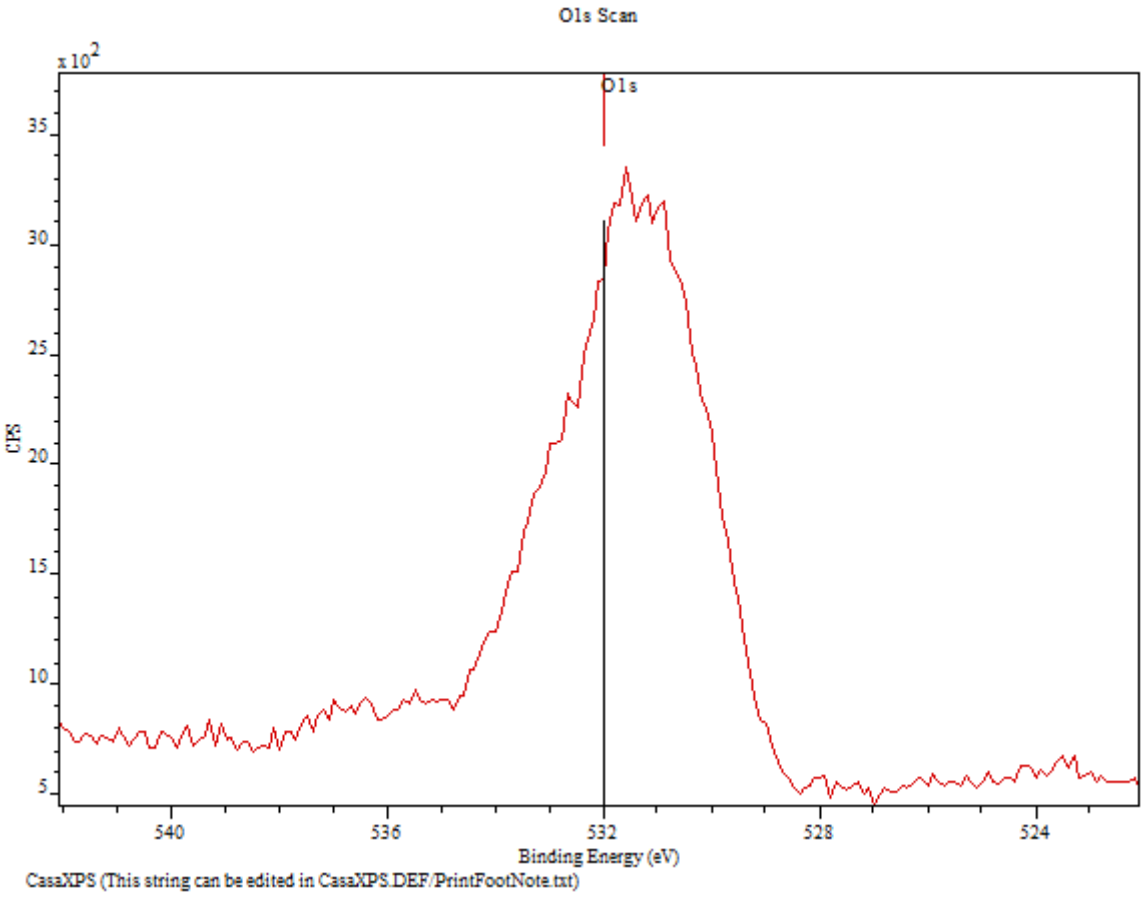


Figure 4.53d: XPS spectrum of O1s following etching of the HT-DNA/Fe_2O_3 nanowires by Ar+ sputtering for (d), 1204seconds

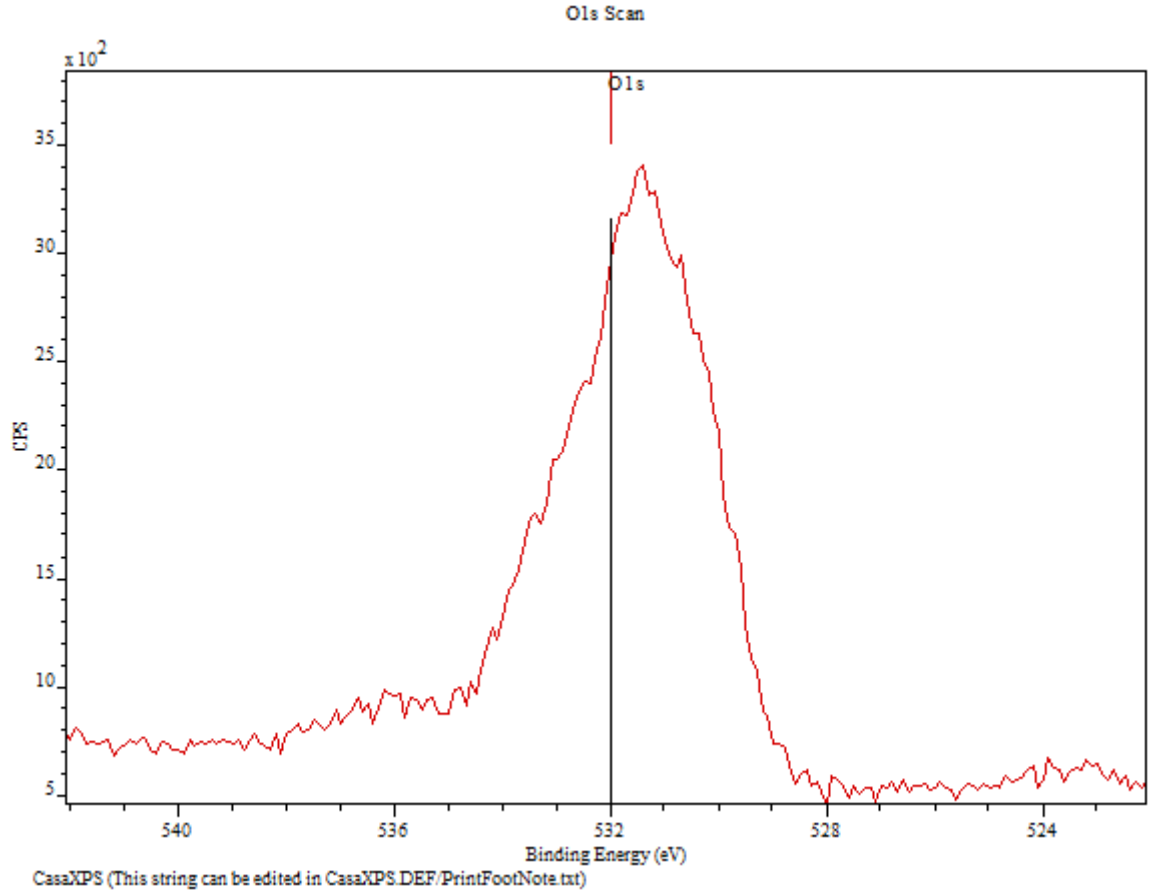


Figure 4.53e: XPS spectrum of O1s following etching of the HT-DNA/Fe_2O_3 nanowires by Ar+ sputtering for (e) 1606 seconds

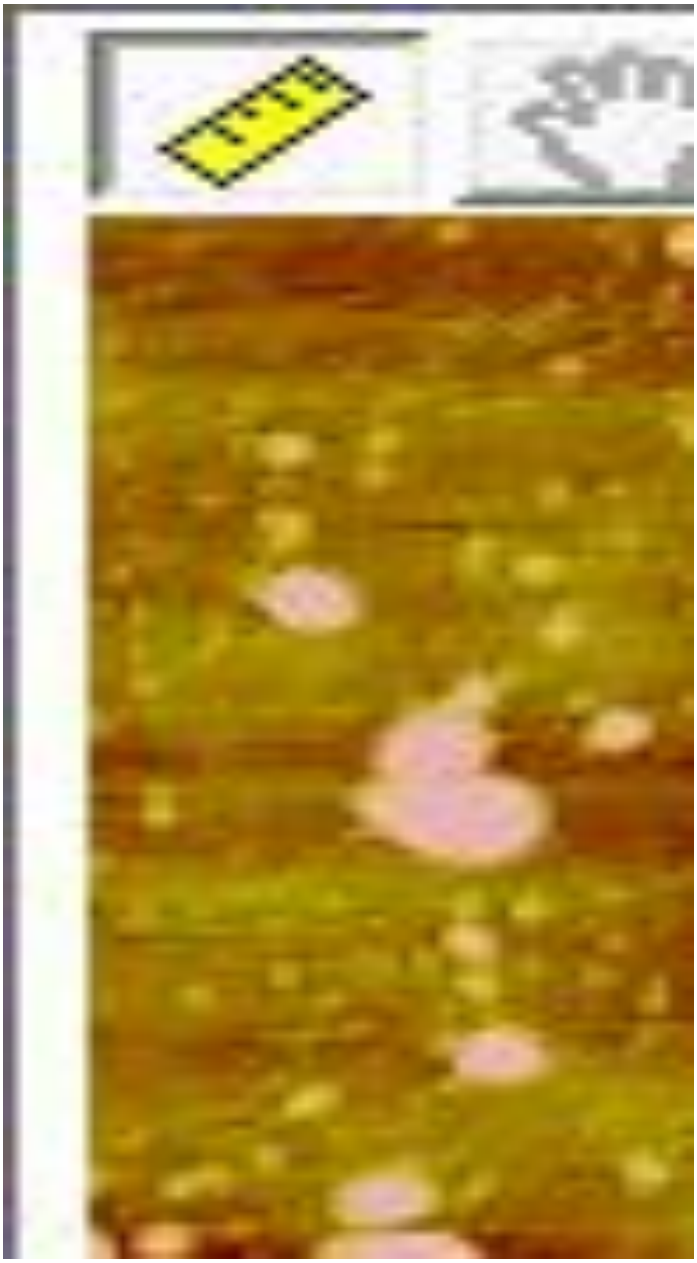


Figure 4.54: Tapping mode AFM image of bare λ-DNA nanowires (top). (Below) AFM image nanostructure with diameter as shown along the wire length and cross-section of measured diameter (right)



Figure 4.55: Tapping mode AFM image of bare λ-DNA nanowires (top) and cross-section of measured diameter (bottom)

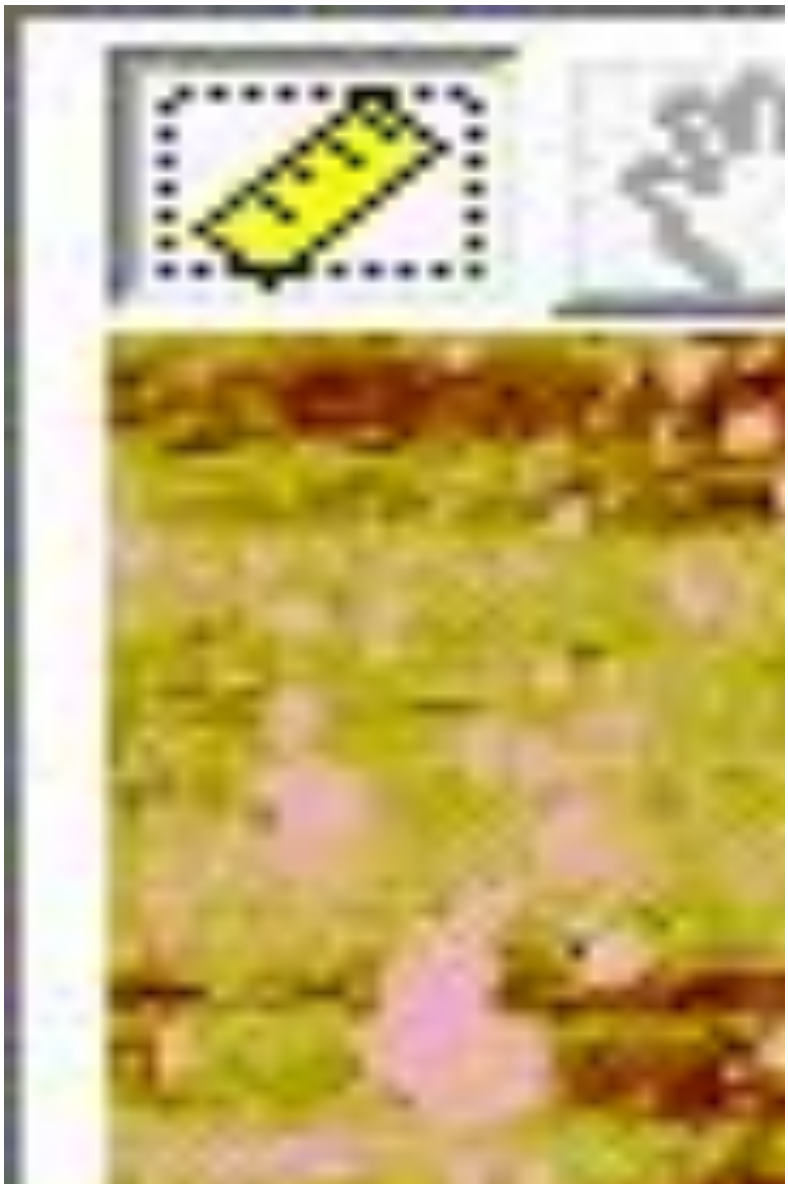


Figure 4.56: Tapping mode AFM image of bare λ-DNA nanowires (top). Cross-section of measured diameter (bottom)

Figure 4.57: Tapping mode AFM image of DNA/Ppy nanowires and histogram of measured diameters.

AFM images of DNA/Plmi with inset and size distributions of the nanowires as histogram are shown in Figure 4.58 and those of AFM images of DNA/FeOOH with inset and size distributions of the nanowires are shown in Figure 4.59. Likewise, AFM images of DNA/Fe_2O_3 with inset and size distributions of the nanowires are also shown in Figure 4.60.

Optical images of AFM cantilever positioned on the dried mass of the nanowire samples showing protrusion of wires from main deposits on CTMS-modified silicon substrate was shown in plate 4.1.

4.10EFM (Electrical studies)

EFM phase images of DNA/Ppy nanowires at different locations along the nanowire at bias voltage are shown in Figure 4.62.

Phase images as a function of applied voltages on DNA/Ppy nanowires at different diameters and table of phase shift (ΔØ) values at different applied potentials are shown in Figure 4.63.

EFM phase images of DNA/Plmi nanowires at different locations along the nanowire at bias voltage are shown in Figure 4.64.

Phase image of DNA/Plmi nanowires as a function of applied voltages at different diameter and table of phase shift (ΔØ) values at different applied potentials are shown in shown in Figure 4.65.

EFM phase images of DNA/Fe_2O_3 nanowires at different locations along the nanowires at bias voltage are illustrated in Figure 4.66.

Phase images of DNA/Fe_2O_3 nanowires as a function of applied voltages at different diameter and table of phase shift (ΔØ) values at different applied potentials are shown in Figure 4.67.

EFM phase images of DNA/FeOOH nanowires at different locations along the nanowire at bias voltage are shown in Figure 4.68.

Phase images of DNA/FeOOH nanowires as a function of applied voltages at different diameter and table of phase shift (ΔØ) values at different applied potentials are shown in Figure 4.69.



Figure 4.58:Tapping mode AFM image of DNA/PImi nanowires and histogram of measured diameters



Figure 4.59:Tapping mode AFM image of DNA/FeOOH nanowires and histogram of measured diameters. Inset: zoomed-in-region of the nanowire



Figure 4.60:Tapping mode AFM image of DNA/Fe_2O_3 nanowires and histogram of measured diameters. Inset: zoomed-in-region of the nanowire

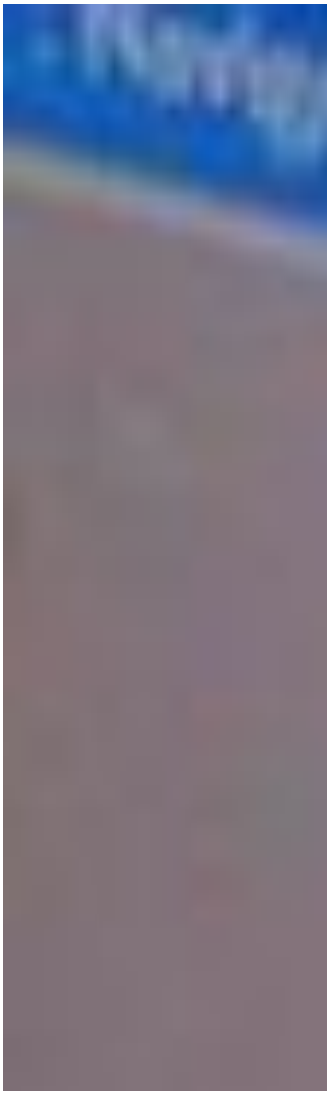


Plate4.1: Optical images of AFM cantilever positioned on protruding dried mass of all the DNA-templated nanowires taken at the edges of dense network before EFM probe measurements

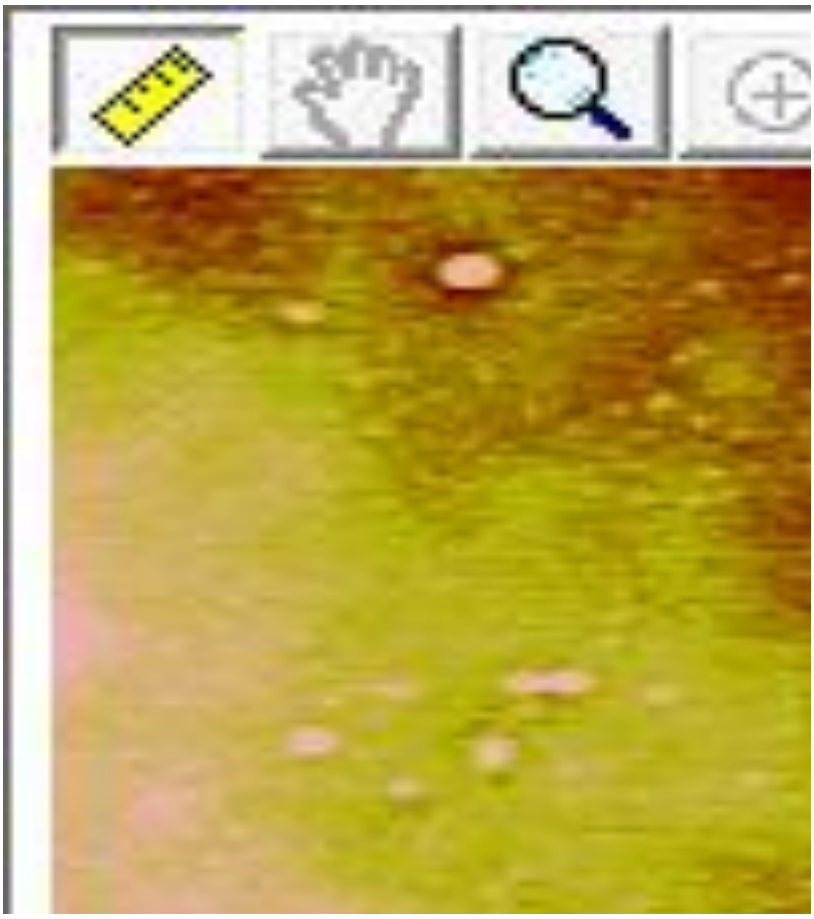


Figure 4.62:EFM phase images of same DNA/Ppy nanowires at different locations showing the phase angle of the tip oscillation as a function of tip/sample biases. (a). +7v, (b). +6 v, (c). +5 v, (d). +4 v, (e). +3 v and lift height of 50nm, scale bar 6.0µm

Figure 4.63:Corresponding phase shift as a function of applied voltage of DNA/Ppy nanowires at different diameters, at grey scale of 5.0^{0} and (down) table of phase shift values at different applied biases

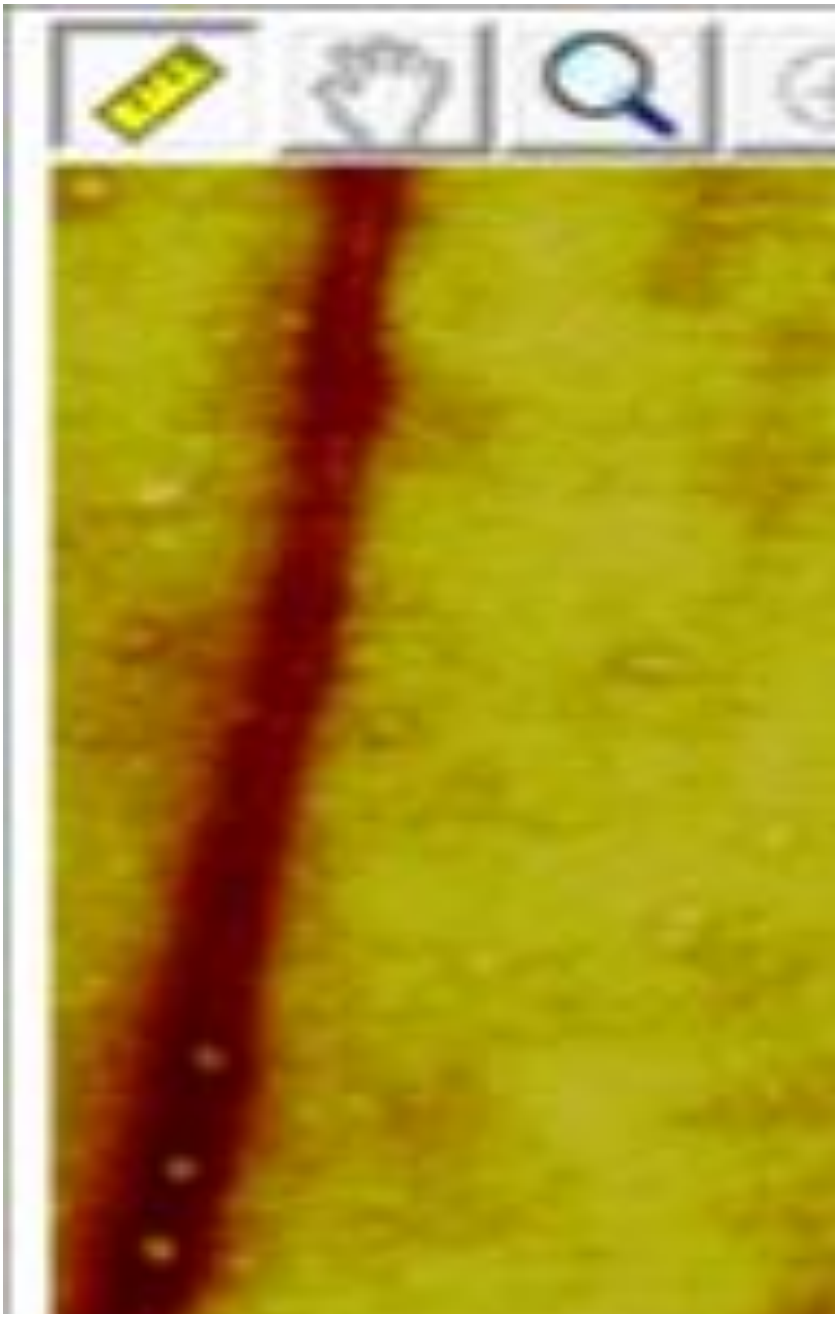


Figure 4.64: EFM phase images of same DNA/PImi nanowires at different locations showing the phase angle of the tip oscillation as a function of tip/sample biases. (a). + 5 v, (b). +4 v, (c). +3 v, (d). -3 v (e). -4 v, (f). -5 v and lift height of 50nm, scale bar 6.0µm

Figure 4.65:Corresponding phase shift as a function of applied voltage of DNA/PImi nanowires at different diameters, at grey scale of 5.0 ^{0}and (down) table of phase shift values at different applied biases

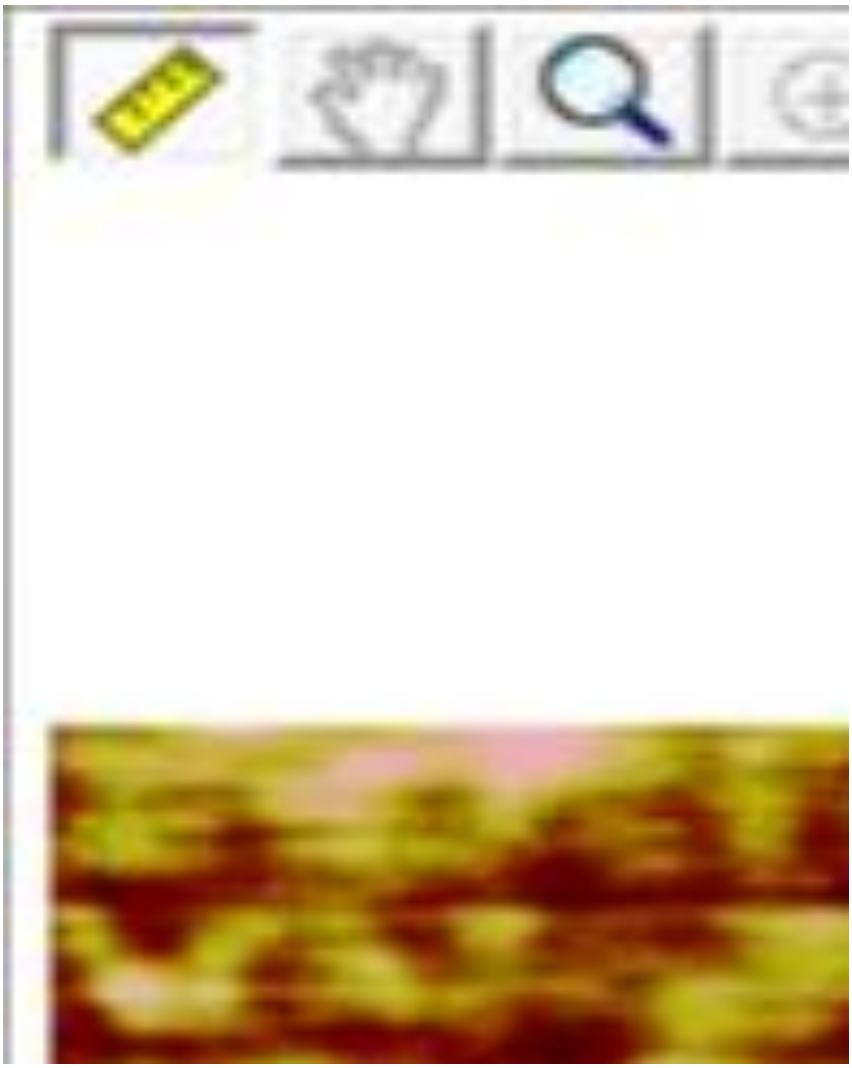


Figure 4.66:EFM phase images of same DNA/Fe_2O_3 nanowires at different locations showing the phase angle of the tip oscillation as a function of tip/sample biases. (a). -3 v, (b). -4 v, (c). -5 v, (d). -6 v (e). -7 v and lift height of 50nm, scale bar 6.0µm

Figure 4.67:Corresponding phase shift as a function of applied voltage of DNA/Fe_2O_3 nanowires at different diameters, at grey scale of 5.0^{0}

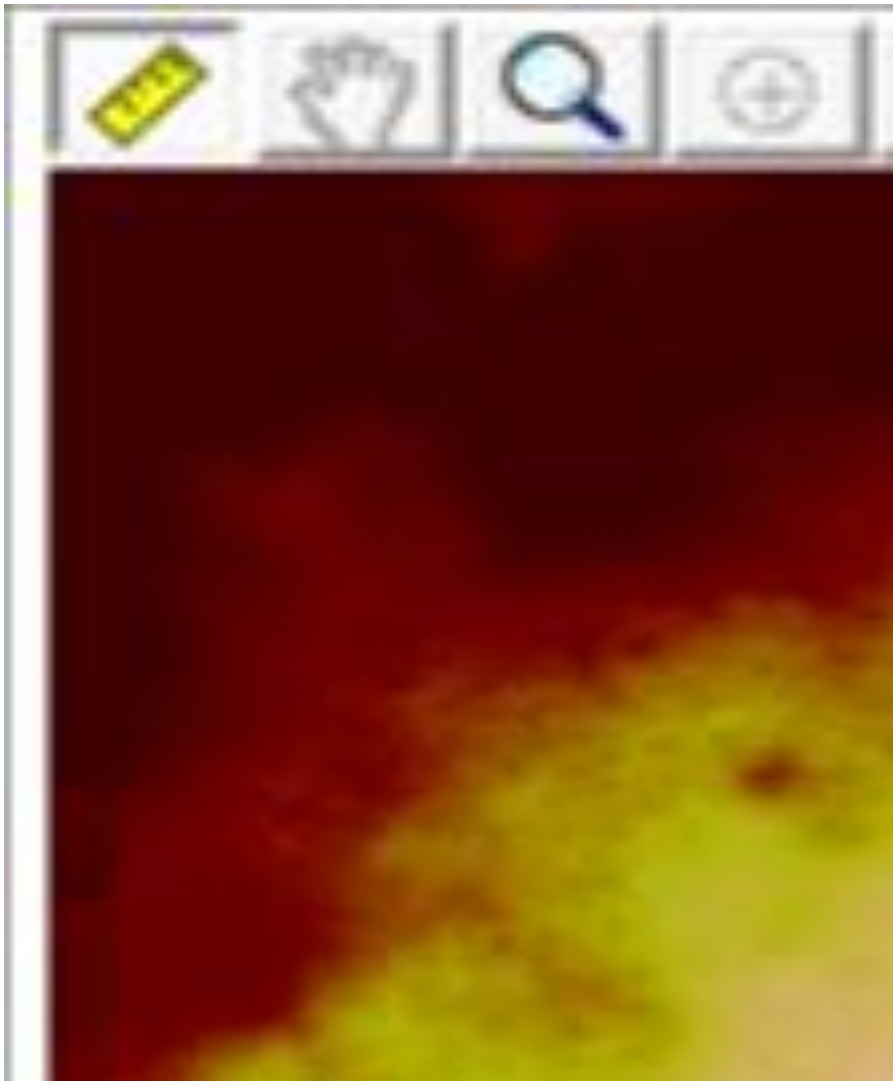


Figure 4.68:EFM phase images of same DNA/FeOOH nanowires at different location showing the phase angle of the tip oscillation as a function of tip/sample biases. (a). +7 v, (b). +6 v, (c). +5 v, (d). +4 v (e). +3 v, (f). +2 v and lift height of 50nm, scale bar 6.0µm.

.

Figure 4.69:Corresponding phase shift as a function of applied voltage of DNA/FeOOH nanowires at different diameters, at grey scale of 5.0^{0} and (down) table of phase shift values at different applied biases

CHAPTER FIVE

5.0 DISCUSSION

5.1Cyclic Voltammetric Studies

The typical voltammogram of Ppy thin film by CV measurements obtained for the polymer and their corresponding DNA-templated preparative electrode reaction mechanism are shown in Figure 4.1. The anodic peak is related to the oxidation of Ppy and the broad cathodic peak to reduction to the Ppy neutral form according to (scheme 3.1). Broad peak nucleation loop with anodic and cathodic peaks for the first four cycles and the first sixth of CV for pyrrole and DNA/Ppy respectively are shown in Figures 4.1 a and b. Pyrrole monomer oxidation (anodic peak) occurs at 0.5 V/Ag^+ and the reduction peak at about +0.0V/Ag^+. The loop indicates the formation of polypyrrole phases. On the reverse scan of the first cycle, the reduction (cathodic peak) occurs at 0.0 V, though the cyclic voltammogram shows one oxidation and reduction peaks. The peak currents for Figure 4.1 b remains constant during the potential scan indicating the occurrence of reversible reactions. Moreover, the anodic peak in same Figure 4.1 b almost shows a plateau with the decrease in the ΔE at reduction peak attributed to decreasing resistance of the DNA monolayers thus adhesion of Ppy to the surface. A distinctive feature of Ppy thin film in the case of anodic peak is the steep anodic wave with almost flat plateau with no peak observed at anodic scan and shift in potential with respect to cathodic wave at -0.2 V.

The same principle is applied to Figures 4.2 c and 4.2d for polyimidazole (PImi) polymerization and DNA/PImi with two defined anodic and cathodic peaks at -9.0 V/Ag^+, 0.0 V and -8.0 V/ Ag^+, +0.4 V/ Ag^+ respectively. This is followed by significant peak current decrease in both anodic and cathodic scans depicting the occurrence of reversible reactions inFigure 4.2. It can also be observed in Figure 4.2 (DNA/Plmi) that

almost flattened anodic peaks occur with decrease in ΔE (single reduction peak at +0.3 V) between polymer reductions at DNA interphase attributed to decreasing resistance of the DNA monolayers. The shapes of Figure 4.2(DNA/Plmi) toa first approximation show rectangular mirror image with symmetry between the anodic and cathodic processes depicting characteristic of capacitive behaviour indicative of excellent materials for electron storage.

5.2FT-IR Spectroscopy Studies

FTIR spectroscopy allows the interaction between the nanoparticles and the DNA to be probed. The spectra are shown in Figures 4.3 - 4.4and Table 4.1, with selected band assignments. Bare DNA and DNA/Ppy spectra are displayed in Figure 4.3with notable bands shift in peak position and intensity as a consequence of interaction between DNA and Ppy when compared with the corresponding bands in the bare DNA spectrum. At DNA/Ppy, the symmetric ($1087^{sh}cm^{-1}$) and asymmetric (1220 cm^{-1}) peaks for PO_2^-vibrations from DNA phosphate backbone are shifted to 1110^{sh} cm^{-1} and 1213 cm^{-1} in the templated material respectively, with broadened intensities. This is as a result of templating reaction indicating the interaction between nanoparticle materials and DNA nucleobases (Alex and Dupuis, 1989). In addition, a peak in $C\text{-}O_{st}$ deoxyribose (1055 cm^{-1}) shows a significant shift to higher frequency (1070 cm^{-1}).

Other changes were also observed in the DNA nucleobases region such as C-N stretches for guanine and cytosine bases at 1371 cm^{-1}, along with the ring vibration of G and C at1481 cm^{-1} are all shifted to higher frequencies at 1373 cm^{-1} and 1523 cm^{-1} respectively. Similarly, changes at other bands like C=O for thymine/cytosine at 1649 cm^{-1} along with the C=O stretches for guanine/thymine at 1681 cm^{-1} are also shifted to

1606 cm^{-1} low frequencies and 1689 cm^{-1} higher frequencies when compared to the bare DNA spectrum.

The broad band centred between 3000 and 3500 cm^{-1}on the templated sample is due to O-H stretches in the bare DNA and also contribution from N-H stretches in the DNA nucleobases is cited to have been reduced in intensity in the DNA/Ppy spectrum. The intensity loss may be induced by the interaction of Ppy due to displacement of some molecules that were bound to the DNA. Evidence that the DNA/Ppy is not just a mixture of Ppy and DNA as template but a hybrid material as a result of intense interaction between the template's acceptor group on the DNA and polymer that took place is shown in Figure 4.3.

Bare DNA and DNA/PImi as shown in Figure 4.4 for comparison with same scenario with Figure 4.3. The presence of PImi is evidenced by N-H stretch at 3334 cm^{-1} assigned to imidazole ring in the PImi units. The position is shifted and become more broadening at 3348 $cm^{-1}$with shoulder, and noted to increase in intensity in the DNA/PImi spectrum.

Presence of DNA in the DNA/PImi nanowires is further confirmed by bands in the region 1800-900 cm^{-1} with assigned features for both symmetric and asymmetric nucleobases vibrations and stretches evidence for phosphate backbone(Dovbeshko *etal*., 2000; Ouameur and Tajmir-Riahi 2004; Arakawat*etal*., 2000). To further confirm the possible interactions between polycation with phosphate backbone groups, strong bands at 1211 and 1062 cm^{-1} were assigned to asymmetric and symmetric stretching vibrations of PO_2^- groups in the spectrum of PImi/DNA respectively(Tailander *etal*., 1984)with decrease in intensity. Meanwhile,deoxyribose C-O stretching at 1010 cm^{-1} shows a change in intensity relative to bare DNA. Both PO_2^- asymmetric and symmetric stretch

vibrations were found to be shifted to lower frequencies (bathochromic shift) in the spectrum of PImi/DNA adducts. In addition, C-N stretch for guanine and cytosine bases at 1381 and 1467 cm^{-1} for cytosine/guanine ring vibrations also shifted bathochromically to 1352 and 1450 cm^{-1} respectively. Changes in other spectral bands of DNA at 1693^{sh} and 1652 cm^{-1} assigned to C=O stretches for guanine/thymine and cytosine/thymine were observed at 1658 and 1620 cm^{-1} respectively with pronounced shift to lower frequencies by several wavenumbers upon PImi addition (Figure 4.4). All these spectral changes reflect the interaction of PImi with oxygen atoms of the phosphate backbone, which indicate continuous cation interaction with carbonyl site and backbone PO_2^-group.

In the case of Figure 4.5 for both bare DNA and HT-DNA/Fe_2O_3, major broad bands at HT-DNA/Fe_2O_3 adduct were observed, in addition to evidences for sharp peaks for Fe^{3+}-O^{2-} vibration located at 580 and 615 cm^{-1} as an indication that pure phase of Fe_2O_3 exist in HT-DNA/Fe_2O_3. The sharp intense peak at 615 cm^{-1} demonstrates high degree of crystallinity of Fe_2O_3 nanoparticles. Other absorption bands within 1290-1000 cm^{-1} were used to establish possible interaction of nanoparticle with backbone phosphate groups as shown in Table 4.1. The asymmetric (1230 cm^{-1}) and symmetric stretching (1087 cm^{-1}) vibrations of the PO_2^- from bare DNA phosphate backbone show shift in frequencies as a result of nanoparticle interactions with asymmetric wavenumber increase →1278 and symmetric stretch wavenumber decrease 1064 cm^{-1}← with increase in intensity after templating reaction. In a similar manner, the P-O/C-O stretches as shoulder on the original bare DNA become broadened into PO_2^- broad band on DNA/Fe_2O_3 hybrid materials. C-N stretches for the cytosine, guanine, thymine and adenine bases (1296 cm^{-1}) with guanine and cytosine ring vibrations (1467 cm^{-1}) are all shifted to 1280 and 1436 cm^{-1} lower wavenumbers respectively. In a similar manner,

the prominent peak at 1676 cm^{-1} is specific to the carbonyl groups due to the C=O stretching vibration in the thymine and cytosine ring of the templated materials in intensity relative to bare DNA at 1562 cm^{-1} when compared.

Typical FTIR for DNA/FeOOH nanowire is displayed in Figure 4.6. The appearance of broad band at 3431 cm^{-1} is due to the O-H stretching vibration as well as contribution from N-H stretches in the DNA molecules. Vibrations associated with the PO_2^- symmetric stretches at 1114 cm^{-1} along with ring vibrations of guanine and cytosine within 1408- 1380 cm^{-1} are observed as broad with split band (1371 and 1406 cm^{-1}) for guanine and cytosine vibrations. The C-O deoxyribose stretching at 1055 cm^{-1} in the bare DNA was also observed to show relative significant shift to high frequency (1097 cm^{-1})in the templated materialwith reduced intensity. Furthermore, the nanoparticles itself shows vibrations at 738 and 825 cm^{-1} attributed to out-plane and in-plane Fe-O-H bending vibrations respectively. Band at 611 cm^{-1} are assigned to Fe-O stretching. Likewise, mode at 1539 cm^{-1} due to in-plane vibration of guanine and cytosine is shifted to lower frequency (1531 cm^{-1}) in the templated hybrid materials. All these spectral changes infer the interactions of the iron oxide nanoparticles with the DNA polyanionic nucleobases.

The sharp spectrum of bare DNA sample as control is shown in Figure 4.7. Bands observed in the region 1000- 1900 cm^{-1} confirmed the presence of DNA as template with characteristic absorption peaks summarized in table 4.2. The symmetric and asymmetric PO_2^-stretches at 1087 cm^{-1} and1230 cm^{-1} respectively, the deoxyribose C-O stretch at 1055 cm^{-1}, the P-O/C-O stretches at 1072 cm^{-1} of the phosphate backbone as shoulder and the carbonyl group due to C=0 stretch within 1640-1690 cm-1 are all shown in the DNA electron sites within the DNA(Eichhorn and Shin,1968). A shoulder

at 1296 cm^{-1} is also observed due to C-N stretches of the nitrogenous bases with the guanine/cytosine ring vibration at 1481 cm^{-1}.

FT-IR spectrum for pyrrole monomer before electrochemical synthesis (blue spectrum) and pure polypyrrole, (red spectrum) are all shown in Figure 4.8. Distinctive features of polypyrrole were observed with bands corresponding to symmetric and asymmetric aromatic ring stretching modes at 1558 (pyrrole ring $C=C_{st}$) and 1460 cm^{-1} (pyrrole ring vibrations) respectively. The peaks at 1300, 1024 and 1159 cm^{-1} are due to =C-H and N-H in-plane vibration and =C-H out-of-plane vibrations at 767 and 966 cm^{-1} for C-C out-of-plane ring deformation vibration are all observed in the spectrum. small peaks occurring below 600 cm^{-1} are due to stretches from the counter ions. Thus FTIR result confirmed the formation of polypyrrole and the presence of counter ions. All the peak selected are in accordance with the expected structure of polypyrrole nanoparticles(Kharat *etal*., 2007; Tian and Zerbi 2009).

Spectra for pure imidazole monomer (blue spectrum) and polyimidazole, PImi (red spectrum) are shown in Figure 4.9. The spectrum shows the presence of absorption band characteristic of polyimidazole consistent with N-N linkages between repeating imidazole units based on the absence of broad band at 2900-2500 cm^{-1}(Wang *etal*., 1994). These bands correspond to N-H stretching at (3658 cm^{-1}), C=N- stretching peak at 1473 cm^{-1} and other bands within 700-1700 cm^{-1}which are all characteristic of polyimidazole in term of ring stretching (ω) at 1473 and 1382 cm^{-1}, out-plane (δ) C-H bending at 813 cm^{-1} and in-plane C-H bending at 1072 and 1251 cm-1. The sharp peaks at 2980 and 2885 cm^{-1} are assigned to asymmetric and symmetric methylene ($–CH_2$ groups) stretching modes of C-H bonds respectively with the sharpness corresponding to the well-ordered chain of PImi.

The FTIR spectrum of neat FeOOH is very typical of intense absorption peak as shown in Figure 4.10at 3132 cm^{-1}, which is characteristic of FeO-OH bonds in terms of O-H stretching mode (Zhong *etal*., 2007; Tong *etal*., 2007). Appearance of small bands at 1789 and 1666 cm^{-1} are due to H-O-H bending vibration in the water molecules present in the FeOOH nanoparticles which are characteristic of FeOOH(Atkinson *etal*., 1974). The presence of sharpstrong intense peaks at 891, 786 and 617 cm^{-1} are all ascribed to in-plane and out-of-plane Fe-O-H bending vibrations and Fe-O stretching vibration respectively, indicating the presence of α-FeOOH crystallographic phases(Deki *etal*., 1997; Liang *et al*., 2011). Typical bands at 894 and 786 $cm^{-1}$are for Fe-O-H bending vibrations and at 617 cm^{-1} with a shoulder at 540 $cm^{-1}$are for Fe-O stretching vibration in FeOOH(Krehula *etal*., 2002).

Representative FTIR spectrum of Fe_2O_3 nanoparticles is also shown in Fig. 4.11. Presence of O-H stretching vibrationsoccurred at 3124 cm^{-1} indicating OH from adsorbed water. Other peaks at 895, 795, and 632 cm^{-1} are all characteristic of α-Fe_2O_3 and are in good agreement with the standard spectrum of Fe_2O_3 (Nyquist and Kagel 1971) representing Fe-O vibrational modes in Fe_2O_3.

5.3UV–vis Spectra of net DNA and its Templated Materials

UV-vis spectroscopy was used to monitor the binding ability, if any, of DNA strands with each of the nanoparticles. The UV absorption bands were observed in the region 200-600 nm. Characteristic absorption spectra for net HT-DNA and its analogues at room temperature are shown in Figures 4.12 to 4.16.Evolution of absorption distinct band at 259.5 nm is associated with λ_{max} signature absorption peak of DNA molecules.

Changes in the UV-vis spectrum at 259.5 nm on addition of various nanoparticles are observed with spectroscopic measure of what have happened as

nanoparticles were assemble on DNA as shown in Figure 4.12 – 4.16. Plasmon bands shift were all observed at 259 nm with extinction drop at λ_{max} significantly as the assembly takes place primarily due to aggregate density effect. Depending on the extent of aggregates generated on DNA template-induced assembly periodicity, the spectroscopic signal decrease in intensity.

5.4 TG/DTA/DSC Measurements

Thermal decomposition temperature and stabilities of the different nanostructured iron oxides obtained by TGA/DTA/DSC measurements are shown in Figures 4.17 – 4.20. Thermal gravimetric analysis (TGA) for FeOOH is shown in Figure 4.17 indicating clear mass loss of about -15 %, which is larger than the theoretical stoichiometric value of (10.13 %) indicating about 5% adsorbed water was present in the FeOOH. In addition, slight weight loss below 100^{o}C is attributed to physically adsorbed water and for Fe_2O_3nanoparticles at -5.62 % as shown in Figure 4.19. On the same Figure 4.17pattern,is the first derivative of the weight loss curve. The first two derivative peaks observed at 270 and 358^{o}Care attributed to transformation (crystallisation process) and/or decomposition of FeOOH precursors into another phase. These first two derivative peak also known as point of inflection indicates the point of greatest rate of changes on the weight loss curve. Accordingly, 400^{o}C was selected as the decomposition temperature for FeOOH to obtain Fe_2O_3 phases. However, Figure. 4.19 only showone peak for Fe_2O_3 at 300^{o}C corresponding to crystallisation of Fe_2O_3. Above 300^{o}C, weight loss no longer changes, indicating the stable residue ascribed to Fe_2O_3 phases which can be confirmed by XRD patterns later.

The DSC curves werealso carried out to identify thermal transitions in the FeOOH and Fe_2O_3phases as shown in Figures 4.18 and 4.20 respectively. Curve for FeOOH in Figure 4.18 shows endothermic peak at 66^{o}C due to the removal of water

molecules present in FeOOH nanoparticles. The second major endothermic peak at 265^{o}C aside other two small endothermic peaks within 200-250 ^{o}C indicates the removal of other low molecular weights such as solvent adsorbed on FeOOH. The exothermic decomposition peak at 354^{o}C corresponds to the TGA extrapolated final phase transition to new component.

The DSC curve for Fe_2O_3 is shown in Figure 4.20 with major endothermic peak at 300^{o}C and final endothermic peak at 369^{o}C corresponding to the onset temperature of 358^{0}C to the final stable crystalline nanoparticles of Fe_2O_3 phases as the sample decomposes.

5.5 X-ray Diffraction Patterns

XRD analysis determine the phases, crystallinity and purity of the materials under study. Figures 4.21 (a) and (b),respectively show X-ray diffraction (XRD) patterns of pure precursor FeOOH and HT-DNA/FeOOH. The XRD patterns of crystallized FeOOH nanoparticles correspond to that of pure α-FeOOH as shown in Figure 4.21 (a) with characteristic peaks indexed by lattice parameter values and assigned to the orthorhombic phase of α-FeOOH which match well with the previously reported value (JCPDS Card No. 29-0713). The sharp diffraction peak observed indicates highly crystalline nature of FeOOH with the broadening in the reflection peaks due to the particle size at nano domain. The nanoparticles were free from commonly found secondary additional phases, such Fe_3O_4 and Fe_2O_3 or γ-FeOOH. The average crystallite size of the pure FeOOH nanoparticles was calculated as 13 nm using the Debye-Scherrer's formula.

The XRD patterns for dried sample of HT-DNA/FeOOH nanowiresare shown in Figure 4.21 b. The spectrum contains four peaks indexed to FeOOH corresponding to (110), (021), (111), (240) crystal planes of crystalline FeOOH. Aside the amorphous

nature of the materials, the peak are broad and weak due to the effect of small ultrafine crystallite size. Line broadening of the diffraction peak (110) was used to determine the average crystallite size, still applying Scherrer's equation was found to be ~ 8.5 nm.

XRD patterns for neat Fe_2O_3thermally treated and its corresponding HT-DNA/Fe_2O_3 nanowires are also shown in Figure 4.22. All the peaks for Fig. 4.6.1 (a) at 2θ = 24.13 (012), 33.14 (104), 35.64 (110), 40.84 (113), 49.44 (024), 54.07 (116) and 54.73 (018) indexed areis in good agreement withthe hexagonal phaseof the previously reported data (JCPDS card No 76-1821) and (JCPDS card No 33-0664) depicting the thermal product was high-purity of α-Fe_2O_3. Particularly, the diffraction peak at (104) is more intense than the (110) peak indicating the latter face to be more prominent on the surfaces of the Fe_2O_3 crystals. Estimation of the crystallite size from peak broadening (104), gives an average value of 16 nm. However, the Raman spectroscopy can easily differentiate the structural phases of the two iron oxides. Fe_2O_3 main bands occur within 220-500 and at 609 cm^{-1}(Wang *etal*., 2008) which confirmed the presence of Fe_2O_3, whereas FeOOH shows bands around 366 and 682 $cm^{-1}$to discriminate FeOOH. Insets in Figures 4.21 and 4.22illustrate the Raman spectra for the two nanoparticles.

The X-ray diffractogramm for HT-DNA/Fe_2O_3 isshown in Figure 4.22.The diffractogramm is typical of an amorphous materials with characteristic [104] crystal plane of crystalline Fe_2O_3 showing presence of the materials on the HT-DNA.

The XRD patterns for Ppy shown in Figure 4.23 reveal that the resulting Ppy was amorphous (Partch, *etal*., 1991)with broad band in the region $24^o \leq 2\theta \leq 30$ revealing a short range chain arrangement dominate the polymer materials as well as scattering from Ppy chains at the interplanar spacing. The average crystallite size from

the peak at 26.8^{o} was estimated using Scherrer equation as ~30 nm for ppy nanoparticle. However, the HT-DNA/ppy was unavoidably not available.

The final XRD spectra for pure PImi and HT-DNA/PImi. Figure 4.24. PImi (top) depict less intense peaks with amorphous characteristic in the presence of DNA range 31^{o} □ 2θ□ 37^{o}.

5.6 Transmission Electron Microscopy (TEM) and EDX Studies

Shape and size of the nanoparticle generated were checked by TEM as shown in Figures. 4.25 –4.32 at low and high magnifications. TEM images of FeOOH nanoparticles with clear uniform rodlike morphology, polycrystalline nature and smooth surface with sharp edges were evident in Figure 4.25. Some of the nanoparticles aggregated into bundles probably due to the high surface energy of the precursor nanoparticles. The length ranged from 400 to 600 nm and the diameter was between 20 and 30 nm with an average size of 18 nm. The particle size from TEM images was larger than that calculated from XRD, indicating the as-prepared particles are polycrystalline.However, Figures. 4.26 shows the growth of the nanoparticles on DNA with wire-like branched agglomeration nature of the HT-DNA/FeOOH nanowires with length 1-2 μm and width of ~ 4.5 nm with submicrometer size observed. The TEM images clearly show the DNA capacity encapsulating the precursor with a thickness of about 20 nm far larger than the diameter of the DNA (∼2 nm) showing the selective deposition of FeOOH on DNA. The corresponding detailed examination of the TEM by selected area electron diffraction pattern of a single crystal nature isshown as inset in Figure 4.26.The diffraction ringsindicate that the nanoparticles are highly crystallized from a number of crystalline orientations, which can readily be indexed as (240), (121), (140), (111), (021) from the outer ring up to the rhombohedral crystal structure

confirming the FeOOH crystalline phase on the DNA. Dark-field and bright-field STEM micrograph of the HT-DNA/FeOOH are also shown as inset inFigure 4.26. The structures present particles density within the morphology as dark spots proportional to the number of atoms present though the dark-field STEM more persuasive than the bright-field STEM.

The results obtained from energy dispersive X-ray spectroscopy (EDX) gave the chemical composition of the nanostructure material as shown in Figure 4.33. From the spectrum, copper, carbon, nitrogen, phosphorus, oxygen and iron were observed. The Fe and O peaks came from the Fe and O on the nanowires and the nitrogen, phosphorus peaks from the DNA. The Cu peaks (the last two peaks from right hand side) came from the carbon coated copper grid.

The size and micro-morphology of the Fe_2O_3 and HT-DNA/Fe_2O_3 are shown in Figures 4.27 and 4.28respectively in different magnifications.The Fe_2O_3nanoparticles depictsmooth rod-like morphology with some aggregated into bundles and shorter singles due to nanoparticle crystallization domains as shown in Figure 4.27. It is evident from TEM micrographs that the nanoparticles width/diameter of about 25-31 nm with length range of 100-200 nm were estimated. The resulting morphology of the HT-DNA/$Fe_2O_3$is dendritic showingdiameter and length of a few micrometres as shown in Figure 4.28. The structure possess the rigid/linear structure of DNA though densely covered with Fe_2O_3 nanoparticles on the templates. Bright-field and dark-field STEM micrographs of the HT-DNA/Fe_2O_3 are also shown as inset in Figure 4.28. Tube structures could be clearly seen in the dark-field STEM while the bright-field STEM image present particles density within the morphology as dark spots proportional to the number of atoms present.

The EDX studies with TEM analysis shown in Figure 4.33 verified the major components as iron, phosphorus, oxygen, carbon with Cu, Cr and Co signals from the carbon-coated copper grid and sample holder used for TEM while the C peak comes from the DNA and as well as TEM grid.

As shown in Figures 4.29 (aandb) for Ppy and its analogues HT-DNA/ppy, the powder Ppy nanoparticles consists of uniformly distributed spherical nanoparticles with mean diameter of about ~35 nm which is larger than the calculated 30 nm from XRD value. This indicates the presence of some polycrystalline nanostructures on the materials. The typical TEM images of the resulting HT-DNA/ppy nanowire and their morphologies from two different points on the copper grid are shown in Figure 4.30 (b and c). As can be seen, continuous uniform wire-like appearance containing nanoparticles as beads-on-a-string morphology on the DNA length with diameter of the nanowire as ~9.5 nm and length on the order of micrometre. The deposition of nanoparticles is clearly seen from the HT-DNA/ppy nanostructure with evident of separate particles packed along the DNA.

TEM images for Plmi nanoparticles and HT-DNA/PImi nanowires arealso shown in Figures 4.31 and 4.32 respectively. TEM micrographs of PImi nanoparticles showpolydisperse with agglomerated nanoparticles. The crystallite size observed on the TEM images in accordance with Scherrer equation is ~ 28 nm. Evidence for the assembly process actually comes from the TEM study of HT-DNA/PImi nanowires as depicted in Figure 4.32 with PImi nanoparticles on the DNA with an average uniform diameter of 24 nm.

5.7 X-ray Photoelectron Spectroscopy (XPS) Measurements

XPS survey spectrum of FeOOH thin film as shown in Figure 4.34shows peaks from the components on the precursor. The Fe2p, 3s, 3p and 3d and O1s are all attributed to the

precursor components. The Fe2p signal from FeOOH as shown in Figure 4.35 a shows doublet with binding energies of 711.3 eV for $2p_{3/2}$ and 724.8 eV for $2p_{1/2}$ in addition to broad satellite peakat ~719.7 eV which is a characteristic of Fe^{3+} species present in in FeOOH that distinguishes the absence of Fe^{2+} (Teng and Yang 2004). The binding energy of Fe3p core level was also identified at 55.2 eV. These finding indicates that the precursor is iron materials present in FeOOH phases. O 1s spectrum from Figure 4.35 bshows two distinct peaks ascribed to O 1s at 529.9 eV and 531 eV with the smaller peak assigned to oxygen present in the FeOOH. This is in good agreement with the previously reported value (Fujii *etal*., 1999). The higher binding value (531 eV) is due to oxygen from SiO_2 that serves as substrate (Miller and Linton 1985). Other peaks were identified arising from Na 1s, CI 2p and C 1s as shown as atoms concentration atthe edge of Figure 4.34 survey spectrum, whichmay likely be due to NaOH as precipitant, carbon from sample exposure before analysis and CI 2p from $Fe(NO_3)_3$ as staring material or anionic charges.

Evidences for the existence of interactions between FeOOH nanoparticles and DNA backbone is shown in Figure 4.36. The survey spectrum displays peaks arising from the four principal elements in DNA (P (p 2p), C (C1s), O (O1s), and N (N 1s) along with Fe (Fe 2p) and O (O1s) which are all present in the survey spectrum. The presence of N and P is an indicationfor DNA because their presence is not affected by sample preparation and handling(Herne and Tarlov 1997).

Evolution of N 1s core level peak with binding energies at 407.9 and 399.0 eV shows that N exist in two states, one at lower binding energy (399.0 eV) being N ascribed to $2p^2$ bonded atoms in the DNA nucleobases base rings and the other N at higher binding energy for sp^3ascribed to bonded N atoms present in the amino group (NH_2) (Howell *etal*., 2011; Villar *etal*., 2008;Lee *etal*., 2006) as shown in Figure 4.37b. Other clear

evidence for DNA presence in the nanostructure is obtained from the P 2p peaks at 133.3 and 134.5 eV for P $2p_{3/2}$ and $P2p_{1/2}$respectively are ascribed to phosphorus in the phosphodiester backbone in the DNA (Howell *etal*., 2011; Villar *etal*., 2008 ; Lee *etal*., 2006; Petrovykh *etal*., 2004).

O 1s inspection as presented in Figure 4.37 c shows peaks at 532 and 531 eV with lower binding energy assigned to the oxygen atoms on the sugar and nucleobases of the DNA. The other are higher core level binding energy peak, which is a contribution from water oxygen adsorbed on the nanostructure(Li and Zhang, 2007). The existence of O^{2-}, OH^{-} and H_2O are normally observed in the iron oxyhydroxides(Grosvenor *etal*., 2004).

The presence of Fe 2p spectrum was also indicated from its core level with evidence of satellite peak at 719 eV for Fe^{3+} species, in addition to Fe $2p_{½}$ at 725.5 eV and Fe $2p_{3/2}$ at 711.5 eVas shown in Figure 4.37 d. The C 1s high resolution spectrum asshown in Figure 4.9.1 e shows most intense peak at 284.9 eV originated from pure DNA spectra, although the peak at 284.4 eV was previously reported(Lee *etal*., 2006).

XPS survey scan for Fe_2O_3thin film is also shown in Figure 4.38. No Si peak was observed which shows that the thin film prepared completely covered the Si surface. The Na, CI and C signals were confirmed and CI in particular from $MgCI_2$ used during the templating.The Fe 2p peaksas shown in Figure 4.9.2 and observed for Fe $2p_{½}$ at 724.8 and Fe $_{3/2}$ at 711.2 eV coincided with the reported binding energy for Fe 2p from α-Fe_2O_3nanoparticles with satellite peak at 719 eV(Wagner *etal*., 1978). The presence of oxygen in two states in the Fe_2O_3 nanoparticles are shown in Figure 4.39 b with the lower peak at 530 eV likely due to O^{2-} in the iron oxide lattice. While the second peak at 531.4 eV is shifted by about 1.4 eV to higher binding energy is ascribed to OH or adsorbed oxygen (Kawade *etal*., 2000). Thus, Fe_2O_3 phase formation was confirmed.

The wide-survey scan for HT-DNA/Fe_2O_3nanowires is displayed in Figure 4.40with some residues in the nanostructure as Na 1sand CI 2p and predominant presence of phosphorus, nitrogen, oxygen, carbon and iron. The Fe 2p spectrum at 711.2 eV for Fe $2p_{3/2}$ and 724.9 eV for Fe $2p_{½}$is shown in Figure 4.41 d with a satellite peak at 719 eV, which is a characteristic of Fe^{3+} in Fe_2O_3 nanoparticles. No Zero-valent Fe and Fe^{2+} components are observed. However, binding energy and line-shape of Fe 2p agrees well with the reported value for Fe_2O_3(Mcintyne and Zetara,1977).

The existence of P 2p binding energy shown in (Figure 4.41a) at 133.6 eV for p $2p_{3/2}$ and 133 eV for $2p_{½}$ indicate that the two states for P arose from DNA backbone. Inspecting N 1s signal as another indicator for DNA in the nanowire as shown in Figure 4.41b is consistence with the two components binding energies at 400.4 and 399.7 eV with the lower binding energy and low intensity consistence with sp^2-bonded N atoms and the more higher intense binding energy assigned to sp^3-bounded N atoms in the -NH_2 group of DNA as previously indicated.

Further confirmation of the presence of O is obtained from the O 1s signal as shown in Figure 4.41c,which reveals two distinct peaks at 530.9 and 531.4 eV with the lower binding energy with a shoulder assigned to the contribution present in the DNA and Fe_2O_3. The C 1s signal as inset appeared due to DNA and by-product from organic contaminants.

XPS wide scan and high resolution spectra of Ppy thin film as shown in Figure 4.42 were recorded for Ppy thin film deposited on Si substrate. The signals that correspond to C 1s at 285 eV is assigned to C-C and N 1s at 399.8 eV) assigned to N-C (Webel, *etal*., 2006) with atom concentration of 67.27 and 11.86 % respectivelyas shown as inset in Figure 4.43. Strong reduction of Cl 1s and Fe 2p as oxidant signals from the starting materials as shown in Figure 4.42 was also observed. There was also a significant

incorporation of O 1s signal. However, it is likely that O moieties occurred upon sample exposure to air, thus indicating a concomitant increase in the peak intensity at 532 eV.

The XPS survey spectrum for HT-DNA/Ppy as illustrated in Figure 4.44with all the major atom componentsand their binding energy. The positions of $P2p_{1/2}$ and P $2p_{3/2}$ signalsat 134.4) and 133.6 eV, respectively, are consistent with the usual binding energyascribed to phosphorus in the phosphodiester backbone in the DNA as previously reported. Two main signatures are observed for N 1s spectrum of the HT-DNA/Ppy survey as shown in Figure 4.45b at 400 and 407 eV. These are also in consistent with the previous stated i.e. the contribution at 400 eV is typical of N atoms in the pyrimidine of DNA (Lee *etal*., 2006). The higher peak at 407 eV could be assigned to Ppy alone which is attributed to NH^+ (polaron) and $=NH^+$ (bipolaron) originally assigned to positively charged N atom associated with the charge carrier in Ppy(Carquigny *etal*., 2009). Characteristic photoelectron peaks for Fe $2p_{3/2}$ and Fe 2p½ (used as $FeCI_3$ to drive polymerization) though at a very low atoms concentration are also present as shown in Figure 4.44. The signals that correspond to C1s at 284.9 eV with a shoulder at ~286.5and O 1s at 532 eV are shown in Fig. 4.45(d and c). The C 1s was assigned to C=C from previous work at 284.6 eV, and C=0 at 286.2 eV (Webel *et al*., 2006). The O 1s spectrum shown in Figure 4.45 c shows the presence of two peaks. After fitting, (not shown), at 532.3 and 531 eV, these peaks is attributed to the presence of oxygen in the DNA and the polymer nanoparticles.

The PImi thin film elemental survey spectrum is shown in Figure 4.46. As usual, the N1s and C 1s were detected at 400.9,399.8 eV and 285 eV with four shoulders respectively which indicated that all these are present in PImi. The carbon and nitrogen atomspercentage concentration are~56 % and 13 % respectively. The N 1s peaks resolved into two peaks corresponding to N=C and N-C indicating the presence of

nitrogen atoms with two different binding energies as shown in Figure 4.47. Contribution from Fe2p core level was also detected.

The wide scan XPS spectrum recorded from HT-DNA/PImi is shown in Figure 4.48 along with the expected O 1s, P2p, N 1s, and C 1s as elemental contributions in addition to Fe 2p and Fe 3p are also indicated. The peak corresponding to P $2p_{1/2}$ and$_{3/2}$ core levels for DNA at 134 and 133.6 eV shown inFigure 4.49aare also indicated respectively, still ascribed to phosphorus in the phosphodiester backbone in the DNA.

N 1s core level peak with binding energies of 401, 400 and 399.0 eV as illustrated in Figure 4.49(b) shows that N have three peaks. The peaks correspond to N-C=O, N=C and N-C as indicated previously. All these represent the presence of N atoms with the three different binding energies. The O 1s spectrum of HT-DNA/PImi nanowires shown in Figure 4.49 (c) reveals two peaks located at 530 and 531 eV, corresponding to nucleobases of the DNA consistent with the previous reports where DNA has an O 1s peak at 532 and 531 eV. Likewise, C 1s major signal in XPS spectrum correspond to C1s (285.3 eV as C-C) with shoulders resolved into four detailed functionalities at C-N (285.7 eV), C-O (286.8 eV), C=O (287.3 eV), C=O (287.8 eV) and C=N (288.7 eV) (Kim *etal*., 2012).

Few Evidences from Fe 2p as $FeCI_3$ and Mg 1s show peak around 730.710 eV due to trivalentFe compounds with characteristic satellite peak on the spectrum.

Series of depth profile XPS spectra were shown in Figures 4.50 -4.53from Fe 2p and O 1s of the two semiconductor nanowires following sample etching by Ar^+ sputtering for a certain period of time. Fe 2p scan from HT-DNA/FeOOH nanowire depicted in Figure 4.50 (a-e) following sputtering for 0, 402s, 803s, 1204s, and ~1606s respectively. Upon etching, Fe $2p_{1/2}$ and Fe $2p_{3/2}$ at 711 & 724 eV with their corresponding little satellite peaks increases in intensity and become constant at 1204

and 1606 s at etching time. The doublet binding energy is consistent with Fe^{3+}core levels which confirmed that the core of the nanowires structure contain trivalent Fe. Further evidence of depth profiling was extended to O 1s as shown in Figure 4.51 (a-e) which appears as doublet at 533 and 531 eV assigned to oxygen atoms present in the sugar and nuleobases units of DNA with increase intensity as a function of etching time, though contribution from silicon wafer as substrate to the O 1s core level signals may not be rule out completely.

However, same depth profile analyses was also applied to HT-DNA/Fe_2O_3 nanowires as shown in Figure 4.52 and 4.53 for Fe 2p and O 1s respectively. Doublet binding energies for Fe^{3+} at 711.5 and 724.5 eV with pronounced satellite peak at 719 eV were observed with small increase intensity as a function of etching time, confirming the core of the HT-DNA/Fe_2O_3 structure comprised of trivalent Fe. For O 1s depth profiling as shown in Figure 4.53. The appearance of single signal with binding energy at 531 eV all through the etching time with shoulders were also located relative to nuleobases unit of the DNA. However, intensity of the core level O 1s remains constant as a function of etching time.

5.8 Atomic Force Microscopy (AFM) Studies

As previously indicated, AFM was used to probe height or diameter, structure and morphology of the aligned nanowire formed by molecular combing. Illustrated in Figure 4.54 is AFM image of bare DNA that serves as template onto which anisotropic growth of the nanoparticles took place. The morphology of the bare DNA appears regular, uniform and distinct wire-like appearance of individual strand with little variation in diameter ~ 2.2 nm along the strand as specified in Figure 4.54 with background deposits of buffer salts. The apparent average height of the bare DNA

molecule as depicted by cross-section (inset in Figure 4.54) is a little much larger than the standard DNA diameter of 2 nm, primarily due to the convulsion effect of the blunt AFM tip. The observed heights along the segment agrees well with double stranded lambda DNA and earlier AFM studies.

The same applies to Figure 4.55on different set of bare nanowire with average apparent diameter of ~ 2 nm with corresponding cross-section, and Figure 4.56 for the last estimated diameter of the last set of bare DNA nanowire as ~1.7 nm with the cross-section of the widths.

After polymerization of Pyrrolemonomer on bare DNA for the formation of DNA/ppy nanowires as shown in Figure 4.57, an organized network was observed and the height image showed a 1D nanostructure. The images reveal greater variation in structural height indicating deposition of Ppy nanoparticles along the strand of the DNA molecule. Close inspection of the DNA/Ppy nanowires shows beads-on-a-string appearance with Ppy nanoparticles packed along the length of the DNA template after an hour reaction incubation times with few Ppy deposits on the background.

Size distribution of the average diameter of the DNA/Ppy were plotted with frequencies as a function of nanowire diameter. The resulting histogram shows a broad size distribution with structure ranging from 6 to 33 nm in height as shownin Figure 4.57 with several modal values of 10, 19 and 32 nm identified, respectively, thus polymodal distributions.The AFM line profiles indicated that the nanowire diameters are not consistent along their length as depicted by the histogram. Nanostructure with diameter less than 2 nm are likely to be bare DNA molecules though not identified from the histogram, but thicker structure greater than 2 nm are DNA Ppy templated nanowires.

AFM images illustrating DNA/PImi nanowires is shown in Figure 4.58which depict evolution of continuous smooth thicker morphology (as shown as inset) with no

evidence of breakages as well as some nanowires on the background as bare DNA indicating that not all the DNA molecules are involved in the templating strategy. This result suggests the feasibility of creating DNA/PImi nanowires with diameter >6 nm. It also showed significant height increase observed along the length of the DNA molecule with substantial number of PImi nanoparticles on the DNA molecules. Overall, thicker nanowires morphology is evident relative to the DNA itself ≤ 2.0 nm, indicating that the PImi nanoparticles successfully deposited on DNA through a series of nucleation and growth mechanism on the DNA template.

Evaluating the size distribution of the nanostructure via statistical analysis of the average diameter was applied. The histogram of the nanowire diameter as shown in Figure 4.58 shows narrow size distribution (7-28 nm) with modal values between 9 and 26 nm identified from the plot.The histogram displayed the nanowire diameter to be relatively consistent along the length with little variation in diameter. The histogram shows diameter with minimum value of 7 nm indicating that a sizeable number of DNA molecules are actually involved in the templating reaction.

AFM height images of typical DNA/FeOOH nanowire with different packing density of FeOOH nanoparticles along the length of the DNAis shown in Figure 4.59. The images display granular irregular structure of the FeOOH nanoparticles deposited with supporting evidence of beads-in-a-string along the DNA molecule (zoomed-in region) as inset with variation in diameter ranging from 3 to 19 nm. Very high surface roughness along the length as illustrated was also observed probably due to uncontrolled and excessive formation of FeOOH. FeOOH nanoparticles assemble along the DNA strand is evident when compared with the theoretical diameter of DNA molecule as previously noted and the diameter of the isolated DNA/FeOOH nanowires depict thicker nanostructure.

Statistical treatment on AFM data on DNA/FeOOH nanowires for size distribution of the nanowire reveals broad size mean diameters as shown in Figure 4.59. A histogram of the structure diameter was obtained. A large number of large structure were observed with diameter between 10-18 nm and smaller diameter. The data also reveal three apparent trimodal distribution values at 9-10, 13-14 and 16-18 nm, respectively. Thicker structures diameter greater than 2 nm as shown in the histogram are predominantly DNA templated FeOOH. It is noted that the last height value is consistent with the estimated FeOOH crystallite size that was established from the XRD data. This agreement suggests that the nanowire structure consists of assemblage of FeOOH grains packed on DNA template. Therefore the thicker structures are predominantly DNA/FeOOH nanowires.

The nanostructure of DNA/Fe_2O_3 nanowire AFM height image is shown in Figure 4.60with more granular character of the Fe_2O_3 coverage with variation in structure height at~ 12 nm and high surface roughness with still uncontrolled Fe_2O_3 formation. The nanostructure was not of good morphology, but still represent an improvement over the DNA/Fe_2O_3reported(Sarkar *etal*., 2011).Size distribution of the nanowire structure heights were evaluated with statistical treatment on AFM data for DNA/Fe_2O_3 nanowires.The frequencies plotted against nanowire diameter as shown in Figure 4.60 showedless broad size mean diameters. The plot reveals broad size distribution with structure height up to 26 nm in diameter. The data also reveal three-apparent trimodal distributions values with distinct modal values at 5, 13 and 20 nm, respectively. In addition, the three modal value is slightly not consistent with the estimated grain size from XRD data. This mismatch between crystallite size and nanowire diameter could be accounted for.

5.9 Electrical Property of all the DNA-Templated Nanowires

Scanned conductance microscopy (SCM) represent probing nanowires electronic properties qualitatively using contactless method that can assess the conductance of 1D structure. Shown in Figure 4.61 are the optical images of all the nanowires from a dried mass. The optical images illustrate nanowires protruding from the mass of individual material which serve as contact to the nanowire and the conductive AFM tip.

In order to assess the conductance of DNA-templated nanowires qualitatively, scanning conductance microscopy (SCM) was used. It is a simple non-contact electrical method to image conductance pathways previously used to image single-wall carbon nanotubes (SWNTs)

Phase signals associated with the DNA/ppy nanowire is shown in Figure 4.62 indicating electronic properties with respect to whether they are conductive (dark/negative contrast) or insulating (bright/positive contrast). In this case, the EFM phase signals as illustrated in Figure 4.62 where dc potential of between +8 to +2 V were applied, provides a satisfactory images displaying dark contrast indicating that the structure, DNA/ppy is electrically conductive allowing charges stored on the nanowire to be spread along the length of the wire, thus a continuous conduction pathway as dark lines.

The SCM data show parabolic dependence of phase shift on bias voltage for voltage +7 to +3 V at different diameters, where the magnitude of the phase shifts on the applied bias as illustrated by the parabolic trend plot of the degree of phase shifts as a function of applied bias, (Figure 4.63). The phase shifts depend on diameter and large shift observed as the nanowire diameter increases.

The corresponding phase images of DNA/PImi is shown in Figure 4.64 recorded at different potentials between +6 and -4 V. The images showed uniform dark line across the nanowire surface. The appearance of dark contrast irrespective of the magnitude of

the applied bias indicate that the DNA/PImi is electrically conductive. Plots of the degree of the DNA/PImi nanowire phase shifts as a function of applied voltage depicts a parabolic dependence upon the bias applied to the sample,(Figure 4.65). Magnitude of phase shift associated with the DNA/PImi structures is dependent on the square of the applied bias voltage ($q \propto V^2$) as previously being established and, as expected, when the interaction of the AFM tip probe with the electric field gradient above the nanowires is dominated by capacitance effects (Watson *etal*., 2010 ; Hassanien *etal*., 2010). The relationship is clearly depicted by the parabolic curves shown when the degree phase shifts are plotted against the dc bias applied to the sample as illustrated in Figure 4.65. Therefore, the SCM data revealed negative phase shifts confirming the capacity for charge carrier conduction through the nanostructure as shown in Figure 4.64 (a-f).

The EFM data/phase shift of DNA/Fe_2O_3 nanowires is shown in Figure 4.66. The nanowires appear bright in the corresponding EFM images. Figure 4.66(a-e) recorded at dc voltages between -3 and -7 V. The appearance of such positive bright phase contrast shifts relative to the background at different bias voltages is a characteristic for insulator which confirm that positive bright phase nanowires are electrically non-conductive. In addition, the magnitude of the phase shifts associated with the DNA/Fe_2O_3 nanostructures showed a positive parabolic dependence upon the dc bias potentials applied to the nanowire. This confirms that the AFM tip-nanowire interaction is not dominated by capacitance effects. In other words, the EFM data show that there is no continuous conduction pathway along the whole length of DNA/Fe_2O_3 nanowires as indicated in Figure 4.66(a-e). Overall, the positive phase shifts as shown in 4.67 noted in the EFM phase images are evidence that Fe_2O_3 nanoparticles formed by co-precipitation on DNA as template are not conductive.

Same EFM was applied to probe the electronic properties of the DNA/FeOOH nanowires in the manner described previously and as shown in Figure 4.68 (a-f).The EFM phase images was recorded at dc potential between +8 and +3 V along with the EFM data illustrated in Figure 4.69. The DNA/FeOOH nanowires as shown in Figure 4.68(a-f) clearly seen as not too uniform,but with a junction where linear nanostructures are connected to form a single extended structure. This knot-like structure has been previously been described to result from DNA bundles unravelling (Pruneanu *et al*., 2008).The negative dark contrast associated with the nanowires not depending on the magnitude of the applied bias voltages (Yan and Bernstein 2007) indicates that DNA/FeOOH nanowire is electrically conductive. However, the phase shift magnitude displayed a parabolic dependence upon the dc applied to the nanowire as shown in Figure 4.69, confirming that the AFM tip-sample interactions are all dominated by capacitance effects. Finally, the negative phase shift associated with the DNA/FeOOH nanowire's structure indicates a continuous coverage of FeOOH nanoparticles on the DNA template.

Measurement of (ΔØ) phase shift of the nanowires for each bias potentials applied to the samples provided data series as shown in Figure 4.62 to 4.69 with parabolic dependence as predicted by EFM theory.

CHAPTER SIX

6.0SUMMARY AND CONCLUSIONS

6.1 Summary

In this work, λ-DNA was used as platform to grow or pattern semiconductor density and polymer nanoparticles as precursors to generate organized one dimensional nanostructures in solution andby electrochemical reduction. One strategy to overcome this was the use of bottom-up approach, in which DNA as a template to direct synthesis of chains of semiconductors rodlike by chemical reduction from iron nitrate hydrate and/or iron chloride hexahydrate and oxidizing pyrrole and imidazole monomer to produce nanowires. Also the ferric oxyhydroxide (FeOOH) nanorods precursor were successfully transformed into Fe_2O_3 by calcining at 350 ^oC. Their conductivities aside DNA/Fe_2O_3nanowires were observed and could be tailored for active component in microfabrication and future sensor operation for the detection of molecules. λ-DNA with 48,502 base-pairs and 16 μm in length were incubated with an appropriate concentration of the chosen nanoparticles. The preparations of DNA/Fe_2O_3 and DNA/FeOOH involve controlled co-precipitation of Fe^{3+} ions using NaOH on the DNA. While the DNA/ppy and DNA/PImi were achieved using aqueous $FeCl_3$solution to induce polymerization of the appropriate monomer and aqueous phase containing DNA at room temperature. To establish the chemical identity of the nanowires, a series of spectroscopic and microscopic techniques were used to probe sample chemical, structural, morphology, size and electrical information.

Structural, interactions and composition of the synthesized nanowires were determined by cyclic voltammetry redox system, TGA/DTA/DSC, FTIR spectroscopy, UV-visible absorption spectroscopy, EDX, X-ray diffraction pattern (XRD), X-ray

photoelectron (XPS) spectroscopy. The morphology and electronic properties were examined by TEM, AFM and EFM.

Electroactive materials were active as seen in the CV plots for the monomer oxidations. TGA/DTA/DSC showed decomposition pathways and thermal stabilities at above 300 ^{o}C for the conversion of FeOOH to Fe_2O_3 and m/z for water and CO_2 evolved was at 18 and 44 respectively as shown in appendix A13 and A14.

Evidence of interactions of the resulting material was confirmed by intensity decrease in the UV-Vis spectra with the development of plasmon band at the same λ_{max} absorption peak registry for bare DNA. Further evidence was also shown by FTIR with features assigned to bands shift associated with nanoparticles accessibility to both nucleobases and phosphodiester backbone on the DNA, thus the resulting materials are not a mixture but product of interactions.

Furthermore, XPS and XRD studies confirmed the presence of DNA and nanoparticles as component on the biomolecule strands as well as other ions. XRD shows that the nanoparticles are α-Fe_2O_3 and α-FeOOH and EDX highlighted the series of components on the nanowires architecture with spectrum containing different peaks for elemental pathways in the nanomaterials.

TEM analysis showed strong preference for the formation of nanoparticles cluster/growth on the DNA template with extended reaction period that led to the formation of continuous coatings on the template. AFM complemented TEM for detailed nanoparticles registry along the DNA strands with some transformation into thicker leaflet nanobundles. The nanowires showed morphologies consisting of linearly densely-packed arrangement of nanoparticles along the biomolecules with diameter less than 40 nm. These phenomena resulted in bead-on-a string patterns, linear arrays, and

irregular morphologies in some regions with evidence of bare DNA. The AFM topographies translated the interactions into the directing ability of the template into high aspect ratio nanostructured materials with densely packed nanoparticles linearly arranged as nanowires.

Studies on the electrical properties of the nanowires using non-contact method showed DNA/FeOOH and the two DNA/polymer systems to be electrically conducting compared to DNA/Fe_2O_3 nanowire which was non-conducting. The nanowires in the scanned conductance images appeared as dark lines for the two DNA/polymer systems and DNA/FeOOH corresponding to the negative phase shifts as the tip crosses the wire thus the existence of charges in the nanowires. The origin of this conductance effects were checked by plotting phase shift against the dc bias and parabolic dependence was observed over a range of -7 to +7 V for all the nanowires studied. However, EFM is as well sensitive to trapped charges, the quadratic variation of phase shift with bias voltages is an indication that the data observed are all due to conductance effects. The DNA/Fe_2O_3 showed typical resistivity behaviour at room temperature and others displayed conductivity tendencies.

6.2 CONCLUSIONS

Simple and solution-based DNA-templating strategies have been demonstrated to generate nanostructures with 1D morphologies with continuous coatings of the nanoparticles. Methods to synthesize electrically conductive nanowires on DNA immobilized on a solid support were also described, thus modification of DNA was successfully achieved via coordination of the DNA backbone with the various nanoparticles. The template-directed method is a good control over uniformity and dimensions.

FTIR, XPS & UV-Vis spectra confirmed the formation of supramolecular structure containing DNA and nano-objects. FTIR data of the nanostructures suggested that the nanoparticles were bound to the phosphodiester backbone of DNA due to shift in PO_2^- stretch. In this approach, DNA presented an attractive template that allowed the formation of controlled nano-objects as organised 1D structure. Chemical characterization via XPS indicated that the structure consisted of the major components of the DNA and the nanoparticles. XRD clarified the nanoparticles as crystalline and material formed after treatment are markedly different from their net precursors.

The evolution of morphology of the nanostructures were observed by AFM which confirmed a general increase in height of bare DNA after treatment and TEM images indicated that DNA template really directs the growth of deposited nanoparticles and organized linear arrangement of nanoparticles into 1D structure. Beads-on-a-string morphology transforms into smooth nanowires.

SCM studies provided a direct qualitative evaluation of the nanowire's electronic properties, confirming one sample to be electrically non-conductive. The nanowires exhibit both negative and positive parabolic behaviours, with the conductance measurements of DNA/Ppy, DNA/Plmi, and DNA/FeOOH showed dark negative bias shift and hence electrical charges pathways.

The synthetic process does not disturb the conformation of the DNA strands and can be extended to serve as building block to fabricate functional nanodevices. This step in this work was vital for investigating the nanowire conductivity by providing a route to performing detailed electrical measurements of the nanowires.

These results indicate clear avenues for future development of engineered nanowire electronic devices and sensors for environmental pollution monitoring and

screening assays in cancer cells.Thus, the next interconnection technology may be conducting nanowires or its analogues!

Work contained in this dissertation is directed toward the realisation of the challenging objectives as specified in the aim and objectives section. In this regard, the objectives have been achieved. It has been shown that the preparation of 1D wires and linear arrays is possible for both compounds and molecular-based materials and the nanowires (not all) were shown to carry appreciable level of currents over micro length scales. Thus while DNA/Fe_2O_3 nanowires produced are highly resistive for the take-off of realistic application as components within electronic devices, the others can be considered as a candidate for the replacement of the current interconnect technology.

A striking outcome in this research was the insight gained into the growth processes of the semiconductor and polymer nanoparticles with binding occurring more efficiently along the template axis leading to denser nucleation and granular wires. An important finding is that the DNA/FeOOH and DNA/Fe_2O_3 TEM images indicated that the nanowires formed on the template in a different way (dendritic features) than previously reported nanowires. This serves as an indicator for more varieduse of the nanowires.

6.3RECOMMENDATIONS

A further investigation on all the DNA/nano-objects stability, their conductivity quantitatively, especially the variation with temperature using the two-terminal I-V method to assess the nature of the conduction mechanism should be carried out. At present, it is not possible to use EFM technique to extract quantitative values of conductance, but powerful techniques such as C-AFM can detect conducting objects quantitatively but require contact to be made.

Areas for further investigation on the fabricated nanowires have been identified. These include using more techniques, such as scanning tunnelling microscopy (STM), magnetic field microscopy (MFM), tunnelling atomic force microscope (TUNA) and torsion resonance tunnelling atomic force microscopy (TR-TUNA) to add to the data available.

Magnetic force microscopy (MFM) can also beused to study the ferroelectric and magnetic response of the nanowires, with the future possibility of using it as a storage element for memory devices. On the other hand, TR-TUNA can be utilised to examine the conductivity of nanowires in further investigation of current or charge transport in nanowires. This method is non-destructive current mapping technique which is a further support for C-AFM. In addition, four-point probe method can also be used to examine charge carrier transport in the nanowires.

A testing system for microelectrode conduction protocol should be fabricated by Ag electrode using probably photolithographic process that serves asa bridge between the nanowires. Evaluating the nanowires as gas sensor and locating the cancer cells as target binding bio-diagnostic assays in hyperthermia therapy for cancer treatment has not been assessed yet.

REFERENCES

Alex, S. and Dupuis, P. (1989). FTIR and Raman investigation of cadmium binding by DNA. *Inorganica Chimica Acta*, 157 (2) 271-281.

Arakawat, H., Ahmed, R., Naoui, M. and Tajmir-Riahi, H. A. (2000). A comparative study of calf thymus DNA binding to Cr (III) and Cr (VI) ions. *Journal Biological Chemistry*,275, 10150-10153.

Artemyev, M., Kisiel, D., Abimiotko, S., Antipina. M, N., Khomutov, G. B., Kislov, V. V. and Rakhnyanskaya, A. A. (2004). Self-organized, highly luminescent CdSe Nanorods-DNA complexes, *Journalof American Chemical Soc*iety, 126, 10594-10597.

Atkinson, R. J., Parfitt, R. L. and Smart, R. St. C. (1974). Infrared study of phosphate adsorption on goethite. *Journal of Chemical Society, Faraday Transaction*, I 70, 1472-1479.

Bachtold, A., Fuheer, M., Plyasunov, S., Forero, M., Anderson, E. H., Zettl, A. and Mceuren, P. L. (2000).Scanned probe microscopy of electronic transport in Carbon Nanotube *Physical Review Letters*, 84, 6082-6085.

Bare, G. (1975). In Magnetic oxides part 2. (Ed). Craik, D. J. Wiley New York p. 689.

Baumann, C. G., Bloomfield, V. A., Smith, S. B., Bustamante, C., Wang, M. D. and Block, S. M. (2000). Stretching of single collapsed DNA molecules, *Biophysics Journal*, 78,1965-1978.

Becerril, H. A. and Woolley A. T. (2009). DNA-templated nanofabrication. *Chemical Society Review*,38 (2) 329-337.

Bensimon, A., Simon, A. J., Chiffaudel, A., Croquette, V., Heslot, F. and Bensimon, D.(1994)Alignment and sensitive detection of DNA by a moving interface. *Science*,265, 2096-2098.

Bensimon, D., Simon, A.J., Croquette. V. and Bensimon, A. (1995). Stretching DNA with a receding meniscus: experiment and model. *Physical Review Letters*, 74,4754-4757.

Berg, J. H., Tymoczko, J. L. and Stryer, L., (2002). Biochemistry 5th ed. W.H. Freeman NewYork, p. 397-400.

Berquand, A., Combined optical and SPM microscopy Bruker Nanosurface Division.Available@combined-optical-AFM_webinar_slides_120118.pdf. (Accessed: 16/05/2013)

Bigham, S.R. and Coffer,J. L. (1995). The influence of adenine content on the properties Q-CdS clusters stabilized by polynucleotides, *Colloid surfaces*, 95, 211-219.

Binnig, G., Quate, C. F. and Gerber, C. (1986). Atomic force microscope. *Physical Rev. Letters*, 56, 930-933.

Blackburn, G. M. and Gait, M. J. (1996). Nucleic acid Chemistry and Biology. 2nd edn. OUP. Oxford, pp. 36-41.

Bockrath, M., Markovic, N., Shepard, A., Tinkham, M., Gurevich, L., Kouwenhoven, L. P., Wu, M. W. and Sohn, L. L. (2002). Scanned conductance microscopy of Carbon nanotube and λ-DNA. *Nano Letters*, 2, 187-190.

Bockrath, M., Markovic, N., Shepard, A., Tinkham, M., Gurevich, L., Kouwenhoven L. P., Wu, M. S.W. and Sohn, L. L. (2002).Scanned conductance microscopy of carbon nanotubes and λ-DNA. *NanoLetters*, 2, 187-190.

Brumlik, C.J., Martin, C. R. and Tokuda, K (1992). Microhole array electrodes based on microporous alumina membrane, *Analytical Chemistry*, 64, 1201-1203.

Busbee, B. D., Obare, S. O., Murphy, C. J. (2003). An improved synthesis of High-aspect-ratio Gold nanorods, *Advanced Materials*, 15, 414-416.

Cao, G. Z. and Wang, Y. (2011). Nanostructure and nanomaterials: Synthesis, properties and applications, World Scientific. Singapore, pp. 87-192.

Carquigny, S., Sanchez, J. B., Berger, F., Lakard, B. and Lallemand, F. (2009). Ammonia gas sensor based on electrosynthesized polypyrrole films, *Talanta*, 78, 199-206.

Chandrasekhar, P. (1999). Conducting polymer fundamentals and applications: a practical approach, Kluwer Academic, Boston, Pp. 306-318.

Chen, M., Yu, H. W., Chen, J. H. and Koo, H. S. (2007). Effect of purification treatment on adsorption characteristics of carbon nanotubes. *Diamond Relative Materials*. 16, 1110-1115.

Coffer, J. L., Bigham, S. R., Li, X., Pinizzotto, R.F., Rho, Y. G., Pirtle, R. M. and Pirtle, I. (1996). Dictation of the shape of mesoscale semiconductor

nanoparticles assembly of plasmid DNA. *Applied Physics Letters*, 69 (25), 3851-3853.

Coffer, J. L., Bigham, S. R., Pinizzotto, R. F. and Yang, H. (1992). Characterization of Quantum-confined CdS Nanocrystallization stabilized by DNA. *Nanotechnology*,69-76.

Coleman, N. R. B., O'sullivan, N., Ryan, K. M., Crowley, T. A., Morris, M. A., Spalding, T. R., Steytler, D. C. and Holmes, J. D. (2001). Synthesis and characterization of dimensionally ordered semiconductor nanowires within mesoporous silica, *Journal of American Chemical Society*, 123, 7010-7116.

Cornell, R. M. and Schwertmann, U. (2003). The Iron oxide: Structure, properties, reaction, occurrence and uses 2nd ed. Wiley-VCH, Weinhein.

Dean, J. R., Jones, A. M., Holmes, D., Reed, R., Weyers, J. and Jones, A (2002) Practical skills in Chemistry, Pearson Education Limited, Essex, pp. 86-100.

De Pablo, P. J., Gomez-Navarro, C., Gil. A., Colchero, J., Martinez, M. T., Benito, A. M., Maser, W. K., Gomez-Herrero, J. and Baro, A. M. (2001).Visualization of single-walled carbon nanotubes electrical network by scanning force microscopy. *Applied Physics Letters*, 79, 2979-2981.

Deki, S., Aoi, Y., Okibe, J., Yanagimoto, H., Kajinami, A. and Mizuhata, M. (1997). Preparation and Characterization of Iron oxyhydroxide and iron oxide thin films by liquid-phase deposition. *Journal of materials Chemistry*, 7, 1769-1772.

Ding, Y., Gao, P. X. and Wang, Z. L. (2004) Catalyst-Nanostructure Interfacial lattice mismatch in determining the shape of VLS grown nanowires and nanobelts: A case of Sn/ZnO, *Journal of American Chemical Society*, 126, 2066-2072.

Dittmer, W. U. and Simmel, F. G. (2004). Chains of semiconductor nanoparticles templated on DNA. *Applied Physics Letters*, 85 (4) 633-635.

Dong, L., Hollis, T., Connolly, B. A., Wright, N. G., Horrocks, B. R. and Houlton, A. (2007). DNA-templated semiconductor nanoparticles, chains and wires. *Advanced Materials*, 1748-1751.

Dong, L., Hollis, T., Fishwick, S., Connolly, B. A., Wright, N. G., Horrocks, B. R. and Houlton, A. (2007). Synthesis, manipulation and conductivity of supramolecular polymer nanowires. *Chemistry - A EuropeanJournal*. 13, 822-828.

Dovbeshko, G. Z., Gridina, N. Y., Kruglova, E. B. and Pashchuk, O. P. (2000). FTIR Spectroscopy studies of Nucleic acid damage *Talanta*, 53, 233-246.

Dresselhaus, M.S., Chen, G., Tang, M.Y. Yang, R.G., Lee, H., Wang, D.Z., Ren, Z.F., Fleurial J.P. and Gogna, P. (2007). New direction for low-dimensional thermoelectric materials. *Advanced Materials*, 19, 1043-1053.

Duckett, S. and Gilbert, B.C. (2000). Fundamentals of spectroscopy, Oxford University press, London, P. 10-25.

Eichhorn, G. I. and Shin, Y. A. (1968). Interaction of metal ions with polynucleotides and related compounds. XII. The relative effect of various metal ions on DNA Helicity *Journal of American Chemical Society*, 90, 7323-7328.

Eigler, D.M. and Schweizer, E.K (1990). Positioning single atoms with Scanning tunnelling microscopy. *Nature*, 344 (6266), 524-526.

Feynman R.P. (1960). There is plenty of room at the bottom, *Engineering. Science*, 22.

Feynman, R. P. (1992). There's plenty of room at the bottom, *Journal of microelectromechanical system*, 1, 60-66.

Fujii, T., de Groot, F. M. F., Sawatzky, F. C., Voogt, F. C., Hibma, T. and Okada, K. (1999). *In-situ* XPS analysis of various Iron oxide film grown by NO_2–assisted molecular beam epitaxy. *Phys. Rev*. B: *Condensed Matter Materials Physics*,59, 3195-3202.

Grosvenor, A. P., Kobe, B. A. and Mcintyne, N. S. (2004). Examination of the oxidation of Iron by oxygen using X-ray photoelectron spectroscopy and QUASES (TM). *Surface Science*, 565, 151-162.

Guo, F., Zhang, Q., Zhang, B., Zhang, H. and Zhang, L.(2009). Preparation and Characterization of magnetic composite microspheres using a free radical polymerization system consisting of DPE. *Polymer*,50, 1887-1894.

Guo, L. J., Cheng, X. and Chou, C. F. (2004).Fabrication of size controllable nanofluidic channels by nanoimpriting and its application for DNA stretching, *Nano Lett*ers, 4, 69-73.

Hall, D. B., Holmlin, R.E. and Barton, J. K. (1996). Oxidative DNA damage through long-range electron transfer, *Nature*, 382, 731-735.

Hassanien R. Farha Al-Said, S. A. B., Siller, L., Little, R., Wright, N. G., Houlton, A. and Horrocks, B. R. (2012). Smooth and conductive DNA-templating Cu_2O nanowires: growth morphology, spectroscopy and electrical characterization. *Nanotechnology*,23, 075601.

Hassanien, R. M., Al-Hinai, M., Al-Said, S. A. F., Little, R., Siller, L., Wright, N. G. and Horrocks, B. R. (2010). Properties and characterization of conductive and photoluminescent DNA-templated polyindole nanowires. ACS, *Nanotechnology*, 4, 2149-2159.

Hatakeyama, T. and Quinin, F. X. (1994). Thermal analysis; Fundamental and application to polymer Science,2nd ed., New York, John Wiley and Sons, Pp. 2-7, 45-61. 68-70.

Heath, J. R. Kuekes, P.J., Snider, G. S. and Williams, R. S., (1998). A defect-tolerant computer Architecture: Opportunities for Nanotechnology, *Science*, 280, 1716-1721.

Heinze, J. (1984). Cyclic voltammetry: Electrochemical spectroscopy New Analytical metho*d, Angewandte Chemie international Edition in English*, 23, (11) 831-847.

Heinze, J. (1991). Electrochemistry of conducting polymer. *Synthetic Materials*. 43, (1-2) 2805-2823.

Herne, T. M. and Tarlov, M. J. (1997). Characterization of DNA probes immobilized on Gold surfaces. *Journal of American Chemical Society*, 119, 8916-8920.

Holmes, J. D., Johnson, K. P., Doty, R. C. and Korgel, B. A. (2000). Control of thickness and orientation of solution-grown silicon nanowires, *Science*, 287, 1471-1473.

Houlton, A. and Watson S. M. D. (2011). DNA-based nanowire: templated bottom-up nanoscale, *Annual Reportson the Progress of Chemistry*. *Sect A: Inorganic Chemistry*, 107, 21-42.

Houlton, A., Pike, A. R. Angel Galindo, M. and Horrocks, B. R. (2009) DNA-based route to semiconducting nanomaterials. *Chemical Communication*,1797-1806.

Howell, C., Zhao, J. L., Koelsch, P. and Zharnikov, M. (2011). Hybridization in ssDNA film: a multi-technique spectroscopy study, *Physical Chemistry, Chemical Physics*. 13, 15512-15522.

Hu, X. and Yu, J. C. (2008). Continuous Aspect-Ratio Tuning and fine shape control of monodisperse α-Fe_2O_3 nanocrystals by a programmed microwave hydrothermal method.*Advanced Functional Materials*, 18, 880-887.

Huang, M. H., Wu, Y., Feick, H., Tran, N., Webber, E.and Yang, P. (2001). Catalytic growth of Zinc oxide nanowires by vapour transport, *Advanced Materials*, 13, 113-116.

Huczko, A. (2000). Template-based synthesis of nanomaterials, *Applied Physics*. A: *Materials Science Process*, 70, 365-376.

Hulteen, C. J. and Martin, C. R. (1997). A general template based method for the preparation of nanomaterials. *Journal of Materials Chemistry*, 7 (7) 1075-1085.

Ito, T. and Okazaki, S. (2009). Pushing the limits of lithography, *Nature*, 406, 1027-1031.

Jia, C., Sun, L., Luo, F., Han, X., Heyderman, L., Yan, Z., Yan, C., Zheng, K., Zheng, Z. and Takano, M. (2008). Large-scale synthesis of single-crystalline iron oxide magnetic nanorings, *Journal American Chemical Society*, 130, 16968-16977.

Jianwei, J., Bat, C., Wang, B., Zhu, C., Lin, Z., Li, Q. and Cao, E. (1998). A convenient method of aligning large DNA molecules on bare mica surface for atomic force microscopy. N*ucleic acids Research*, 26, 4785-4786.

Kawade, T., Shimomura, S., Karasuda, T., Tabata, K., Suzuki, E. and Yamaguchi, Y. (2000). Photoemission study of dissociating adsorbed methane on a pre-oxidized SnO_2 thin film. *Surface Science*. 448, 101-107.

Khalid, M. A. Anees, A. A. and Salman, A. A. (2010). DNA-based application in Nanotechnology. *Journal of Biomedicine and Biotechnology*, 2010, 1-15.

Kharat, H. J., Kakade, K. P., Savale, P. A., Dutta, K., Ghosh, P. and Shirsat, M. D. (2007), Synthesis of ppy film for the development of Ammonia sensor. *Polymer. Advanced Technology* 18, 397-402.

Kim, H. J., Bae, I., Cho, S., Boo, J., Lee, B., Heo, J., Chung, I. and Hong, B. (2012). Synthesis and characterization of NH_2-functionalized polymer films to align and immobilize DNA molecules, *Nanoscale Research Letters*. 7-30. doi 10.1186/1556-276x-7-30.

Kim, Y., Torrens, O. N., Kikkawa, J. M., Abou-Hamad, E., Goze-Bac, C. and Luzzi, D. E (2007). High-purity diamagnetic single-wall carbon-nanotube Bucky paper. *Chemistry Materials*. 19, 2982-2986.

Klug, H. P. and Alexander, L. E. (1954). X-ray Diffraction procedure for crystalline and amorphous materials, Wiley, New York, 491-539.

Krehula, S., Popovic, S. and Music. (2002). Synthesis of acicular FeOOH particles at a very high pH. *Materials Letters.* 54, 108-113.

Langea, U., Roznyatovskayal N. V. and Mirsky, V. M. (2008) Conducting polymer in chemical sensor and arrays. *Analytical Chimica Acta,* 614 (1), 1-26.

Law, M., Greene, L. E., Johnson, J. C., Saykally, R. and Yang, P. (2005). Nano dye-sensitized solar cells. *Natural Materials,* 4, 455-459.

Lee, C. Y., Gong, P., Harbers, G. M., Grainger, D. M., Castner, D. G. and Gamble, L. J. (2006). Surface coverage and structure of mixed DNA/alkylthiol monolayer on Au: characterization by XPS, NEXAFS and fluorescence intensity measurements, *Analytical Chemistry,* 78, 3316-3325.

Levina, L., Sukhovatkin, W., Nusikhin, S., Cauch, R., Nisman, R., Bazett-Jones, D. P. and Sargent, E. H. (2005). Efficient Infrared emitting PbS Quantum Dot grown on DNA and stable in aqueous solution and blood plasma. *Advanced Materials.*17 (15), 1854-1857.

Li, N., Gao, F., Hou, L. and Gao, D. (2010). DNA-templated rational assembly of BaWO4 nano pair-linear arrays, *Journal of Physical Chemistry*. C. 114, 16114-16121.

Li, X. Q. and Zhang, W. X. (2007). Sequestration of metal cations with zerovalent iron nanoparticles: a study with high resolution XPS. *Journal of Physical Chemistry*C, 111, 6939-6946.

Li, Z., Chen, H., Bao, H. and Gao, M. (2004). One-pot reaction to synthesize water soluble magnetic nanocrystals. *Chemistry Materials* 16, 1391-1393.

Liang, J., Luo, M., Yang, G., Fang, J. and Li, L. (2011). Synthesis of spindle-shaped α-FeOOH and Fe_2O_3 nanocrystals. *Crystallography. Research Technology,* 46, 493-496.

Liu, J., Wang, X., Peng, Q. and Li, Y. (2005). Vanadium Pentoxide nanobelts: Highly selective stable ethanol sensor materials. *Advanced Materials,* 17, 764-767

Ma, Y., Zhang, J., Zhang, J. Zhang, G. and He, H. (2004). Polyaniline nanowire on Si surface fabrication with DNA templates. *Journal of American Chemical Society,* 126, (22), 7097-7101.

Malinauskas, A., Malinauskiene, J. and Ramanavicius, A. (2005). Conducting polymer-based nanostructure materials, electrochemical aspects. *Nanotechnology,* 16 (10), R51-R 62.

Mao, Y., Park, T. J., Zhong, F., Zhou, H. and Wong, S. S. (2007). Environmentally friendly methodologies for nanostructure synthesis, *Small*, 3, 1122-1139.

Mariam, A. H. (2013).Self-assembly of conductive nanowires using DNA as a template. PhD dissertation, Newcastle University.

Martin, C.R. (1994). Nanomaterials: a membrane-based synthetic approach, *Science*, 266, 1961-1966.

McCord, M. and Rooks. M. (1997). Electron beam lithography: In Handbook of microlithography, micromachining and microfabrication. Raichoudhury, P., Ed., SPIE Press, Bellingham, 11, 139-249.

McCullough, R. D. (1998). The Chemistry of conducting polythiophene. *Advanced Materials,*10, (2), 93-116.

Mcintyre, N. S. and Zetaruk, D. G. (1977). X-ray photoelectron spectroscopic studies of iron oxides. *Analytical Chemistry*, 49, 1521-1529.

Michalet, X., Ekong, R., Fougerousse, F., Rousseaux, S., Schurra, C., Hornigold, N., Slegtemhorst, M., Wolfe, J., Povey, S., Beckmann, J. S. and Bensimon, A. (1997). Dynamic molecular combing: Stretching the whole human genome for high-resolution studies,*Science*, 277, 1518-1523.

Miller, M. L. and Linton, R. W. (1985). X-ray photoelectron Spectroscopy of thermally treated SiO_2, *Surface, Analytical Chemistry*, 57, 2314-2319.

Mirkin, C. A. (2000). Programming the assembly of two and three dimensional architecture with DNA and nanoscale building blocks. *Inorganic Chemistry*, 39, 2258-2272.

Mirkin, C. A., Letsinger, R. L., Mucic, R C. and Storhoff, J. J. (1996). A DNA based method for rationally assembly nanoparticles into macroscopic materials. *Nature*, 382, 607-609.

Mohammed, H. D.A., Watson, S. M. D., Horrocks, B. R. and Houlton, A. (2012). Magnetic and conductive nanowires by DNA-templating. *Nanoscale*, 14, 5936-5945.

Moore G.E. (1965). Cramming more components on integrated circuits, *Electronics* 38, 114-116.

Moulder, J. F., Stickle, W.F., Sobol, P. E. and Bomben, K. D. (1992). Handbook of X-ray photoelectron Spectroscopy, Perkin-Elmer Corp. Eden prairie.

Nagarajan, R., Roy, S., Kumar, J., Tripathy, S. K. Dolukhanyan, T., Sung, C., Bruno, F.and Samuelson, L. A. (2001). Enzymatic synthesis of molecular complexes of polyaniline with DNA and synthetic oligonucleotides: thermal and morphological characterization. *Journal of macromolecule Science, Pure and Applied Chemistry,*38, 1519-1537.

Nair, M. T. S, Guerrero, L. and Nair, P. K. (1998). Conversion of chemically deposited CuS thin films to $Cu_{1.8}$ S and $Cu_{1.96}$ S by annealing, *Semiconductor ScienceTechnology*, 13, 1164-1169.

Nasari, Z. E. and Gurevich, L. (2003). Molecular combing of DNA: Method and application. *Journal self-assembly and molecular Electronics*, 1, 125-148.

Nasibulin, A. G., Rakauskas, S., Jiang, H., Tian, Y., Mudimela, P. R., Shandakov, S. D, Nasibulina, L., Sainio J. and Kauppinen, E. I. (2009). Simple and rapid synthesis of α- Fe_2O_3 nanowires under ambient conditions, *Nano Research* 2, 373-379.

Nazari, Z. E. and Gurevich, L. (2013). Molecular combing of DNA: Method and application, *Journal self-assembly and molecular Electronics*, 1, 125-148.

Neal F. (2009). Introduction to XPS and AES (Casa XPS Manual 2-3.15) CASA software Ltd. P. 1-176.

Nicholson, R. S. (1965). Theory and application of cyclic voltammetry for measurement of electrode reaction kinetic, *Analytical Chemistry*, 37, 1351-1355.

Nickels. P., Dittmer, W. U., Beyer, S., Kotthaus, J .P. and Simmel, F. C. (2004). Polyaniline nanowires synthesis templated by DNA, *Nanotechnology*, 15, 1524-1529.

Spiro T.G.(1980) Nucleic acid - Metal Ions Interactions, John Wiley, New York, Vol. 1, 98-135.

Nuffield, E. W. (1966). X-ray diffraction methods New York, Wiley 409-430.

Nyamjav, D. and Ivanisevic, A. (2005). Templates for DNA templated Fe_3O_4 nanoparticles. *Biomaterials*, 26, 2749-2757.

Nyquist, R. A. and Kagel, R.O. (1971). Infrared Spectra of Inorganic compounds, Academic press, San Diego, p.76-85.

Oh, S. J., Cook, D. C. and Townsend, H. E. (1998) Characterization of iron oxides commonly formed as corrosion products on steel, *Hyperfine Interactions*., 112, 59-65.

Ouameur, A. A. and Tagmir-Riahi, H. A. (2004). Structural analysis of DNA interactions with biogenic polyamines and cobalt (III) hexamine studied by FTIR and capillary electrophoresis. *Journal of Biological Chemistry*, 279, 42041-42054.

Ozin, G.A. Arsenault A.C. and Cademartin, L. (2009). Nanochemistry: A Chemical approach to nanomaterials 2nd, RSC, Cambridge, pp. 1-53, pp.117-334.

Padalkar, S., Capadona, J. R., Rowan, S. J., Weder, C., Won, Y. H., Stanciu, L. A. and Moon, R. J. (2010). Natural biopolymer: Templates for the synthesis of nanostructure. *Langmuir*, 26 (11), 8497-8502.

Partch, R. E., Gangoli, S.G, Matijevic, E., Cai, W. and Arajs, S. (1991). Conducting polymer composition: Surface-induced polymerization of pyrrole on Iron (III) and Cerium (IV) oxide particles. *Journal of Colloid and Interface Sci*ence, 144, 27-35.

Parthasarathy, R.V. and Martin, C. R. (1994). Template-synthesized polyaniline microtubules. *Chemistryof Materials*, 6, 1627-1632.

Parviz, B. A., Ryan, D. and Whitesides, G. M. (2003). Using self-assembly for the fabrication of nanoscale electronic and photonic devices. *IEEE. Transactions on advanced packaging.* 26 (3), 233-241.

Patolsky, P. and Leiber, C.M. (2005). Nanowire Nanosensors, *Materials Today*, 8 (4) 20-28.

Penner, R. M. (2002). Mesoscopic metal particles and wires by electrodeposition. *Journal of Physical Chemistry*, B, 106, 3339-3353.

Penner, R. M. and Martin, C. R. (1986). Controlling the morphology of electronically conductive polymer. *Journal of Electrochemical Society*, 133 (10), 2206-2207.

Petrovykh, D. Y., Kimura-Suda, H., Tarlov, M. J. and Whiteman, L. J. (2004). Quantitative characterization of DNA film by XPS. *Langmuir*, 20, 429-440.

Pruneanus, S., Al-Said, S. A. F., Dong, L., Hollis, T. A., Galindo, M. A., Wright, N. G., Houlton, A. and Horrocks, B. R. (2008). Self-assembly of DNA-templated polypyrrole nanowires, spontaneous formation of conductive nanowires, *Advanced Functional Materials*, 18, 2444-2454.

Punger, E. (1995). A practical guide to instrumental analysis, Florida. Boca Raton, 181-191.

Rao, C.N.R., Muller, A. and Cheetham, A.K. (2004). The Chemistry of nanomaterials, Synthesis, properties and application Vol.1, Wiley-VCH, Weinheim.Pp. 3-26.

Richter, J. (2003). "Metallization of DNA", Low dimensional systems and nanostructure, *Physica E,* 16, 157-173.

Roduner, E. (2006). Size matters: Why nanomaterials are different. *Chemical Society Review*, 35 (7), 583-592.

Sarkar, D. and Mandal, M (2012). Static and dynamic magnetic characterization of DNA-templated Chain-like magnetite nanoparticles, *Journal of Physical Chemistry*. C., 116, 3227-3234.

Sarkar, J., Khan, G. G. and Basumallick, A.(2007). Nanowires: properties, application and synthesis via porous aluminium oxide template. *Bulletin of materials Science*, 30 (3), pp. 271-290.

Schiffrin, D.J., Haiss, W., Nichols, R. J., Higgins, S. J., Bethell, D. and Hobenreich, H. (2004). Wiring nanoparticles with redox molecules.*Faraday Discussion*, 125, 179-194.

Schuth, F. (2003). Endo and exotemplating to create high-surface-area inorganic materials *Angewandte Chemical International Ed*ition, 42, 3604-3622.

Skotheim, T. A., Elsenbaumer, R. L. and Reynolds, J. R. (1998). Handbook of conducting polymers 2nd ed., Marcel Dekker, New York. Pp.35-65.

Staii, C., Johnson, A. T. and Pinto, N, J. (2004). Quantitative analysis of scanning conductive microscopy. *Nano Letters* 4, 859-862.

Steele, D. (2002). Infrared spectroscopy: Theory, in Handbook of vibrational Spectroscopy, Vol. 1 Chalmers, J.M. and Griffiths, P.R (Ed). Wiley Chichester,pp 44-70.

Smith, G. C. (1994). Surface analysis by electron Spectroscopy: measurements and interpretation, Plenum press. New York, Pp. 160-173.

Stoltenberg, R. M. and Woolley, A. T. (2004). DNA-templated nanowire fabrication. *Biomedical Microdevice,* 6, 105-111.

Storm, A. J., Van Noort, J., De Vries, S. and Dekker, C. (2001). Insulating behaviour for DNA Molecules between Nanoelectrodes at the 100 nm length scale. *AppliedPhysics Letters* 79, 3881-3883.

Stryer, L. (1988). Biochemistry 3 edn. W.H. Freeman, NewYork P. 1089.

Sun, Y., Wang, B. Wang, H. and Jiang, J. (2007). Controllable preparation of magnetic polymer mesosphere with different morphologies by miniemulsion polymerization. *Journal of Colloid interface Science,*308, 332-336.

Tailander, E., Liquier, J., Taboury, J. A. and Ghomi, M., (1984). In spectroscopy of Biological molecules (Sandorfy, C. and Theophanides, T. Ed) Reidel, Dordrecht, Amsterdam, pp. 171-189.

Tang, B., Wang, G., Zhou, L., Ge, J. and Cui, L. (2006). Facile Route to α-FeOOH and α- Fe_2O_3 nanorods and magnetic property of α-Fe_2O_3 nanorods.*Inorganic Chemistry.*45, 5196-5200.

Taniguchi T., Nakagawa, K., Watanabe, T., Matsushita, N. and Yoshimura, M. (2009).Hydrothermal growth of Fatty Acid stabilized Iron oxide nanocrystals. *Physical Chemistry,* C, 113, pp. 839-843.

Teng, X. W. and Yang, H. (2004). Effects of surfactant and synthetic conditions on the sizes and self-assembly of monodisperse Iron oxide nanoparticles, *Journal of Materials Chemistry*, 14, 774-779.

Tentler, T. J., Hickman, K. M., Geol, S. C., Viano, A. M., Gibbons, P. C. and Buhro, W. E. (1995). Solid-liquid–solid growth of crystalline III-V semiconductor: An analogy of vapour-liquid-Solid,*Science*. 270, 1791-1794.

Tian, B. and Zerbt, G. (2009). Lattice-dynamic and vibrational spectra of Ppy, *Journal of Chemical Physics*, 92, 3886-3891.

Tong, G., Guan, J. and Zhang, Q. (2007). Goethite hierarchical nanostructure: Glucose-assisted synthesis, chemical conversion into hematite with excellent photocatalytic properties. *Materials Chemical, Physics*, 127, 371-378.

Torimoto, T., Yamashita, M., Kuwabata, S., Sakata, T., Mori H. and Yoneyama, H. (1999). Fabrication of CdS nanoparticles chain along DNA double strands. *Journal. Physical Chemistry*, B. 103, 8799-8803.

Vickerman, J. C. (1997). Surface analysis: the principal techniques, Chichester, John Wiley, p. 457.

Vilar, M. R., do rego, A. M. B., Ferraria, A. M., Jgnet, Y., Nogules, C., Peled, D. and Naaman, R. (2008). Interaction of self-assembly monolayers of DNA with electron: HREELS and XPS studies, *Journal of Physical Chemistry*, B, 112, (23), 6957-6964.

Wagner, C. D., Naumkin, A. V., Kraut-Vass, A., Allison, J. W., Powell, C. J. and Rumble Jr. J. R. (2003). NIST standard reference database, 20, version 3.4 (http:/srdata.nist.gov/xps/) (Accessed: 25/04/2013

Wagner, C. D., Riggs, W. M., Davis, L. E., Moulde, J. F., (1979). In G. E. Muienherg (Ed.), Handbook of the X-ray photoelectron spectroscopy, Perkin-Elmer, Physical Electronic Division, Massachusetts, p. 76.

Wallace, G. G., Spinks, G. M. and Kane-Maguir, L. A. P. (2002). Conducting electroactive polymer intelligent materials system 2nd Ed, CRC Press, New York, PP. 10-69

Wang, G., Guo, X., Horvat, J. and Park, J. (2008). Facile synthesis and characterization of iron oxide semiconducting nanowires for gas sensing application, *Journal of Physical Chemistry*, C., 112, 15220-15225.

Wang, H. L., O' Malbey, R. M. and Fernandez, J. E. (1994). Electrical and chemical polymerization of imidazole and some of its derivative, *Macromolecules*, 27, 893-901.

Wang, X. and Li, Y. (2002). Selected-control hydrothermal synthesis of α- and β-MnO_2 single crystal nanowires, *Journal of American Chemical Society*, 124, 2880-2881.

Wang, X., Summers, C. J. and Wang, Z.L. (2004). Large-scale hexagonal–patterned growth of Aligned ZnO nanorods for nano-optoelectronics and nanosensors arrays,*Nano letters*, 4, 423-426.

Watson, J. D. and Crick, F. H. C. (1953). Molecular structure of nucleic acid: A structure of deoxyribonucleic acid. N*ature*, 171, (4356), 737-738.

Watson, J. D., Baker, T. A., Bell, S.P., Gann, A., Levine, M. and Losick, R.(2008). Molecular biology of gene, Pearson. Benjamin Cummings, San Francisco, 6th edn. P.812-830.

Watson, S. M.D., Wright, N. G., Horrocks, B. R. and Houlton, A. (2010). Preparation and Characterization and Scanned Conductance Microscopy Studies of DNA-templated 1D Copper nanostructure. *Langmuir* 26, 2068-2075.

Watson, S.M.D, Hedley, S. H., Galindo, M. A., Al-said, S.A.F., Wright, N.G., Connolly, B. A., Horrocks, B. R. and Houlton, (2012). A. Synthetic, characterization of electronic properties of supramolecular DNA- templated polymer nanowires of 2, 5- (Bis-2-thienyl) pyrrole. *Chemistry- A European Journal*, 18 (38), 12008-12019.

Weibel, D. E., Vilani, B. C., Habert, A. C. and Achete, C. A. (2006). Surface modification of polyurethane membrane using RF-plasma treatment with polymerization and non-polymerizable gases, *Surfaceand Coatings Technology*, 201, (7) 4190-4194.

Winfree, E., Liu, F., Wenzler, L. A. and Seeman, N. C. (1998). Design and self-assembly of two dimensional DNA crystals,*Nature*, 394, 539-544.

Wu, Y., Fan, R., Yang, P. (2002). Block-by-block growth of single crystalline Si/SiGe superlattice nanowires. *Nano Letters*, 2, 83-86.

Xia, L., Wei, Z.X. and Wan, M. X. (2010). Conducting polymer nanostructure and their application in biosensors. *Journal of Colloid and interface Science*, 341, 1-11.

Xia, Y. N., Yang, P. D., Sun., Y. G., Wu, Y. Y., Mayers, B., Gates, B., Yin, Y. D., Kim, F. and Yan, Y. Q. (2003). One dimensional nanostructure: Synthesis, characterization and applications. *Advanced Mater*ials, 15, 353-389.

Xia, Y., Rogers, J. A., Paul, K. E. and Whitesides, G. M (1999). Unconventional methods for fabricating and patterning Nanostructures, *Chemical Review*, 99, 1823-1848.

Yan, M. and Bernstein, G. H. (2007). A quantitative method for dual-pass electrostatic force microscopy phase measurements. *Surface and Interface Analysis*,39, 354-358.

Yao, N. and Wang, Z. I. (2005). Handbook of microscopy for nanotechnology, 2005, Kluwer Academic Publishers, New York. P. 300-745.

Yokota, H., Sunwoo, J., Sarikaya, M., Van den, Engh, G., Aebersold (1999). Spin-Stretching of DNA and protein molecules for detection by fluorescence and atomic force microscop*y. Analytical Chemistry*,71, 4418-4422.

Zhang, B., Ye, X., Dai, W., Hou, W., Zou, F. and Xie, Y. (2006). Biomolecules-assisted synthesis of single crystalline Selenium nanowires and nanoribbons via a novel flake-cracking mechanism.*Nanotechnolog*y, 17, 385-390.

Zhong, Z., Ho, J., Tao, J., Shen, S. and Gedanken, A. (2007). Synthesis of porous α-Fe_2O_3 Nanorods and deposition of very small Gold particles in the pores for catalytic oxidation of CO. *Chemistry of Materials*, 19, 4776-4782.

Zhou, H., Park, T. J. and Wang, S. S. (2006). Synthesis, characterization and photocatalytic properties of pyrochlore $Bi_2Ti_2O_7$nanotubes. *Journal of Materials. Research*,2941-2947.

Zhou, Y., Freitag, M., Home, J., Staii, C., Johnson, A. T., Pinto, N. J. and MacDiamid, A. G. (2003). Fabrication and electrical characterization of polyaniline-based nanofibers with diameter below 30 nm. *Applied Physics Letters*, 83, 3800-3802.

Zubairu, S.M. J., Iyun, J. F., Gimba, C. E., Uzairu, A., Idris, O. S., Watson, S. M. D.and Horrocks, B. R. (2013). DNA-Inorganic materials preparation, characterization and microscopy and spectroscopy studies, postgraduate Chemistry Conference, University of York Postgraduate Chemistry Conference. 26th July.

APPENDICES

Plate A1.AFM of DNA/Ppy nanowires

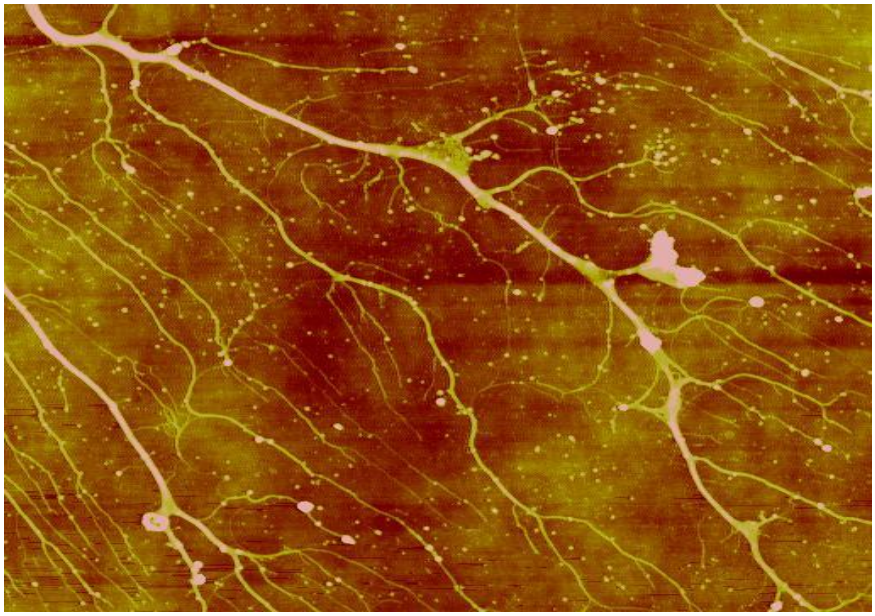


Plate A1 indicates, the generation of DNA/Ppy nanowires with uniform structures along with some bare DNA and polymer nanoparticles at the background.

Plate A2. AFM of DNA/Fe_2O_3nanowires

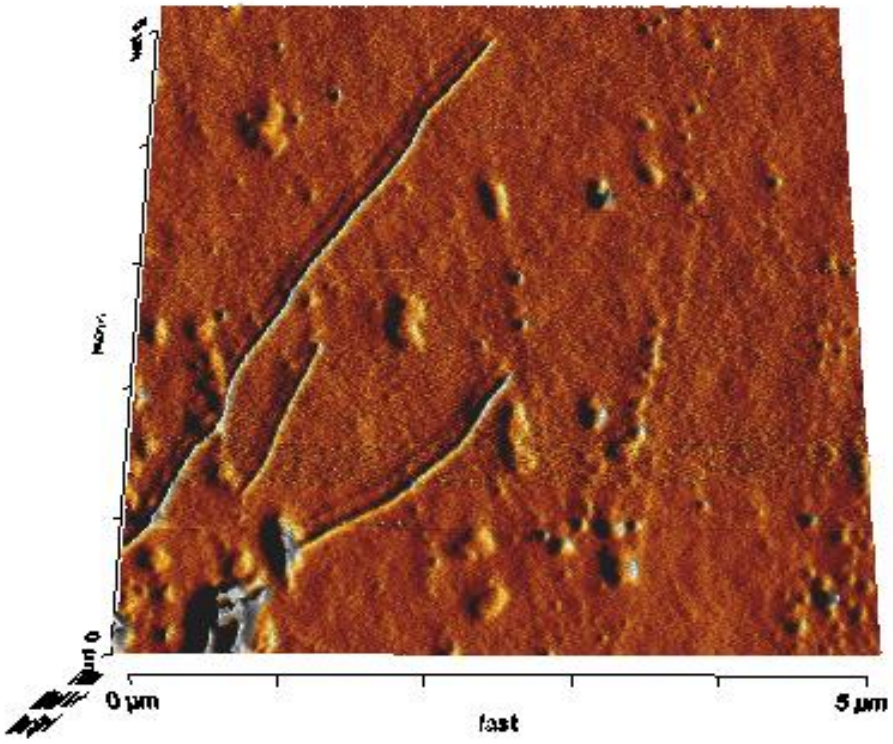


Plate A2 displayed the 3D image of DNA/Fe_2O_3nanowires with granular coverage of the Fe_2O_3 nanoparticles.

Plate A3. AFM for DNA/PIminanowires in 3D

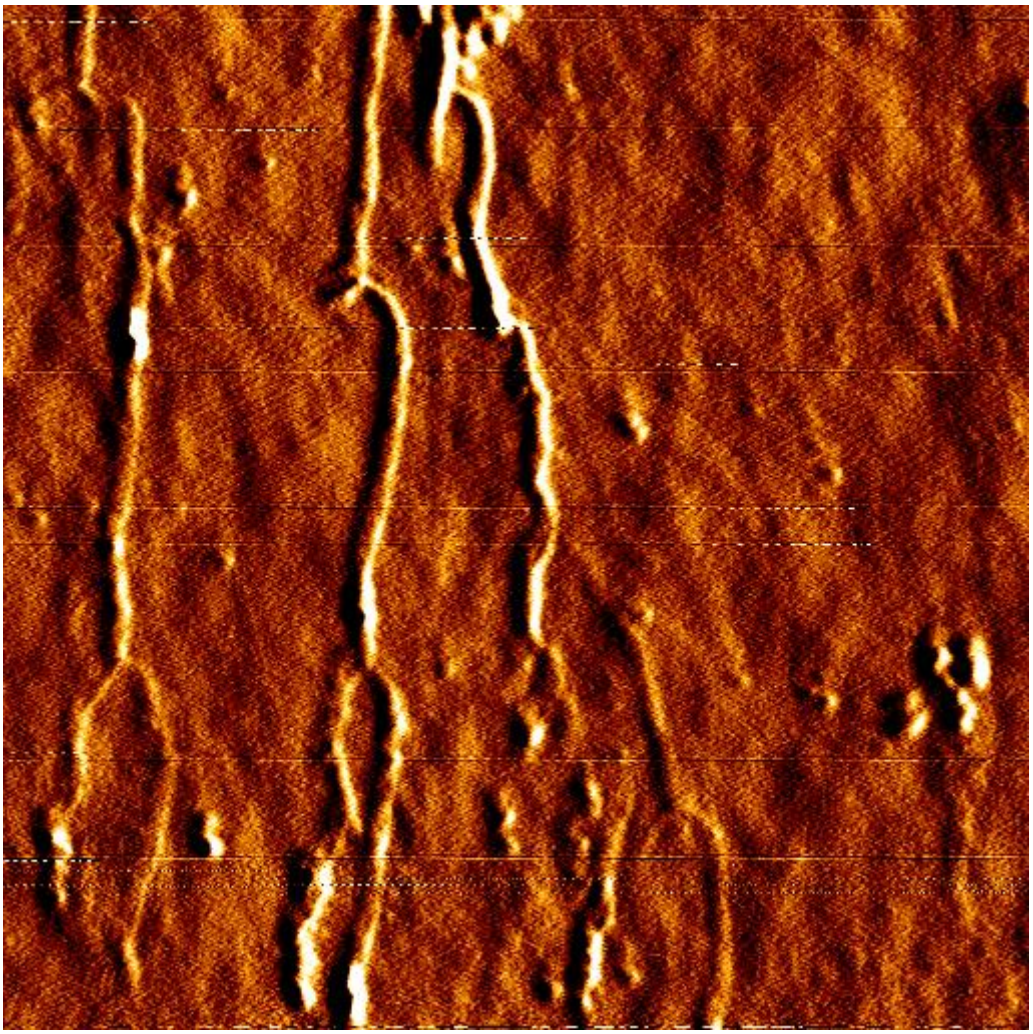


Plate A3 displayed the same 3D image of DNA/Fe_2O_3nanowires at different times, still with granular coverage of the Fe_2O_3 nanoparticles

Plate A4. AFM for DNA/FeOOH nanowires in 3D

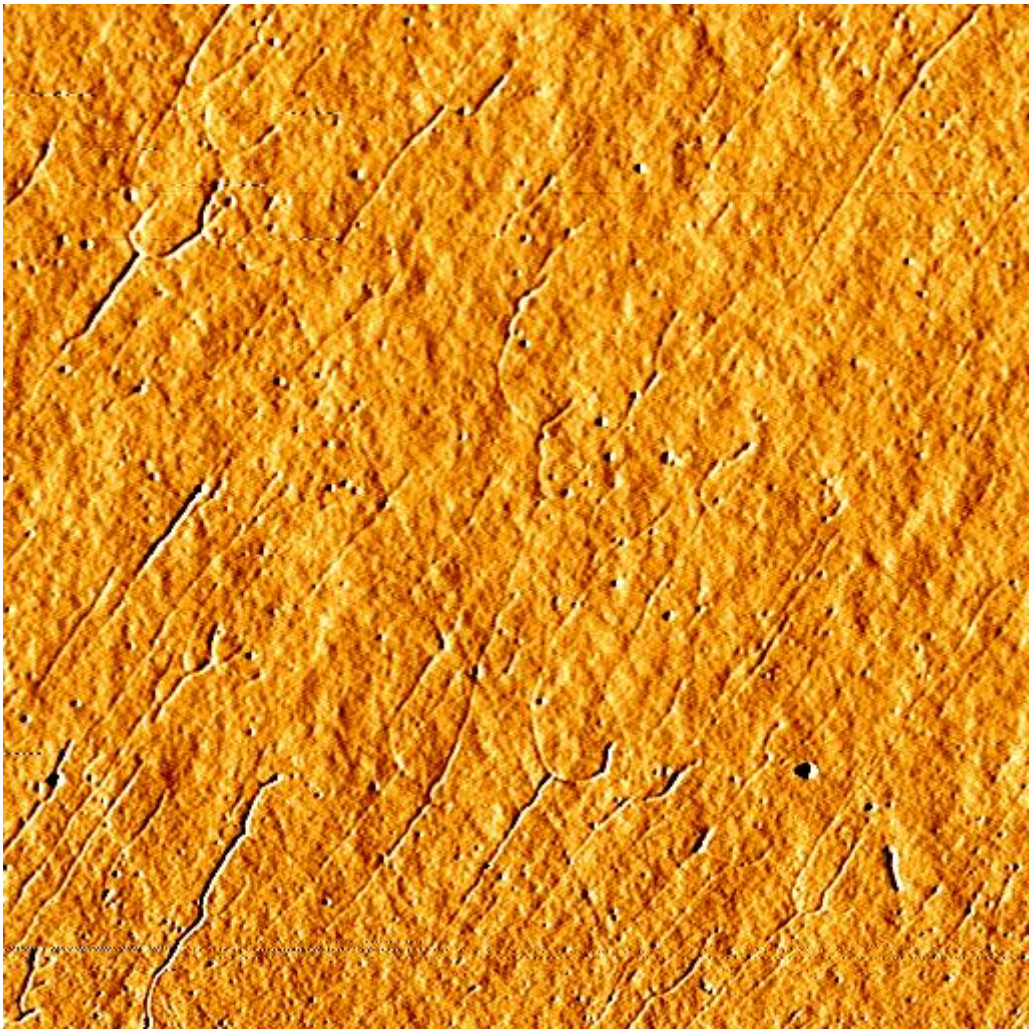


Plate A4 displayed 3D image of DNA/FeOOH nanowires with broken nanowires but evidences of uniform coverage of nanoparticle materials

Fig. A5. XPS for neat DNA as template

Figure A5 represent the XPS survey scan, elemental profile as elemental signals for neat DNA and the inset as percentage composition.

Plate A6. TEM image of DNA/ppy nanowires with spot of Ppy nanoparticles (white arrow)

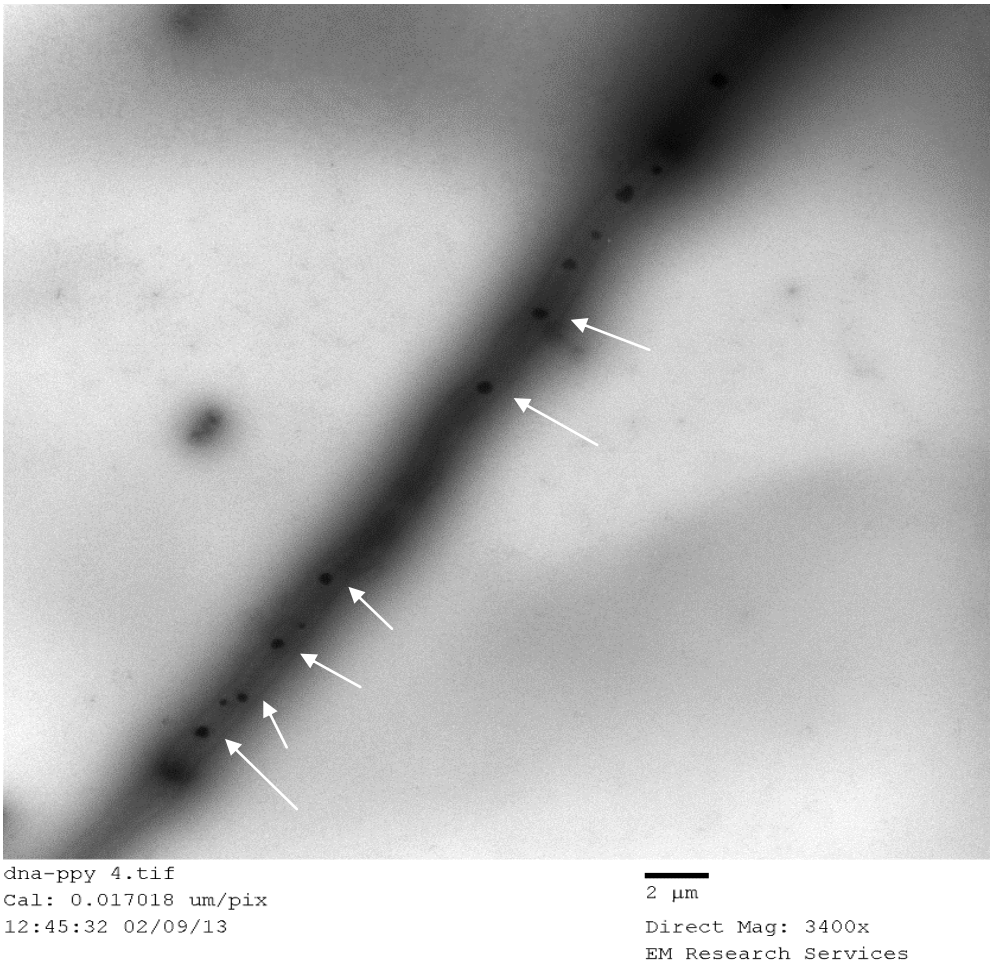


Plate A6 shows the beads-on-a-string morphology of DNA/Ppy nanowire

Fig. A7. TEM image of DNA/FeOOH.



Figure A7, with features of interest as the dendritic features; we believe they comprise ofFeOOH templated on DNA molecules

Fig. A8. TEM image of DNA/Fe_2O_3 nanowire

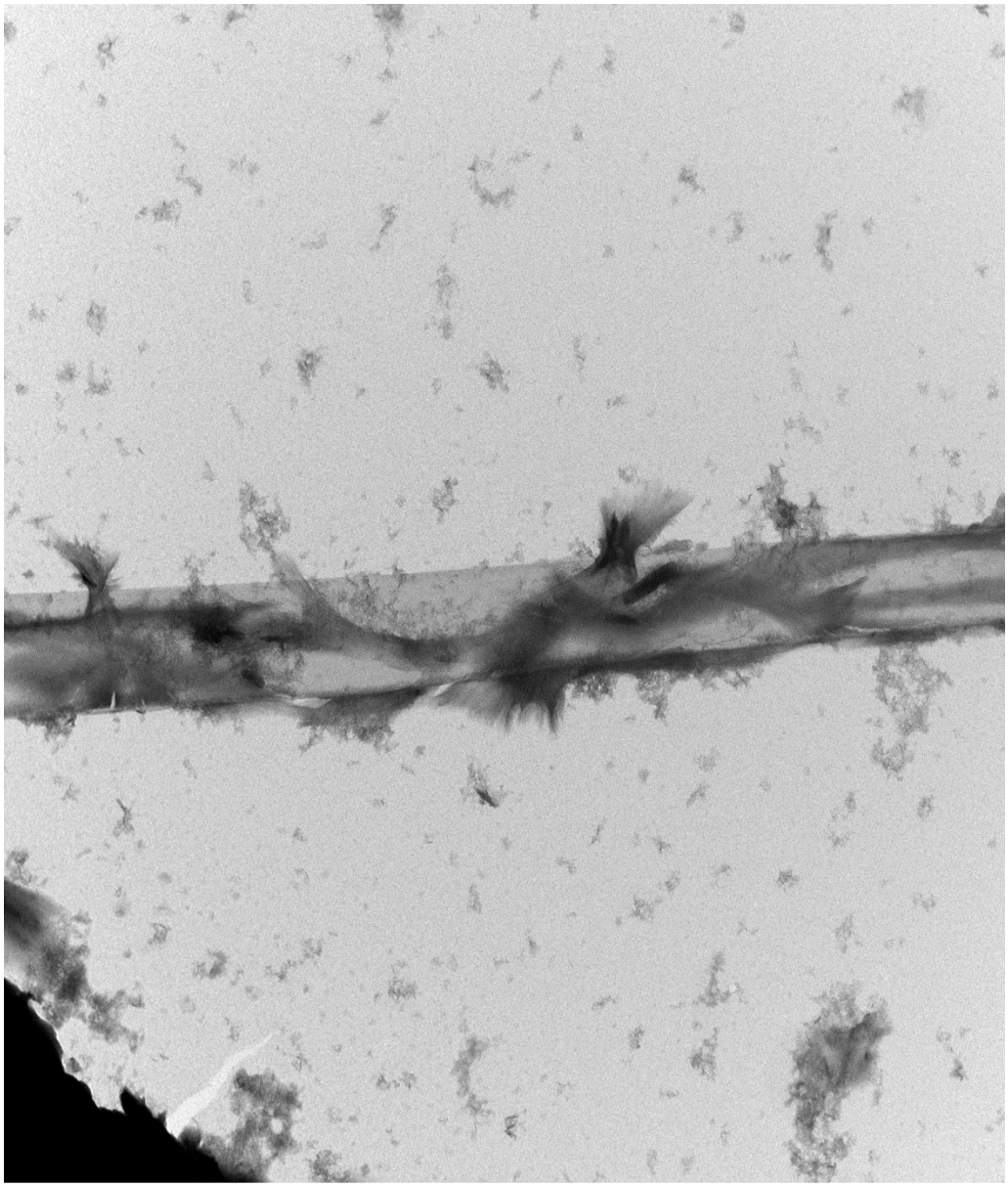
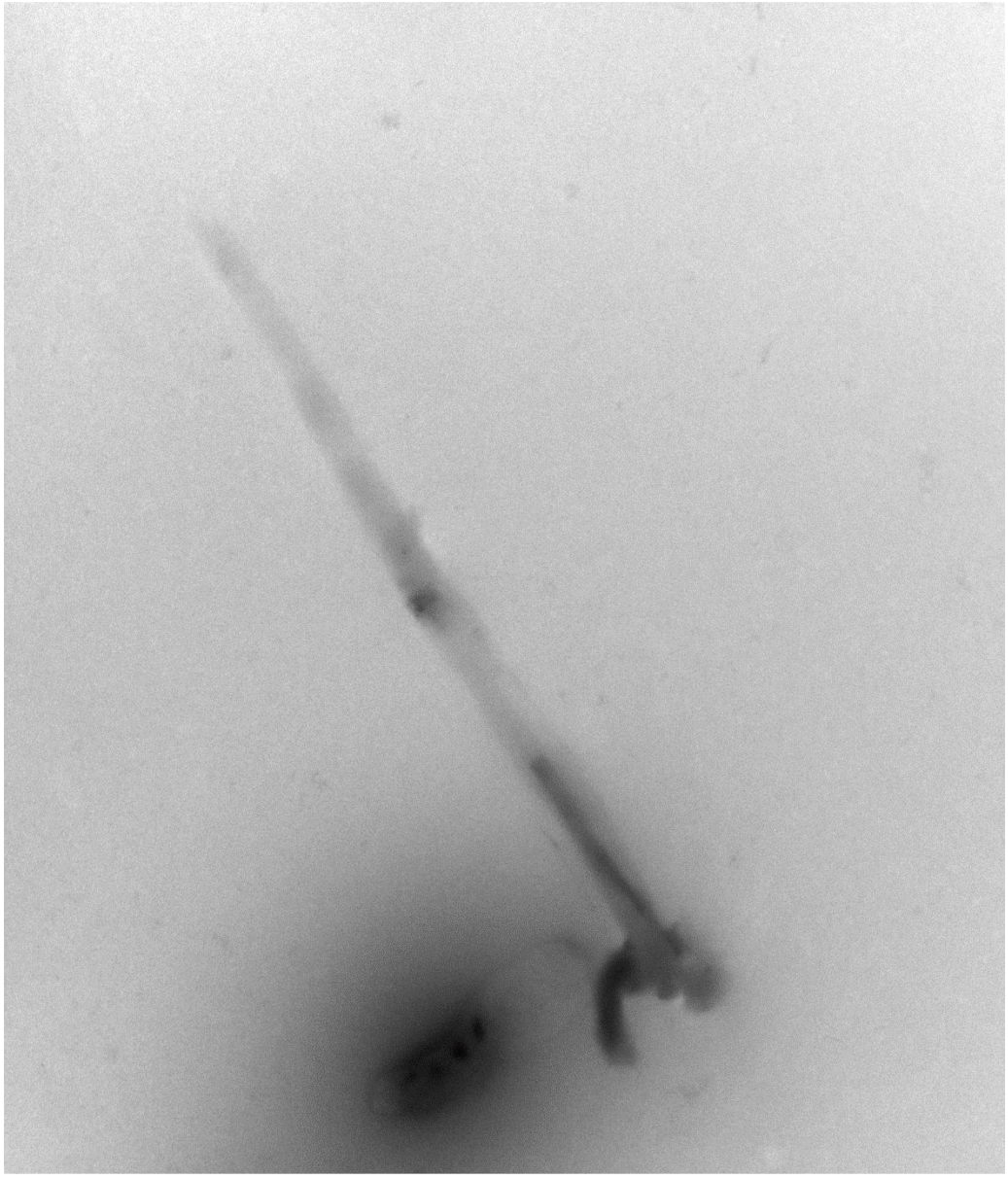


Fig. A9. TEM image for DNA/PImi nanowire



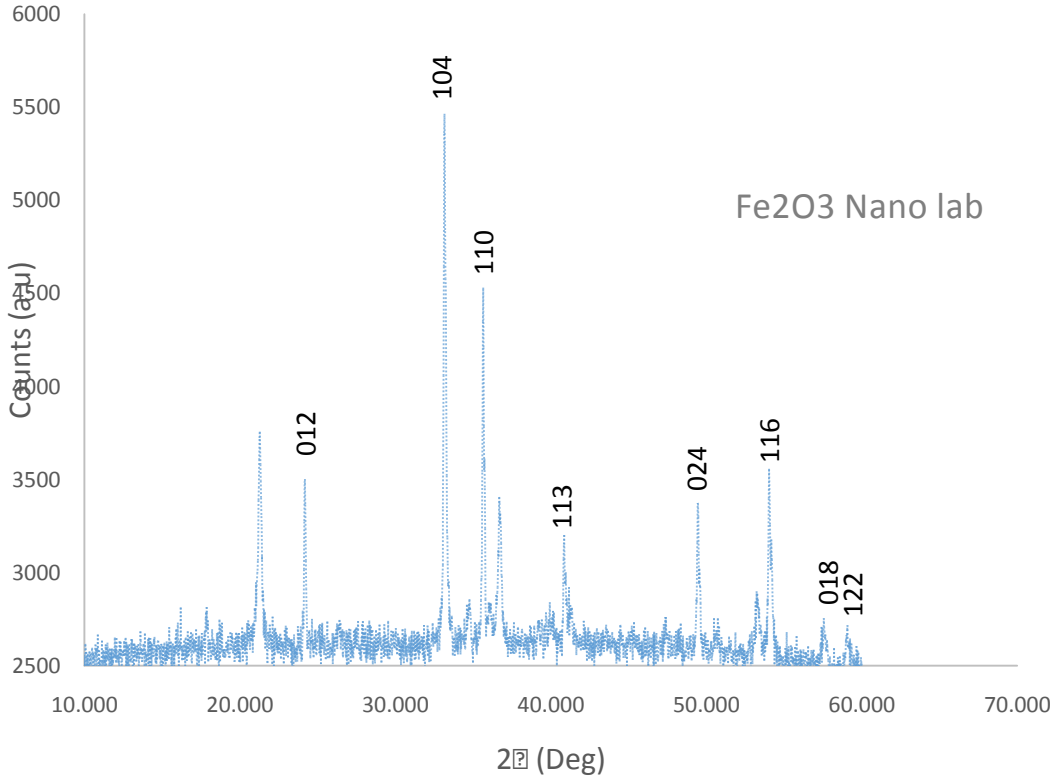


Fig. A10. XRD of FeOOH nanoparticles transformed at 400 ^{o}C into Fe_2O_3 nanoparticles

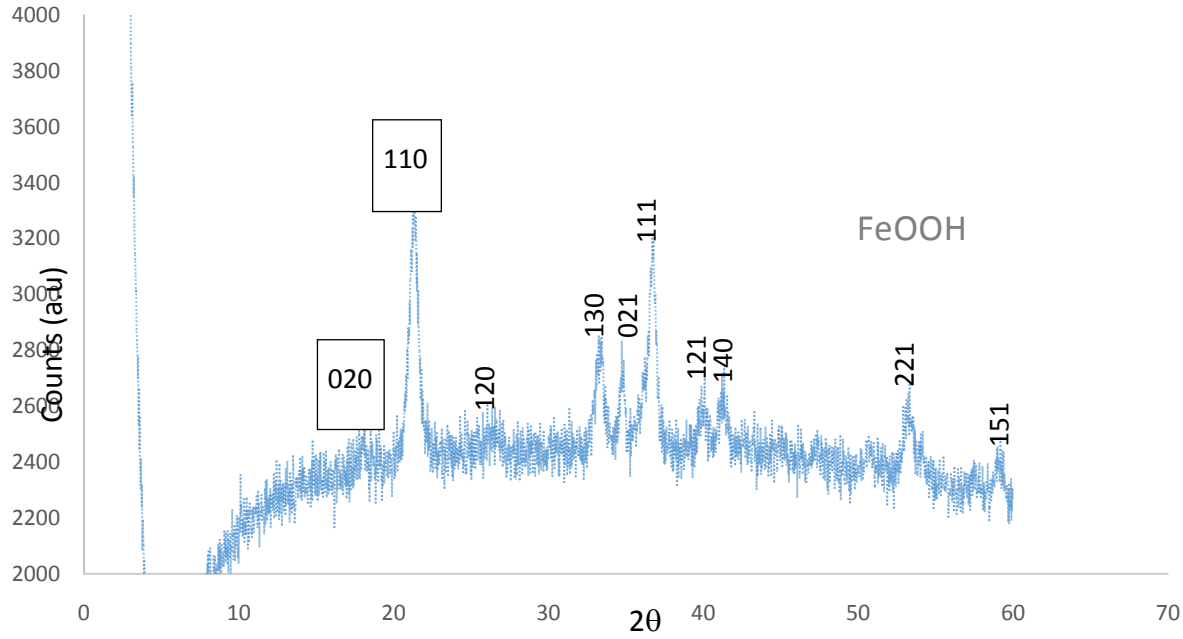


Figure A10 shows theXRD patterns of Fe_2O_3 nanoparticles (top) formed after calcining FeOOHat 400 ^{o}C with same diffraction patterns with the synthetic Fe_2O_3 nanoparticles

Fig. A11. Rama spectra of FeOOH and Fe_2O_3 nanoparticles.

Figure A11 shows the Raman spectra of FeOOH (top) and Fe_2O_3 (below) nanoparticles measured in this work as complimentary data. For FeOOH, strong peak at 377 cm^{-1} and 682 cm^{-1} is easy to distinguish from other ferrite.It corresponds to the spectra shown by Oh *et al*., (1998). The Fe_2O_3nanoparticles are also measured with well-established Oh *et al*., (1998),bands at 247, 263, 473 cm^{-1}

Fig. A12. FTIR for bare DNA drop-casted as solid on Silicon wafer.

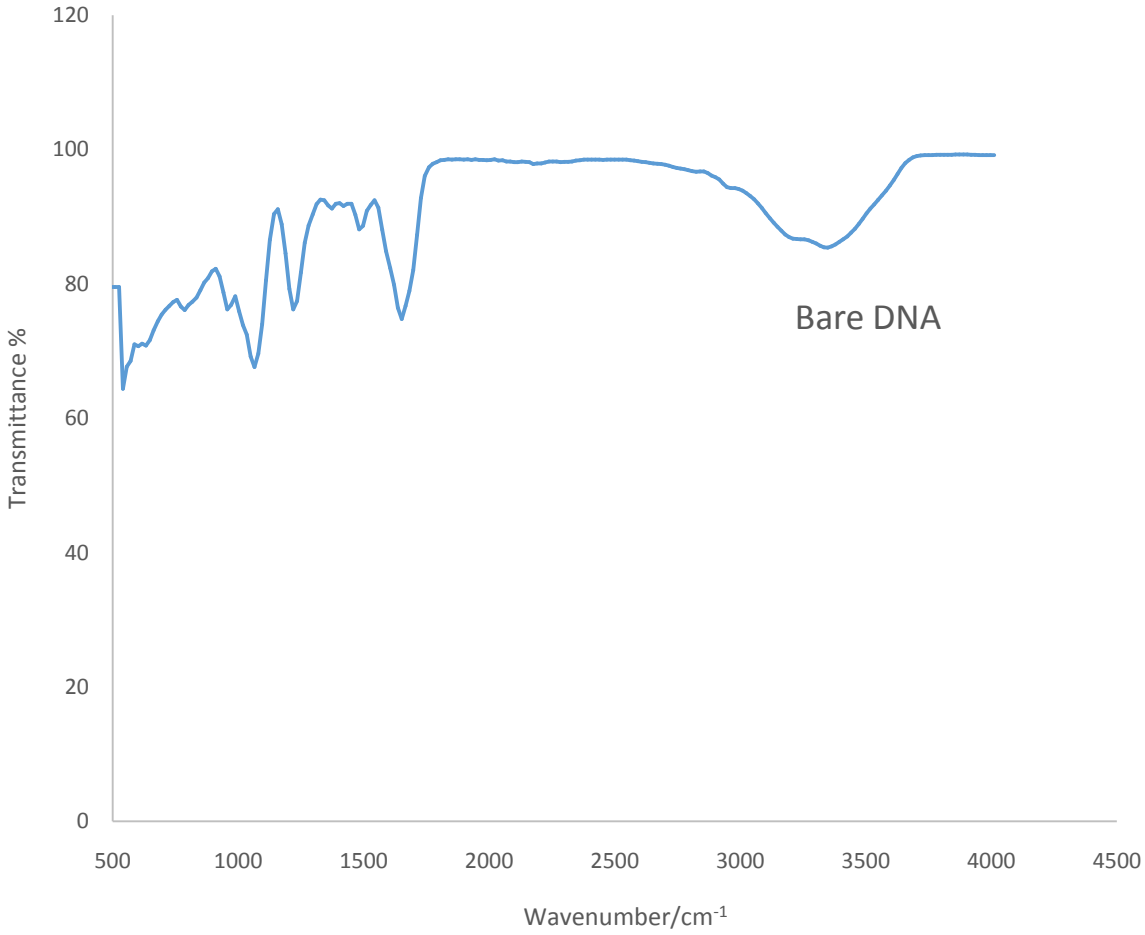


Fig. A13. TG/DTA/DSC for FeOOH with m/z for H_2O and CO_2

Fig. A14. TG/DTA/DSC for Fe_2O_3 with m/z for H_2O only